

Laser Link Acquisition for the GRACE Follow-On Laser Ranging Interferometer

Der Fakultät für Mathematik und Physik der
Gottfried Wilhelm Leibniz Universität Hannover
zur Erlangung des Grades

Doktor der Naturwissenschaften
- Dr. rer. nat -

genehmigte Dissertation
von

Dipl. -Phys. Christoph Mahrtdt
geboren am 29. Januar 1983 in Lemgo

2014

Referent: Prof. Dr. Karsten Danzmann (Leibniz Universität Hannover)
Korreferent: Prof. Daniel Shaddock (Australian National University, Canberra)
Tag der Promotion: 28.01.2014

Abstract

GRACE Follow-On is a space mission consisting of two spacecraft in a Low Earth orbit that map the gravitational potential of the Earth by continuously measuring changes in their relative separation. In addition to the main microwave ranging instrument, GRACE Follow-On will carry a laser ranging interferometer (LRI) as a technology demonstrator. The LRI, as well as GRACE, is a US-German collaboration with substantial contributions from AEI. The work presented in this thesis is concerned with the development of an acquisition procedure for the LRI on GRACE Follow-On.

Laser link acquisition is the process of reducing possibly large biases in the alignment of the laser beam axes and the laser frequency, such that tracking of the satellites can be initiated. Successful laser link acquisition is an essential first step to enable science operation. Due to tight constraints on available resources, GRACE Follow-On does not carry dedicated acquisition hardware such that the heterodyne signals of the science photodiode have to be utilised. Additionally, no direct communication between the satellites is available. Without dedicated hardware, laser link acquisition is a search in five-degrees of freedom over a possibly large uncertainty space.

In this thesis, a detailed analysis of laser link acquisition using only heterodyne signals is given. A comprehensive analysis of the tilt dependence of the interferometer signals is carried out. This involves the simulation of tophat beams and fibre modes for which the common approximation by Gaussian fundamental modes does not hold. For this reason, the mode expansion method was implemented in IFOCAD and successfully applied to the simulation of tophat beams and the fundamental fibre mode. For the latter case, a realistic model of the electric field distribution at the distant spacecraft could be obtained. Furthermore, a data processing algorithm was designed for the detection of the heterodyne signal and extensively analysed to obtain the distribution of its output in the presence of noise. The models of the signals and the data processing are henceforth combined with models of the instrument subsystems to develop a high-fidelity simulation of the LRI.

This sophisticated simulation tool is used to investigate an initial line-of-sight calibration scan to reduce the large initial angular and frequency biases, to ease a subsequent autonomous laser link acquisition. Along with an in-depth analysis of spatial scan patterns to cover the angular uncertainty cone, realistic timing and accuracy estimates could be obtained as well as limits to the scan resolution.

Finally, an algorithm was developed for the autonomous laser link acquisition, which is able to acquire the heterodyne signal starting from the smaller alignment biases that remain after the initial line-of-sight calibration and initiate tracking. This is done, autonomously without the need for communication between the satellites. The proposed algorithm is tested with the high-fidelity simulation for a broad range of parameters and was found suitable regarding its high success rates of more than 99 %.

The results of the work described in this thesis have been used to define the baseline acquisition procedure for the LRI within the GRACE Follow-On project.

Keywords: GRACE Follow-On, laser link acquisition, mode expansion method

Kurzzusammenfassung

GRACE Follow-On ist eine Satellitenmission zur Vermessung des Erdschwerefeldes, bestehend aus zwei Satelliten die kontinuierlich kleine Änderungen ihres gegenseitigen Abstandes vermessen. Zusätzlich zu dem Hauptmessinstrument, welches den Abstand mit Mikrowellen vermisst, wird GRACE Follow-On ein Laserinterferometer (LRI) als Technologiedemonstrator tragen. Das LRI ist, wie auch GRACE, eine US-deutsche Zusammenarbeit mit wesentlichen Beiträgen vom AEI. Die vorliegende Arbeit befasst sich mit "Laser Link Akquisition" für das LRI an Bord von GRACE Follow-On.

Laser Link Akquisition bezeichnet die Ausrichtung der Laserstrahlen und das Einstellen der Laserfrequenz, so dass ein Heterodynsignal detektiert werden kann. Die anfängliche Ausrichtung der Laserstrahlen und Laserfrequenz nach dem Start, können dabei stark von den optimalen Werten abweichen. Eine erfolgreiche Laser Link Akquisition ist notwendig um den Wissenschaftsbetrieb aufnehmen zu können. GRACE Follow-On wird keine zusätzlichen Instrumente tragen oder eine direkte Kommunikation zwischen den Satelliten ermöglichen, um diesen Prozess zu vereinfachen, so dass allein das Heterodynsignal zur Verfügung steht. Ohne spezielle Instrumente muss ein fünf dimensionaler Parameterraum nach dem Signal durchsucht werden.

In dieser Arbeit wird eine detaillierte Analyse der Laser Link Akquisition für GRACE Follow-On vorgestellt. Eine Analyse der Abhängigkeit der Interferometersignale von der Strahlachsenverkipfung unter Berücksichtigung von nicht-Gaussischen Strahlen wird präsentiert, für deren Simulation die Zerlegung in höhere Gaussmoden in der am AEI entwickelten Software IFOCAD implementiert wurde. Dieses ermöglichte die Simulation von nicht-Gaussischen Strahlen wie z.B. Tophat Strahlen oder Fasernmoden. Hiermit konnte ein realitätsgetreues Modell der Intensitätsverteilung im Fernfeld entwickelt werden.

Außerdem wurde ein Algorithmus für die Detektion des Heterodynsignals analysiert, um die Verteilung seiner Ausgabewerte zu bestimmen. Die Modelle für die Interferometersignale und den Detektionsalgorithmus wurden mit Modellen für Subsysteme des LRI benutzt um eine realitätsgetreue Simulation des LRI zu entwickeln. Die Simulation wird in dieser Arbeit benutzt um eine Kalibration der Sichtlinie zu untersuchen, die die anfänglich großen Unsicherheiten in der Strahlausrichtung und Laserfrequenz reduzieren soll. Zusammen mit einer ausführlichen Analyse von möglichen Abtastschemas für die Ausrichtung der Laserstrahlen wurden Schätzungen der benötigten Zeit und Genauigkeit, sowie Grenzen der Auflösung der Abtastschemas bestimmt.

Zum Schluss dieser Arbeit, wird ein entwickelter Algorithmus für die autonome Laser Link Akquisition vorgestellt, der in der Lage ist unabhängig vom zweiten Satelliten, von anfänglichen Fehlern in der Strahlausrichtung, das Heterodynsignal zu detektieren und die automatische Verfolgung des Partnersatelliten zu starten. Der vorgestellte Algorithmus wird mit Hilfe der entwickelten Simulation des Laserinterferometers für eine große Auswahl an Parameterwerten getestet und ist in mehr als 99 % erfolgreich.

Die Ergebnisse dieser Arbeit wurden benutzt, um die grundlegende Prozedur für Laser Link Akquisition für das LRI von GRACE Follow-On zu definieren.

Schlagnworte: GRACE Follow-On, Laser Link Akquisition, Modenzerlegung

Contents

Abstract	i
Kurzzusammenfassung	i
Contents	v
List of Figures	ix
List of Tables	xiii
List of Abbreviations	xvi
1. Introduction	1
1.1. Aim and Structure of the Thesis	3
2. Mode Expansion Method for Optical Simulations of Precision Interferometers	5
2.1. Heterodyne Signals	5
2.1.1. Heterodyne Photocurrent and Heterodyne Efficiency	7
2.1.2. Heterodyne Signals	11
2.2. Simulation of Interferometers by Gaussian Beam Tracing	12
2.3. Mode Expansion Method	16
2.4. Propagation of Tophat Beams	26
2.4.1. Decomposition of Tophat beams	27
2.4.2. Fresnel Diffraction of Tophat Beams	31
2.4.3. Far-Field Intensity Distribution of Tophat Beams	36
2.4.4. On-Axial Electric Field	38
2.4.5. Expression for the Required Mode Order	41
2.5. Propagation of the Fundamental Fibre Mode	42
2.5.1. A Brief Introduction to Fibre Modes	43
2.5.2. Propagation of $LP_{0,1}$ with the Mode Expansion Method	48
2.5.3. GRACE Follow-On Far-Field Intensity Pattern	52
2.5.4. Analytical Model for the Far-Field Intensity Pattern	55
2.6. Conclusions	57

3. Laser Link Acquisition for Inter-Satellite Laser Interferometers	61
3.1. Introduction	61
3.1.1. Previous Work on Laser Link Acquisition	62
3.1.2. Laser Link Acquisition for GRACE Follow-On	63
3.2. GRACE Follow-On Laser Ranging Interferometer	65
3.3. Sensor Signals	68
3.3.1. Heterodyne Photocurrent	68
3.3.2. Effective Received Power	71
3.3.3. Heterodyne Efficiency	73
3.3.4. Received Power	75
3.3.5. Differential Wavefront Sensing	77
3.4. Noise Sources	78
3.4.1. Additive Noise Sources	78
3.4.2. Non-Additive Noise Sources	82
3.5. Beatnote Frequencies	84
3.6. Acquisition Schemes	86
3.7. Conclusions	87
4. Detection Algorithm, Signal- and Noise Distributions	89
4.1. Detection Algorithm	90
4.1.1. Maximum Likelihood Estimator for the Heterodyne Signal Param- eters	90
4.1.2. Detector for the Heterodyne Signal	92
4.2. Signal and Noise Distributions	96
4.2.1. Distribution of a Single Channel	97
4.2.2. Distributions of the Coherent Sum of Photodiode Segments	102
4.2.3. Distribution of Incoherently Summed Channels	104
4.3. Distribution of the Detector Output	107
4.3.1. Probability Distribution of the Detector Output	107
4.3.2. Noise RMS of the Detector Output	111
4.4. Distribution of the Detector Output for Time Dependent Frequency . . .	115
4.4.1. Constant Arbitrary Frequency	115
4.4.2. Distribution of the Detector Output with Frequency Noise	118
4.4.3. Distribution of the Detector Output with a Linear Frequency Sweep	122
4.5. Conclusions	124

5. High-Fidelity Simulation of the GRACE Follow-On Laser Ranging Interferometer	127
5.1. Overview	127
5.2. Model of the Laser Ranging Interferometer	129
5.2.1. Optical Bench Layout	129
5.2.2. Fine-Steering Mirror	130
5.2.3. FSM DWS Control Loop	133
5.2.4. Laser	134
5.2.5. Phasemeter	137
5.2.6. Frequency Response of the Quadrant Photodiodes	138
5.3. Signal Calculation	139
5.4. Detection Algorithm	140
5.4.1. Detection Algorithm for Constant Amplitude	141
5.4.2. Detection Algorithm for Varying Amplitude	143
5.5. Conclusions	145
6. Initial Line-of-Sight Calibration	147
6.1. Spatial Scan Patterns for the Initial LOS Calibration	147
6.1.1. Scan Patterns	148
6.1.2. Synchronising the Spatial Scans	155
6.1.3. Fast Spatial Scan	157
6.1.4. Slow Spatial Scan	159
6.2. Frequency Scan, Scan Order and Total Acquisition Time	162
6.3. Detector Signals for the Initial LOS Calibration	166
6.3.1. Effective Heterodyne Efficiency for the CS and ICS	167
6.3.2. Effective Received Power for the CS and ICS	171
6.3.3. Variation of the Heterodyne Efficiency	173
6.4. Maximum LOS-to-Scan Track Separation	177
6.5. Distributions of the Found Maxima	186
6.6. Conclusions	194
7. Autonomous Laser Link Acquisition	197
7.1. Introduction	197
7.2. Signals and Thresholds	199
7.2.1. Detector Signal for Autonomous Laser Link Acquisition	200
7.2.2. Threshold Selection for the CS Detector	203
7.2.3. A Naive Approach	205

7.2.4. An Improved Approach	207
7.2.5. Thresholds for the Three Far-Field Distributions	209
7.3. Spatial Scan for the Autonomous Laser Link Acquisition	210
7.4. Proposed Algorithm and State Diagram	215
7.4.1. Initialisation Phase	221
7.4.2. Scanning Phase and Detection	222
7.4.3. Signal Verification Phase	222
7.4.4. Centring the Beatnote Frequency on the Slave Spacecraft	223
7.4.5. Initiate Tracking	224
7.4.6. Buffer State and Decision State	225
7.5. Results	227
7.5.1. Fibre Mode Far-Field	228
7.5.2. Gaussian Beam, $M^2 = 1$	231
7.5.3. Gaussian Beam, $M^2 = 1.2$	232
7.5.4. Summary of Simulation Runs	233
7.5.5. Time-Outs and Failures	235
7.6. Conclusions	238
8. Summary and Conclusions	239
A. Normalisation of LP fibre modes	243
B. Some Statistics	247
B.1. CDF of the noncentral χ^2 -distribution	247
B.2. Transforming a PDF	248
Bibliography	249
List of publications	261
Acknowledgements	263
Curriculum Vitae	263

List of Figures

2.1. Simplified sketch of an inter-spacecraft heterodyne interferometer	6
2.2. Sketch of a quadrant photodiode and schematic of the photocurrent measured on a single segment	7
2.3. DWS signal caused by horizontal misalignment of the RX and LO beam axes	11
2.4. Geometry of the fundamental Gaussian beam	14
2.5. Explanation of Gaussian beam tracing	16
2.6. Intensity distributions of the first Hermite- and Laguerre Gaussian modes	18
2.7. Beam tracing of non-Gaussian beams	22
2.8. Generation and propagation of a circular symmetric tophat beam	27
2.9. Power in approximated Tophat beam depending on the waist radius and maximum mode order of the modal set	29
2.10. Intensity cross-section of decomposed tophat beam and mode amplitudes of series expansion	30
2.11. optimum waist radius and Rayleigh range for decomposition of tophat beam	32
2.12. Electric field amplitude of propagated tophat beam in Fresnel region . . .	33
2.13. Electric field amplitude of propagated tophat beam in Fresnel region, continued	34
2.14. Far-field intensity distribution for the propagated tophat beam	37
2.15. Deviation of the on-axis electric field of the tophat beam	39
2.16. Power in fundamental Gaussian mode for decomposition and on-axial electric field for two goodness-of-fit criterion	40
2.17. Cross sectional amplitude profile of the $LP_{0,1}$ fibre mode	47
2.18. Coupling coefficients for the two $LP_{0,1}$ modes and cross-section of amplitude distribution	50
2.19. Intensity pattern of the propagated Hermite-Gaussian expansion of the LP_{01} compared to analytical far-field intensity	51
2.20. Schematic of the simulated setup for the generation of the fibre mode far-field	53

2.21. Intensity pattern of LP ₀₁ behind the end-face of the fibre outcoupler and far-field distribution with clipping	54
2.22. Comparison of the far-field intensity between the analytical model and the mode-expanded	56
3.1. Schematic of acquisition spatial and frequency scan	64
3.2. GRACE Follow-On laser ranging interferometer	65
3.3. Triple-mirror assembly and fine-steering mirror coordinate system	67
3.4. Dimensions and labels of a quadrant photodiode and combination of segments to channels	69
3.5. Local and remote misalignment angles	71
3.6. Single segment heterodyne efficiency for segments A and B	73
3.7. Far-field intensity distributions	76
3.8. DWS signal caused by horizontal misalignment of the RX and LO beam axes	77
3.9. Single channel and coherent sum noise equivalent effective received power depending on local oscillator power	81
3.10. Orbit prediction error: time series and spectra	83
3.11. Beatnote frequencies and Doppler shift	85
4.1. Mean-shift Gauss-Gauss and Receiver Operating Characteristic	93
4.2. Left: Detection algorithm and further processing	95
4.3. Chi-square probability density function and cumulative distribution function	99
4.4. Noncentral chi-square probability density function and cumulative distribution function	101
4.5. Distribution of the detector output: probability density and cumulative distribution function	110
4.6. Normalised noise RMS of maximum detector output	113
4.7. Normalised amplitude response of a DFT and scalloping loss	116
4.8. Distribution of detector output for constant arbitrary frequency	117
4.9. Frequency noise, amplitude spectral density and time series	119
4.10. Distribution of detector output for a signal with frequency noise	120
4.11. Distribution of detector output for signal with frequency sweep	122
5.1. Overview over simulated satellite model	128
5.2. Optical bench layout implemented into the discrete-time simulation	129
5.3. Fine-steering mirror transfer function and step response	132

5.4. Block diagram of the implemented DWS control loop	133
5.5. Methods to compute differential wave front sensing signal and step re- sponse of control-loop	135
5.6. Laser thermal actuator: transfer function and step response	136
5.7. State diagram of a phase-lock loop and complete phasemeter	138
6.1. Explanation of spatial scan terminology	149
6.2. Hexagonal spatial scan	150
6.3. Archimedean spiral scan	152
6.4. Lissajous raster scan	153
6.5. Maximum LOS-to-scan-track separation during Lissajous scan	154
6.6. Synchronising the Spatial Scans	156
6.7. Scan time fast scan, scan points slow scan	159
6.8. Total scan time for a complete four dimensional spatial scan	162
6.9. Total scan time for a five-dimensional LOS calibration scan	164
6.10. Frequency sweep rates during line-of-sight calibration scan	165
6.11. Detection Algorithm for initial line-of-sight calibration scan	167
6.12. Effective heterodyne efficiency for the coherent and incoherent sum of the phasemeter channels	169
6.13. Cross-sectional plot of the coherent and incoherent sum heterodyne effi- ciencies	171
6.14. Local and Remote beam axis tilt	172
6.15. Object and imaging planes of the imaging system and curvature error in the wave front	173
6.16. Coherent and Incoherent sum heterodyne efficiency for change in local oscillator waist radius	174
6.17. Coherent and Incoherent sum heterodyne efficiency for change in the slit width of the quadrant photodiode	175
6.18. Coherent and Incoherent sum heterodyne efficiency for an additional cur- vature error in the phasefront	176
6.19. Explanation of the calculations done to find the maximum simultaneous scan track separation	179
6.20. Maximum allowable LOS-to-scan-track separation for varied spacecraft separation and transmitted power	182
6.21. Loss of effective received power due to local and remote beam axis tilts .	183

6.22. Maximum allowable LOS-to-scan-track separation for varied beam quality factor and scan speed	184
6.23. Distribution of the TX beam angles	188
6.24. Distribution of the carrier-to-noise density	190
6.25. Percentage of simulation runs with excess misalignments	191
6.26. Distribution of the TX beam angles for TMA coalignment error and larger DFT size	192
6.27. Distribution of carrier-to-noise density for TMA coalignment error and larger DFT size	193
7.1. Comparison of the effective received power for autonomous acquisition . .	201
7.2. Two methods how to choose the coherent sum threshold	206
7.3. Chose threshold for coherent sum detector for Gaussian beam far-fields . .	208
7.4. Concept of the slipping scan	210
7.5. Geometry of the Lissajous scan and LOS scan track separation over frequency ratio	212
7.6. Synchronise the two slipping Lissajous scans	213
7.7. Time series plots to visualise acquisition process	216
7.8. State diagram for the acquisition algorithm of the slave satellite	217
7.9. State diagram for the acquisition algorithm of the master satellite	218
7.10. Time series of an acquisition process for motivating the buffer state	225
7.11. Close-up of time series of an acquisition process for motivating the buffer state	226
7.12. Simulation results for the fibre mode far-field	230
7.13. Simulation results for a Gaussian beam with beam quality factor $M^2 = 1.0232$	
7.14. Simulation results for a Gaussian beam with beam quality factor $M^2 = 1.2233$	
7.15. Signal loss during the beatnote centring	237

List of Tables

2.1. Summary of the specified and computed values of the CORNING PM98-U25A PANDA fibre	47
3.1. Overview of the salient parameters for the beams, photodiode and the optical bench used in this analysis	67
3.2. Noise equivalent current and Relative Intensity Noise	79
3.3. Noise floor, \hat{P}_{RX}^{noise} , in the DFT frequency bins	82
4.1. Normalised noise RMS of the maximum of the CS and ICS detector output	114
4.2. Maximum frequency sweep rates for FFTs of different size	124
5.1. List of the main optical components of the optical bench model	130
5.2. Laser thermal actuator pole-zero model	137
6.1. Maximum scan speeds of the Lissajous scan	155
6.2. Default parameters used in the determination of the minimum scan resolution	178
6.3. Maximum allowable simultaneous misalignments	185
6.4. Default parameters used to determine distributions of residual misalignments	186
7.1. Summarising the maximum simultaneous misalignments and thresholds .	209
7.2. Global constants used to control the acquisition algorithm	221
7.3. Spatial scan parameters for autonomous acquisition scan	228
7.4. Default parameters used for the simulations of the autonomous laser link acquisition	229
7.5. Ranges of the randomised parameters in the simulation runs	229
7.6. Summary of simulation outcomes	234

List of Abbreviations

AC	Alternating Current
ADC	Analogue-to-Digital Converter
AEI	Albert Einstein Institut
ANU	Australian National University
AOCS	Attitude and Orbit Control System
APD	Avalanche photodiode
AWGN	Additive White Gaussian Noise
B.V.	Frequency Bin Veto in the Detection Algorithm
CCD	Charge-coupled Device
CDF	Cumulative Distribution Function
CHAN	Single Phasemeter Channel
CS	Coherent Sum of Phasemeter Channels
DC	Direct Current
DFT	Discrete Fourier Transform
DWS	Differential Wavefront Sensing
FFT	Fast Fourier Transform
FOV	Field of View
FSM	Fine-Steering Mirror
GRACE	Gravity Recovery and Climate Experiment
ICS	Incoherent Sum of Phasemeter Channels
IfoCad	A software package developed at the AEI to simulate 3D interferometer setups
IID	Independent and Identically Distributed
IIR	Infinite Impulse Response

JPL	Jet Propulsion Laboratory
LISA	Laser Interferometer Space Antenna
LO	Local Oscillator
LOS	Line Of Sight
LP	Linear Polarised (Fibre Modes)
LRI	Laser Ranging Interferometer
MEM	Mode Expansion Method
MLE	Maximum Likelihood Estimator
NA	Numerical Aperture
NASA	National Aeronautics and Space Administration
Nd:YAG	Neodymium-Doped Yttrium Aluminum Garnet
NEI	Noise Equivalent Current
NPRO	Non-Planar Ring Oscillator
PD	Photodiode
PDF	Probability Density Function
PSD	Power Spectral Density
QPD	Quadrant Photodiode
RIN	Relative Intensity Noise
RMS	Root Mean Square
ROC	Receiver Operating Characteristic
RTP	Right Tail Probability function
RX	Receive Beam
SCA	Star-Camera Assembly
SNR	Signal to Noise Ratio
STI	SpaceTech GmbH, Immenstaad
TMA	Triple-Mirror Assembly
TX	Transmitted Beam

1. Introduction

Inter-satellite laser interferometry is envisaged as the next generation technology for inter-satellite ranging. The development of laser interferometers for space missions that exchange laser light over hundreds or even millions of kilometers is highly demanding. However, it promises to enable measurements of gravitational waves and mapping of Earth's gravitational potential with unprecedented accuracy.

This thesis is written in the context of eLISA, a mission proposed to the European Space Agency (ESA) to measure gravitational waves, and GRACE Follow-On, a planned successor to the Gravity Recovery and Climate Experiment (GRACE), that is scheduled for launch in 2017. The following two sections will shortly introduce these two missions before the aim and structure of this thesis is given.

Measuring Gravity with GRACE Follow-On

The Gravity Recovery and Climate Experiment (GRACE) was launched in 2002 to measure Earth's gravitational potential on a global scale [Ada02, TBWR04]. GRACE consists of two satellites that fly in a low Earth orbit at an altitude of approximately 400 km. Their mean separation is 200 km and varies due to changes induced by variations in the gravitational potential. GRACE maps the gravitational potential by continuously measuring the distance changes between the two satellites by a microwave ranging instrument with a noise level of around $2 \mu\text{m}/\sqrt{\text{Hz}}$. Initially designed for an operational lifetime of 5 years, GRACE is now in its 11th year in orbit and is still delivering data. The orbit of the GRACE satellites has been chosen such that every month a snapshot of the global gravitational field is obtained with a spatial resolution of approximately 400 km. The monthly snapshots of the gravitational potential reveal the time variability of mass transportation in the Earth system. Over the years, GRACE provided impressive results showing accelerated ice mass loss in Greenland and Antarctica [VW13], evidence of large scale ground water depletion in northern India [RVF09] or the mass transportations in the Amazon basin due to the yearly water cycle [TBR⁺04].

The current life time expectation sees the two satellites re-enter atmosphere between 2015 and 2016, while already the duration of science runs have been strongly reduced due to the worn out batteries. However, longer time series of gravity data are needed [WBvdB⁺13] to track the accelerated ice mass loss in the arctic regions. A successor

mission to GRACE is in development and scheduled for launch in 2017. In order to keep the gap in the data as small as possible, the planned mission GRACE Follow-On, is essentially a rebuild of the current GRACE mission. However, in addition to the microwave ranging instrument, GRACE Follow-On will carry a laser interferometer (LRI) as a technology demonstrator for future missions. The laser ranging interferometer will provide improved ranging performance with an anticipated noise level of $80 \text{ nm}/\sqrt{\text{Hz}}$ and thereby increase the sensitivity of the ranging measurement as compared to the microwave system by a factor of 25. In addition to the increased ranging performance, the interferometer will also provide enhanced attitude data, which might be also valuable for data analysis of the data provided by the microwave ranging instrument. Once operational, the laser ranging interferometer aboard GRACE Follow-On will be the first ever flown inter-spacecraft interferometer.

Measuring Gravitational Waves with eLISA

Another extremely demanding application of inter-spacecraft interferometry is the observation of gravitational waves. Since the first mentioning of gravitational waves by Albert Einstein in the year 1916 [Ein16], indirect observations made by Hulse and Taylor [HT75, TM80] gave evidence of their existence and proved once more the profound accuracy of predictions made by his General Theory of Relativity. The wealth of scientific insight that could be unveiled by direct observations of gravitational waves is due to their weak interaction with matter. Once gravitational waves are created, they reach Earth nearly unperturbed and carry information about the interior of their astrophysical or cosmological sources which is inaccessible by optical telescopes. Gravitational waves cause oscillatory, extremely small deformations of the space-time that periodically change the relative distance between free-falling test masses. They are expected to be emitted at a wide range of frequencies starting from 10^{-18} Hz at the very low end and reaching beyond 10 kHz [Tho95].

In order to measure gravitational waves, laser interferometers were proposed and currently the second generation of ground based detectors is being built, aiming for the first direct detection. Ground based detectors such as LIGO, VIRGO or GEO600 reach the necessary sensitivity in the frequency range between a few Hz and 10 kHz, thus probing the higher frequencies of the expected gravitational wave spectrum. However, ground based detectors are limited at low frequencies, due to seismic and gravity gradient noise which excite the suspended mirror test masses in the interferometers [Wei72]. For this reason, space based inter-spacecraft interferometers are required to measure gravitational waves at frequencies below 1 Hz. The proposed mission, eLISA, will consist of

three spacecraft, one mother and two daughter spacecraft, that are located at the vertices of an equilateral triangle with a side length of 1 million kilometres. The separation between the mother and the two daughters will be sensed by a laser interferometer with a sensitivity goal of $10 \text{ pm}/\sqrt{\text{Hz}}$ in the frequency range between 0.1 mHz and 1 Hz. In this frequency range, eLISA will detect such cataclysmic events as colliding massive black holes or merging neutron stars as well as in-spirals of stellar mass black holes into massive black holes, thereby probing the very edge of the massive black holes' horizon. eLISA will measure these events throughout the whole universe up to redshifts of $z \approx 20$ and help to generate a more complete understanding of our universe.

1.1. Aim and Structure of the Thesis

In order to design and optimise the layouts of highly complex optical instruments such as the eLISA and the GRACE Follow-On laser interferometers, computer simulations are indispensable tools. Despite the fact that only experiments can provide certainty of the performance of the instrument, some conditions under which the interferometers are operated in space cannot be realised in laboratories. For example, the laser beams that are transmitted to the distant spacecraft expand due to the large inter-spacecraft separations and the divergence of the beams. The light field that is received in the receive aperture will have an approximately flat phase and intensity profile. Such beams are hard to generate in laboratory-scale experiments with sufficient quality but computer simulations allow to study interferometer designs for this type of laser beams.

Chapter 2 gives an introduction to heterodyne interferometry with an emphasis on inter-spacecraft interferometers. Also, it presents the mode expansion method as a tool to simulate the propagation of non-Gaussian beams through interferometers in the framework of Gaussian beam tracing. Results are presented for the application of the mode expansion method to the propagation of tophat beams and the fundamental fibre mode. Furthermore, computer simulations can be used to test the instrument as a whole with expected noise and signal levels before the actual system has been built. This, for example, allows to study certain instrument operations such as the initial laser link acquisition which is the process of aligning the laser beams and of tuning the laser frequency such that a signal can be detected. A robust acquisition process that successfully establishes the laser link with high probability in a limited amount of time is crucial in order to enable science operation. Simulations can assist in designing and optimising and thereby evaluating and minimising the risk associated with laser link acquisition. Chapters 3 to 7 provide a detailed analysis of laser link acquisition for GRACE Follow-On.

Chapter 3 gives an introduction to laser link acquisition with heterodyne signals for GRACE Follow-On.

Chapter 4 presents the design and detailed analysis of an algorithm to detect the heterodyne signal in the presence of additive white Gaussian noise.

Chapter 5 introduces a high-fidelity simulation and the employed models of the instrument subsystems that were developed as part of this thesis to simulate and test the acquisition process.

Chapter 6 analyses an initial line-of-sight calibration scan, including a detailed discussion of possible scan patterns, timing estimates and calibration accuracies.

Chapter 7 proposes an algorithm for an autonomous laser link acquisition for the GRACE Follow-On laser ranging interferometer. Furthermore, simulation results are presented estimating run times of the algorithm and success rates.

Chapter 8 concludes the thesis with a summary and an outlook for future work.

2. Mode Expansion Method for Optical Simulations of Precision Interferometers

In this chapter, heterodyne interferometry will be introduced for the case of inter-spacecraft interferometers. Furthermore, the concept of Gaussian beam tracing is explained, which is a technique to simulate the propagation and transformation of Gaussian beams in paraxial optical system.

Subsequently, the *mode expansion method* is presented, which enables the simulation of non-Gaussian beams in interferometers. As part of this thesis, the mode expansion method as described in this chapter was implemented into IFOCAD which is an interferometer simulation toolkit developed at the Albert Einstein Institute [Hei12].

In the last part of this chapter the implemented mode expansion method is evaluated for the propagation of tophat beams, which are generated at the receive aperture on the optical benches aboard LISA and GRACE Follow-On.

A second important result is obtained from the application of the mode expansion method to the propagation of the fundamental fibre mode. For the case of GRACE Follow-On it yields a model for the far-field intensity pattern of the transmitted beam at the distant spacecraft. The obtained model is further used as an important input for the study of laser link acquisition in the second part of this thesis.

2.1. Heterodyne Signals

In LISA and GRACE Follow-On the interferometer determines changes in the relative separation between the satellites by exchanging laser beams between the spacecraft and measuring the phase difference between the local and received beam. A fraction of the local laser beam that is emitted by the laser on each spacecraft is made to interfere with the weak received light and is usually referred to as the *local oscillator* (LO).

In order to measure the phase difference between the local oscillator and the received beam, the laser beams are superimposed on a beamsplitter and the power in the resulting interference pattern is sensed by a photodiode. The laser frequencies are arranged such that, together with the Doppler shift caused by the orbit-related relative line-of-sight velocities between the spacecraft, the beatnote frequencies end up in the range of a few

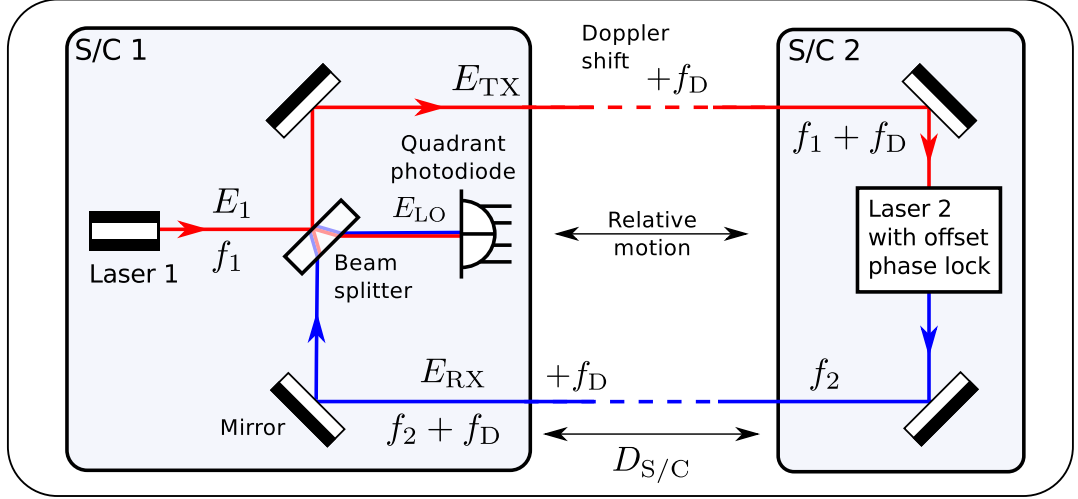


Figure 2.1.: Simplified sketch of an inter-spacecraft heterodyne interferometer that shows the beam path of the local oscillator beam, E_{LO} , and of the transmitted beam, E_{TX} . The beam that is transmitted from S/C 1 is received on S/C 2 with an additional Doppler shift, due to the relative motion of the two spacecraft. The laser on S/C 2 is offset phase locked to the received beam and sends its laser beam back to S/C 1, where it is eventually received again, E_{RX} , and interfered with the local oscillator on the photodiode.

MHz, e.g. 4 MHz to 16 MHz on GRACE Follow-On.

The photodiode converts the impinging light power into an AC photocurrent, from which the relative phase between the beams is determined by the phasemeter. See for example [GSB⁺13, WFS⁺06] for details on the phasemeter.

Figure 2.1 shows a simplified sketch of an inter-spacecraft laser interferometer. The local laser beam is split at a beamsplitter and the part reflected off the beamsplitter is sent to the distant spacecraft. At the distant spacecraft the beam is detected and an amplified fresh laser beam is sent back to the first satellite. The other part of the local laser beam that is transmitted through the beamsplitter is superimposed with the received beam and propagates directly to the photodiode, serving as local oscillator.

The frequency of the received laser light is shifted with respect to the frequency of the local oscillator beam due to the relative motion of the spacecraft. The frequency difference is twice the one-way Doppler shift, f_D , which occurs once on the way to the distant spacecraft and once when the beam is returned. The one-way Doppler shift for the case of GRACE Follow-On and LISA is expected to reach several MHz. Therefore, the interferometers developed for GRACE Follow-On and LISA are *heterodyne interferometers*.

In this chapter, the heterodyne photocurrent is derived and the main interferometer

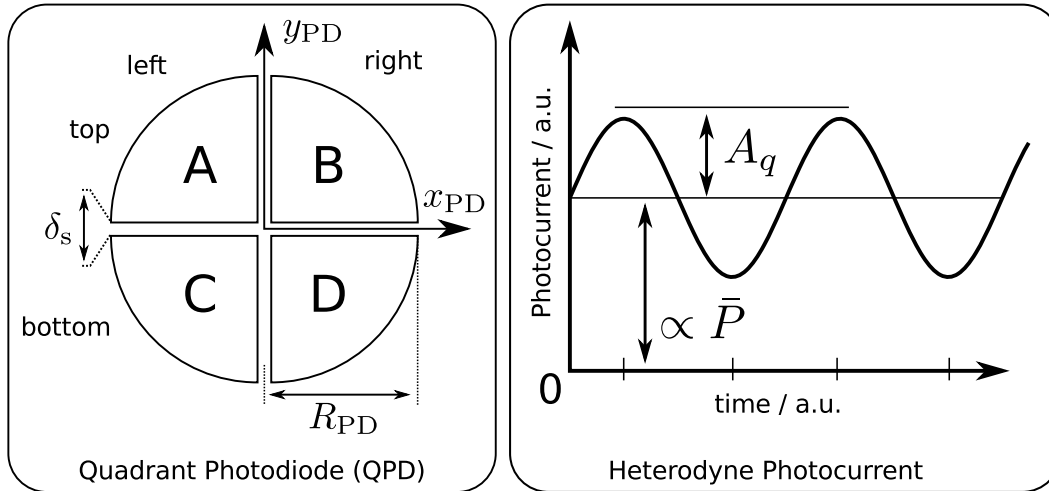


Figure 2.2.: Left: Sketch of a quadrant photodiode which shows the segment labelling, the radius of the photodiode, R_{PD} , and the width of the inactive slits between the segments, δ_s . Right: Schematic of the photocurrent measured on a single segment, showing the amplitude of the AC-part of the photocurrent, A_q , and the mean value of the photocurrent. The mean photocurrent is proportional to the sum of the power in the local oscillator and of the received beam impinging onto the active area of the segment.

signals are introduced. These are the longitudinal path length signal, which is the main signal used to determine the changes in the separation between the spacecraft and the *differential wavefront sensing* (DWS) signal, which provides an accurate measure of the angular alignment between the two beams. Also the heterodyne efficiency will be introduced which is a measure of the quality of the interference of the two beams. It is also independent of the power of the individual beams.

2.1.1. Heterodyne Photocurrent and Heterodyne Efficiency

The photodiode used for the heterodyne measurement is typically a *quadrant photodiode* (QPD) which consists of four individual photosensitive segments that can be read out separately. The left panel in Figure 2.2 shows a quadrant photodiode and the labelling of the segments that is used throughout this thesis. Two important quantities for the characterisation of a quadrant photodiode are the radius of the active area R_{PD} and the width δ_s of the insensitive slits between the segments. The conversion ratio from impinging light power to photocurrent is called the *photodiode responsivity* and denoted by ρ_{PD} . It is around 0.7 A/W for InGaAs diodes at a wavelength of 1064 nm.

The shape of the heterodyne photocurrent that is derived in this section, is depicted in the right panel of Figure 2.2. It is a sinusoid that is offset from zero, due to a constant

average light power impinging on the detector. In the following, the photocurrent measured on a single segment of a quadrant photodiode is derived. However, no assumptions for the geometric shape of the segments are made, so that the results are equally valid for single element diodes.

The signal measured by the QPD is the photocurrent produced by the interference of the local oscillator beam (LO) and the incoming received beam (RX) coming from the remote spacecraft. The electric field amplitudes of the two beams expressed in photodiode coordinates, \mathbf{r} , are assumed to be of the form,

$$E_l(\mathbf{r}, t) = a_l(\mathbf{r}, t) \exp(-i\psi_l(\mathbf{r}, t)) \exp(-2\pi i f_l t). \quad (2.1.1)$$

Here, $a_l(\mathbf{r}, t)$ is the real valued amplitude of the electric field and $\psi_l(\mathbf{r}, t)$ contains the phase of the electric field that generally varies over the surface of the photodiode segment. The time evolution of both terms is assumed to be slow compared to the sampling frequency f_s of the photodiode. f_l is the frequency of the laser beam and the label, l , will be either RX or LO to denote the received beam or the local oscillator beam.

For a single segment the photocurrent is proportional to the time averaged power, $P_q(t)$, of the superposition of the electric field of the local oscillator beam $E_{\text{LO}}(\mathbf{r}, t)$ and the received beam $E_{\text{RX}}(\mathbf{r}, t)$ on the active area, B_q , of the segment,

$$\begin{aligned} P_q(t) &\propto \iint_{B_q} |E_{\text{LO}}(\mathbf{r}, t) + E_{\text{RX}}(\mathbf{r}, t)|^2 d^2\mathbf{r} \\ &= \iint_{B_q} |E_{\text{LO}}(\mathbf{r}, t)|^2 d^2\mathbf{r} + \iint_{B_q} |E_{\text{RX}}(\mathbf{r}, t)|^2 d^2\mathbf{r} \end{aligned} \quad (2.1.2)$$

$$+ 2\mathcal{R} \left[\iint_{B_q} E_{\text{LO}}(\mathbf{r}, t) \cdot E_{\text{RX}}^*(\mathbf{r}, t) d^2\mathbf{r} \right]. \quad (2.1.3)$$

$\mathcal{R}(x)$ yields the real part of x and E_{RX}^* is the complex conjugate of E_{RX} . The first two terms are proportional to the powers, $P_{\text{LO},q}$ and $P_{\text{RX},q}$, of the local oscillator and the received beam respectively, that impinge on the active area of the segment q . These are defined by

$$P_{\text{LO},q} \propto \iint_{B_q} |E_{\text{LO}}(\mathbf{r}, t)|^2 d^2\mathbf{r} = \iint_{B_q} |a_{\text{LO}}(\mathbf{r}, t)|^2 d^2\mathbf{r}, \quad (2.1.4)$$

$$P_{\text{RX},q} \propto \iint_{B_q} |E_{\text{RX}}(\mathbf{r}, t)|^2 d^2\mathbf{r} = \iint_{B_q} |a_{\text{RX}}(\mathbf{r}, t)|^2 d^2\mathbf{r}. \quad (2.1.5)$$

The sum of these two terms is the mean light power, \bar{P}_q , impinging onto the photodiode

segment,

$$\bar{P}_q = P_{\text{LO},q} + P_{\text{RX},q}. \quad (2.1.6)$$

\bar{P}_q does not carry information about the relative phase between the local oscillator and the received beam. However, this term is the main source of photon shot noise, which is proportional to the square root of the mean power on the detector surface.

The last term in equation (2.1.3) is proportional to the AC part of the photocurrent, which carries the information about the phase difference between the LO and the RX beams. In the following, an expression for the time variable part of the photocurrent is derived which depends on the relative phase between the interfering beams and the heterodyne efficiency.

With equation (2.1.1) the time variable part of the impinging light power, $\tilde{P}_q(t)$, can be written as

$$\begin{aligned} \tilde{P}_q(t) &\propto 2\mathcal{R} \left[\iint_{B_q} E_{\text{LO}}(\mathbf{r}, t) \cdot E_{\text{RX}}^*(\mathbf{r}, t) d^2\mathbf{r} \right] \\ &= 2\mathcal{R} \left[\exp(-2\pi i f_b t) \iint_{B_q} a_{\text{LO}}(\mathbf{r}, t) a_{\text{RX}}(\mathbf{r}, t) \exp(-i\delta\psi_q(\mathbf{r}, t)) d^2\mathbf{r} \right], \end{aligned} \quad (2.1.7)$$

In the last line, the phase terms of the electric fields are combined and the beatnote frequency, f_b , is defined as the difference of the frequencies of the two laser beams, $f_b = f_{\text{LO}} - f_{\text{RX}}$. The relative phase difference between the local oscillator and the received beam was defined by $\delta\psi(\mathbf{r}, t) = \psi_{\text{LO}}(\mathbf{r}, t) - \psi_{\text{RX}}(\mathbf{r}, t)$. The remaining integral in equation (2.1.7) is also called *overlap integral*.

The final result of this section is obtained after defining the normalised overlap integral $\mathcal{O}_q(t)$ over the segment with area B_q as

$$\mathcal{O}_q(t) := \frac{\iint_{B_q} a_{\text{LO}}(\mathbf{r}, t) a_{\text{RX}}(\mathbf{r}, t) \exp(-i\delta\psi_q(\mathbf{r}, t)) d^2\mathbf{r}}{\sqrt{\iint_{B_q} |a_{\text{LO}}(\mathbf{r}, t)|^2 d^2\mathbf{r} \iint_{B_q} |a_{\text{RX}}(\mathbf{r}, t)|^2 d^2\mathbf{r}}}. \quad (2.1.8)$$

The normalisation of the integral ensures that its value is independent of the power of the individual beams that falls onto the detector surface. The two double integrals in the denominator are proportional to the power of the local oscillator, $P_{\text{LO},q}$, and the received beam, $P_{\text{RX},q}$, as defined by equations (2.1.4) and (2.1.5). With this assumption and writing $\mathcal{O}_q = |\mathcal{O}_q| \exp(i \arg \mathcal{O}_q)$, the time variable part of the impinging

light power can be written as

$$\tilde{P}_q(t) = 2 \sqrt{P_{\text{LO},q} P_{\text{RX},q}} |\mathcal{O}_q(t)| \cos(2\pi f_b t + \arg \mathcal{O}_q(t)). \quad (2.1.9)$$

Fink [Fin75] defined a coherent detection signal-to-noise ratio, the *heterodyne efficiency*, which is similar to the previously defined overlap integral. The heterodyne efficiency, η_q , for the interference on segment q is then fully defined by the properties of the electric field on the detector surface and can be given by

$$\eta_q = |\mathcal{O}_q|^2. \quad (2.1.10)$$

The phase of the time variable part of the light power which was defined in equation (2.1.9), is the phase that the phasemeter measures. It encodes the path length signal as well as local changes of the phase due to relative tilts of the wavefronts. For the rest of the thesis the phase of the heterodyne signal for a single segment will be denoted by

$$\phi_q = \arg \mathcal{O}_q. \quad (2.1.11)$$

The total light power measured by a single segment of a quadrant photodiode can finally be given as

$$P_q(t) = \bar{P}_q + \tilde{P}_q(t) \quad (2.1.12)$$

$$= P_{\text{LO},q} + P_{\text{RX},q} + 2 \sqrt{P_{\text{LO},q} P_{\text{RX},q} \eta_q} \cos(2\pi f_b t + \phi_q). \quad (2.1.13)$$

For the purpose of this thesis only the time variable part of the photocurrent will be used. Here and in the following chapters, it will be denoted by $s_q(t)$, for a single segment of the quadrant photodiode.

The photocurrent generated by the photodiode is proportional to the photodiode responsivity, ρ_{PD} , which was introduced at the beginning of this section. Generally, the amplitude of the photocurrent will also depend on the frequency of the beatnote, f_b , due to the finite measurement bandwidth of the photodiodes. Taking into account the frequency dependence by the function $g(f_b)$ and the conversion from light power to photocurrent by the photodiode responsivity, ρ_{PD} , the AC part of the heterodyne photocurrent is found to be:

$$s_q(t) = 2 \rho_{\text{PD}} g(f_b) \sqrt{P_{\text{LO},q} P_{\text{RX},q} \eta_q} \cos(2\pi f_b t + \phi_q). \quad (2.1.14)$$

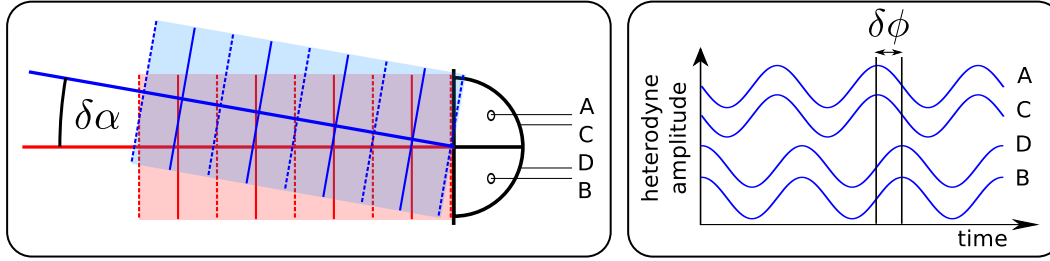


Figure 2.3.: DWS signal caused by horizontal misalignment between the RX and LO beam axes at the QPD by an angle of $\delta\alpha$. The misalignment causes a phase difference, $\delta\phi$, between the heterodyne currents of the left and right half of the QPD in the plane of incidence.

2.1.2. Heterodyne Signals

In this section the main interferometer signals used in this thesis are defined. They are derived from the phase ϕ_q of the heterodyne signal, which is computed by the phasemeter. See for example [WFS⁺06] for details on the phasemeter for GRACE Follow-On. The resulting signals use combinations of the phases computed for the individual segments of the quadrant photodiode, in order to suppress common mode effects or average out phase changes between the different segments.

Longitudinal Pathlength Signal

The longitudinal pathlength signal is obtained from the phase of the heterodyne signal by directly interpreting changes of the phase as changes in the propagated pathlength of either beam. The pathlength difference between the local oscillator and the received beam, δz , is computed from the average of the phases of all segments by

$$\delta z = \frac{\lambda}{2\pi} \frac{\phi_A + \phi_B + \phi_C + \phi_D}{4}, \quad (2.1.15)$$

where λ is the wavelength of the light. However, any deviation of the phase that is not due to pathlength differences will directly couple into the length measurement as measurement error. For example, the largest contributor to the error in the longitudinal signal is frequency noise that cannot be distinguished from a change in the phase due to pathlength changes. For this reason, excellent frequency stability is required for high-precision heterodyne interferometers.

Differential Wavefront Sensing

The second important signal generated from the heterodyne measurement that will be briefly mentioned here, is the differential wavefront sensing (DWS) signal. The DWS signal is routinely used to measure the relative tilt between the wavefronts of two interfering beams, for example to automatically align beams in interferometers [MMRW94a, MMRW94b].

The basic idea is that the phase of the heterodyne signal has opposite sign for the two sides of the QPD if the interfering beams are tilted with respect to each other. See Figure 2.3 for an illustration of a tilt in the horizontal direction in QPD coordinates. Subtracting the phases of the corresponding halves of the quadrant photodiode gives a measure of the relative wavefront tilt. The horizontal and vertical DWS signals are here defined by

$$\text{DWS}_{\text{hor}} = (\phi_A + \phi_C) - (\phi_B + \phi_D), \quad (2.1.16)$$

$$\text{DWS}_{\text{ver}} = (\phi_A + \phi_B) - (\phi_C + \phi_D). \quad (2.1.17)$$

For small relative tilt angles, $\delta\alpha$ and $\delta\beta$, the DWS signal is directly proportional to the tilt of the beam axes of the two interfering beams

$$\text{DWS}_{\text{hor}} \approx c_{\text{DWS}} \delta\alpha \quad (2.1.18)$$

$$\text{DWS}_{\text{ver}} \approx c_{\text{DWS}} \delta\beta. \quad (2.1.19)$$

The coupling factor, c_{DWS} , for two interfering tophat beams was calculated by Sheard et al. [SHD⁺12] and for two interfering Gaussian beams, for an infinitely large photodiode radius and zero slit width by Hechenblaikner et al. [Hec10]. It is usually of the order of 10^3 to 10^4 rad_{elec}/rad_{opt}. Here rad_{elec} is the unit of the phase that the phasemeter measures and rad_{opt} is the unit of the misalignment angle between the optical wavefronts. The order of magnitude of the coupling factor can be estimated by w/λ , where w is the radius of the Gaussian beams and λ is the wavelength of the light.

2.2. Simulation of Interferometers by Gaussian Beam Tracing

In this section a short introduction of interferometer simulations by means of Gaussian beam tracing is given. The methods described here are included in the core functionality of IFOCAD [Hei12], a C library containing functions to plan and optimise interferometers. It has the capability to simulate the propagation of stigmatic, simple or general

astigmatic Gaussian beams through 3D optical setups under the paraxial approximation of the scalar wave equation [ST91]. Also, all heterodyne signals discussed in the last section can be computed with IFOCAD.

The purpose of this section is to give a brief introduction to IFOCAD into which the mode expansion method was implemented, and to optics related terms used throughout this thesis. Here, only the stigmatic Gaussian beam is shortly introduced. The interested reader is referred to the following references for further details [WHK⁺12, KWS⁺13].

Gaussian Beam

In order to simulate interferometers, the electric field provided by the lasers is usually approximated by Gaussian beams. Circular symmetric Gaussian beams are the simplest class of these beams, for which the electric field distribution can be given by

$$E(x, y, z) = \sqrt{\frac{2P}{\pi}} \frac{1}{w(z)} \exp\left(-\frac{x^2 + y^2}{w^2(z)}\right) \exp\left(-ik\frac{x^2 + y^2}{2R(z)} + i\zeta(z)\right) \exp(-iks). \quad (2.2.1)$$

E is for convenience defined here with absorbed constants such that $|E|^2$ directly yields the intensity in units of W/m². Here, $w(z)$ is the radius of the Gaussian beam, $R(z)$ is the radius of curvature of the wavefront, and $\zeta(z)$ is the so called Gouy phase shift. The term $\exp(-iks)$ is an additional phase shift, which depends on the propagated geometrical path length, s , and the wavenumber $k = 2\pi/\lambda$.

The *radius* of the Gaussian beam, $w(z)$, is smallest for $z = 0$, where it is equal to the *waist radius*, w_0 . Figure 2.4 shows a schematic of a Gaussian beam, explaining the most important quantities introduced in this section. The *Rayleigh range*, z_R , can be defined by the wavelength, λ , and the waist radius, w_0 , by

$$z_R = \pi \frac{w_0^2}{\lambda}. \quad (2.2.2)$$

The Rayleigh range is the characteristic length scale of the Gaussian beam in propagation direction, which determines the evolution of the width, radius of curvature and Gouy phase, along the optical axis. The width of the Gaussian beam can be given in terms of the waist radius, w_0 , and the Rayleigh range, z_R , by

$$w(z) = w_0 \sqrt{1 + \left(\frac{z}{z_R}\right)^2}. \quad (2.2.3)$$

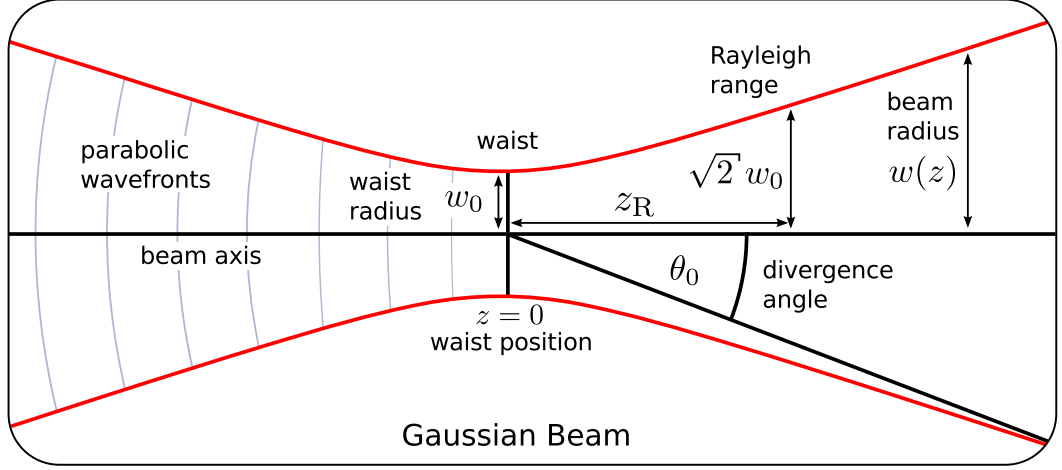


Figure 2.4.: Geometry of the fundamental Gaussian beam.

At the Rayleigh range the width of the Gaussian beam is $\sqrt{2} w_0$, while for $z \gg z_R$, the width scales approximately linear with the distance from the waist,

$$w(z) \approx \frac{w_0}{z_R} z = \theta_0 z, \quad \text{for } z \gg z_R. \quad (2.2.4)$$

The proportionality factor, θ_0 , is called the *divergence angle* of the Gaussian beam. The radius of curvature of the Gaussian beam's phasefront can also be defined in terms of the Rayleigh range as follows:

$$R(z) = z \left(1 + \left(\frac{z_R}{z} \right)^2 \right). \quad (2.2.5)$$

The radius of curvature approaches infinity for $z \rightarrow 0$, such that the Gaussian beam has plane wavefronts at the waist. At the Rayleigh range the radius of curvature reaches a minimum value of $R(z_R) = 2 z_R$. In the far-field, for large propagation distances compared to the Rayleigh range, the radius of curvature is approximately equal to the distance from the waist, z . For this case the phasefront can be well approximated by a spherical wave, originating from the waist position. The Gouy phase, $\zeta(z)$, describes an additional phase shift of π when the beam propagates through its waist position. It can also be given in terms of the Rayleigh range by

$$\zeta(z) = \tan^{-1} \left(\frac{z}{z_R} \right). \quad (2.2.6)$$

The Gouy phase is zero at the waist and approaches $\pm\pi/2$ for $z \rightarrow \pm\infty$.

The circular symmetric Gaussian beam defined in equation (2.2.1) can also be parametrised by the complex parameter q , which can be given in terms of the distance to the waist and the Rayleigh range by

$$q = z + iz_R. \quad (2.2.7)$$

The width and radius of curvature of the beam can be obtained from the inverse of the q -parameter by

$$\frac{1}{q} = \frac{1}{R} - i \frac{2}{k} \frac{1}{w^2}. \quad (2.2.8)$$

More general beam types, i.e. simple and general astigmatic Gaussian fundamental modes, that occur in general misaligned optical systems can be simulated with IFOCAD, but are not part of this thesis.

Beam Tracing

Interferometers for high precision metrology usually consist of numerous optical components, such as lenses, beamsplitters, mirrors, apertures, photodiodes and lasers. The left panel in Figure 2.5 shows a schematic of the optical bench of the laser ranging instrument on GRACE Follow-On, as an example for a comparatively simple interferometer. The local laser beam that is provided by the laser is routed via a movable fine-steering mirror (FSM), a beamsplitter (BS) and two lenses (L1 and L2) to the quadrant photodiode (QPD), to serve as local oscillator (LO). *Gaussian beam tracing* as implemented in IFOCAD models the laser beam as a combination of its beam axis and q -parameter. The beam axis is traced through the interferometer by means of geometrical optics, while the complete path of the beam is split into segments, which span between intersection points of the beam axis with subsequent optical surfaces.

The right panel in Figure 2.5 shows three segments of a beam path, \mathbf{r}_0 , \mathbf{r}_1 and \mathbf{r}_2 . The first segment starts at the intersection point, A , of the beam axis with the surface of the previous component. From there the intersection point, B , of the beam axis with the front surface of the next optical component is determined.

At the new intersection point the local normal vector to the surface is computed and the reflected and refracted beam axes are found from Snell's law and the well known law of reflection [ST91]. The new beam axis segment, for example that of the refracted beam, is then traced in exactly the same way to the next intersection point, C , with the back surface of the optical component.

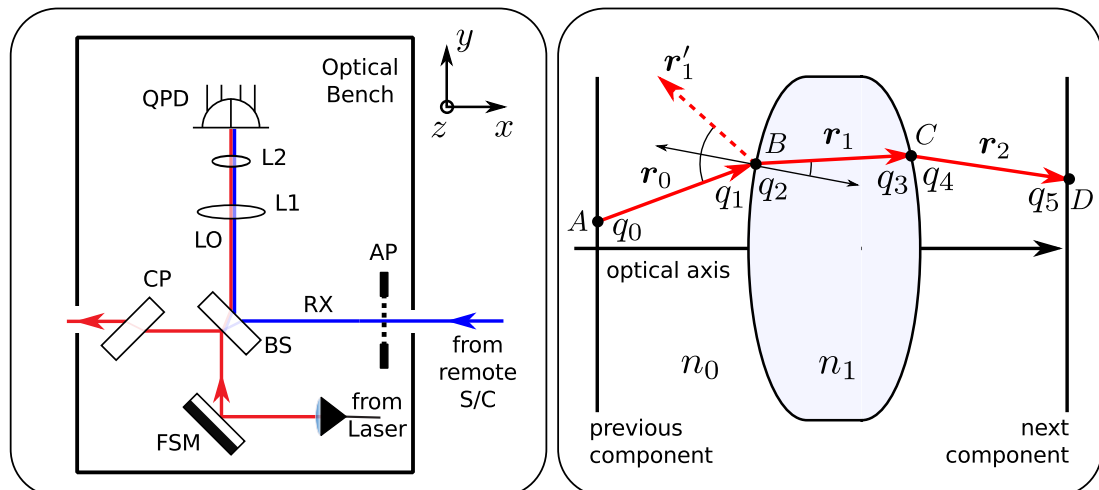


Figure 2.5.: Left: Schematic of the optical bench of the Laser Ranging Interferometer on board GRACE Follow-On. Right: Tracing of the beam axis r_0 to r_2 , and transforming the q -parameter to propagate and transform the Gaussian beam at surfaces of optical components.

The length of a beam axis segment is the geometrical pathlength, s , that the beam propagated by. In order to calculate the correct phase of the beam at the final surface, the optical pathlength along the beam path is accumulated. The optical pathlength is computed from the geometrical pathlength by multiplying with the refracted index n_i of the medium [WHK⁺12].

The other part of the beam model in IFOCAD, the q -parameter of the Gaussian beam, is transformed according to the well known ABCD law for paraxial optical systems [ST91], generalised for the handling of tilted ellipsoidal surfaces [MS69]. A new q -parameter is computed at each intersection point and for each propagation between intersection points. This leads to the sequence of q -parameters depicted in the right panel of Figure 2.5.

The beam axis is traced up to a final surface at which the electric field needs to be computed, for example a quadrant photodiode to compute the interferometer signals. In order to compute the interferometer signals IFOCAD implements the expressions for the interferometer signals given in Section 2.1.

2.3. Mode Expansion Method

Not all beam types occurring in real interferometers can be well approximated by Gaussian beams. The schematic setup of the GRACE Follow-On optical bench that is shown in the left panel of Figure 2.5 indicates two examples. On the one hand, the local oscil-

lator is delivered by an optical fibre to the optical bench. The beam coming out of the fibre is not a perfect Gaussian beam. On the other hand, the beam received from the distant spacecraft has a nearly flat phase and intensity profile across the receive aperture. These non-Gaussian beams will show diffraction effects, while propagating through the interferometer, which cannot be simulated by the simple Gaussian beam tracing.

For the propagation of arbitrary light fields, efficient methods were developed in the past, such as fast-Fourier transform based direct integration of the Rayleigh-Sommerfeld diffraction integral [SW06, NL09] or the angular spectrum decomposition [DH98, DH01, MSW03, MS09]. These methods transform an arbitrary electric field distribution given on a regular spaced grid in the input plane, to an arbitrarily aligned and offset output plane. Optical components like apertures or lenses are simulated by modifying the phase and amplitude of the electric field in the input plane, before the transformation is applied. Special care needs to be taken to accommodate large wavefront curvatures, for example as introduced by strongly curved surfaces, in order to avoid aliasing effects [OKT⁺11].

In this thesis, however, the *mode expansion method*, is used to study the propagation of non-Gaussian beams through interferometers. This method is based on the fact that certain families of beams constitute a *complete* and *orthonormal* basis for solutions of the paraxial wave equation. Any other solution of the paraxial wave equation can be represented by a weighted sum over members of these families, [FS10]. This is also often called a *mode decomposition*.

The mode expansion method as described in this chapter was implemented into IFOCAD as part of this thesis and can be used to trace non-Gaussian beams through interferometers. In the past the method was applied to study free-space optical interconnects [PR03] and general effects of diffraction [PR05, Sny07, CFAA10]. Also the effect of a finite aperture lens on the heterodyne efficiency was studied using the mode expansion method [STF81].

The well known Hermite-Gaussian or Laguerre-Gaussian modes [Sie86, ST91] both constitute a complete orthonormal set of base functions. The difference between these two basis sets is their symmetry. While Hermite-Gaussian beams have rectangular symmetry, Laguerre-Gaussian beams are circular symmetric. The transversal intensity distribution of the first Hermite-Gaussian modes is shown on the left in Figure 2.6 and the intensity distribution of the first Laguerre-Gaussian modes is shown on the right. The Hermite-Gaussian mode, $u_{mn}(x, y; z, w_0)$, with horizontal index m and vertical index n

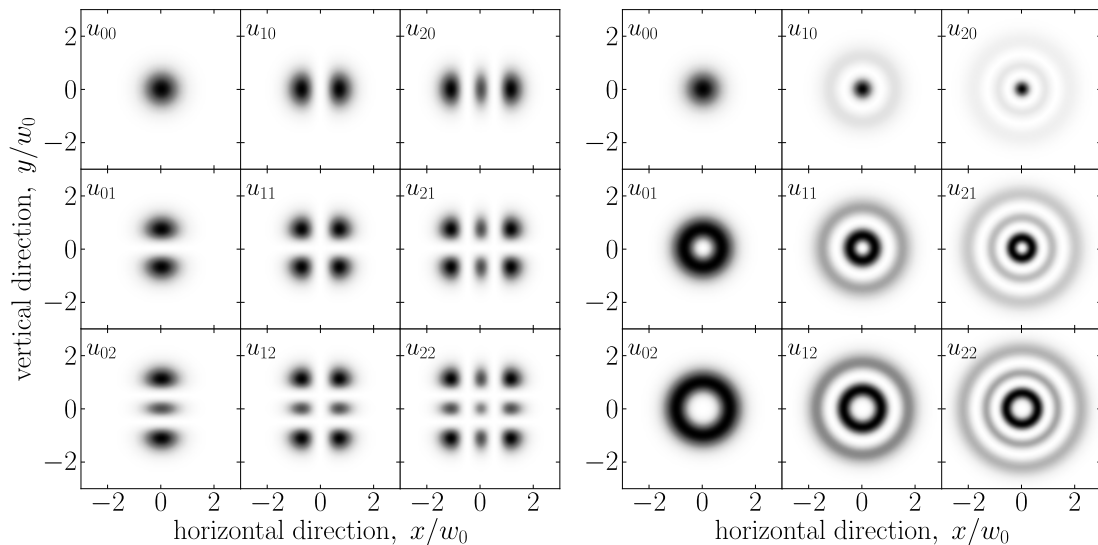


Figure 2.6.: Left: Transversal intensity distribution of the first Hermite-Gaussian modes, u_{mn} . Right: Transversal intensity distribution of the first Laguerre-Gaussian modes, u_{pl} .

can be defined as:

$$\begin{aligned}
 u_{mn}(x, y; z, w_0) = & \frac{c_{mn}}{w(z)} H_m \left(\frac{\sqrt{2} x}{w(z)} \right) H_n \left(\frac{\sqrt{2} y}{w(z)} \right) \exp \left(-\frac{x^2 + y^2}{w^2(z)} \right) \\
 & \cdot \exp \left(-ik \frac{x^2 + y^2}{2R(z)} + i(m + n + 1)\zeta(z) \right),
 \end{aligned} \tag{2.3.1}$$

where $k = 2\pi/\lambda$ is the wavenumber of the beam. The waist radius w_0 is hidden in the definitions of the beam radius $w(z)$, radius of curvature $R(z)$ and Gouy phase $\zeta(z)$. The definitions of these functions for the Hermite-Gaussian modes are in analogy to the definitions given for the fundamental Gaussian beam in equations (2.2.3), (2.2.5) and (2.2.6). The normalisation constants, c_{mn} , are given by

$$c_{mn} = (\pi m! n! 2^{m+n-1})^{-\frac{1}{2}}. \tag{2.3.2}$$

The Laguerre-Gaussian modes, as the second mentioned set of complete orthonormal solutions to the paraxial wave equation [FS10], can be defined in cylindrical coordinates,

(r, ϕ) , as

$$u_{pl}(r, \phi; z, w_0) = \frac{c_{pl}}{w(z)} \left(\frac{\sqrt{2} r}{w(z)} \right)^{|l|} L_p^l \left(\frac{2r^2}{w^2(z)} \right) \exp \left(-\frac{r^2}{w^2(z)} \right) \cdot \exp \left(il\phi - ik \frac{r^2}{2R(z)} + i(2p + |l| + 1)\zeta(z) \right), \quad (2.3.3)$$

with the same width, radius of curvature and Gouy phase shift as before. The function, L_p^l , appearing in the definition above is the associated Laguerre polynomial with the radial mode index, $p \in \mathbb{N}_0$, and the azimuthal mode index, $l \in \mathbb{Z}$. The normalisation factor, c_{pl} , is defined by

$$c_{pl} = \sqrt{\frac{2p!}{\pi(|l| + p)!}}. \quad (2.3.4)$$

Similar to the fundamental Gaussian mode discussed in Section 2.2, one can define the same q -parameter, that parametrises the Hermite- and Laguerre-Gaussian modes, see equation (2.2.7). The connection between the q -parameter and the distance from the waist z , as well as the waist radius w_0 , can be given by inserting the definition of the Rayleigh range, from equation (2.2.2), into equation (2.2.7) by

$$q = z + i\pi \frac{w_0^2}{\lambda}. \quad (2.3.5)$$

For this reason the modes will be parametrised by the q -factor, instead of the distance to the waist z , and the waist radius w_0 , for example $u_{mn}(x, y; q) = u_{mn}(x, y; z, w_0)$.

The principle idea of the mode expansion method is the following. Let $u_{mn}(x, y; q)$ be a *mode* of a complete orthonormal set, e.g. the Hermite-Gaussian modes. Let further, m , and n with $m, n = 0, \dots, \infty$, index different modes within the set. Any electric field, $E(x, y)$, given in a plane perpendicular to the propagation direction of the modes $u_{mn}(x, y; q)$, can be written as the sum over the u_{mn} , weighted by unique coefficients a_{mn} , as

$$E(x, y) = \sum_{m=0}^{\infty} \sum_{n=0}^{\infty} a_{mn} u_{mn}(x, y; q) \exp(-iks), \quad (2.3.6)$$

where s is the propagated geometrical pathlength. The input electric field is now expressed in terms of Hermite- or Laguerre-Gaussian modes, for which the propagation and transformation through a paraxial optical system is known.

The propagation and transformation of the electric field $E(x, y)$, through a paraxial optical system can then be computed by transforming the Hermite- or Laguerre Gaussian modes and calculating the weighted sum of equation (2.3.6). The beam tracing can be realised in exactly the same way as it was introduced for the fundamental Gaussian beam. The beam axis is transformed according to geometrical optics, and the modes are transformed by transforming the q -parameter, according to the ABCD formalism, [MS69, SAC70, ST91].

The unique weighting coefficients or *mode amplitudes*, are invariant under paraxial transformations of the modes. Hence, the amplitudes only need to be computed once, in the beginning, and then only the beam axis and the q -parameter have to be transformed. As such, most of the computational cost of the mode expansion method is due to the decomposition of the electric field at the input plane, and evaluating the sum over the modes to reconstruct the approximated field at the output plane. The propagation and the transformation at optical components involves only few arithmetic operations. In order to calculate the mode amplitudes, the *inner product*, or *overlap integral* of two electric fields, E_1 and E_2 , given in the x-y-plane, is defined as follows:

$$\langle E_1 | E_2 \rangle := \int_{-\infty}^{\infty} \int_{-\infty}^{\infty} E_1(x, y) E_2^*(x, y) dx dy. \quad (2.3.7)$$

Here, E_2^* is the complex conjugate of E_2 . The orthonormality of the Hermite-Gaussian modes ensures that the overlap integral between two modes, $u_{mn}(q)$ and $u_{m'n'}(q)$, vanishes if $m \neq m' \vee n \neq n'$, and it is equal to 1, if the modes are identical:

$$\langle u_{mn}(q) | u_{m'n'}(q) \rangle = \delta_{mm'} \delta_{nn'}. \quad (2.3.8)$$

However, modes which are evaluated at different propagation distances z , or have different waist radii w_0 , are not orthogonal, (2.3.8) does not hold.

The mode amplitudes, a_{mn} , which occur in the series expansion of the electric field $E(x, y)$ in equation (2.3.6) can be computed by the overlap integral over the input electric field and the mode $u_{mn}(q)$ by

$$a_{mn} = \langle u_{mn}(q) | E \rangle. \quad (2.3.9)$$

The q -parameter that is used in the mode expansion, can be chosen arbitrarily. For different values, different mode amplitudes will be obtained resulting in a different series expansion, although the completeness of the set of the modes ensures that for $m, n \rightarrow \infty$

the total electric field distribution is independent of q .

However, this is only true if the number of modes used in the decomposition is infinite. For any real application, the series expansion of equation (2.3.6) needs to be truncated at a finite number of modes, which will result in deviations of the input electric field from the approximate series expansion. By choosing an appropriate value for the q -parameter, the error introduced by truncating the series expansion can be reduced for a given total number of modes, while inappropriate values may lead to slower convergence of the series. The truncated mode expansion of the input electric field $E(x, y)$ given in the x - y -plane into Hermite-Gaussian modes, can be given by

$$E_{\text{MEM}}(x, y) \approx \sum_{m=0}^{m_{\text{max}}} \sum_{n=0}^{n_{\text{max}}} a_{mn} u_{mn}(q) \exp(-iks), \quad \text{with} \quad (2.3.10)$$

$$a_{mn} = \langle u_{mn}(q) | E \rangle, \quad (2.3.11)$$

whereas for Laguerre-Gaussian modes the sum over the azimuthal index needs to include the negative values as well. It can be defined as

$$E_{\text{MEM}}(x, y) \approx \sum_{p=0}^{p_{\text{max}}} \sum_{l=-l_{\text{max}}}^{l_{\text{max}}} a_{pl} u_{pl}(q) \exp(-iks), \quad \text{with} \quad (2.3.12)$$

$$a_{pl} = \langle u_{pl}(q) | E \rangle. \quad (2.3.13)$$

As mentioned before, the propagation of the input electric field, E_{MEM} , through a paraxial optical system can be realised by tracing the beam axis of the modes by geometrical optics and transform the q -parameter of the modal set by the ABCD formalism. The mode amplitudes are invariant under such transformations.

However, if non-paraxial transformations need to be simulated, such as clipping of the beam at limiting apertures, new coefficients need to be computed. In the left panel of Figure 2.7 a simple schematic of an interferometer is shown, where the beam passes through two apertures and a number of optical components in between. At each aperture the electric field of the incoming beam needs to be computed in the aperture plane and then decomposed into a set of higher-order Gaussian modes, which propagate perpendicular to the aperture plane. This is shown in the right panel of Figure 2.7.

Astigmatic Hermite-Gaussian Modes

The Hermite-Gaussian modes can also be used to describe simple astigmatic beams. For this case the mode $u_{mn}(q)$ is separated for the two orthogonal coordinates and

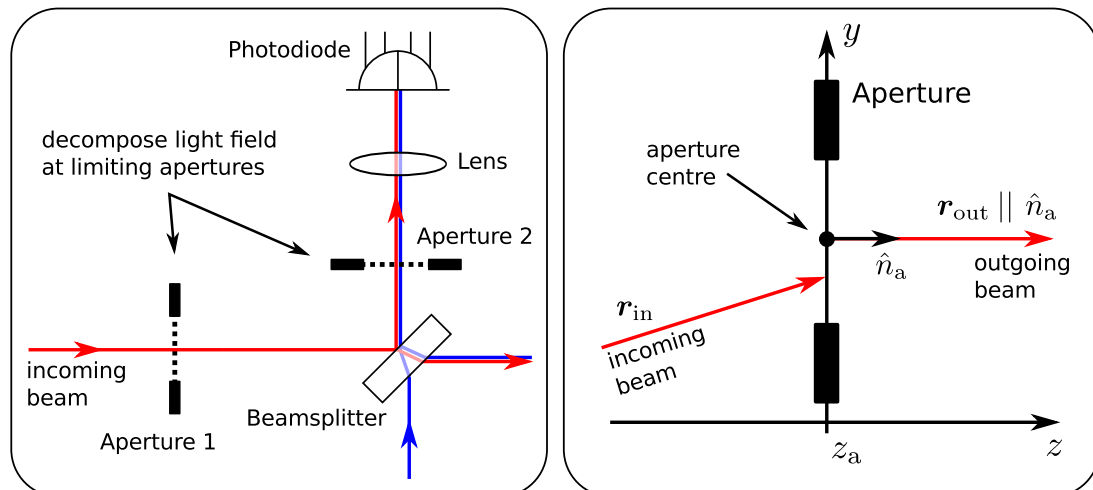


Figure 2.7.: Left: Tracing a non-Gaussian beam through an interferometer. Reflection and refraction of the beam axis at optical components is handled by Snell's law [ST91], while the transformation of the beam's q -parameter is done using the ABCD formalism [MS69]. At limiting apertures the beam has to be decomposed again. Right: Decomposition at a limiting aperture. The electric field distribution in the aperture plane needs to be computed. The overlap integral for decomposition has to be evaluated in the aperture plane, such that the direction of the outgoing beam is perpendicular to the aperture plane.

for each dimension separate q -parameters, q_x and q_y , are defined, leading to individual waist radii w_{0x} and w_{0y} , as well as distances from the waist, z_x and z_y . Compare this to equation (2.3.5), which gives the relation between the q -parameter, z and w_0 . The astigmatic Hermite-Gaussian mode, $u'_{mn}(x, y; q_x, q_y)$ is then given by

$$u'_{mn}(x, y; q_x, q_y) = v_m(x; q_x) v_n(y; q_y), \quad (2.3.14)$$

where the functions $v_m(x; q_x)$ and $v_n(y; q_y)$ are defined by

$$v_m(x; q_x) = \frac{c_m}{\sqrt{w_x(z_x)}} H_m \left(\frac{\sqrt{2} x}{w_x(z_x)} \right) \times \exp \left(-\frac{x^2}{w_x^2(z_x)} - ik \frac{x^2}{2R_x(z_x)} + i \left(m + \frac{1}{2} \right) \zeta_x(z_x) \right) \quad (2.3.15)$$

and

$$v_n(y; q_y) = \frac{c_n}{\sqrt{w_y(z_y)}} H_n \left(\frac{\sqrt{2} y}{w_y(z_y)} \right) \times \exp \left(-\frac{y^2}{w_y^2(z_y)} - ik \frac{y^2}{2R_y(z_y)} + i \left(n + \frac{1}{2} \right) \zeta_y(z_y) \right) \quad (2.3.16)$$

The normalisation factors c_m and c_n are of the form $c_m = (m! 2^{m-1/2} \sqrt{\pi})^{-1/2}$. The orthonormality is also valid for the astigmatic modes if the two modes have the same q -parameter in each direction,

$$\langle u'_{mn}(q_x, q_y) | u'_{m'n'}(q_x, q_y) \rangle = \delta_{m m'} \delta_{n n'}. \quad (2.3.17)$$

When tracing astigmatic modes through a paraxial optical system the q -parameter for each dimension needs to be transformed separately.

Basis Transformations

Sometimes it is advantageous to change the basis of the mode expansion from a Laguerre-Gaussian basis into a Hermite-Gaussian basis or vice versa. A situation where this reduces computational cost, is for example, when a non-Gaussian circular symmetric input field needs to be traced through a simple astigmatic system.

Due to the symmetry of the input field, Laguerre-Gaussian modes are preferred for the decomposition, as far less modes are necessary to approximate it. For a circular symmetric input beam all those azimuthal Laguerre-Gaussian modes, with $l \neq 0$ have an amplitude of $a_{pl} = 0$. However, the description of simple astigmatic Laguerre-Gaussian modes is usually done in the Hermite-Gaussian basis, as simple astigmatic transformations of these modes are straightforward [WOMT05].

The basis transformation between Laguerre- and Hermite-Gaussian modes is widely discussed in the literature, for example in [OC00, BAvdVW93, FS10]. Throughout this work the approach of O'Neil et al. is used [OC00], whereas the notation is slightly altered to allow for an easy algorithmic implementation. It is required that the modes are stigmatic and the Hermite- and Laguerre-Gaussian modes need to have the same q -parameter.

An important property of the basis transformation between Hermite- and Laguerre-Gaussian modes is that the *order* of a mode is preserved. The *order*, N , of a mode is

typically defined as [OC00],

$$N := \begin{cases} m + n, & \text{for Hermite-Gaussian modes,} \\ 2p + |l|, & \text{for Laguerre-Gaussian modes.} \end{cases} \quad (2.3.18)$$

Modes of the same order have the same phase evolution in propagation direction, which is given by the Gouy phase shift of $(2p+|l|+1)\zeta(z)$ and $(m+n+1)\zeta(z)$, for the Laguerre- and the Hermite-Gaussian modes respectively. Hence, modes of the same order form a closed subspace under the basis transformation. The dimension of the subspace for order N is $N + 1$.

In fact, the transformation between the two modal sets is just a special case of the previously defined generally applicable decomposition which for a Hermite-Gaussian mode of order N , in Laguerre-Gaussian modes of the same order is given by

$$u_{mn}(x, y; q) = \sum_{2p+|l|=N} \langle u_{pl}(q) | u_{mn}(q) \rangle u_{pl}(q). \quad (2.3.19)$$

Since, both sets of modes form an orthonormal basis, one can define a unitary matrix, \mathbf{M}_N , for a given order, N , that transforms the vector of all mode amplitudes \mathbf{A}_N^{HG} , of Hermite-Gaussian modes of order N , into a vector \mathbf{A}_N^{LG} , containing the corresponding mode amplitudes in the Laguerre-Gaussian basis. The unitarity of \mathbf{M}_N ensures that its complex conjugate transposed, \mathbf{M}_N^\dagger , is the transformation matrix that transforms Laguerre-Gaussian modes into Hermite-Gaussian modes. Hence,

$$\mathbf{A}_N^{LG} = \mathbf{M}_N \mathbf{A}_N^{HG}, \quad \text{and} \quad (2.3.20)$$

$$\mathbf{A}_N^{HG} = \mathbf{M}_N^\dagger \mathbf{A}_N^{LG}. \quad (2.3.21)$$

The last step, before the actual transformation coefficients can be computed, is to define a specific ordering of the modes of a fixed order N , in the vectors \mathbf{A}_N^{HG} and \mathbf{A}_N^{LG} , that allows for scaling with N . The following order is proposed by O'Neil et al. [OC00]. If $i = 0, \dots, N$ indexes the position in the vector, then for Hermite-Gaussian modes the horizontal and vertical mode indices, m and n , are computed by

$$m = i, \quad \text{and} \quad n = N - i. \quad (2.3.22)$$

The resulting vector of modes of order N can be given, with the mode amplitudes $a_{m,n}$,

as defined by equation (2.3.11), as follows:

$$\mathbf{A}_N^{\text{HG}} = (a_{0,N}, a_{1,N-1}, \dots, a_{i,N-i}, \dots, a_{N,0})^t. \quad (2.3.23)$$

Here, t means transposition of the vector. For the case of the Laguerre-Gaussian modes of order N , the mapping of the position in the vector, $i = 0, \dots, N$, to the radial and azimuthal mode indices, p and l , can be given by

$$p = N - |N - 2i|, \quad \text{and} \quad l = N - 2i. \quad (2.3.24)$$

This results in the following vector of Laguerre-Gaussian mode amplitudes $a_{p,l}$, which were defined in equation (2.3.13). For mode orders of N this is

$$\mathbf{A}_N^{\text{LG}} = (a_{0,N}, a_{2,N-2}, \dots, a_{N-|N-2i|,N-2i}, \dots, a_{0,-N})^t. \quad (2.3.25)$$

With the given order, the transformation matrix \mathbf{M}_N can be defined in terms of the coupling coefficients $\langle u_{pl}(q) | u_{mn}(q) \rangle$, between Hermite-Gaussian and Laguerre-Gaussian modes. A restriction that needs to be made is that the Hermite and Laguerre-Gaussian modes share the same q -parameter. As such the coupling coefficients are given by

$$\langle u_{pl}(q) | u_{mn}(q) \rangle = c(p, l, m, n). \quad (2.3.26)$$

The coefficients can be given analytically by the following relation

$$c(p, l, m, n) = \begin{cases} 0, & 2p + |l| \neq m + n, \\ (-1)^p i^m B \left[\frac{m+n+l}{2}, \frac{m+n-l}{2}, m \right], & 2p + |l| = m + n, \end{cases} \quad (2.3.27)$$

where i is the imaginary unit and the function B is defined by [BAvdVW93, FS10],

$$B(n, m, k) = \sqrt{\frac{(n+m-k)!k!}{2^{n+m}n!m!}} \frac{1}{k!} \frac{d^k}{dt^k} [(1-t)^n(1+t)^m] |_{t=0} \quad (2.3.28)$$

With the given coefficients of equation (2.3.27) and the ordering defined in equations (2.3.22) and (2.3.24) the transformation matrix \mathbf{M}_N for transforming Hermite-Gaussian to Laguerre Gaussian modes, can finally be given by,

$$(\mathbf{M}_N)_{i,j} = c(N - |N - 2i|, N - 2i, j, N - j). \quad (2.3.29)$$

The columns of the matrix \mathbf{M}_N , contain the images of the Hermite-Gaussian modes

expressed in the Laguerre-Gaussian basis.

For completeness it should be mentioned that analytical expressions for coupling coefficients have been derived also for transformations between Gaussian modes that have different q -parameters. The underlying theory is thoroughly described in [BH84, FS10].

2.4. Propagation of Tophat Beams

In this section the mode expansion method is used to propagate a perfect circular symmetric, tophat beam through free-space. Tophat beams are produced on the GRACE Follow-On optical bench by clipping the beam transmitted by the remote spacecraft at the receive aperture. The long propagation distance and the small size of the receive aperture, cause the portion of the beam that is clipped to be close to a perfect tophat with flat phase and amplitude distribution.

For this reason the tophat beam is of special interest for simulations of interferometers as flat phase and intensity profiles are hard to generate in experiments. Thus, it is important to evaluate the accuracy of the mode expansion method for this case. The electric field, $E_{\text{TH}}(r, \phi)$, of the tophat beam in the aperture plane, at $z = 0$, can be given as

$$E_{\text{TH}}(r, \phi) = \begin{cases} \sqrt{\frac{P_{\text{TH}}}{\pi}} \frac{1}{R_{\text{TH}}} \exp(i\psi_0), & \text{if } r \leq R_{\text{TH}}, \\ 0 & \text{if } r > R_{\text{TH}}. \end{cases} \quad (2.4.1)$$

with the radius of the tophat beam R_{TH} , its power P_{TH} , and a constant phase ψ_0 . Figure 2.8 depicts the setup that is simulated in this section. The incoming plane wave approximates the broadened incoming beam and is clipped at the aperture of radius R_{TH} . The electric field in the aperture plane is decomposed into a set of Laguerre-Gaussian modes, in order to exploit the tophat's symmetry, and eventually the Laguerre-Gaussian modes are propagated to the observation screen at which the electric field is evaluated.

The accuracy of the mode expansion method will depend on the number of modes included in the series expansion and the propagation distance between the aperture plane and the observation plane. The accuracy is evaluated by comparing the electric field computed with the mode expansion method to known analytical expressions for the transversal distribution in the Fresnel region and the far-field as well as for the on-axis electric field.

Comparing the electric field in the transversal direction leads to an empirical model that estimates the maximum transversal range up to which the mode expansion method

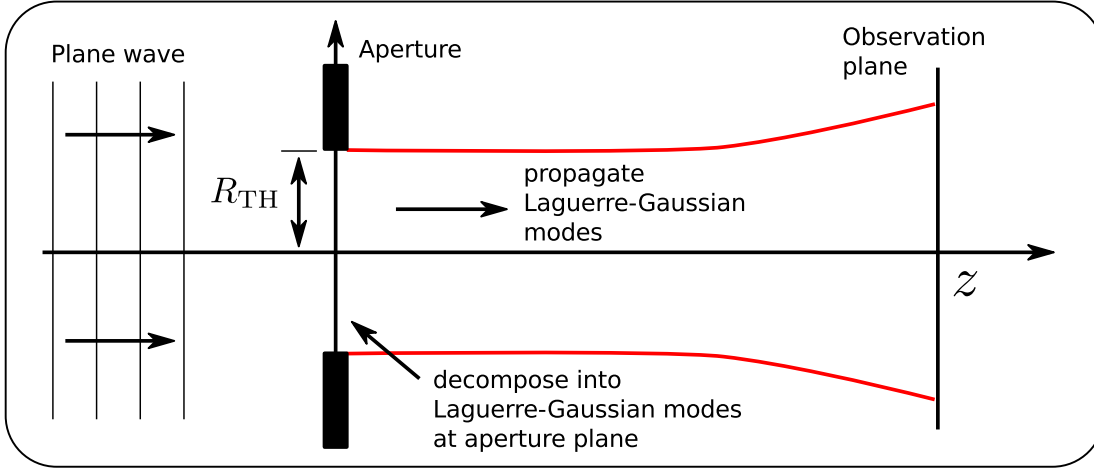


Figure 2.8.: Explanation of the studied setup. Incoming plane waves are clipped at the circular symmetric aperture of radius R_{TH} . The electric field distribution in the aperture plane is decomposed into a set of Laguerre-Gaussian modes and then the Laguerre-Gaussian modes are propagated along the distance of z up to the observation screen, at which the electric field is evaluated.

is providing accurate results. Subsequently, the comparison of the on-axis electric field to an analytical expression yields a model to estimate the required maximum mode order for the decomposition of a tophat beam, as a function of its radius and the desired propagation distance.

The mode order was defined in equation (2.3.18). For Hermite-Gaussian modes the mode order was defined as $N = m + n$ and for Laguerre-Gaussian modes as $N = 2p + |l|$. Here, m and n are the horizontal and vertical mode number of the Hermite-Gaussian modes and p and l are the radial and azimuthal index of the Laguerre-Gaussian modes respectively. The mode order is preserved under a transformation between the two modal sets. As such the maximum mode order required in a decomposition is a good indicator for the accuracy of the modal decomposition, independent of the used basis system.

2.4.1. Decomposition of Tophat beams

The decomposition of the circular symmetric tophat beam in Laguerre-Gaussian modes can be done analytically, because a recurrence relation can be given to compute the amplitudes, $a_{p,0}$, as defined by equation (2.3.13). For a tophat beam of intensity

$|E_{\text{TH}}(r, \phi)|^2 = 1$ over the aperture plane and radius R_{TH} , it reads [CFAA10, BGS96]:

$$a_{0,0} = \sqrt{2\pi} w_0 \left[1 - \exp\left(-\frac{R_{\text{TH}}^2}{w_0^2}\right) \right], \quad (2.4.2)$$

$$a_{1,0} = \sqrt{2\pi} w_0 \left[\left(1 - 2\frac{R_{\text{TH}}^2}{w_0^2}\right) \exp\left(-\frac{R_{\text{TH}}^2}{w_0^2}\right) - 1 \right], \quad (2.4.3)$$

$$a_{p,0} = \frac{1}{p} \left[\frac{\sqrt{2\pi}}{w_0} R_{\text{TH}}^2 L_{p-1}^0\left(2\frac{R_{\text{TH}}^2}{w_0^2}\right) \exp\left(-\frac{R_{\text{TH}}^2}{w_0^2}\right) - a_{p-1,0} + (p-1)a_{p-2,0} \right]. \quad (2.4.4)$$

Here, w_0 is the waist radius of the fundamental Laguerre-Gaussian mode used in the decomposition. It is a free parameter in the above recurrence relation. The value of w_0 relative to the radius of the tophat beam will determine the accuracy of the approximation for a given maximum radial index p_{max} considered in the decomposition. The Laguerre-Gaussian modes are evaluated at their waist position, in order to match the flat wavefront of the tophat beam. L_p^0 is the associated Laguerre polynomial of radial index p and azimuthal index $l = 0$ [BSMM01].

The recurrence formula computes only the amplitudes of radial Laguerre-Gaussian modes, as the amplitudes of all azimuthal modes are zero, due to the cylindrical symmetry of the tophat beam. The order of the beam for the radial modes is just $N = 2p$. The mode expansion of the tophat beam up to a maximum considered mode order of $\hat{N} = 2p_{\text{max}}$, can be given in terms of the Laguerre-Gaussian modes $u_{p,0}$ as given in equation (2.3.3), and the mode amplitudes, $a_{p,0}$, by

$$E_{\text{MEM}}(r, z) = \sqrt{\frac{P_{\text{TH}}}{\pi}} \frac{1}{R_{\text{TH}}} \sum_{p=0}^{\hat{N}/2} a_{p,0} u_{p,0}(r, z), \quad (2.4.5)$$

where the dependence on the azimuthal angle ϕ was neglected, due to the circular symmetry. The mode-amplitudes are also scaled for the correct power of the tophat beam, P_{TH} .

An indicator for the accuracy of the decomposition is the difference of the power contained in the perfect tophat beam, P_{TH} , and the set of Laguerre Gaussian modes, $P_{\hat{N}}$, for a decomposition of up to order of \hat{N} which can be given as

$$P_{\hat{N}} = \frac{P_{\text{TH}}}{\pi} \frac{1}{R_{\text{TH}}^2} \sum_{p=0}^{\hat{N}/2} |a_{p,0}|^2. \quad (2.4.6)$$

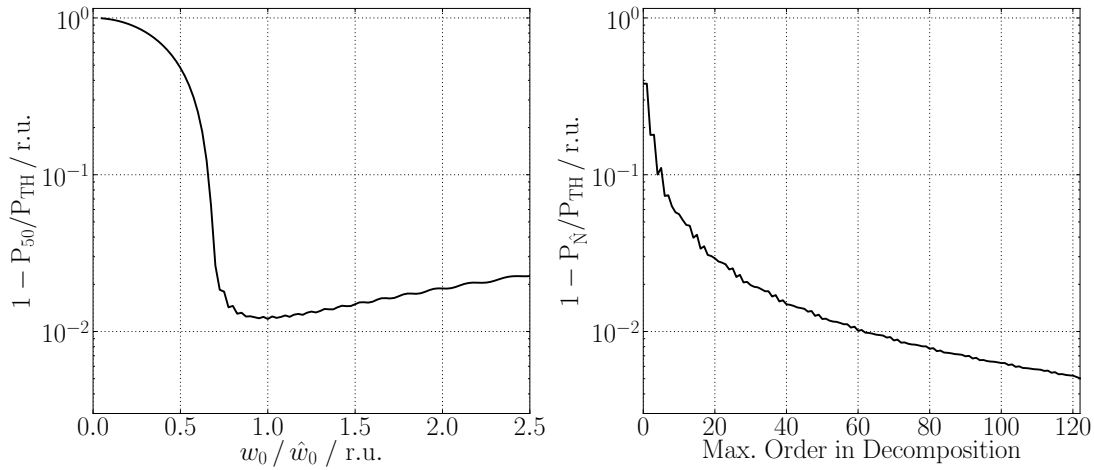


Figure 2.9.: Left: Power, P_{50} , in the set of Laguerre-Gaussian modes up to order 50, approximating a tophat beam of power P_{TH} , as a function of the waist radius of the fundamental mode, relative to the optimal waist radius \hat{w}_0 of equation (2.4.8). Right: Relative difference of the power in the decomposed and perfect tophat beam as a function of the maximum considered mode order \hat{N} . Here, the waist radius of the fundamental mode is the optimum radius, \hat{w}_0 .

Normalised to P_{TH} the error estimate can be given by

$$\delta P_{\hat{N}} = \frac{P_{\text{TH}} - P_{\hat{N}}}{P_{\text{TH}}} = 1 - \frac{1}{\pi R_{\text{TH}}^2} \sum_{p=0}^{\hat{N}/2} |a_{p,0}|^2. \quad (2.4.7)$$

The left plot in Figure 2.9 shows the dependence of δP_{50} , for a decomposition up to order $\hat{N} = 50$, as a function of the waist radius of the fundamental Laguerre-Gaussian beam. The waist radius is given relative to an optimum waist radius, \hat{w}_0 , for which the error, δP_{50} , reaches a minimum. For a decomposition of a perfect tophat beam into Laguerre-Gaussian modes Borghi et al. [BGS96] found an analytical expression for the optimum waist radius that minimises the mean squared error as defined by equation (2.4.7). The result can be given by

$$\hat{w}_0 = \sqrt{\frac{2}{\hat{N}}} R_{\text{TH}}. \quad (2.4.8)$$

The right plot in Figure 2.9 shows the error $\delta P_{\hat{N}}$, as a function of the maximum order, \hat{N} , in the decomposition, if the optimum waist radius is used. An error of 1% is obtained for a maximum mode order of $\hat{N} = 60$.

The criterion given in equation (2.4.7) is an integral measure which does not give

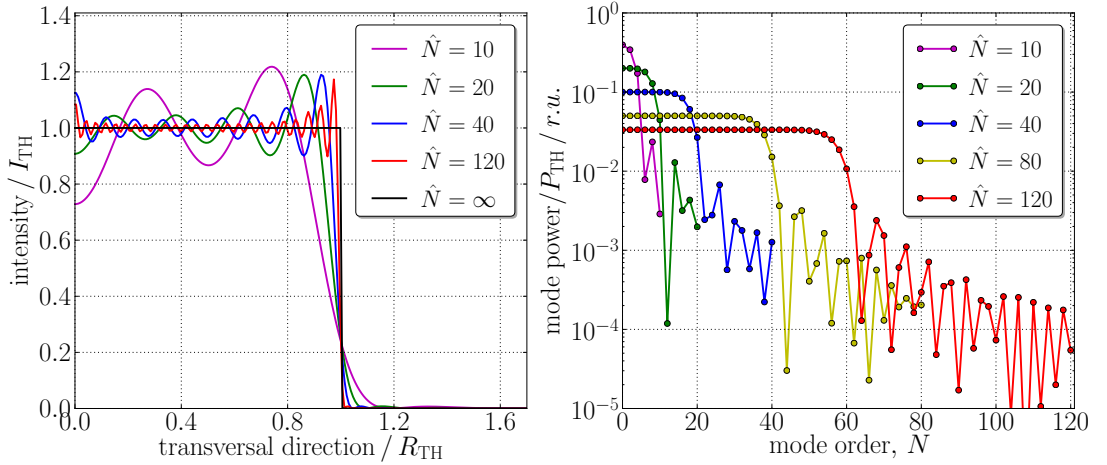


Figure 2.10.: Left: Intensity profile of the approximated tophat beam, for a decomposition with different maximum orders. The waist radius of the fundamental mode is set to the optimal value, \hat{w}_0 defined in equation (2.4.8). Right: Mode amplitudes of the Laguerre-Gaussian modes for the decomposition of the tophat beam, for different maximum orders \hat{N} . Only even orders are plotted and joined with a solid line as a guide for the reader.

details about the spatial distribution of the remaining error. The left plot in Figure 2.10 shows a cross-section of the intensity distribution of the approximated tophat beam for different maximum orders considered in the decomposition. The plot only shows one half of the tophat beam, as it is symmetric about its propagation axis. The intensity of the approximated tophat beam oscillates around the intensity of the perfect tophat.

Increasing the maximum considered order in the decomposition increases the frequency of the oscillations, whereas the amplitude decreases. Another feature of the approximation is the strong overshoot near the discontinuity of the tophat beam. The overshoot is not changed significantly, if more modes are added to the expansion, only the width is reduced. This behaviour can be seen in the Fourier series expansion of a rectangular function as well, and is generally called *Gibb's phenomenon* [HH79].

The right plot in Figure 2.10 shows the power of the N -th order Laguerre-Gaussian mode in the series expansion. The plot only shows even orders, as odd orders are zero due to the symmetry of the tophat beam. The single points are connected as guide for the reader. It can be observed that increasing the number of considered modes in a decomposition, distributes the total power in the tophat beam evenly for the lower order modes of up to $N = \hat{N}/2$, if the optimal waist radius, \hat{w}_0 , from equation (2.4.8) is used. For higher orders the power in the modes drastically decreases.

The reason is that the radius of the modes of lower order are smaller than the radius

of the tophat beam and virtually all of their power is contained within the aperture hole. For this case the mode amplitudes are constant due to the normalisation of the Laguerre-Gaussian modes, and the constant amplitude of the tophat beam. If the mode radius of the Laguerre-Gaussian modes are compared to the aperture radius, it can be understood, why the drop in power starts for orders of $N \approx \hat{N}/2$. The mode radius of a Hermite- or Laguerre-Gaussian mode of order N can be defined as the location of the outermost inflection point of the intensity profile. With the radius of the fundamental mode, $w(z)$, it can be given by

$$W_N(z) = \sqrt{N + \frac{1}{2}} w(z). \quad (2.4.9)$$

For the decomposition the Laguerre-Gaussian modes were evaluated at the waist position. Hence, for $w(z = 0) = \hat{w}_0$, the mode radius for a mode of order $N = \hat{N}/2$ is

$$W_{\hat{N}/2} = \sqrt{1 + \frac{1}{\hat{N}}} R_{\text{TH}} \approx R_{\text{TH}}. \quad (2.4.10)$$

Hence, the drop in power for the upper half of the considered mode amplitudes happens, because an increasing fraction of the power of the Laguerre-Gaussian mode is located outside of the aperture.

2.4.2. Fresnel Diffraction of Tophat Beams

In order to evaluate the accuracy of the mode expansion method for the propagation of tophat beams, the electric field intensity for different propagation distances is computed and compared to an analytic solution of the Fresnel diffraction of the circular symmetric tophat beam [TLL05].

Fresnel diffraction is valid, if the Fresnel number, $N_{\text{Fres}} \geq 1$, and the distance from the optical axis is smaller than the propagation distance, $r < z$. The Fresnel number is defined by

$$N_{\text{Fres}} = \frac{R_{\text{TH}}^2}{\lambda z}, \quad (2.4.11)$$

for the radius of the aperture or tophat beam, R_{TH} , the wavelength of the light, λ , and the propagation distance along the optical axis, z . Also the propagation distance should be much larger than the wavelength, $z \gg \lambda$. If these requirements are met, the electric

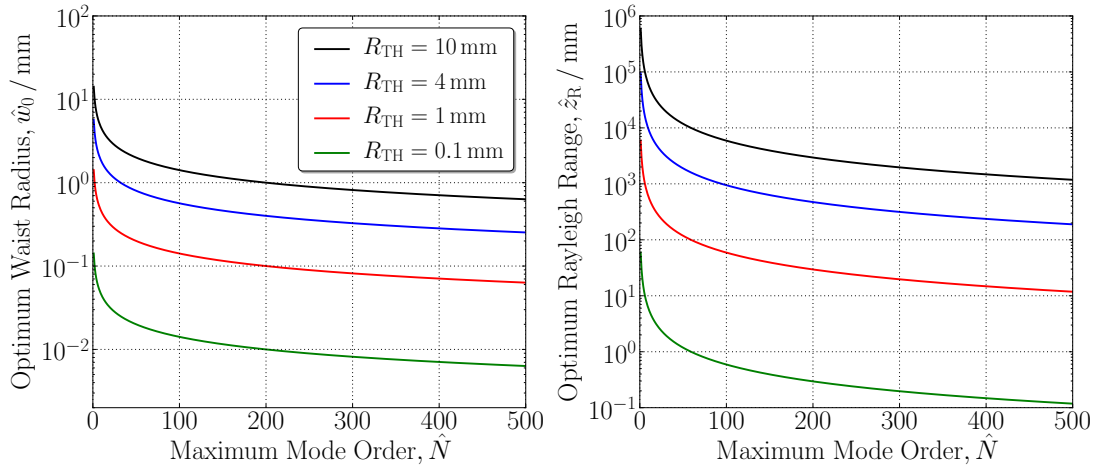


Figure 2.11.: Left: Optimum waist radius computed from equation (2.4.8) for different tophat radii. Right: Rayleigh range, corresponding to the optimum waist radius, computed from equation (2.4.13).

field distribution behind the circular aperture is given by [TLL05]

$$E_{\text{Fres}}(r, z) = \frac{2\pi\sqrt{P_{\text{TH}}}\exp(-ikz)}{-i\lambda z} \int_0^{R_{\text{TH}}} J_0\left(2\pi\frac{r\rho}{\lambda z}\right) \exp\left(-i\frac{\pi(\rho^2 + r^2)}{\lambda z}\right) \rho d\rho. \quad (2.4.12)$$

Figures 2.12 and 2.13 show the electric field amplitude distribution for the tophat beam, approximated by the mode expansion method, $|E_{\text{MEM}}(r, z)|$, and the analytical formula from equation (2.4.12), $|E_{\text{Fres}}(r, z)|$, as well as the amplitude of the difference, $|E_{\text{MEM}}(r, z) - E_{\text{Fres}}(r, z)|$. The electric field is computed at different propagation distances behind the aperture plane. The propagation distances are given in terms of the Rayleigh range, z_R , of the fundamental Gaussian mode of the mode expansion.

Here and in the following it is assumed that the waist radius of the fundamental mode corresponds to the optimum, \hat{w}_0 , which was defined in equation (2.4.8). The order of the highest considered mode is set to $\hat{N} = 120$.

The optimum waist radius \hat{w}_0 , and the corresponding Rayleigh range \hat{z}_R , are plotted against the maximum considered mode order \hat{N} , in Figure 2.11. The Rayleigh range z_R was defined in equation (2.2.2) and can be given with the optimum waist radius, \hat{w}_0 , from equation (2.4.8) by

$$\hat{z}_R = \pi \frac{\hat{w}_0^2}{\lambda} = \frac{2\pi}{\lambda} \frac{R_{\text{TH}}^2}{\hat{N}}. \quad (2.4.13)$$

To check if the Fresnel diffraction is valid in the considered region one can consult the

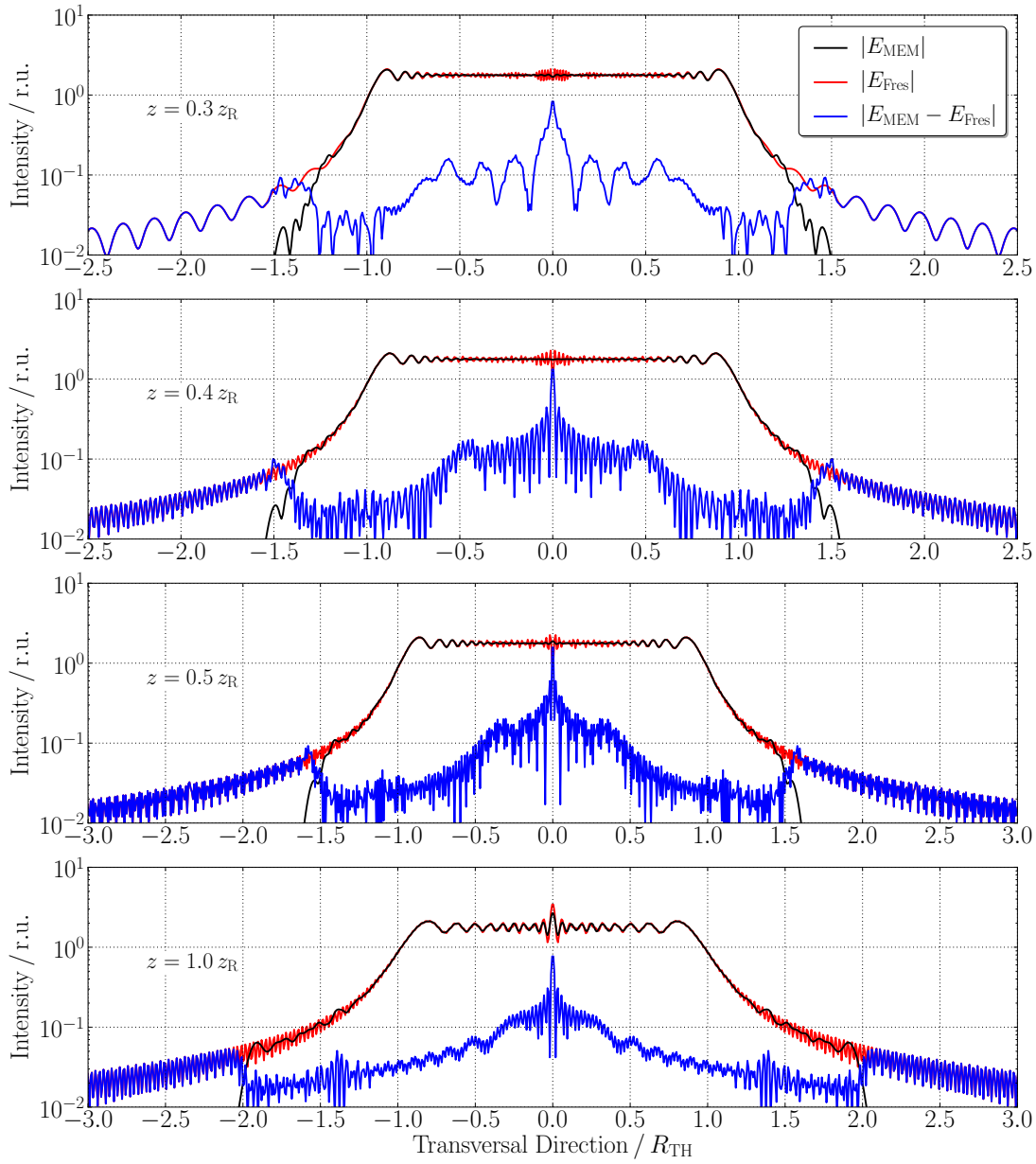


Figure 2.12.: Electric field amplitude for the propagated tophat beam, as computed from the mode expansion method, $|E_{\text{MEM}}|$, for a maximum considered mode order of $\hat{N} = 120$, and the Fresnel integral from equation (2.4.12), $|E_{\text{Fres}}|$. Also, the amplitude of the difference $|E_{\text{MEM}} - E_{\text{Fres}}|$ is plotted. The electric fields are computed for different propagation distances up to $z = 1 z_{\text{R}}$ after the aperture plane. The propagation distances are given in terms of the Rayleigh range, z_{R} , of the fundamental Gaussian mode.

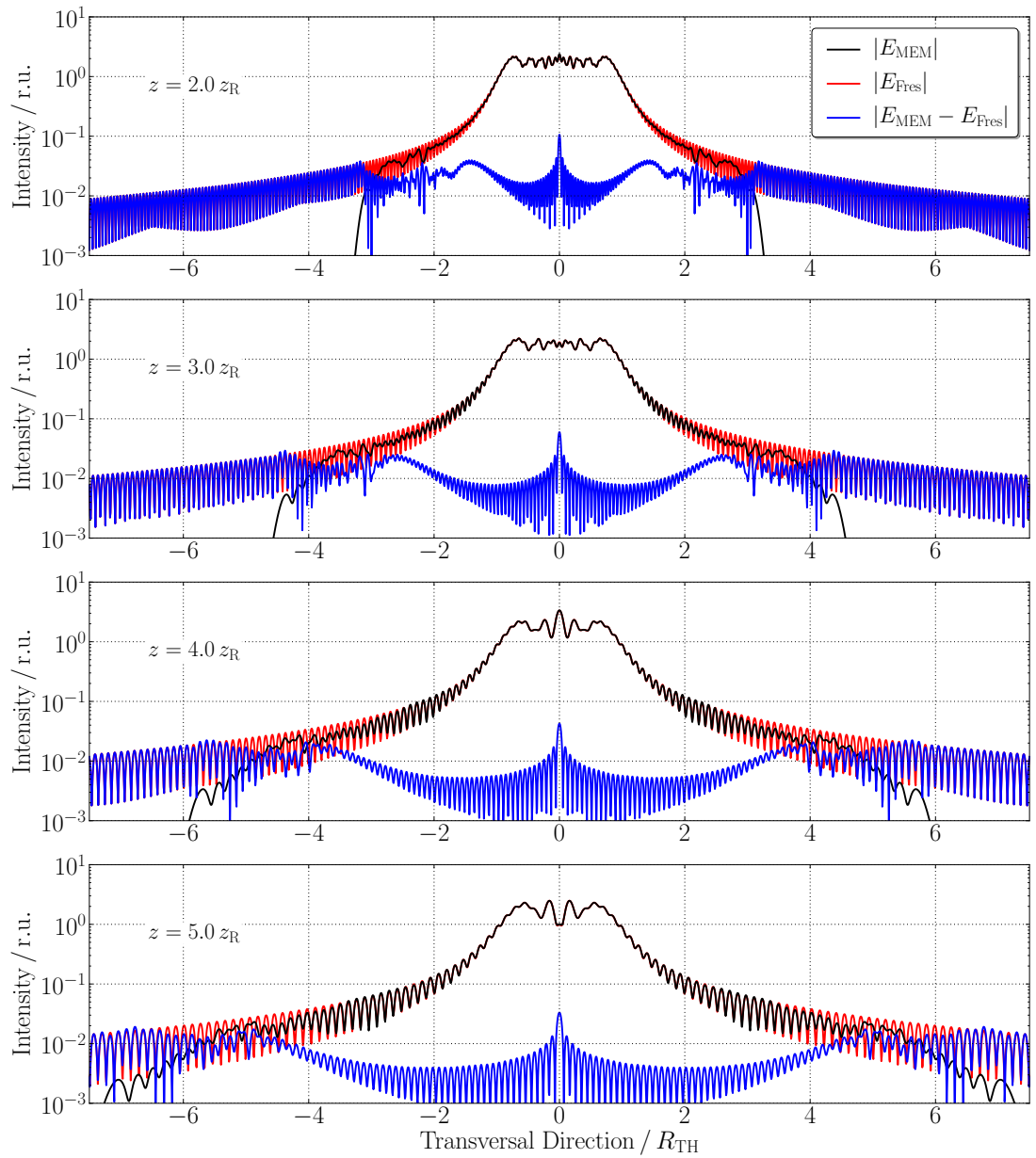


Figure 2.13.: Electric field amplitude for the propagated tophat beam, as computed from the mode expansion method, $|E_{\text{MEM}}|$, for a maximum considered mode order of $\hat{N} = 120$, and the Fresnel integral from equation (2.4.12), $|E_{\text{Fres}}|$, as well as the amplitude of the difference $|E_{\text{MEM}} - E_{\text{Fres}}|$, for different propagation distances up to $z = 1 z_R$ after the aperture plane. The propagation distances are given in terms of the Rayleigh range, z_R , of the fundamental Gaussian mode. These plots continue the series of plots of Figure 2.12 to larger propagation distances.

Fresnel number from equations (2.4.11) and (2.4.13). It can be computed from the maximum order in the decomposition and the ratio between the Rayleigh range and the propagation distance by

$$N_{\text{Fres}} = \frac{\hat{N}}{2\pi} \frac{\hat{z}_R}{z}. \quad (2.4.14)$$

The Fresnel numbers for the plots in the two figures range from $N_{\text{Fres}} \approx 64$, for $z = 0.3 z_R$, down to $N_{\text{Fres}} \approx 3.8$, for $z = 5 z_R$ and thus, the Fresnel diffraction is valid in this regime.

Following are some numbers for the propagation distances for which the electric field distributions are plotted: For a tophat beam of 4 mm radius, the Rayleigh range for the used parameters, $\hat{N} = 120$ and $w_0 = \hat{w}_0$, is $z_R \approx 79$ cm. The plots thus show the evolution of the tophat beam starting from $z = 23$ mm after the aperture plane, in the upper most plot of Figure 2.12, to $z = 3.95$ m for the bottom plot in Figure 2.13. For an aperture of 1 mm radius the Rayleigh range is 49 mm and the plots correspond to propagation distances between $z = 1.47$ cm and $z = 25$ cm after the aperture plane.

The comparison between the electric field distributions, computed with the two methods, show deviations of the order of 10 % for the central region close to the optical axis, in the plots of shorter propagation distances, in Figure 2.12. However, the difference is smaller in the outer regions, closer to the edge of the tophat beam. The mode expansion method does not reproduce the small scale features of the diffracted beam, which can be observed for the Fresnel diffraction.

For larger propagation distances these features become smaller and structures of larger scale become dominant which can be approximated by the mode expansion method with higher accuracy. This is the reason why the accuracy of the mode decomposition increases for larger propagation distances after the aperture plane. Figure 2.13 shows the evolution of the tophat beam for larger propagation distances behind the aperture plane. The difference between the two electric field distributions computed with the two methods decreases rapidly and monotonically for larger z . Most of the small scale, oscillatory features that are visible for small propagation distances vanish at propagation distances equal to the Rayleigh range of the optimally decomposed beam, and the mode expansion gains in accuracy.

The transversal width of the region for which the mode expansion yields accurate results, is limited by the mode radius of the highest order Laguerre-Gaussian mode, $W_{\hat{N}}(z)$, used in the mode expansion. The mode radius of the mode of order N was already given in equation (2.4.9) as $W_N(z) = \sqrt{N + 1/2} w(z)$. Note that the waist radius, w_0 , and the mode radius of the fundamental mode, W_0 , as defined by equation (2.4.9)

are not identical $W_0(0) \neq w_0$.

The bottom plot in Figure 2.12 shows the intensity distribution after a propagation by the Rayleigh range of the modal set. The width of the fundamental mode at the Rayleigh range is $\sqrt{2}$ times its waist radius. The mode radii of the higher order modes scale accordingly. Hence, at the Rayleigh range, the mode radius of the highest order mode is $\sqrt{2} W_{\hat{N}}(0)$ which is

$$\sqrt{2} W_{\hat{N}}(0) = 2 \sqrt{1 + \frac{1}{2\hat{N}}} R_{\text{TH}} \approx 2 R_{\text{TH}}. \quad (2.4.15)$$

This is exactly the location where the intensity of the distribution decreases rapidly. However, the approximation seems to worsen already at about $\sqrt{2} R_{\text{TH}}$. For a propagation distance of $z = 2 z_{\text{R}}$ the mode radius of the highest order mode is roughly $W_{\hat{N}}(2 z_{\text{R}}) \approx 3.2 R_{\text{TH}}$. This also corresponds to the location where the intensity starts to drop rapidly, though the difference between the intensity computed by the mode expansion and the Fresnel integral reaches the magnitude of the intensity computed by the mode expansion at about $2 R_{\text{TH}}$.

These results suggest to define a transversal region for which the mode expansion method yields accurate results, under the assumption that the optimum waist radius is used, by the following inequality:

$$r \lesssim \frac{W_{\hat{N}}(z)}{\sqrt{2}} \approx R_{\text{TH}} \sqrt{1 + \left(\frac{z}{z_{\text{R}}}\right)^2}. \quad (2.4.16)$$

2.4.3. Far-Field Intensity Distribution of Tophat Beams

The far-field intensity distribution of the electric field behind a circular aperture is the well known *Airy* pattern [ST91] which is obtained using Fraunhofer diffraction theory. The formula to compute the intensity pattern is given by

$$I_{\text{Airy}}(r, z) = I_0 \left[\frac{\lambda z}{\pi r R_{\text{TH}}} J_1 \left(\frac{2\pi r R_{\text{TH}}}{\lambda z} \right) \right]^2. \quad (2.4.17)$$

Figure 2.14 shows three plots comparing the intensity pattern, computed with the mode expansion method and the expression for the Airy disk intensity pattern, for different propagation distances behind the aperture plane. The decomposition of the tophat beam again uses the optimal waist radius, \hat{w}_0 from equation (2.4.8), and a maximum order of $\hat{N} = 120$. Additionally, the difference, $|I_{\text{MEM}} - I_{\text{Airy}}|$, is shown in the plots.

For a propagation distance of $z = 20 z_{\text{R}}$, the intensity distribution computed by the

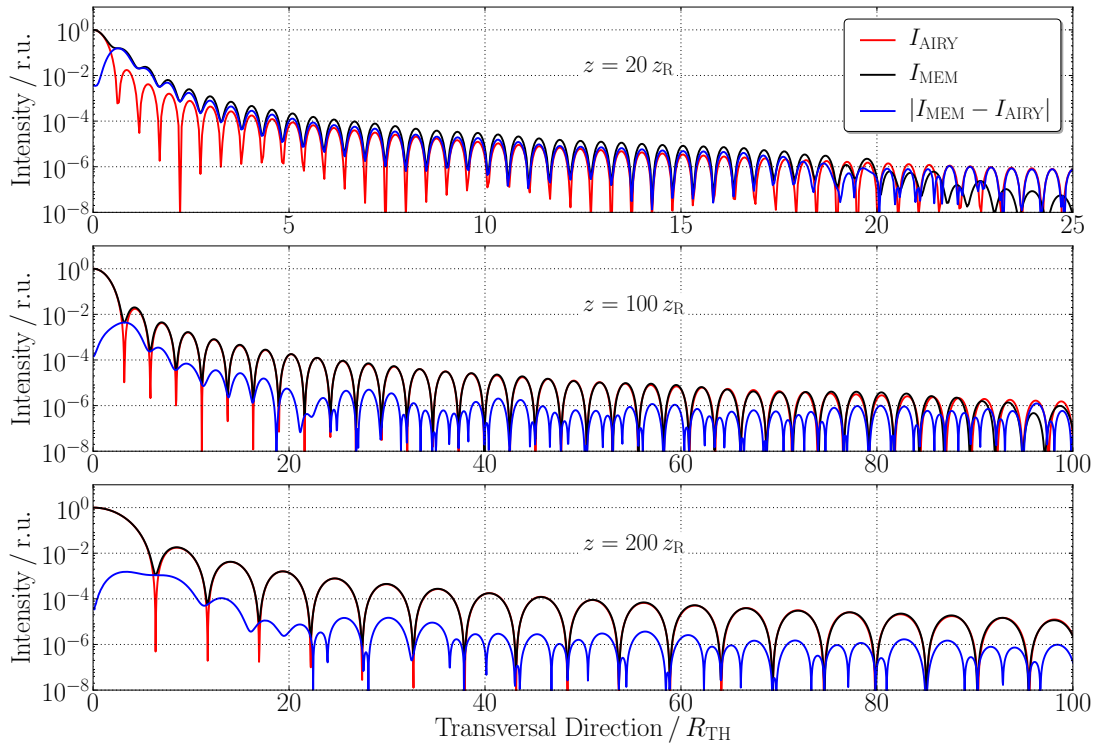


Figure 2.14.: Far-field intensity distribution for the propagated tophat beam, as computed from the mode expansion method, I_{MEM} , and the Airy disk pattern from equation (2.4.17), I_{Airy} , as well as the difference $|I_{\text{MEM}} - I_{\text{Airy}}|$, for three different propagation distances after the aperture plane.

mode expansion method, still deviates from the Airy disk pattern at the tails of the central peak, whereas the central peak can be reproduced with an error of less than 10%. Starting from about $z = 100 z_{\text{R}}$ the two distributions match closely, except for the dips which are not as pronounced in I_{MEM} . An additional increase of accuracy is observed for a propagation by $z = 200 z_{\text{R}}$.

The results obtained from the former section about the validity of the approximation by the mode expansion method in transversal direction, which are summarised in equation (2.4.16), suggest the following inequality for the far-field, by assuming that $z \gg z_{\text{R}}$:

$$r \lesssim R_{\text{TH}} \frac{z}{z_{\text{R}}}. \quad (2.4.18)$$

This is confirmed by the middle plot in Figure 2.14, where the difference approaches the level of the intensity given by the Airy pattern at about $100 R_{\text{TH}}$.

The transversal range shown in the bottom plot does not suffice to show the full extent of the validity region which reaches up to $200 R_{\text{TH}}$. The Airy disk far-field intensity pattern of the circular tophat beam, starting around $z = 100 z_{\text{R}}$, is reproduced by the mode expansion method with high accuracy for a wide range in transversal direction.

2.4.4. On-Axial Electric Field

The on-axial electric field has been known for more than 50 years and was first published by Osterberg et al. in 1961 [OS61]. Dubra et al. [DF99] derived it in an easier form which can be given in terms of the aperture radius, R_{TH} , the propagation distance, z , the wavenumber, $k = 2\pi/\lambda$, and the power contained in the tophat beam, P_{TH} , by

$$E_{\text{OA}}(z) = \sqrt{\frac{P_{\text{TH}}}{\pi}} \frac{\exp(-ikz)}{R_{\text{TH}}} \left[1 - \frac{\exp[ikz(1-\alpha)]}{\alpha} \right], \quad \text{with} \quad (2.4.19)$$

$$\alpha = \sqrt{1 + \frac{R_{\text{TH}}^2}{z^2}}. \quad (2.4.20)$$

Using the difference of the on-axis electric field, computed by the mode expansion method and the above formula, as an indicator for the overall accuracy of the mode expansion method, the error of the approximation can be studied for different aperture sizes and mode orders in the decomposition. This will show that the Rayleigh range of the optimally decomposed tophat beam is the limit for which good approximation can be obtained.

Figure 2.15 shows the normalised difference, $|E_{\text{MEM}} - E_{\text{OA}}|/|E_{\text{OA}}|$, of the on-axis intensity distributions computed by the mode expansion method and the analytical formula given in equation (2.4.20). The plot on the left shows the difference for three different aperture sizes: $R_{\text{TH}} = 0.1 \text{ mm}$, $R_{\text{TH}} = 1 \text{ mm}$ and $R_{\text{TH}} = 4 \text{ mm}$. The error drastically decreases for propagation distances longer than the Rayleigh range of the modal set in the mode expansion. The error reaches its lowest value after propagation by about $z \geq 20 z_{\text{R}}$.

However, it should be stressed that the Rayleigh range depends on the square of the aperture radius, R_{TH} , as was shown in equation (2.4.13),

$$\frac{z}{\hat{z}_{\text{R}}} = \frac{\lambda \hat{N}}{2\pi} \frac{z}{R_{\text{TH}}^2}. \quad (2.4.21)$$

Hence, doubling the radius of the aperture, quadruples the propagation distance at which the same electric field distribution is obtained. This means that the same accuracy of the

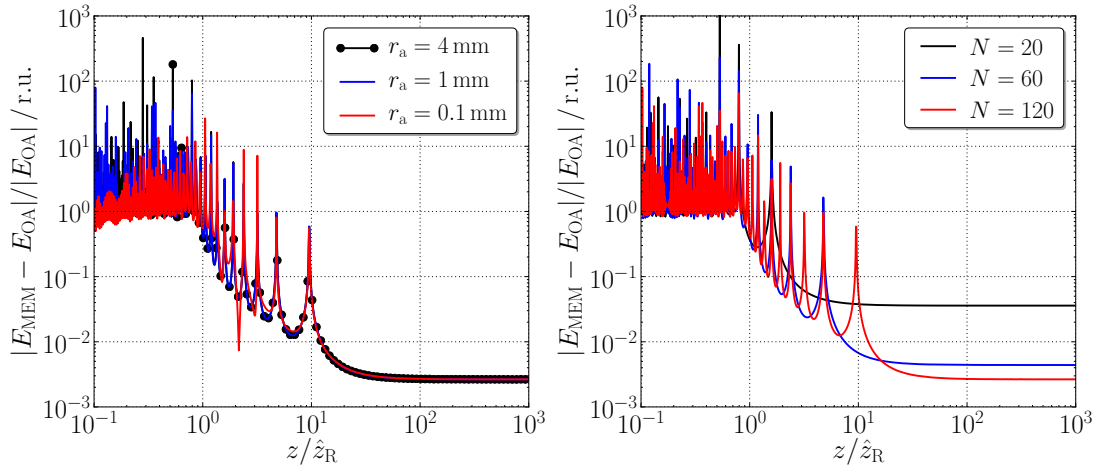


Figure 2.15.: Left: Deviation of the on-axis electric field of the tophat beam approximated by the mode expansion method, E_{MEM} , and the electric field, E_{OA} , computed by the analytical formula of equation (2.4.20). The curves show the normalised amplitude of the difference of the two fields, $|E_{\text{MEM}} - E_{\text{OA}}|/|E_{\text{OA}}|$, for three different tophat beam radii. Right: $|E_{\text{MEM}} - E_{\text{OA}}|/|E_{\text{OA}}|$ for three different maximum orders in the mode expansion. In both plots the propagation distance, z , normalised to the Rayleigh range, z_{R} , of the fundamental mode in the mode expansion.

approximation is reached at four times the distance, than was obtained for the aperture of half the size.

The right plot in Figure 2.15 shows the normalised difference, $|E_{\text{MEM}} - E_{\text{OA}}|/|E_{\text{OA}}|$, for different maximum mode orders used in the decomposition. The same general trend can be observed for this case as well: the magnitude of the error between the on-axis intensity distributions is only depending on the ratio, z/z_{R} , between the propagation distance and the Rayleigh range. Equation (2.4.21) shows that the ratio depends linearly on the maximum mode order, \hat{N} , used in the decomposition. However, an increased number of modes reduces the minimum error reached for large propagation distances.

An interesting effect can be observed in the data for the smallest shown aperture size of $R_{\text{TH}} = 0.1 \text{ mm}$. For this case the difference between the analytical solution and the mode expansion method slightly increases. In order to understand the origin and its consequences, the phase term of the analytic expression of equation (2.4.20) needs to be

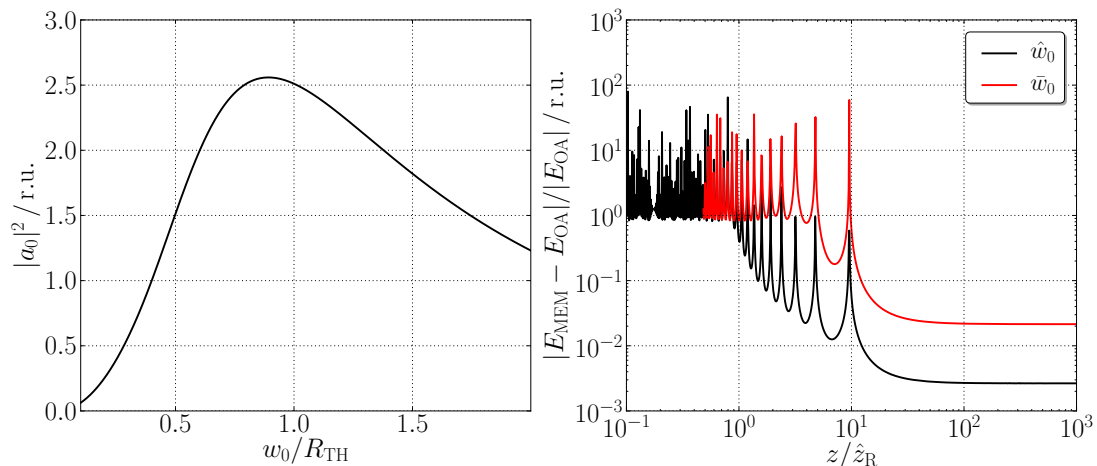


Figure 2.16.: Left: Power of the fundamental Gaussian mode in a mode expansion of a tophat beam, as a function of its waist radius. Right: Comparison of the on-axis electric field for a mode expansion of a tophat beam of 1 mm radius using the optimal waist radius, \hat{w}_0 , from equation (2.4.8) and the waist radius, \bar{w}_0 , from equation (2.4.25) that maximises the power in the fundamental mode. The mode expansion uses a maximum mode order of $\hat{N} = 120$.

studied in more detail. For the assumption that $R_{\text{TH}}^2 / z^2 \ll 1$ it can be approximated by

$$\phi(z) = -k\sqrt{z^2 + R_{\text{TH}}^2} + kz \quad (2.4.22)$$

$$\approx -k\frac{R_{\text{TH}}^2}{2z} + k\frac{R_{\text{TH}}^4}{8z^3}, \quad \text{if } \frac{R_{\text{TH}}^2}{z^2} \ll 1. \quad (2.4.23)$$

For the case of the smallest aperture size in Figure 2.15, the second term of order, R_{TH}^4 / z^3 is not negligible anymore and the error between the analytical solution and the mode expansion method increases. Reducing the radius of the tophat beam amplifies this effect.

For completeness it should be mentioned that a different *goodness-of-fit* criterion for the decomposition into higher-order Gaussian modes, then given in equation (2.4.7), is used by different authors.

For example, Petrovic et al. [PR03, PR05] use the mode expansion method to study diffraction losses in free-space optical interconnects, whereas Cagniot et al. [CFAA10] and Snyder et al. [Sny07] use the mode expansion method to study general diffraction effects such as the propagation of clipped higher order Laguerre-Gaussian modes. In contrast to maximising the power in the approximated electric field distribution, the authors of the aforementioned publications determine the optimum waist radius for the

decomposition by maximising the power in the fundamental mode.

For the case of the tophat beam the power in the fundamental mode is determined by its amplitude which was given by equation (2.4.2) as

$$a_{0,0} = \sqrt{2\pi} w_0 \left[1 - \exp\left(-\frac{R_{\text{TH}}^2}{w_0^2}\right) \right]. \quad (2.4.24)$$

The left plot in Figure 2.16 shows $|a_{0,0}|^2$ as a function of the waist radius. The power in the fundamental mode is maximised for a waist radius of

$$\bar{w}_0 \approx 0.892 R_{\text{TH}}. \quad (2.4.25)$$

For the two cases of a decomposition using the optimal waist radius, \hat{w}_0 , of equation (2.4.8) and the waist radius, \bar{w}_0 , that maximises the power in the fundamental mode, the right plot in Figure 2.16 compares the amplitude of the difference between the electric field computed by the mode expansion with the analytically calculated on-axial electric field, $|E_{\text{MEM}} - E_{\text{OA}}|/|E_{\text{OA}}|$.

It can be seen that using the optimal waist radius, \hat{w}_0 , results in a more accurate approximation of the on-axial electric field for shorter propagation distances behind the aperture plane.

2.4.5. Expression for the Required Mode Order

The results obtained in the last sections will be used now to deduce an expression for the necessary mode order in the mode expansion of the tophat beam, as a function of the radius of the tophat beam and the desired propagation distance after the aperture plane. It is assumed that the waist radius of the fundamental mode of the mode expansion is chosen as the optimal waist radius of equation (2.4.8).

In Section 2.4.2 the transverse electric field amplitude is compared for the case of the tophat beam approximated by the mode expansion method, equation (2.4.5), and the Fresnel integral of equation (2.4.12). The far-field intensity of the mode-expanded tophat beam is compared to the Airy disk intensity pattern in Section 2.4.3. The Airy disk pattern is given in equation (2.4.17).

For the far-field intensity pattern and the electric field in the Fresnel region, the largest error is seen on the optical axis. In Section 2.4.4 the on-axial electric field is computed with an analytic expression and compared to the on-axial electric field computed with the mode expansion method. Independent of the radius of the tophat beam and the maximum mode order used in the decomposition, the error drastically

decreases for propagation distances larger than the Rayleigh range of the modes in the mode expansion.

As the error is largely independent of the tophat beam radius and the considered mode order, the following relation can be given. The aim of the derived formula is to give a lower limit for the mode order. For a desired propagation distance after the aperture of z , the required mode order is such that the propagation distance corresponds to the Rayleigh range of the modes in the decomposition:

$$z \equiv \hat{z}_R = \frac{2\pi}{\lambda} \frac{R_{\text{TH}}^2}{\hat{N}}. \quad (2.4.26)$$

and hence, the required mode order can be given by

$$\hat{N} = 2\pi \frac{R_{\text{TH}}^2}{\lambda z} = 2\pi N_{\text{Fres}}, \quad (2.4.27)$$

with the Fresnel number, N_{Fres} , given in equation (2.4.11).

If for example the electric field after a circular aperture of radius $R_{\text{TH}} = 4$ mm is desired for a propagation distance of $z = 20$ cm, modes up to order of at least $\hat{N} \approx 472$ are required. However, these high mode orders are computationally demanding.

For a larger aperture radius of for example $R_{\text{TH}} = 10$ mm and a desired propagation distance of $z = 1$ m the mode order should at least be $\hat{N} = 590$. For these high modal orders to consider, other methods might be preferable.

2.5. Propagation of the Fundamental Fibre Mode

Another example of an application for the mode expansion method is the propagation of fibre modes through the interferometer, as they are sufficiently smooth and non-Gaussian. Fibre modes are of interest in precision metrological interferometers like the LRI in GRACE Follow-On or LISA because usually the laser light is delivered by optical fibres to the optical bench. In the case of GRACE Follow-On, the beam emitted by the fibre will be split off the central beamsplitter and routed via the triple-mirror assembly to the other spacecraft. Hence, the far-field intensity pattern will be the fibre mode, transformed by the fibre outcoupler optics and then propagated through approximately 200 km of free-space. The use of higher-order Gaussian modes will enable the propagation of fibre modes in interferometers under the limit of the paraxial wave equation.

This section gives a brief introduction to the theory of fibre modes and uses the mode expansion method to compute the far-field intensity pattern for the case of GRACE

Follow-On. Based on the results of these investigations a simple model for the far-field intensity pattern is developed and used to efficiently compute the received power in the simulation of laser link acquisition.

2.5.1. A Brief Introduction to Fibre Modes

Fibre modes were extensively studied in the past with a history of more than 100 years. A short historical summary was published by Doerr and Kogelnik [DK08] who give a brief introduction to fibre modes of various types. A good and comprehensive summary of the theory of optical fibres can also be found in [Buc04], while in [Sny81] the emphasis is on deriving basic properties of fibre modes by approximating the fundamental fibre mode by a Gaussian beam.

The fibre modes discussed here are derived under the *weak-guiding condition* and for cylinder-symmetric dielectric waveguides with step index profiles. The fibres used for high precision interferometers usually use polarisation maintaining fibres. These fibres have additional stress-inducing elements that introduce birefringence [SSOH83]. Here, polarisation is neglected but the weakly-guiding and symmetrical waveguide is a good approximation. Also, the phase propagation within optical fibres is of no interest here and will thus not be covered. Only the amplitude distribution of the fundamental fibre mode at the end-face of the optical fibre is needed.

The weak-guiding condition for a fibre is met if the following relation for the refractive indices of the core n_{core} and the cladding n_{clad} hold:

$$n_{\text{core}} \gtrsim n_{\text{clad}}. \quad (2.5.1)$$

The index profile in step index fibres is characterised by a discontinuous change in the refractive index at the core-cladding interface. In this case, the modes of the fibre can be described as the linear-polarised (LP) modes which were first derived by D. Gloge in 1971 [Glo71]. As the name suggests, due to the weak guidance, the electric field in the fibre can be well approximated by freely propagating plane waves which are linearly polarised and have a negligible field amplitude in propagation direction.

The transverse amplitude distribution of these modes is characterised by only two parameters which are the core radius a and the normalised frequency V . The normalised frequency determines the number and type of modes that are guided in a fibre.

Manufacturers usually characterise optical fibres in terms of the numerical aperture, the mode-field radius r_0 , or cut-off wavelength λ_{cut} given at an operating wavelength λ_{op} . They usually do not specify the refractive indices or the core diameter. This section

will briefly review the theory of fibre modes so that the functional dependence between these quantities and V and a can be given.

The normalised frequency is a function of the vacuum wavelength λ of the light propagating in the fibre as well as the core radius a and the refractive indices of the core n_{core} and cladding n_{clad} . It can be expressed by

$$V = \frac{2\pi a}{\lambda} \sqrt{n_{\text{core}}^2 - n_{\text{clad}}^2}. \quad (2.5.2)$$

The electric field of the linearly polarised LP modes can be given by the following expressions for the inner core and the cladding region. It is expressed in cylindrical coordinates (r, ϕ, z) , where r is the radial distance from the centre of the core, ϕ is the azimuthal angle in the plane orthogonal to the fibre axis and z is the propagation distance along the fibre axis. The field amplitude is then given by

$$E(r, \phi, z)_{l,m} = \begin{cases} E_0 J_l(\sigma r/a) \cos(l\phi) \exp(-i\beta z), & \text{if } r \leq a \\ E_0 [J_l(\sigma)/K_l(\tau)] K_l(\tau r/a) \cos(l\phi) \exp(-i\beta z), & \text{if } r > a. \end{cases} \quad (2.5.3)$$

The V -parameter is not explicitly visible in this equation but the parameters σ , τ and β are functions of it. The radial dependence in the core region is described by Bessel functions of the first kind, J_l , of order l which appear due to the cylindrical symmetry of the system and the discontinuous boundary at the core-cladding interface.

The amplitude of the electric field outside of the core region, in the cladding, is exponentially damped by the modified Bessel function of the second kind K_l . This can be deduced from the asymptotic behaviour for large arguments x , $K_l(x) \approx \sqrt{\pi/(2x)} \exp(-x)$ [BSMM01]. The dependence in azimuthal direction is given by the term $\cos(l\phi)$, where l has to be an integer such that the field is reproduced for angles larger than 2π and $l = 0$ represents the fundamental mode with cylindrical symmetry.

The propagation along the fibre axis is taken care of by the factor $\exp(-i\beta z)$ with the propagation constant β that takes the role of the wavenumber k . It varies for different LP modes and depends on the frequency and the refractive indices. The two new parameters σ and τ are connected via $V = \sqrt{\sigma^2 + \tau^2}$ and are constants for a given V and fibre mode $\text{LP}_{l,m}$. In general, they are functions of the core diameter, refractive indices and the propagation constant β . The index m does not appear explicitly in equation (2.5.3) but it is used to index allowed regions for the σ parameter.

The on-axial electric field amplitude can be given in terms of the power contained in the fibre mode. Here, the impedance of the medium is set to unity as before in the case

of the Gaussian beam, which leads to the following equation:

$$E_0 = \sqrt{\frac{2P}{c_l}} \frac{\sigma}{V} \frac{1}{aJ_l(\sigma)} \frac{K_l(\tau)}{\sqrt{K_{l-1}(\tau)K_{l+1}(\tau)}}. \quad (2.5.4)$$

The constant factor c_l which appears in equation (2.5.4), is defined as

$$c_l := \begin{cases} 2\pi & \text{if } l = 0, \\ \pi & \text{if } l \neq 0. \end{cases} \quad (2.5.5)$$

A derivation of equation (2.5.4) is given in the Appendix A. For a given V , the parameter σ can be obtained by numerically solving the eigenvalue equation of the LP modes which is given here because besides approximate formulae it is the more accurate method of determining σ [Buc04, Sny81]. It reads:

$$\frac{J_{l-1}(\sigma)}{J_l(\sigma)} = -\frac{\tau}{\sigma} \frac{K_{l-1}(\tau)}{K_l(\tau)}. \quad (2.5.6)$$

The number of solutions of this equation is finite for a given value of V and increases with increasing V . For $0 < V < 2.405$ only one solution exists if $l = 0$. The index m for this first mode arising is set to $m = 1$ and the mode $\text{LP}_{0,1}$ is called the *fundamental fibre mode*. If $2.405 < V < 3.832$ the two modes that are allowed to propagate are the fundamental mode and additionally the $\text{LP}_{1,1}$ mode.

These so called *cut-off frequencies* exist for every guided fibre mode and only the fundamental mode has a cut-off frequency of $V_{\text{cut}} = 0$. For a detailed summary of the designation of the LP modes see one of [Glo71, Buc04]. Thus, if a fibre should be single-mode, a normalised frequency of $V < 2.405$ has to be realised. The cut-off frequencies define the cut-off wavelength for a given fibre by

$$V_{\text{cut}} = \frac{2\pi a}{\lambda_{\text{cut}}} \sqrt{n_{\text{core}}^2 - n_{\text{clad}}^2}. \quad (2.5.7)$$

Hence, if the cut-off wavelength is given for a fibre, the normalised frequency V for any other wavelength λ is just given by

$$V = (\lambda_{\text{cut}}/\lambda)V_{\text{cut}}. \quad (2.5.8)$$

For a single-mode fibre the cut-off wavelength for the second fibre mode $\text{LP}_{1,1}$ is usually given such that $V_{\text{cut}} = 2.405$. Knowing V for the desired operating frequency, the eigenvalue equation (2.5.6) can be solved for σ by inserting $\tau = \sqrt{V^2 - \sigma^2}$.

A useful property of the LP modes is that they are orthonormal such that any light field at the input of the fibre decomposes into different LP modes. If a Gaussian beam is coupled under normal incidence and properly matched into the fibre, most of the power will couple into the fundamental fibre mode as it is the mode that closest resembles a Gaussian beam [Buc04]. The mode field radius \hat{r} is now defined as the radius of the Gaussian fundamental mode that maximises the coupling into the fundamental fibre mode. An approximate empirical formula can be given that connects the core radius a , and the normalised frequency V , to the mode field radius by [Mar77]

$$\frac{\hat{r}}{a} \approx 0.65 + \frac{1.619}{V^{3/2}} + \frac{2.879}{V^6}. \quad (2.5.9)$$

If the normalised frequency is computed for the same wavelength for which the mode field radius is known, the core radius a can be computed from equation (2.5.9). Together with V for the desired operating wavelength, all parameters required to compute the electric field of the fibre modes with equation (2.5.3) are known.

If instead of the cut-off frequency the numerical aperture of the fibre is given, equation (2.5.9) can be transformed into a nonlinear equation for the core radius with the following relations: The numerical aperture, NA, is the sine of the maximum acceptance angle θ_{NA} , of a fibre and can be given in terms of the refractive indices of the fibre and that of the surrounding medium n_0 as

$$\text{NA} = \sin \theta_{\text{NA}} = \frac{1}{n_0} \sqrt{n_{\text{core}}^2 - n_{\text{clad}}^2}. \quad (2.5.10)$$

Here the fibre is assumed to be in air or vacuum such that $n_0 \approx 1$. For this case, the normalised frequency can be given as a function of NA by (compare to equation 2.5.2)

$$V = \frac{2\pi a}{\lambda} \text{NA}. \quad (2.5.11)$$

Inserting equation (2.5.11) into equation (2.5.9), with λ set to the wavelength for which the mode field radius is given, the core radius can be computed, and successively with equation (2.5.11) and the desired operating wavelength, the V -parameter.

For the analysis presented in this section, the following fibre parameters were used which correspond to a CORNING PM98-U25A polarisation maintaining PANDA structured fibre. The mode field radius is given as $\hat{r} = 3.05 \mu\text{m} - 3.55 \mu\text{m}$ at a wavelength of $\lambda_{\text{spec}} = 980 \text{ nm}$ and the cut-off wavelength for the second mode $\text{LP}_{1,1}$ is given as $\lambda_{\text{cut}} = 870 \text{ nm} - 950 \text{ nm}$. The finite ranges given for the mode field diameter and the cut-off wavelength result from uncertainties in the core diameter and the normalised

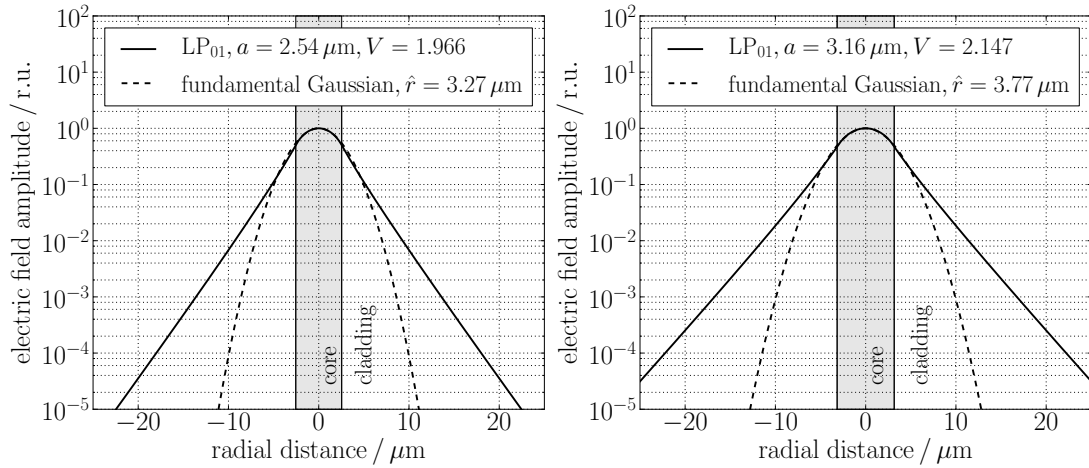


Figure 2.17.: Cross sectional amplitude profile of the LP_{0,1} fibre mode as compared to the Gaussian beam that maximises the input coupling. Left: Profile for the smaller core diameter. Right: Profile for the larger core diameter.

frequency. To accommodate these uncertainties, the smallest and largest core diameter are computed and a comparison of the resulting fibre modes is done. From the cut-off wavelengths the normalised frequency V_{spec} at the specified wavelength λ_{spec} can be computed by equation (2.5.8), with $V_{\text{cut}} = 2.405$ to $V_{\text{spec}} = 2.135$ – 2.331 .

Table 2.1.: Summary of the specified and computed values of the CORNING PM98-U25A PANDA fibre used for the analysis of this section. The specified mode field radius \hat{r}_{spec} and normalised frequency V_{spec} are given for $\lambda_{\text{spec}} = 980 \text{ nm}$. The computed parameters at the operating wavelength of $\lambda = 1064 \text{ nm}$ are V_{op} , σ_{op} -parameter and the mode field radius \hat{r}_{op} . The best fit Gaussian radius, r_{fit} , was found by fitting a Gaussian profile to the fibre mode using a least squares fit.

Item		Case 1: smaller core	Case 2: larger core
Description	Symbol		
Cut-off wavelength	λ_{cut}	870 nm	950 nm
Mode field radius	\hat{r}_{spec}	3.05 μm	3.55 μm
Normalised frequency	V_{spec}	2.135	2.331
Core radius	a	2.54 μm	3.16 μm
Normalised frequency	V_{op}	1.967	2.147
σ -parameter	σ_{op}	1.517	1.575
Mode field radius	\hat{r}_{op}	3.27 μm	3.77 μm
Best fit Gaussian radius	r_{fit}	3.15 μm	3.70 μm

From there, the core radius, a , can be computed by equation (2.5.9). A higher normalised frequency results in stronger mode confinement and thus a smaller mode field radius compared to the core radius. For a fixed mode field radius, a higher frequency will result in a larger core radius as computed from equation (2.5.9). To obtain the range of possible core radii which fit to the provided specifications, the smaller V parameter is used with the lower value for the mode field radius, under the assumption that the errors are uncorrelated. This results in $a = 2.54\mu\text{m} - 3.16\mu\text{m}$.

After computing V_{op} for the operating wavelength $\lambda = 1064\text{nm}$, the σ parameter can be computed with help of the eigenvalue equation (2.5.6) and the parameter τ , by $\tau^2 = V^2 - \sigma^2$. The specified and computed values for the parameters for the two cases are summarised in Table 2.1. The resulting field amplitudes for the fundamental fibre mode are given in Figure (2.17) compared to the Gaussian beam with the corresponding mode field radius, \hat{r}_{op} . The mode field radius \hat{r}_{op} is computed from equation (2.5.9) using V_{op} at the operating wavelength.

If instead of equation (2.5.9) a least squares fit is used to fit a Gaussian profile to the fibre mode, a slightly different radius is found deviating from the computed value by roughly 2%-3.5% which gives a rough indication of the error of the empirical formula.

The fibre mode and the Gaussian beam with maximised overlap fit well in the core region, while starting from a radial distance of roughly $1.5\hat{r}$, the two beam types start to deviate.

The prominent difference between the two beams, however, is the decay in transversal direction that is, on a log scale, quadratic in the case of the Gaussian beam and linear for the fibre modes. Thus, the amplitude distribution will change differently under propagation.

2.5.2. Propagation of $\text{LP}_{0,1}$ with the Mode Expansion Method

The propagation of the $\text{LP}_{0,1}$ mode will be studied here with the use of the mode expansion method which was described in Section 2.3. The mode expansion method is well suited to simulate the propagation of the fibre mode as the fibre modes are non-Gaussian but sufficiently smooth to be well approximated by a suitable set of higher order Gaussian modes.

For the decomposition of the fibre mode the implementation of the mode expansion in IfoCad was used. At first, the electric field amplitude of the fibre mode at the fibre end-face was computed on a regular square grid with help of the analytical formula of equation (2.5.3). The core radius and normalised frequency were set to the values computed for the CORNING PM98-U25A polarisation maintaining fibre which are sum-

marised in Table 2.1.

Due to the rectangular symmetry of the underlying grid, Hermite-Gaussian modes were used as the basis set for the mode expansion, and the mode amplitudes were computed according to equation (2.3.11). However, the circular symmetry of the fibre mode was taken into account by limiting the mode expansion to modes of even orders. The order N of a Gaussian mode was defined in equation (2.3.18) as $N = m + n$ for the case of Hermite-Gaussian modes and $N = 2p + |l|$ for the case of Laguerre-Gaussian modes. Here, m and n are the horizontal and vertical mode indices of the Hermite-Gaussian modes and p and l are the radial and azimuthal mode indices of the Laguerre-Gaussian modes. The series expansion of a circular symmetric electric field distribution into Laguerre-Gaussian modes contains only modes for which the azimuthal index $l = 0$. The order of the modes contained in the series expansion is therefore given by $N = 2p$, for $p = 0, \dots, p_{\max}$. Hence, also the expansion into Hermite-Gaussian modes contains only even orders, as the order of a mode is preserved under a basis transformation from Laguerre- to Hermite-Gaussian modes. For further details see Section 2.3.

The phase front of the fibre mode is that of a plane wave under the weak-guiding approximation such that the waist position of the Hermite-Gaussian modes was set to coincide with the fibre end-face. The waist radius of the fundamental mode, w_0 , in the set of Hermite-Gaussian modes was set to the mode field radius $w_0 = \hat{r}$ that was derived with the empirical formula given in equation (2.5.9). As this particular choice of the mode field radius maximises the coefficient of the fundamental Gaussian mode in the decomposition, it leads to a reasonably small number of required higher order modes.

The result of the mode decomposition is shown in Figure 2.18 for the two cases of the last section. Shown is the sum of the power over modes with the same order $N = m + n$ for a decomposition in Hermite-Gaussian modes. The left plot in Figure 2.18 only shows the non-zero even orders and the connecting line is meant as a help for the reader. It can be seen that the power in the fundamental mode is quite high, reaching $|a_{0,0}|^2 = 0.986$ for the smaller core radius and $|a_{0,0}|^2 = 0.994$ for the larger core radius, for the case of a fibre mode of power $P = 1$.

A Gaussian beam is already a good approximation to the fibre mode in terms of the strong localisation of the beam power. To model the propagation of the fibre mode after it emerged into free-space and keep high precision of the amplitude distribution, also in the flanks, the higher order modes are needed. To estimate the number of higher order modes necessary to approximate the fibre mode, the right plot in Figure 2.18 shows an analytical amplitude distribution compared to the approximation by a set of Gaussian modes for different maximum orders N , considered in the mode expansion.

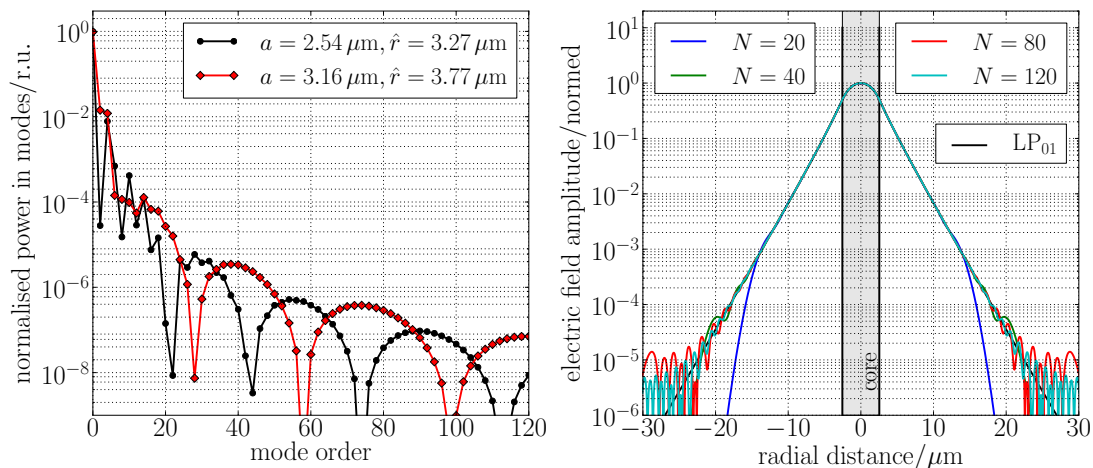


Figure 2.18.: Left: Power in the modes of the same order for the decomposition of the two $\text{LP}_{0,1}$ modes presented in Table 2.1. The waist radius of the Gaussian fundamental mode is chosen as the mode field radius of the fibre mode. Only even orders are plotted. The line through the single points is meant as a guide for the reader. Right: Electric field amplitude for the LP mode and the approximating mode expansion for different maximum orders N , considered in the mode expansion. The fibre mode corresponds to the case with the smaller core radius.

A good approximation within about 6 mode field radii can already be obtained for a maximum order of $N = 40$. Adding higher orders only slightly increases the region for which the deviation between the exact and approximated LP amplitudes is small. This is due to the fact that the mode radius of the higher order modes increases only proportional to \sqrt{N} , making it necessary to increase N quadratically for a linear increase in the width of the matching region. The mode radius of a higher-order mode was defined in equation (2.4.9) as $W(z) = \sqrt{N + 1/2} w(z)$, as a function of the beam radius $w(z)$ of the fundamental Gaussian mode which was defined in equation (2.2.3).

The propagation of the LP mode in free-space is now accomplished by propagating the set of higher order Gaussian modes. In order to determine the accuracy of the approximation for the propagated fibre mode an analytical expression for the normalised far-field intensity pattern of the fundamental fibre mode is used which was derived by Gambling et al. [GPMD76] based on the work of Snyder [Sny69]. For $\alpha = ak \sin \theta$ it is given by

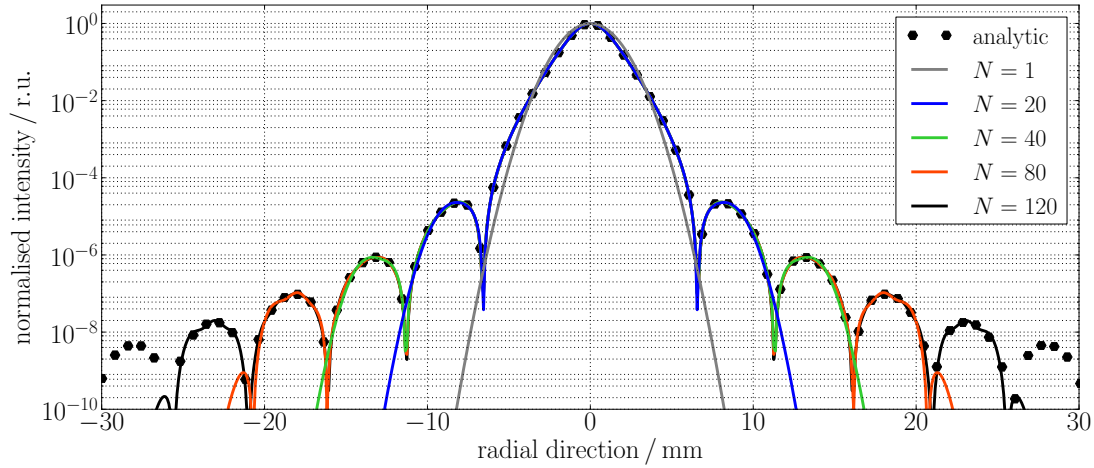


Figure 2.19.: Intensity pattern of the propagated Hermite-Gaussian expansion of the LP_{01} mode for the smaller core case of the last section for expansions including different maximum orders of Hermite-Gaussian modes. The intensity pattern is compared to the analytical far-field intensity pattern of equation (2.5.12). The Hermite-Gaussian modes are propagated by 3.394 cm in homogeneous Fused Silica with an index of refraction $n = 1.44963$. The width of the fundamental mode is $w(z = 3.394 \text{ cm}) = 2.42 \text{ mm}$.

$$|E_{0,1}|^2 = \begin{cases} \frac{\sigma^4 \tau^4}{(\sigma^2 - \alpha^2)^2 (\tau^2 + \alpha^2)^2} \left[J_0(\alpha) - \alpha J_1(\alpha) \frac{J_0(\sigma)}{\sigma J_1(\sigma)} \right]^2 & \text{if } \sigma \neq \alpha \\ \frac{\sigma^4 \tau^4}{4V^4} \frac{1}{\sigma^2 J_1^2(\sigma)} (J_0^2(\alpha) + J_1^2(\alpha))^2 & \text{if } \sigma = \alpha. \end{cases} \quad (2.5.12)$$

The intensity distribution is given on a sphere with radius equal to the propagation distance, with its centre at the fibre end-face and θ being the polar angle between the fibre axis and the direction for which the intensity should be computed. The normalised frequency V and the core radius a are defined as before. Also, σ and τ are the fibre mode parameters connected to the normalised frequency by $V^2 = \sigma^2 + \tau^2$ and k is the wavenumber in the medium surrounding the fibre.

Anticipating a result from the next section for comparison, the $LP_{0,1}$ fibre mode was decomposed into a set of Hermite-Gaussian modes. Here, again the waist location is set to coincide with the fiber end-face and the waist radius of the fundamental Gaussian mode is set to the mode field radius of the fibre mode, $w_0 = \hat{r}$. After this, the set of higher-order modes is propagated through Fused Silica, with an index of refraction of $n_{\text{FS}} = 1.44963$, by a distance of 3.394 cm. Thereafter, the electric field intensity was computed and compared to the analytical expression of equation (2.5.12). The

computed field distribution corresponds to the field distribution at the end surface of the fibre outcoupler that is discussed in the next section.

The comparison is excellent as can be seen in Figure 2.19. For orders of $N = 40$ the far-field intensity can be reproduced by up to 6 times the width of the fundamental Gaussian mode, whereas for $N = 120$ the approximation agrees to up to 10 times the width. The width of the propagated fundamental mode was computed to $w(z) = 2.42$ mm. In the following part of this chapter, the waist radius of the fundamental Gaussian mode that is used to decompose the fibre mode is always set to the mode field radius of the fibre, as computed by equation (2.5.9). The width of the fundamental Gaussian mode as it propagates will be called the *mode radius of the fibre mode* and denoted by the usual $w(z)$.

The results of this sections are now used in the following section to determine the expected far-field intensity pattern for the case of a special design of a fibre outcoupler on the GRACE Follow-On optical bench.

2.5.3. GRACE Follow-On Far-Field Intensity Pattern

Simulating the far-field intensity pattern is important for acquisition as it determines the dependence of the power received by the distant spacecraft on misalignments of the transmitted beam. For this analysis a special design for a fibre outcoupler is assumed which is depicted in Figure 2.20. The actual design for the GRACE Follow-On mission uses an aspheric end-surface (private communication M. Dehne, STI, 2013). However, aspherical surfaces cannot be simulated by the mode expansion method in IFOCAD as it is implemented at the moment. Due to this, the end-surface of the fibre outcoupler will be approximated by a parabolic surface with a radius of curvature of R_S .

The fibre outcoupler is assumed to be a monolithic block of Fused Silica with index of refraction of $n_{FS} = 1.44963$ to which the fibre is rigidly attached. The end surface of the outcoupler is a parabolic surface with a radius of curvature of $R_S = -10.527$ mm. The length of the outcoupler is chosen such that the fibre end-face is located at the back focal plane of the curved front surface. This means that the length is fixed to $z_1 = 33.94$ mm. This also implies that the waist position of the modal set used in the decomposition is close to the end surface of the fibre outcoupler such that here, $w(z) \approx w_0$.

In order to determine the far-field intensity pattern, the fibre mode amplitude is analytically calculated for the small core radius case of the former section. This is done because the mode field radius of the fibre mode of the smaller core fibre, at the end surface of the fibre outcoupler, is $w(z) = 2.42$ mm. This is closer to the nominal Gaussian beam expected for GRACE Follow-On of $w_0 = 2.5$ mm. The amplitude distribution of

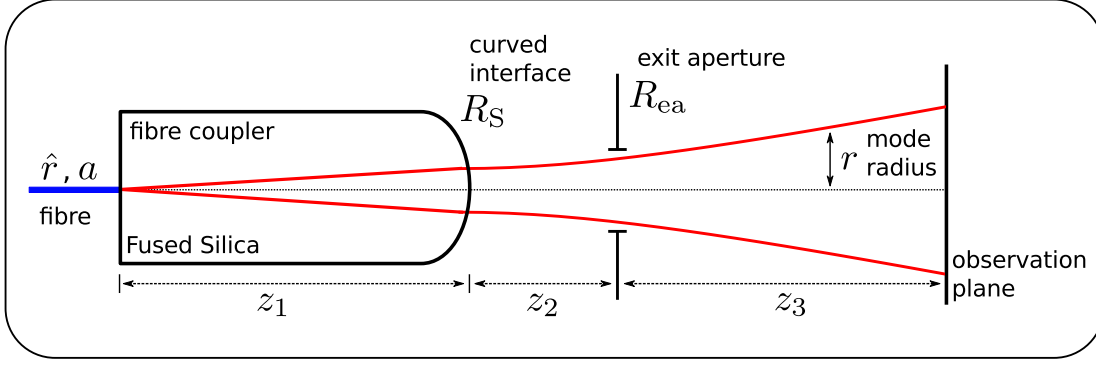


Figure 2.20.: Schematic of the simulated setup. The fibre mode is decomposed into a set of Hermite-Gaussian modes at the fibre end-face and propagated via the fibre outcoupler to the exit aperture with radius R_{ea} . After clipping at the exit aperture, the beam is propagated to the remote spacecraft where the intensity pattern is calculated. The distances are assumed to be: $z_1 = 33.94$ mm, $z_2 = 2.38$ m and $z_3 = 220$ km.

the fibre mode is then decomposed into a set of higher order Hermite-Gaussian modes up to order $N = 120$.

The set of Hermite-Gaussian modes is then propagated in Fused Silica to the tip of the curved interface of the fibre outcoupler. The assumption is that the fibre is perfectly aligned and that the beam passes through the glass-air interface on the optical axis of the parabolic surface. In this case the effect of the lens can be taken into account by transforming the q-parameter of the Gaussian beam. Generally, the ABCD-matrix for the transformation of the Gaussian beam at the curved interface between Fused Silica with a refractive index of $n_{FS} = 1.44963$ and vacuum with $n_0 = 1$ and radius of curvature R_S is [MS69]:

$$M = \begin{pmatrix} 1 & 0 \\ \frac{n_{FS} - 1}{R_S} & \frac{1}{n_{FS}} \end{pmatrix}. \quad (2.5.13)$$

After the beam is transformed through the lens, the Gaussian beam is propagated by $z_2 = 2.38$ m to the exit aperture with radius R_{ea} . The field distribution in the exit aperture is computed and the field is again decomposed into a different set of Hermite-Gaussian modes of maximum order $N = 120$. The waist radius w_0 of the Gaussian modes is chosen to be the optimal radius of equation (2.4.8), namely $w_0 = R_{ea}/\sqrt{N/2}$ for a circular aperture. The waist position is set to coincide with the aperture plane. The Hermite-Gaussian modes approximating the clipped beam are then propagated by $z_3 = 220$ km and after this, the intensity pattern is computed.

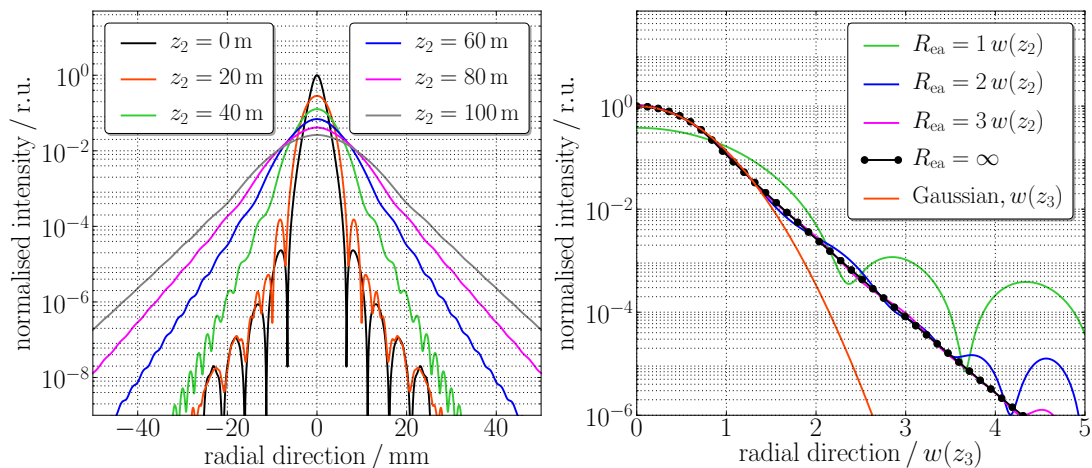


Figure 2.21.: Left: Intensity pattern behind the curved interface for several propagation distances z_2 after passing through the front surface of the fiber outcoupler. Here, no clipping at the exit aperture is simulated. The curve for $z_2 = 0$ m shows the field directly at the curved surface, which corresponds to the field-distribution shown in Figure 2.19. Right: Far-field intensity pattern of the clipped and transmitted fibre mode in 220 km distance at the remote spacecraft and for comparison the fundamental Gaussian mode in the series expansion. The radius of the exit aperture, R_{ea} , is varied by multiples of $w(z_2 = 0) = 2.42$ mm, which is approximately the mode radius of the fiber mode at the exit aperture. The horizontal axis is normalised to the mode radius of the propagated fiber mode which is $w(z_3) = 29.7$ m with $z_3 = 220$ km.

In the left plot of Figure 2.21 the change of the intensity pattern after the curved surface of the fiber outcoupler is shown for several propagation distances, z_2 . The field at $z_2 = 0$ m corresponds to the field distribution directly at the surface and coincides with the intensity distribution shown in Figure 2.19 for $N = 120$. A comparison was made also for different maximal orders of the decomposition in order to investigate if additional modes alter the intensity pattern. It was found that convergence was reached starting from mode orders of $N = 100$.

The Rayleigh range of the Hermite-Gaussian beam used in the expansion is equal to $z_R \approx 17.3$ m and generally the biggest changes to the field should be seen within a region of the order of z_R because the relative phase shift between the higher-order modes is due to the Gouy phase. For a stigmatic mode this is equal to

$$\zeta(z_3) = (N + 1) \tan^{-1} \left(\frac{z_3}{z_R} \right). \quad (2.5.14)$$

In the plot a *stable* state of the intensity pattern, that only scales linear with the propa-

gation distance is reached at $z_3 \approx 40$ m, i.e. roughly of $2.3 z_R$. From there on, only small ripples in the left and right tail of the distribution remain.

In the right plot of Figure 2.21 the far-field pattern for a propagation distance of $z_3 = 220$ km is shown for different radii of the exit aperture and compared to the propagated Gaussian beam maximising the coupling into the fibre mode, which was computed with the help of equation (2.5.9). The Gaussian beam and the propagated fibre mode match well in the transversal direction up to about 1.5 times the width of the Gaussian beam. After this, the propagated fibre mode falls off significantly slower than a Gaussian beam. If the outgoing beam is clipped by the exit aperture at the mode radius of the fibre mode $w(z_2)$, a significant change of the far-field intensity pattern can be observed.

For larger aperture sizes the effect decreases but does not vanish. If for example the beam is clipped at $2 w(z_2)$ the intensity pattern in the far field is only slightly different from the non-clipped beam for intensities larger than 10^{-4} of the on-axis intensity. For clipping at $3 w(z_2)$ hardly any effect of the aperture can be seen at all, but the difference to a Gaussian beam remains.

The far-field intensity of the fibre mode transformed by the parabolic surface is seen to be equal to the intensity of the fibre mode itself, except for scaling, which is due to the imaging properties of the perfect lens, when the fibre is located at the back focal point. During the laser link acquisition of the LRI on GRACE Follow-On, the far-field intensity distribution determines the power that is received by the spacecraft, depending on the misalignment of the transmitted beam relative to the line-of-sight between the satellites. The results obtained in this section give a model of the far-field intensity pattern, based on a realistic beam model and output optics and consider clipping of the transmitted beam.

2.5.4. Analytical Model for the Far-Field Intensity Pattern

The computation of the far-field intensity in the high-fidelity simulation of the laser link acquisition for GRACE Follow-On should be fast and easy to implement, as it has to be computed several 10 000 times for different beam alignments in order to compute the amplitude of the heterodyne signal. For this, a simple analytical expression taking the decrease of the amplitude with propagation distance and the divergence of the beam into account is preferred.

As no analytic expression for the intensity pattern was found a new model was developed based on the observation that the shape of the intensity pattern resembles that of the $LP_{0,1}$ fibre mode as found in the last section for the case that clipping of the beam can be neglected. If an electric field can be decomposed into a finite number of

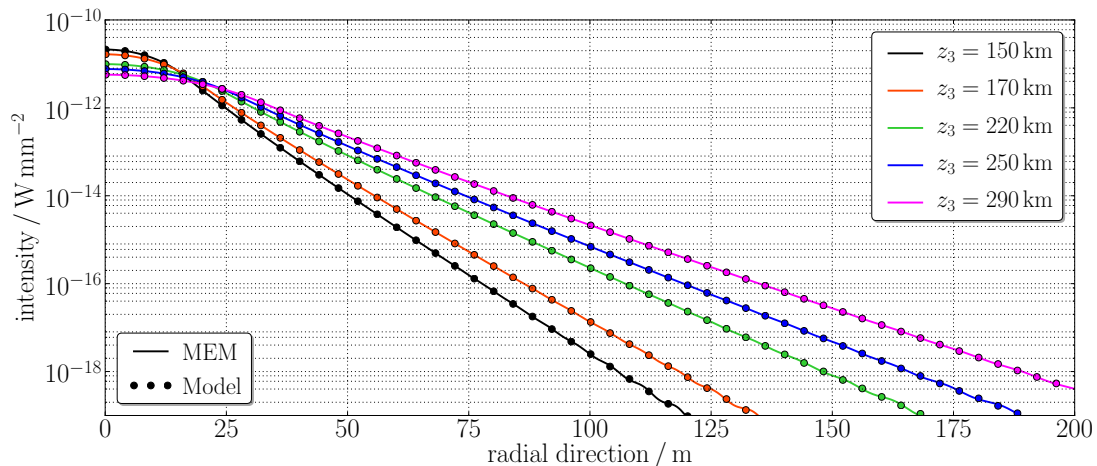


Figure 2.22.: Comparison between the far-field intensity pattern as computed by the mode expansion method and the simple model developed in this section. The comparison is made for various propagation distances over the expected spacecraft separation in the GRACE Follow-On mission. The transmitted power is set to 13.7 mW. The propagated fibre mode is the small core case of the former sections.

higher-order modes with sufficient accuracy the far-field properties of the decomposed beam are given by the far-field properties of the higher-order modes. The change of the beam parameters upon propagation in the far-field, i.e. for $z_3 \gg z_R$, are given by:

$$\begin{aligned} R(z_3) &\approx z_3 \\ w(z_3) &\approx \frac{w_0}{z_R} z_3 = \theta_0 z_3, \end{aligned} \quad (2.5.15)$$

meaning that the wavefronts are approximately spherical and the width of the modes scales linear with the propagation distance. Again most of the power in the fibre mode is in a Gaussian fundamental mode and the far field properties should be governed by the far-field properties of this mode.

The setup that is simulated here is the same that was studied in the last section and was shown in Figure 2.20. The fiber mode for the fibre with the smaller core is decomposed into a set of higher-order Gaussian modes and then propagated to the end surface of the fibre outcoupler. It is then transformed by the curved glass-air interface and finally propagated into the far-field. The smaller core fibre is used as its mode radius is closer to the nominal beam radius expected for the LRI on GRACE Follow-On.

At the end surface of the fibre outcoupler the waist radius of the Gaussian modes can be computed as $w_0 = 2.43$ mm. The beam radius as it propagates by a distance z_3 is

denoted by $w(z_3)$. In the far-field the beam radius can be approximated by

$$w(z_3) \approx \theta_0 z_3, \quad \text{with} \quad \theta_0 = \lambda/(\pi w_0). \quad (2.5.16)$$

The expression for the electric field of the fibre modes in equation (2.5.3) only depends on the ratio of the radial coordinate to the core radius a . The core radius is proportional to the mode field radius \hat{r} for fixed σ , τ and hence V , and can be written with the proportionality constant α as $a = \alpha \hat{r}$.

Correct scaling of the intensity pattern can be achieved by using the scaling of the mode field radius with the propagation distance taken from equation (2.5.15) which yields

$$a(z_3) = \alpha w(z_3). \quad (2.5.17)$$

The proportionality constant can be set to $\alpha = a/\hat{r}$ in order to resemble the shape of the intensity pattern of the fiber mode itself. Rewriting the electric field of the fundamental fibre mode as a function of the mode field radius and using the connection between the power in the beam and the on-axis electric field E_0 from equation (2.5.4), the following model for the far-field beam is obtained:

$$|E_{\text{FF}}(\rho, z)|^2 = \frac{P}{\pi(\alpha w(z))^2} \frac{V^2}{\tau^2 J_1^2(\sigma)} \begin{cases} J_0^2\left(\frac{\sigma \rho}{\alpha w(z)}\right), & \text{if } \rho \leq \alpha w(z) \\ \left[\frac{J_0(\sigma)}{K_0(\tau)}\right]^2 K_0^2\left(\frac{\tau \rho}{\alpha w(z)}\right), & \text{if } \rho > \alpha w(z). \end{cases} \quad (2.5.18)$$

Figure (2.22) shows a plot comparing the simple model for the far-field of equation (2.5.18) with the far-field computed with the mode expansion method neglecting clipping at the exit aperture. Over the range of expected spacecraft separations for GRACE Follow-On the developed model yields accurate results and can be used as an efficient method to compute the far-field in the acquisition simulation.

2.6. Conclusions

In this chapter an introduction to heterodyne interferometry was given with a derivation of the heterodyne photocurrent. Subsequently, the longitudinal pathlength signal and the differential wavefront sensing signal were presented.

The mode expansion method is introduced, after a presentation of Gaussian beam

tracing, as a tool to simulate high-precision interferometers under the paraxial approximation of the scalar wave equation for non-Gaussian beams. The mode expansion method makes use of the fact that both the Laguerre- and Hermite-Gaussian modes form complete orthonormal sets of solutions of the paraxial wave equation. Any light field given in an input plane can be expressed as a unique series expansion of these modes.

The propagation of higher-order Gaussian modes through a paraxial optical system can be handled by transforming the q -parameter of the modal set by means of the ABCD formalism, whereas the amplitudes of the modes are invariant under these transformations. As such, the mode amplitudes in a mode decomposition need to be computed only once at the input plane, while the propagation through the paraxial system involves just a few arithmetic operations.

The mode expansion method was implemented into IFOCAD, an interferometer simulation toolkit developed at the Albert Einstein Institute. It was successfully applied to the propagation of the important cases of a tophat beam and a fundamental fibre mode. For the case of the tophat beam, the validity of the mode expansion method could be verified by comparisons to analytical expressions for Fresnel- and Fraunhofer diffraction. If an optimal waist radius is used for the decomposition, the range in transversal direction for which the approximation yields accurate results, could be linked to the mode radius of the highest order mode considered in the series expansion.

A subsequent comparison of the on-axial electric field to a known analytical solution yields an expression for a lower limit of the required mode order in a mode expansion of the tophat beam. The obtained expression is a function of the tophat beam's radius and the desired propagation distance after the aperture plane.

The mode expansion method accurately computes the propagation of tophat beams for small aperture radii, even for small propagation distances. Also, the far-field intensity can be reproduced with high accuracy for arbitrary aperture radii. However, the dependence of the required mode order to the square of the aperture radius makes it computationally expensive to simulate the electric field close to the aperture for large aperture radii. For cases where this is required different simulation tools might be a better choice. This needs to be evaluated in future studies.

As a second application of the mode expansion method the propagation and transformation of the fundamental fibre mode was investigated. The far-field intensity pattern at the location of the distant spacecraft could be obtained for the case of a specific design of a fibre outcoupler on the GRACE Follow-On optical bench. Clipping at the exit aperture was considered for different clipping ratios. It could be found that clipping at

more than twice the radius of the fibre mode leads to negligible changes of the far-field intensity pattern as compared to the case of no clipping. For the case of negligible clipping, a comparison of the far-field intensity distribution of the transformed fibre-mode with the shape of the fundamental fibre mode at the fibre end-face leads to an analytical model for the far-field intensity distribution with more than sufficient accuracy which can be efficiently evaluated.

As a result, one can put to record that the mode expansion method is well suited to simulate the electric field of non-Gaussian light fields, with some restrictions for the simulation of hard-edge apertures. For the investigation of the far-field intensity pattern of the fundamental fibre mode for the case of the LRI, the actually aspheric surface of the fibre outcoupler had to be approximated by a parabolic surface. Combining the description of aspheric surfaces with the description of non-Gaussian beams by a set of higher-order modes would be highly valuable. Also, in the decomposition of the tophat beam an effect generally known as Gibbs phenomenon could be observed that originates due to the discontinuous boundary of the electric field amplitude at the edge of the tophat beam. Here, techniques such as low pass filtering the input field might increase the accuracy of the approximation.

3. Laser Link Acquisition for Inter-Satellite Laser Interferometers

In the following chapters laser link acquisition for the case of the GRACE Follow-On mission is studied. This chapter is meant as an introduction to give background information on the design of the Laser Ranging Interferometer (LRI), whereas In the following chapters, the information which is given here will be used to design and investigate an algorithm for the detection of the heterodyne signal and explain a high-fidelity simulation that was developed as part of this thesis in order to test acquisition procedures. After this, the actual acquisition process will be studied. At first, results for an initial line-of-sight calibration scan are given and in the subsequent chapter an algorithm for an autonomous laser link acquisition is discussed.

This chapter starts with a short summary of work that was done on laser link acquisition for other space missions and relates this to the work done in this thesis by explaining the main differences. Thereafter, the focus is on laser link acquisition for GRACE Follow-On.

At first, the laser ranging interferometer is explained by highlighting the subsystems important for acquisition. This is followed by a summary of the sensor signals that are available for acquisition and a presentation of the main noise sources. The noise sources are separately discussed for the case of additive noise sources such as laser shot noise or electronic noise and for the case of non-additive noise sources such as pointing noise of the beam axes and laser frequency noise. The relation between the beatnote frequency of the heterodyne signal and the Doppler shift due to the relative motion of the satellites is discussed after this. The chapter ends with a discussion on possible acquisition schemes.

3.1. Introduction

One of the critical phases of missions exploiting inter-satellite laser interferometry such as GRACE Follow-On [SHD⁺12], is to establish a working laser link after launching the satellites into space. These missions use heterodyne interferometry to measure the distance changes between the satellites. The heterodyne signal amplitude strongly depends on the alignment of the two interfering beams and precise pointing of the laser beams

is required in order to enable signal detection. The finite frequency bandwidth of the photoreceiver also limits the frequency difference between the two interfering beams such that a signal is still measurable.

In nominal operation the beam axis alignment is automatically controlled using differential wavefront sensing [MMRW94a] to correct for relative wavefront tilts between the received beam and the local oscillator beam. The frequency is also automatically held in the frequency band of the photodiodes by offset phase locking the laser on one of the spacecraft to the received light. The laser on the other spacecraft is locked to a reference cavity.

However, initially after launch, unknown biases of attitude sensors, misalignments due to launch or thermal effects, result in possibly large uncertainties, relative to the beam divergence, in the initial beam alignment and in the frequency of the lasers. The largest contribution to these uncertainties are static biases which need to be identified by the initial laser link acquisition. Once these biases are known, the resulting uncertainty space for subsequent acquisitions is much smaller. The problem of laser link acquisition can thus be divided into two separate problems. On the one hand, the initial laser link acquisition to determine the large initial biases, and on the other hand reacquisitions over much smaller uncertainties.

3.1.1. Previous Work on Laser Link Acquisition

Laser link acquisition has been studied in the past by several authors in the context of inter-satellite laser communication between satellites in Low Earth orbits, for example between the NFIRE and TerraSAR-X satellites [HKC⁺10, LS05]. Also ground-to-satellite links have been discussed [TY⁺04] and laser links between satellites in Low Earth and geostationary orbits, for example by the Japanese OICETS satellite [JT⁺99] and the french SPOT-4 satellite [TNO02], who both established a working laser link to the European ARTEMIS satellite. Furthermore, the acquisition procedure and control algorithms for the fundamental physics mission LISA has been studied [MHK05, CG09].

One noticeable difference between the aforementioned and this study is that the payload of the satellites include dedicated hardware to simplify acquisition. These are for example, dedicated high power, high divergence beacon beams that cover big portions of the spatial uncertainty cone [PPS86, JT⁺99, LYMT11] or beam shaping mechanism to widen the narrow measurement or communications beam [HHL⁺07, GKK⁺04]. Besides that, beaconless acquisition was studied by Hindman et al. [HR04] or Guelman et al. [GKK⁺04], though these instruments rely on a beam-shaping mechanism to increase the beam divergence.

Another important part of the payload of all of these satellites are dedicated acquisition sensors for coarse and fine pointing. Some of the designs use a combination of a wide field-of-view (FOV) sensor with low pointing accuracy and a fine pointing or tracking sensor with high accuracy in a two stage process. These are proposed to be used by LISA and OICETS. These missions use focal plane array detectors [Cox85, IK93], such as a CCD sensor, with FOV sizes of several beam widths to roughly point the beam in the right direction and steer it into the FOV of the fine pointing sensor which has a smaller FOV but a higher accuracy. The control of the beam direction is then handed over to the fine pointing sensor to sufficiently narrow down the pointing error to be able to acquire lock.

Other possibilities include a single sensor with different modes for coarse and fine pointing. The Laser Inter-satellite Transmission Experiment (LITE) [KS89, Bor93, GBD94] uses a combination of four high sensitive avalanche photodiodes (APD) with the output summed for coarse pointing and a differential measurement between the APDs for fine pointing. However, all of the above sensors have in common that the sensor output is independent of the pointing of the outgoing beam which significantly reduces the complexity of determining the correct pointing direction.

3.1.2. Laser Link Acquisition for GRACE Follow-On

The design choices made for the LRI on GRACE Follow-On do not include dedicated acquisition hardware, due to tight constraints on available resources. For example, no beam shaping mechanisms or acquisition sensors are available. As a result the sensors to be exploited for laser link acquisition in GRACE Follow-On are the same quadrant photodiodes (QPD) that are used for the science measurement. Analysis show that using the QPD to directly measure the incoming light with the local laser switched off is not feasible due to the received low power levels and that exploiting the interferometer signals is the best option to detect the signal of the remote spacecraft [SH11].

Given the current design of the LRI, using the heterodyne signal for acquisition leads to a coupling of the sensor output to local and remote beam axis misalignments simultaneously. Misalignments of the remote spacecraft's beam axis to the line-of-sight (LOS) between the satellites reduces the received power. Relative tilts between the local oscillator and the received beam reduce the heterodyne amplitude due to a loss in heterodyne efficiency. Additionally, the sensor output is dependent on the frequency of the beat-note between the received and transmitted beam which has to be within the photodiode bandwidth between 4 MHz and 16 MHz, in order to be detectable. The initial frequency uncertainty is expected to be larger than the detection bandwidth making it necessary

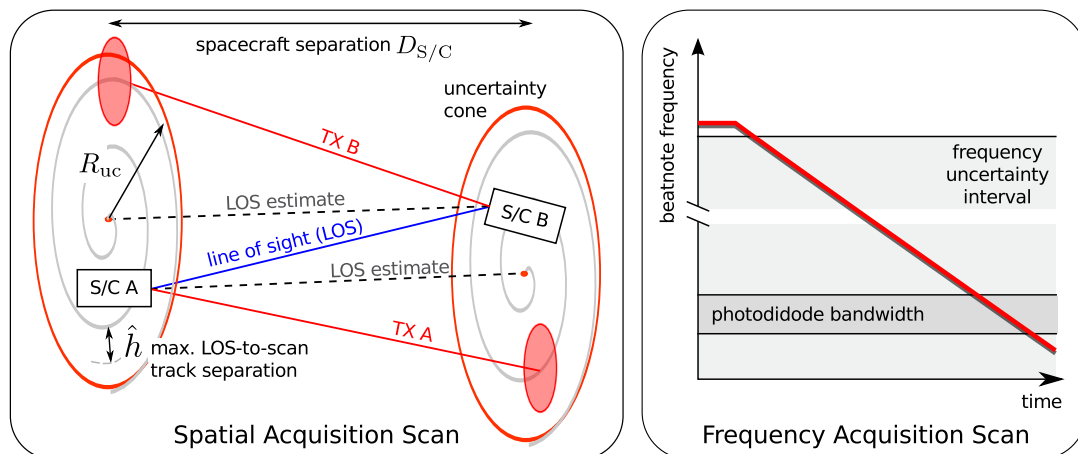


Figure 3.1.: Left: Important geometric parameters for the *spatial acquisition scan*. Shown are the uncertainty cone radius, R_{uc} , the maximum separation between the line-of-sight and the scan track, \hat{h} , the spacecraft separation, $D_{S/C}$, and the difference between the estimated and real line-of-sight (LOS). Right: The frequency of the free-running slave laser has to be swept, in order to place the beatnote frequencies of the two spacecraft into the usable photodiode bandwidth.

to scan the frequency.

Use of the heterodyne signal render the acquisition process in GRACE Follow-On a search in five degrees of freedom, over a possibly large uncertainty space. An additional constraint is that there will be no direct communication between the satellites. Figure 3.1 summarises the acquisition problem. In the left panel, the two spacecraft are shown, with the true LOS connecting them. The estimate of the LOS produced by either spacecraft deviates from the true LOS by a predetermined maximum, although the true misalignment is unknown. The range of angles around the LOS that are bounded by the expected maximum misalignment is the uncertainty cone. The maximum misalignment, R_{uc} , is called the *uncertainty cone radius*. As the true alignment is unknown, each spacecraft has to scan its transmitted beam over the uncertainty cone, in order to enable signal detection. The maximum separation between the line-of-sight and the scan track, \hat{h} , that occurs during a spatial scan sets a lower limit to the maximum signal power that will be detected during the scan. Hence, determining, \hat{h} for the considered spatial scan patterns is essential for a successful acquisition. The right plot in Figure 3.1 depicts a frequency scan. The laser frequency has to be tuned over a potentially large uncertainty interval, such that the beatnote frequency at some point enters the usable photodiode bandwidth.

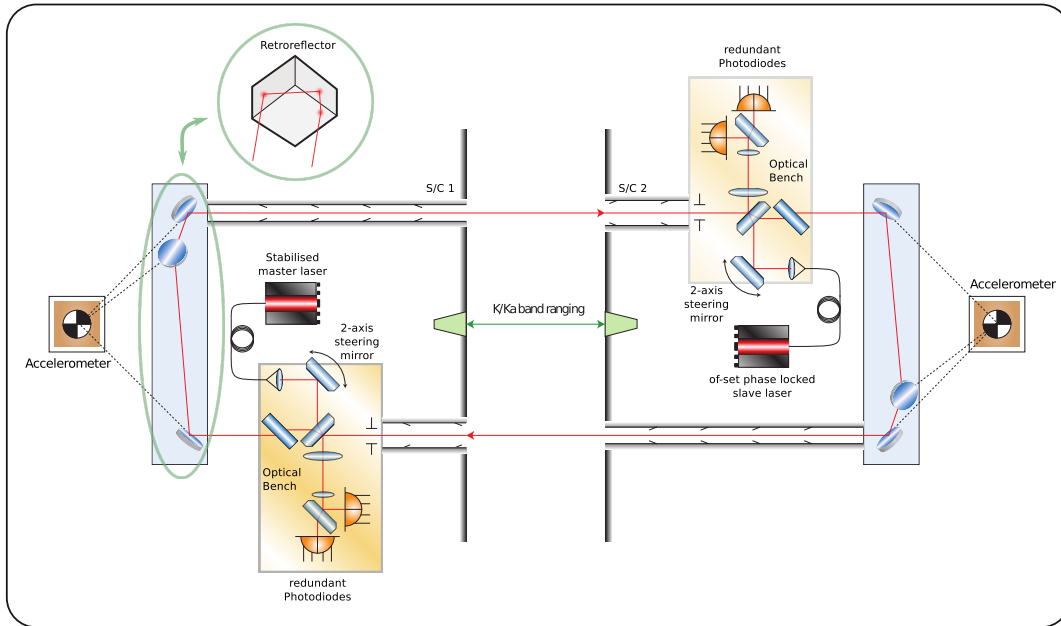


Figure 3.2.: Shows the design of the GRACE Follow-On laser ranging interferometer (LRI), including the optical benches with photodiodes and fine-steering mirrors (FSM) and the triple mirror assembly (TMA). The K/Ka-band ranging instrument, occupying the main axis, is shown in the centre. Adapted from [SHD⁺12].

3.2. GRACE Follow-On Laser Ranging Interferometer

The LRI on board GRACE Follow-On is presented in Figure 3.2. Shown are the two spacecraft and a schematic of the LRI layout. The principle of operation is well described in [SHD⁺12] and here only the parts important for acquisition will be mentioned in more detail. Although both spacecraft carry identical payloads, the LRI components will be operated in two different modes. One spacecraft, from now on called the *master* spacecraft, will be frequency stabilised to an ultra-stable cavity [TFdV⁺11]. The laser on the other spacecraft will be offset phase locked to the received laser light from the master, once a working laser link has been established. The latter spacecraft will be called *slave* spacecraft within the rest of this thesis.

This implies two important points for acquisition. First, the absolute frequency of the master laser will be unknown after it has been locked to the reference cavity. Also the absolute frequency of the slave laser will be unknown because it is initially operated free-running. Secondly, due to the fact that the slave laser will initially be operated free-running, the beatnote frequency will be subject to frequency noise.

An additional complication is that the spacecraft will move with respect to each other

which will introduce a Doppler shift of the laser frequency. The Doppler shift might be as large as 3 MHz. This additional frequency offset has to be taken into account during acquisition since the bandwidth of the photodiode is limited.

The optical bench of the LRI also includes a *fine steering mirror* (FSM) which in nominal operation steers the local oscillator beam axis in order to align it with the beam axis of the incoming received beam. The FSM coordinate system and tilt angles are shown in the right panel of Figure 3.3. The automatic beam pointing is accomplished using *differential wavefront sensing* (DWS) signals [MMRW94a] as error signals. Matching the alignment of the local oscillator to the alignment of the received beam also aligns the beam transmitted to the other spacecraft to the received beam. This is achieved because the local oscillator beam is split at the central beamsplitter and most of the light will be directed through the *triple-mirror assembly* (TMA) and used as the transmit beam (TX) which is sent to the distant spacecraft.

During acquisition the FSM is used to scan the spatial uncertainty cone. This illustrates that a tilt of the FSM simultaneously affects the signal amplitude of the measurement on both spacecraft, since tilting the FSM will tilt the *local oscillator beam* (LO) with respect to the received beam (RX) which decreases the heterodyne efficiency. On the other hand, it will change the direction of the TX beam relative to the nominal LOS which alters the power that is received by the remote spacecraft. This means that only if the beam axes of the transmitted beams of both spacecraft are aligned with sufficient accuracy the heterodyne signal will be intense enough to be detectable.

The properties of the TMA ensure that a beam being reflected from it will be sent in exactly the opposite direction of the incoming beam, independent of the angle and position of the beam axis. Misalignments of the individual mirrors of the TMA though, will result in deflection from the nominal reflection axis. This *coalignment error* γ_{TMA} is assumed, here, to be less than 40 μrad . The effect of a non-zero coalignment error is a misalignment of only the transmitted beam. Hence, for perfect alignment of the local oscillator with the received beam, the outgoing beam will be misaligned by the coalignment error and the power received by the remote spacecraft will be decreased. See Figure 3.3 for a schematic of the triple-mirror assembly and the coalignment error.

The quadrant photodiode (QPD) on the optical bench, is taking the science data during science operations and is the only available acquisition sensor. The measurements taken by the QPD will be sent to the *phasermeter* which computes the amplitudes and the phases of the photocurrent of each of the segments. For details on the phasermeter for GRACE Follow-On see, for example [WFS⁺06]. The phasermeter will also be used to run the detection algorithm discussed in the next chapter.

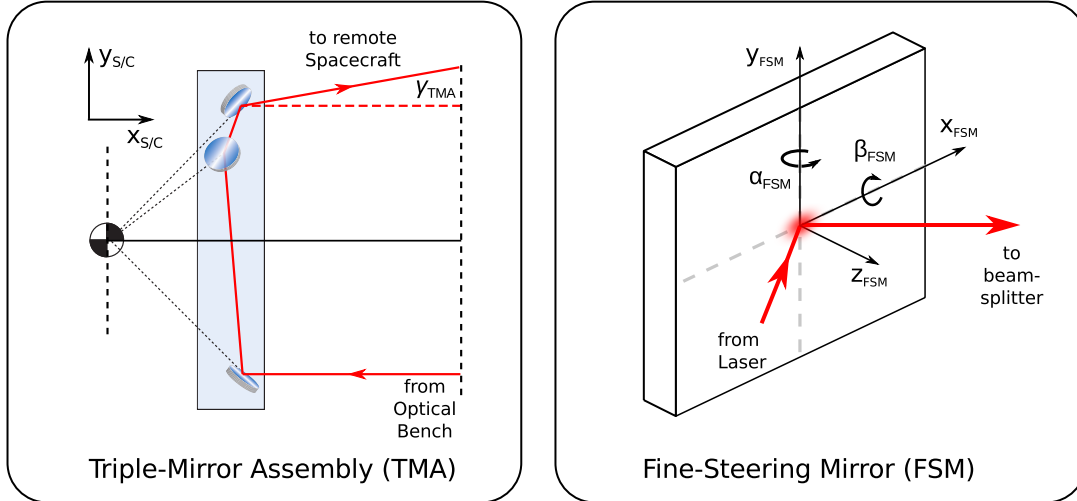


Figure 3.3.: Left: Triple-mirror assembly (TMA) with incoming and outgoing beam. The intersection point of the mirror surfaces is aligned to the gravitational-reference point of the accelerometer. For a non-perfect TMA with mirror misalignments the outgoing beam axis will be misaligned from the nominal beam axis by the TMA coalignment error, γ_{TMA} . Right: Fine-steering mirror (FSM) coordinate system and tilt angles, α_{FSM} and β_{FSM} , in the two orthogonal directions.

The average of the phases of the four segments is the longitudinal signal, encoding the distance changes between the two satellites. Differences of the top and bottom or the

Table 3.1.: Overview of the salient parameters for the beams, photodiode and the optical bench used in this analysis.

Item			
Description	Symbol	Value	Unit
Wavelength	λ	1064	nm
Waist radius	w_0	2.5	mm
Beam quality factor	M^2	1.0 - 1.2	r.u.
Nominal divergence half angle	θ_0	135.5	μrad
Transmitted power	P_{TX}	13.7–19	mW
LO power at QPD	P_{LO}	0.54–0.93	mW
Receive aperture radius	r_a	4	mm
Photodiode radius	R_{PD}	0.5	mm
Photodiode responsivity	ρ_{PD}	0.6	A/W
Photodiode slit width	δ_s	20, 30, 45	μm
S/C separation	$D_{S/C}$	170–270	km

left and right segments' phases give a sensitive measurement of the relative wavefront tilt between the two interfering beams. The latter signal combination is the already mentioned DWS signal. In nominal operations it keeps the beam axis of the incoming and outgoing beam aligned. To note an important comparison: the QPD together with the phasemeter and DWS as error signal can be seen as the tracking or fine pointing sensor as it is called in former publications dealing with laser link acquisition. The goal of acquisition here also is to align the beams accurately enough such that the tracking sensor can take over.

Up to the point when the DWS signal is available the satellites have no means to assess the actual direction or size of the misalignment of the received beam with respect to the local oscillator. The only available information is the amplitude of the heterodyne signal which is dependent on the received beam power, the local beam alignment as well as the frequency difference between the RX and LO beams.

3.3. Sensor Signals

This section will give an overview of the sensor signals available for acquisition. At first the heterodyne signal current is reviewed. The *effective received power* will be introduced thereafter, which separates the dependence of the heterodyne amplitude on beam misalignments from the dependence on the frequency of the signal. The different constituents of the effective received power, i.e. the heterodyne efficiency and the power received in the receive aperture, are studied in the following. The end of this section is reserved to a presentation of the differential wavefront sensing signal.

3.3.1. Heterodyne Photocurrent

The science data is taken by the pair of redundant quadrant photodiodes. A quadrant photodiode consists of four individual photosensitive *segments*, whose photocurrents can be read out separately. The segments are here labelled by A, B, C, and D in the order: top left, top right, bottom left and bottom right. The left panel in Figure 3.4 illustrates the labelling of the segments.

Two hot redundant QPDs are mounted onto the optical bench of the LRI, which are labelled QPD1 and QPD2, in the following. QPD1 receives the light in transmission through the beamsplitter in front of the redundant pair, whereas QPD2 receives the beam after reflection off the beamsplitter. The mirroring of the beam, for only one of the photodiodes, reverses the horizontal tilt direction of the beam axis for QPD2 as compared to QPD1.

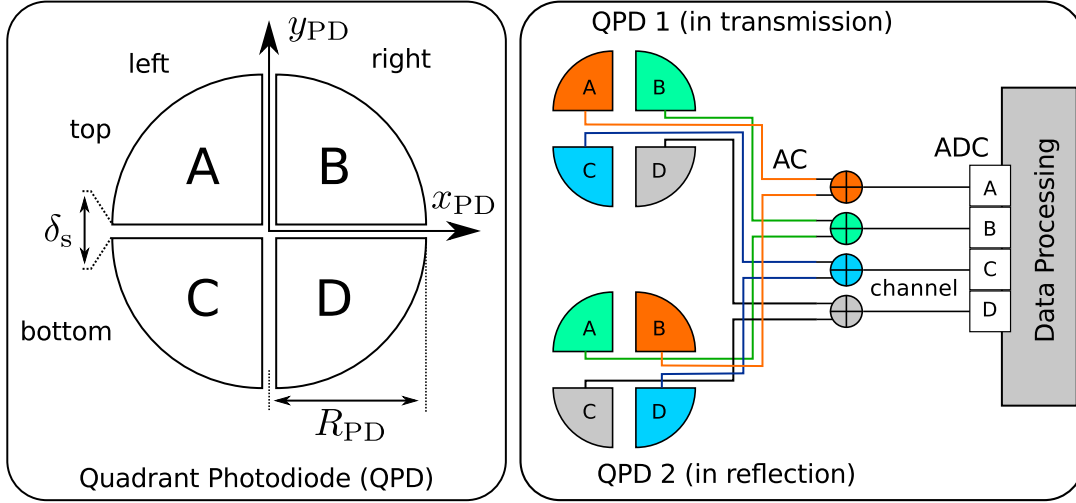


Figure 3.4.: Left: Dimensions and labels of a quadrant photodiode, showing the location of the segments. Also shows the radius and the slit width of the QPD. Right: Combination of the single element AC photocurrents of the two redundant photodiodes, into channels, for further data processing.

The signals of the two redundant QPDs are coherently summed while the mentioned asymmetry has to be taken into account. The right panel in Figure 3.4 shows the combination of the data coming from the segments into channels, whereas the right half of QPD1 is connected with the left half of QPD2. The label of the resulting sum of the two segments, in the following called a *channel*, is set to A, B, C and D, according to the label of the segment on QPD1.

Specific quantities, affecting the signals, are the radius of the active area, R_{PD} , the width of the insensitive slit between the segments, δ_s , and the photodiode responsivity ρ_{PD} . Table 3.1 lists the ranges of values of the QPD parameters used throughout this thesis.

The signal measured by the QPD is the photocurrent produced by the interference of the local oscillator beam (LO) and the incoming received beam (RX) sent by the remote spacecraft. A detailed derivation of a mathematical expression for the expected photocurrent of the heterodyne signal was already given in Section 2.1.1. The time dependent AC part of the heterodyne photocurrent, s_q , of a single segment was given in equation (2.1.14) by

$$s_q(t) = 2 \rho_{PD} g(f_b) \sqrt{P_{LO,q} P_{RX,q} \eta_q} \cos(2\pi f_b t + \phi_q). \quad (3.3.1)$$

Here, ρ_{PD} is the photodiode responsivity and $g(f_b)$ is the frequency response of the

photodiode. Although the frequency response of the photodiode $g(f_b)$ will generally also introduce a change of the phase of the heterodyne signal, this is neglected in the treatment of laser link acquisition in this thesis. Moreover, the photocurrent is depending on the power of the LO beam and the power of the RX beam impinging on the active area of the segment q as well as the heterodyne efficiency η_q for the interference on segment q .

The heterodyne efficiency was defined in equation (2.1.8) as the value of the normalised overlap integral of the electric field of the LO and the RX beam over the segment's surface. The phase of the heterodyne signal, ϕ_q , was defined as the argument of the overlap integral in equation (2.1.11). The beatnote frequency f_b was defined as the difference of the frequency of the LO beam and the RX beam.

The remaining step is to combine the heterodyne signal of the two redundant segments into a channel. However, in order to simplify the treatment, it is assumed that during the combination of the two segments the phase of the signals is not changed and also the electric field on the segment surface is identical.

Adding up the signals of the two redundant segments results in the following signal for a single channel, s_c , which differs from the single segment signal only by an amplitude that is twice as high,

$$s_c(t) = 2 s_q(t) \tag{3.3.2}$$

$$= 4 \rho_{\text{PD}} g(f_b) \sqrt{P_{\text{LO},q} P_{\text{RX},q} \eta_q} \cos(2\pi f_b t + \phi_q) \tag{3.3.3}$$

$$= 2 \rho_{\text{PD}} g(f_b) \sqrt{P_{\text{LO},c} P_{\text{RX},c} \eta_c} \cos(2\pi f_b t + \phi_c). \tag{3.3.4}$$

In going from the second to the last line the phase, ϕ_c , heterodyne efficiency, η_c , local oscillator power, $P_{\text{LO},c}$ and received power, $P_{\text{RX},c}$ are defined as follows:

$$\phi_c = \phi_q, \tag{3.3.5}$$

$$\eta_c = \eta_q, \tag{3.3.6}$$

$$P_{\text{LO},c} = 2 P_{\text{LO},q}, \quad \text{and} \tag{3.3.7}$$

$$P_{\text{RX},c} = 2 P_{\text{RX},q}. \tag{3.3.8}$$

Equation (3.3.4) defines the heterodyne signal in a single channel, which will from now on be used.

The next sections will discuss the individual quantities in the expression for the heterodyne amplitude found above and most importantly their dependence on the tilt of the beam axis.

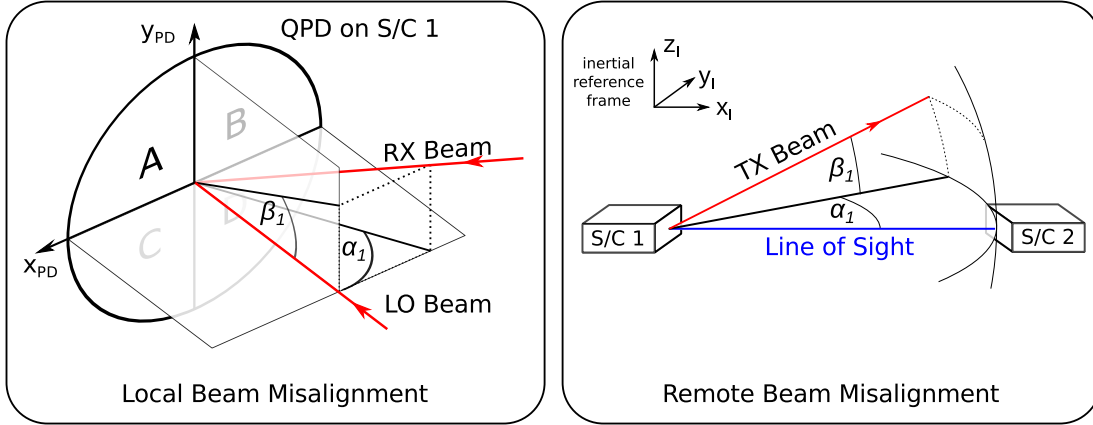


Figure 3.5.: Left: Local misalignment angles as the relative beam axis tilt between the LO and the RX beams in QPD coordinates of spacecraft 1. Right: TX beam misalignment of spacecraft 1 in inertial frame.

3.3.2. Effective Received Power

The general form of the AC part of the photocurrent of a single channel, c , of a heterodyne measurement was given in equation (3.3.4) which can be written as,

$$s_c(t) = A_c \cos(2\pi f_b t + \phi_c).$$

Here, A_c , is the heterodyne amplitude

$$A_c = 2 \rho_{PD} g(f_b) \sqrt{P_{LO,c} P_{RX,c} \eta_c}. \quad (3.3.9)$$

The quantities appearing in the above expressions are the same as defined before for equations (3.3.1) and (3.3.4).

The amplitude of the heterodyne signal will in general depend on the alignment of the RX beam to the LO beam through the heterodyne efficiency, and also on the alignment of the TX beam which is transmitted from the remote spacecraft through the received power.

The left panel in Figure 3.5 shows the relative misalignment angles, α_1 and β_1 , for a misalignment of the LO beam with respect to the RX beam in horizontal and vertical direction in the QPD coordinate system of spacecraft 1. The local oscillator beam is generally not aligned orthogonal to the QPD surface. This alignment is chosen to simplify the drawing.

The right panel in Figure 3.5 explains the alignment angles, α_1 and β_1 , of the TX beam

that is transmitted by spacecraft 1 for the case of a horizontal and vertical misalignment, relative to the LOS. These two angles determine the light power received by the limiting aperture on the optical bench of spacecraft 2.

Thus, the heterodyne amplitude measured by spacecraft $i = 1, 2$ can be given as

$$A_{c,i}(\alpha_i, \beta_i, \alpha_j, \beta_j, f_b) = 2 \rho_{\text{PD}} g(f_b) \sqrt{P_{\text{LO},c} P_{\text{RX},c}(\alpha_j, \beta_j) \eta_c(\alpha_i, \beta_i)}. \quad (3.3.10)$$

Here, $i, j = 1, 2$ with $i \neq j$. The angles α_i and β_i are the relative wavefront tilts between the LO and RX beam for horizontal and vertical misalignment, in the photodiode coordinate system. This is illustrated in the left panel of Figure 3.5. α_j and β_j are the horizontal and vertical misalignment angles of the axis of the beam transmitted by the remote spacecraft relative to the LOS in the inertial reference frame. This is depicted in the right panel of Figure 3.5.

The heterodyne efficiency is only depending on the relative alignment of the LO beam to the RX beam and it is independent of the alignment of the TX beam transmitted by the remote spacecraft. This is due to the fact that the wavefronts are approximately spherical at the receiving spacecraft. Hence, a tilt of the transmitted beam does not change the phasefront of the received beam, thus the phasefronts are always perpendicular to the LOS and the heterodyne efficiency is not changed. Most importantly, maximising the heterodyne efficiency means aligning the LO beam to the LOS. For a perfect TMA which routes the LO to the distant spacecraft, this implies that also the TX beam is automatically aligned to the LOS. However, for a TMA coalignment error $\gamma_{\text{TMA}} \neq 0$, the TX beam is misaligned from the LOS by γ_{TMA} .

In order to combine the tilt dependence in a single quantity, the *effective received power*, $\hat{P}_{\text{RX},c}$, is defined as

$$\hat{P}_{\text{RX},c}(\alpha_i, \beta_i, \alpha_j, \beta_j) = P_{\text{RX},c}(\alpha_j, \beta_j) \eta_c(\alpha_i, \beta_i), \quad (3.3.11)$$

as function of the received power in channel, c , and the heterodyne efficiency η_c . The tilt dependence of these two quantities will be investigated in the next two sections.

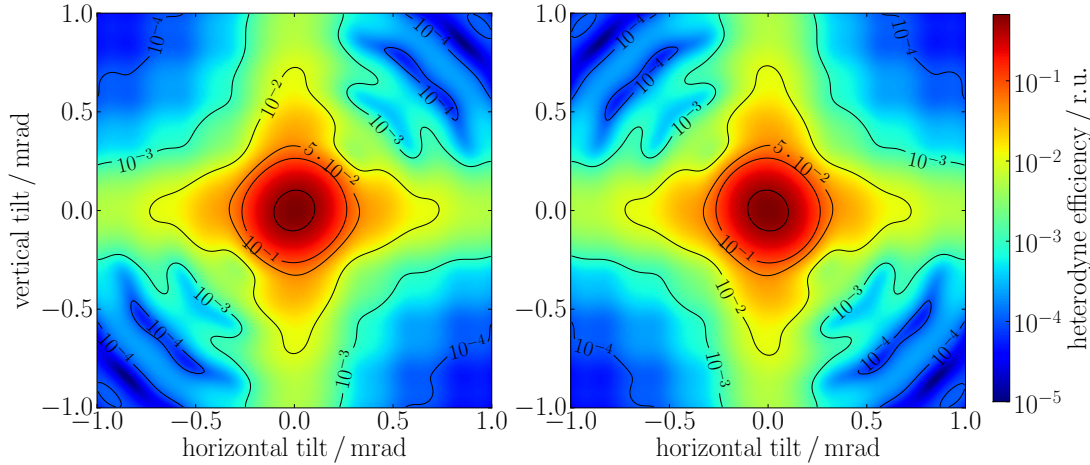


Figure 3.6.: Left: Heterodyne efficiency of quadrant A as a function of relative misalignment between interfering tophat beam with radius $r_a = 0.5$ mm and Gaussian LO with waist radius of $w_0 = 0.3125$ mm on a QPD with radius of $R_{PD} = 0.5$ mm and slit width of $\delta_s = 20$ μm . Right: Heterodyne efficiency of quadrant B. The heterodyne efficiency for the quadrant C is a horizontally mirrored version of the image of quadrant A, and quadrant D is horizontally mirrored version of B.

3.3.3. Heterodyne Efficiency

The heterodyne efficiency is a measure of the interference quality and defined as the normalised power of the overlap integral over the active area B_q of the considered quadrant:

$$\begin{aligned} \eta_q &= |\mathcal{O}_q|^2 \\ &= \frac{\left| \iint_{B_q} e_{LO}(\mathbf{r}, t) e_{RX}(\mathbf{r}, t) e^{i\delta\psi(\mathbf{r}, t)} d^2\mathbf{r} \right|^2}{\iint_{B_q} |e_{LO}(\mathbf{r}, t)|^2 d^2\mathbf{r} \iint_{B_q} |e_{RX}(\mathbf{r}, t)|^2 d^2\mathbf{r}} \end{aligned} \quad (3.3.12)$$

See equation (2.1.8) for the definition of the symbols appearing in the above expression. As defined before in equation (3.3.6) the single quadrant heterodyne efficiency is assumed to be equal to the single channel heterodyne efficiency, $\eta_q = \eta_c$. Though here, for clarity it is mentioned as the single quadrant heterodyne efficiency.

The heterodyne efficiency is constrained between zero and one ($0 \leq \eta_q \leq 1$), where it is 1 for identical wavefronts, interfering perfectly. Any deviation from perfect interference, such as wavefront errors or beam shape mismatch and most importantly, relative tilts between the LO and RX beam wavefronts, decrease the heterodyne efficiency. Takenaka et al. [TTF78] computed the dependence of the heterodyne efficiency for a single element detector as a function of the relative wavefront tilt for interference of two Gaussian beams

and two plane waves, whereas Tanaka et al. [TO87] include a square aperture in the input plane.

The layout of the optical bench for the case of the laser ranging interferometer on GRACE Follow-On, see Figure 3.2, is such that the field in the receive aperture is imaged onto the QPDs and therefore no diffraction effects should be visible at the plane of the detector. The imaging system consisting of the two lenses is designed to image a tilt in the receive aperture into a pure tilt at the photodetector with no beam walk. Hence, for a perfect alignment of the imaging system the transverse profile of the received beam over the active area of the QPD is a plane wave tilted around the centre of the QPD.

On the other hand, the LO is approximately a Gaussian beam with 2.5 mm waist radius whose waist position is imaged onto the QPD surface. The object plane of the image system for the Gaussian beam is roughly located at the surface of the fine-steering mirror, such that a tilt of the LO at the FSM is mapped to a tilt at the QPD. The imaging system will decrease the spot size of the incoming beam in the receive aperture and the Gaussian beam by the same amount that it will magnify the tilt angle between both beams. The heterodyne efficiency, as defined by equation (3.3.12), is invariant under such transformations for small tilt angles, which can easily be verified.

Hence, the heterodyne efficiency can either be calculated over the imaged fields at the photodiode or by calculating the overlap integral \mathcal{O}_q over the RX beam in the receive aperture and the Gaussian beam at the FSM. Only the integration regions have to be scaled by the magnification of the imaging system. The normalised electric fields of the RX beam in the receive aperture and the Gaussian LO at the FSM will here be defined by

$$E_{\text{RX}} = \sqrt{\frac{1}{\pi}} \frac{1}{r_a} \exp(-ikx\alpha -iky\beta), \quad \text{and} \quad (3.3.13)$$

$$E_{\text{LO}} = \sqrt{\frac{2}{\pi}} \frac{1}{w_0} \exp\left(-\frac{x^2 + y^2}{w_0^2}\right). \quad (3.3.14)$$

With the values for the receive aperture of radius $r_a = 4$ mm, $k = 2\pi/\lambda$ for the wavelength of λ listed in Table 3.1 and $w_0 = 2.5$ mm, the heterodyne efficiency was calculated for various tilt angles α , β of the received beam for the segments of the QPD. The effective QPD slit width was chosen as 20 μm . The results for the upper two segments, A and B, are shown in Figure 3.6.

The asymmetry of the pattern for rotation around the centre is due to the geometry of a single quadrant. Another obvious feature of the heterodyne efficiency pattern is

the cross shape, which means that the decrease in heterodyne efficiency for only vertical or horizontal tilts is less than in diagonal direction. The peak value of the heterodyne efficiency is reached for zero tilt. For a tophat beam and a local oscillator with the given parameters the maximum value is $\eta_q(0,0) = 0.699$. Symmetry arguments give the pattern of the bottom segments, C and D, as mirrored horizontally. The heterodyne efficiency limits the field of view of the detector for local beam misalignments. A factor of 10 decrease in the single segment signal power due to local beam misalignments is reached at roughly $250 \mu\text{rad}$.

3.3.4. Received Power

The second quantity in the single channel effective received power, $\hat{P}_{\text{RX},c}$, is the received power in a channel, $P_{\text{RX},c}$, which is proportional to the power in the limiting receive aperture, P_{RX} , and the losses in the optical path from the receive aperture to the QPD of ρ_{rx} . It is further assumed that the incoming beam is imaged perfectly onto the centre of the QPD and the received power is the same in each channel.

If the separation of the spacecraft is large, the intensity of the transmitted beam, I_{TX} , can be treated as constant over the receive aperture of radius, r_a . Hence, the total received power, P_{RX} , can be given as

$$P_{\text{RX}} = \rho_{\text{rx}} I_{\text{TX}} \cdot \pi r_a^2. \quad (3.3.15)$$

The losses in the optical path are due to absorption in optical components, diffraction effects, finite reflectivity at beamsplitters and also the loss due to the finite width of the inactive slits of the QPD. All these effects are combined in ρ_{rx} . The received power in a channel, $P_{\text{RX},c}$, will be defined by

$$P_{\text{RX},c} = \frac{P_{\text{RX}}}{n_c}, \quad (3.3.16)$$

where n_c is the number of channels. The power passing through the receive aperture is depending on the alignment of the beam transmitted by the remote spacecraft. If the transmitted beam is aligned to the LOS maximum light power is received.

The beam sent to the other spacecraft is tapped off the LO beam by the beamsplitter and routed through the TMA to the exit aperture of the optical instrument. Due to the fact that the LO beam is delivered to the optical bench through an optical fibre, the true beam shape will not be a perfect Gaussian beam. Thus, different far-field intensity patterns are analysed. On the one hand, the propagated fiber mode of Section 2.5

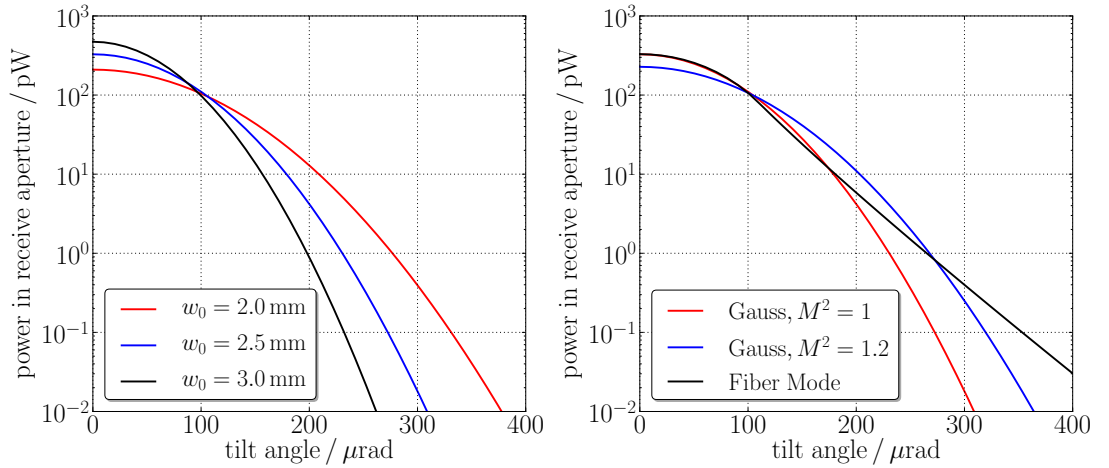


Figure 3.7.: Left: Power in receive aperture, P_{RX} , for Gaussian beams with different waist radii and beam quality factor $M^2 = 1$. Right: Power in the receive aperture, P_{RX} , for a Gaussian beam with waist radius $w_0 = 2.5$ mm and beam quality factors $M^2 = 1$ and $M^2 = 1.2$ to the propagated fibre mode from equation (2.5.18). The parameters for the fibre mode are: $\alpha = 0.78$, $r_0 = 2.43$ mm and $V = 1.967$, which compares to the small core case of Table 2.1.

defined by equation (2.5.18). The parameters used for this beam type are the ones listed under *small-core case* in Table 2.1, because the resulting beam resembles more closely the nominal Gaussian beam. The Gaussian beam fitted to the field distribution at the end-face of the fibre-coupler has a waist radius of roughly 2.5 mm.

The second type of beam considered, is a Gaussian beam with a beam propagation factor, $M^2 \neq 1$, which will increase the divergence of the beam compared to the perfect Gaussian beam. The intensity of the Gaussian beam with arbitrary M^2 -factor will depend on the distance between the spacecraft, $D_{S/C}$, the transmitted power, P_{TX} , and the waist radius of the Gaussian beam, w_0 . With the horizontal and vertical misalignment angles, α and β , of the TX beam relative to the LOS, it can be approximated by [Sie93]:

$$I_{TX}(\alpha, \beta, D_{S/C}) \simeq \frac{2P_{TX}}{\pi} \frac{1}{w^2(D_{S/C})} \exp\left(-2 \frac{(\alpha^2 + \beta^2) D_{S/C}^2}{w^2(D_{S/C})}\right), \quad \text{and} \quad (3.3.17)$$

$$w(D_{S/C}) = w_0 \sqrt{1 + \left(\frac{\lambda D_{S/C} M^2}{\pi w_0^2}\right)^2}. \quad (3.3.18)$$

Since the LO beam waist will roughly be located at the photodiode of its spacecraft, the M^2 -factor will not significantly influence the heterodyne efficiency but will affect the far-field intensity pattern of the transmitted beam at the distant spacecraft.

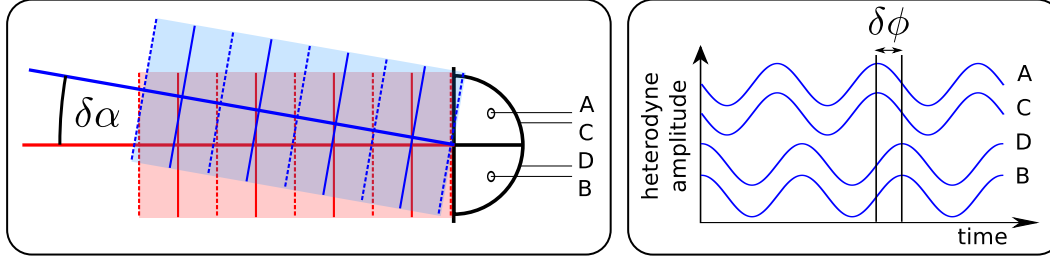


Figure 3.8.: DWS signal caused by horizontal misalignment of the RX and LO beam axes at the QPD by an angle $\delta\alpha$. The misalignment causes a phase difference, $\delta\phi$, in the heterodyne currents of the left and right half of the QPD in the plane of incidence.

A plot of the total received power P_{RX} as a function of the tilt angle $\gamma = \sqrt{\alpha^2 + \beta^2}$ is given in the left plot of Figure 3.7 for different waist radii of the Gaussian beam. It shows how the beam divergence increases for smaller waist radii. The right plot in Figure 3.7 compares the beam models used in the analysis. Shown is the received power of the fiber-mode, a Gaussian beam with waist radius of 2.5 mm and beam quality factor of $M^2 = 1$ as well as $M^2 = 1.2$. The divergence, θ_M , of the Gaussian beam with $M^2 \neq 1$ is equal to $\theta_M = M^2 \theta_0$, where $\theta_0 = \lambda/(\pi w_0)$ is the divergence angle of the Gaussian beam with $M^2 = 1$. The on-axis intensity, $\gamma = 0$, of the Gaussian beam with $M^2 \neq 1$ is reduced by a factor of $1/(M^2)^2$.

A factor of 10 reduction in the signal power for a tilt of the remote beam axis is already reached between $150 \mu\text{rad}$ for the fibre-mode and the Gaussian beam with $M^2 = 1$, as well as about $180 \mu\text{rad}$ in case of the Gaussian beam with $M^2 = 1.2$.

3.3.5. Differential Wavefront Sensing

The last important signal generated from the heterodyne measurement which is briefly mentioned here, is the differential wavefront sensing (DWS) signal. It was already introduced in Section 2.1.2 and here just the expressions for the signal combinations are given. For more details the reader is referred to the previous discussion. The horizontal and vertical DWS signals can be defined by

$$\text{DWS}_{\text{hor}} = (\phi_A + \phi_C) - (\phi_B + \phi_D), \quad (3.3.19)$$

$$\text{DWS}_{\text{ver}} = (\phi_A + \phi_B) - (\phi_C + \phi_D), \quad (3.3.20)$$

where the phases ϕ_A to ϕ_C are the phases of the heterodyne signal of the individual channels as were given in equation (3.3.4). Figure 3.8 illustrates the change of the phase of the heterodyne signal due to a tilt in horizontal direction.

The beams interfering on the optical bench in GRACE Follow-On will be a Gaussian beam and a tophat beam, due to clipping at the receive aperture. The DWS signal on GRACE Follow-On will be used to automatically align the LO beam to the RX beam, once the phasemeter is locked, thus it acts as a tracking sensor. The goal of the autonomous laser link acquisition is to decrease the misalignment of the transmitted beams sufficiently, such that the phasemeter can lock and the DWS signal is available to automatically track the signal.

3.4. Noise Sources

For now only the heterodyne signals in absence of noise were discussed. To complete the introduction, the most important noise sources are now presented. Two types of noise sources have to be distinguished. These are on the one hand noise sources which can be treated as additive to the heterodyne photocurrent and on the other hand variations of the heterodyne photocurrent that are due to changes in the beam pointing and thus enter in a non-linear fashion. At first the additive noise sources are discussed and later the most important non-additive noise sources are given.

3.4.1. Additive Noise Sources

The most important additive noise sources that enter into the measurement of the heterodyne signal are photon shot-noise, detector equivalent input current noise and laser intensity noise. Quantisation noise introduced by the ADCs is considered negligible. In general, these noise sources are not white. Laser intensity noise dominates at frequencies below about 3 MHz–4 MHz but rapidly decreases for higher frequencies [NC12]. Detector equivalent input current noise is assumed to increase towards higher frequencies of the detection bandwidth and flattens out at lower frequencies. Shot noise can be considered as white Gaussian noise, as shown for example by Barber et al. [BDSE13].

For the analysis presented in this thesis the additive noise sources are treated as white, Gaussian processes. The used values for the power spectral densities (PSD) correspond to an assumed worst case over the measurement band. All PSDs given here are one-sided and are first given for a single photodiode segment, before they are combined into channels. The PSD of electronic noise, $\tilde{S}_{e,q}^2$, is just given in terms of the noise equivalent current (NEI) by

$$\tilde{S}_{e,q}^2 = \text{NEI}^2, \quad (3.4.1)$$

whereas the PSD of shot noise, $\tilde{S}_{s,q}^2$, is proportional to the square root of the light power at the photodiode. For a strong local oscillator and weak measurement beam the light power at the photodiode is approximately equal to the local oscillator power, $P_{LO,q}$. For this case the shot noise amplitude spectral density can be approximated by

$$\tilde{S}_{s,q}^2 = 2 q_e \rho_{PD} P_{LO,q}, \quad (3.4.2)$$

with the *electron's charge* q_e and the photodiode responsivity ρ_{PD} . The PSD of laser intensity noise is proportional to the power of the local oscillator and can be given in terms of the relative intensity noise PSD (RIN) by

$$\tilde{S}_{i,q}^2 = (\rho_{PD} P_{LO,q} \text{RIN})^2. \quad (3.4.3)$$

The values for the noise equivalent current and the relative intensity noise assumed for the analysis in this thesis are given in Table 3.2.

The total noise PSD, \tilde{S}_q^2 , for a single quadrant is easily obtained by the sum of the PSDs of the individual noise sources as they are uncorrelated on a single segment,

$$\tilde{S}_q^2 = \tilde{S}_{e,q}^2 + \tilde{S}_{s,q}^2 + \tilde{S}_{i,q}^2. \quad (3.4.4)$$

If the noise for a sum of segments is desired, the different correlation properties of the different noise sources have to be taken into account. Detector electronic noise and shot noise are uncorrelated between the segments, but laser intensity noise is correlated. In terms of the single segment PSDs of the individual noise sources the total PSD, \tilde{S}_{CS}^2 , for the sum of n photodiode segments, also called the *coherent sum*, is given by,

$$\tilde{S}_{CS}^2 = n(\tilde{S}_{e,q}^2 + \tilde{S}_{s,q}^2) + n^2 \tilde{S}_{i,q}^2. \quad (3.4.5)$$

The noise PSD in a single channel, \tilde{S}_c^2 , can be obtained by setting $n = 2$, in equa-

Table 3.2.: Noise equivalent current (NEI) of single QPD segment and relative intensity noise (RIN), for one-sided power spectral densities.

Item			
Description	Symbol	Value	Unit
noise equivalent current	NEI	5	pA/ $\sqrt{\text{Hz}}$
relative intensity noise	RIN	$3 \cdot 10^{-8}$	$1/\sqrt{\text{Hz}}$

tion (3.4.5), resulting in

$$\tilde{S}_c^2 = 2(\tilde{S}_{e,q}^2 + \tilde{S}_{s,q}^2) + 4\tilde{S}_{i,q}^2. \quad (3.4.6)$$

For a sampling frequency of f_s for the case of zero-mean Gaussian noise, the variance of the noise, σ^2 , in a single channel can be computed by

$$\sigma_c^2 = \frac{f_s}{2} \tilde{S}_c^2. \quad (3.4.7)$$

As a first application, a *noise equivalent effective received power* NEP_{RX} is defined for a single channel as well as the coherent sum of n_c channels. The NEP_{RX} corresponds to the effective received power required for a signal-to-noise ratio of 1 for a given bandwidth.

This requires that the noise variance is equal to the RMS squared of the heterodyne amplitude which is equivalent of having a SNR of unity, hence

$$\text{SNR} = 1 \quad \Leftrightarrow \quad \frac{A_c^2}{2} = \frac{f_s}{2} \tilde{S}_c^2 \quad (3.4.8)$$

This equation can then be solved for the effective received power in A_c , using equation (3.3.9). Under the assumption of a perfect photodiode response $g(f_b) = 1$, and normalised by the sampling frequency the $\text{NEP}_{\text{RX},c}$ in a single channel can be computed by

$$\text{NEP}_{\text{RX},c} = \frac{\tilde{S}_c^2}{8 \rho_{\text{PD}}^2 P_{\text{LO},q}}. \quad (3.4.9)$$

Here, the local oscillator power in a single channel was exchanged by the local oscillator power per photodiode segment, $P_{\text{LO},c} = 2 P_{\text{LO},q}$.

For the coherent sum of the quadrants one can also compute the noise equivalent effective received power $\text{NEP}_{\text{RX,CS}}$. However, in order to do so the coherent sum heterodyne amplitude, A_{CS} , has to be defined. This will be done in detail in Section 6.3.1. To anticipate a result obtained in equation (6.3.7), the coherent sum amplitude can be written in analogy to the single channel heterodyne amplitude and can be given for $g(f_b) = 1$ as

$$A_{\text{CS}} = 2\rho_{\text{PD}} \sqrt{P_{\text{LO}} \hat{P}_{\text{RX,CS}}}. \quad (3.4.10)$$

which depends on the total local oscillator power collected on all segments, $P_{\text{LO}} = n_{\text{seg}} P_{\text{LO},q}$. With this one can find the noise equivalent effective received power for the coherent sum of n_{seg} segments by also inserting the coherent sum noise PSD \tilde{S}_{CS}^2 from

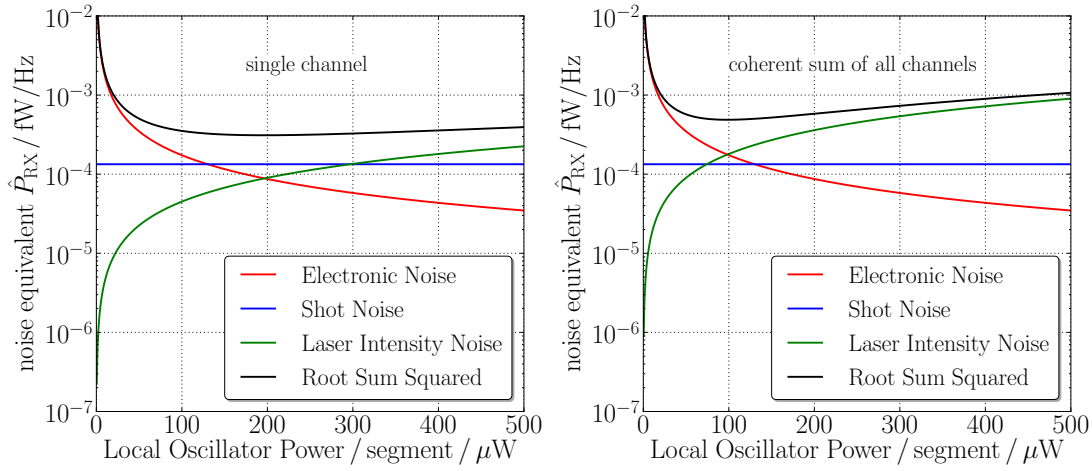


Figure 3.9.: Left: Single channel noise equivalent effective received power as a function of the local oscillator power. Right: noise equivalent effective received power for the coherent sum of eight QPD segments, as a function of the local oscillator power. For the noise PSDs of Table 3.2 and photodiode responsivity of $\rho_{\text{PD}} = 0.6 \text{ A/W}$.

equation (3.4.5),

$$\text{NEP}_{\text{RX,CS}} = \frac{\tilde{S}_{\text{CS}}^2}{4 \rho_{\text{PD}}^2 n_{\text{seg}} P_{\text{LO},q}}. \quad (3.4.11)$$

The found expressions for the noise equivalent power as a function of the LO power on a single quadrant are plotted in Figure 3.9. It should be noted that the PSDs of the noise in a single channel and of the coherent sum of the channels are depending on the local oscillator power which is not explicitly shown in equations (3.4.9) and (3.4.11).

The left plot shows the equivalent power for a single channel also broken down into the contributions of the individual noise sources. It is seen that the effective received power mimicked by the total noise is largely independent of the local oscillator power. The location of the minimum, however, is clearly visible by the location of the intersection between the curves for the detector noise and the laser intensity noise. The right plot in Figure 3.9 shows the noise equivalent power for the sum of eight segments, here the optimum is much more pronounced and at lower local oscillator powers. Though still, the change in the effective received power is small, while increasing the local oscillator power.

The algorithm used to process the data, for detecting the heterodyne signal will contain discrete Fourier transforms, as will be discussed in the next chapter. The noise floor in the frequency bins of the Fourier transform, due to the additive noise sources discussed

here, can be estimated by multiplying the noise equivalent effective received power by the bandwidth of the DFT. For a sampling frequency of f_s , and a DFT computed from N_{DFT} samples, the DFT bandwidth is given by $\delta f_{\text{DFT}} = f_s/N_{\text{DFT}}$. The effective received power mimicked by noise, $\hat{P}_{\text{RX}}^{\text{noise}}$, in the frequency bin is then computed by

$$\hat{P}_{\text{RX}}^{\text{noise}} = \delta f_{\text{DFT}} \cdot \text{NEP}_{\text{RX}}. \quad (3.4.12)$$

Table 3.3 lists the effective received power due to noise for some LO powers and DFT sample sizes for the CS of the channels and the single channel. However, in practice the considered noise sources are not white and the optimum local oscillator will depend on the frequency.

3.4.2. Non-Additive Noise Sources

Important non-additive noise sources are pointing noise and frequency noise. Frequency noise enters into the heterodyne signal through the frequency response of the photodiode as well as the frequency dependence of the data processing. In the next chapter, the detection algorithm is discussed which uses an FFT to estimate the frequency of the

Table 3.3.: Noise floor, $\hat{P}_{\text{RX}}^{\text{noise}}$, in the DFT frequency bins of width δf_{DFT} , due to the presented additive noise sources, in terms of the effective received power. The assumed values for the detector electronic noise and the laser intensity noise are given in Table 3.2 and the sampling frequency is assumed to be $f_s = 38$ MHz. The effective received power due to noise, $\hat{P}_{\text{RX}}^{\text{noise}}$, is given for different DFT sizes, N_{DFT} , and local oscillator powers per photodiode channel, $P_{\text{LO},c}$.

Item						
Signal Type	$P_{\text{LO},q} / \mu\text{W}$	$\hat{P}_{\text{RX}}^{\text{noise}} / \text{fW}_{\text{rms}}$				
N_{DFT}		512	1024	2048	4096	8192
$\delta f_{\text{DFT}} / \text{kHz}$		74.2	37.1	18.6	9.28	4.64
Single Channel	100	26.13	13.07	6.53	3.27	1.63
	150	23.51	11.75	5.88	2.94	1.47
	200	23.03	11.52	5.76	2.88	1.44
	400	26.49	13.24	6.62	3.31	1.66
Coherent Sum of Channels	100	36.2	18.1	9.0	4.5	2.3
	150	38.5	19.3	9.6	4.8	2.4
	200	43.1	21.5	10.8	5.4	2.7
	400	66.6	33.3	16.6	8.3	4.2

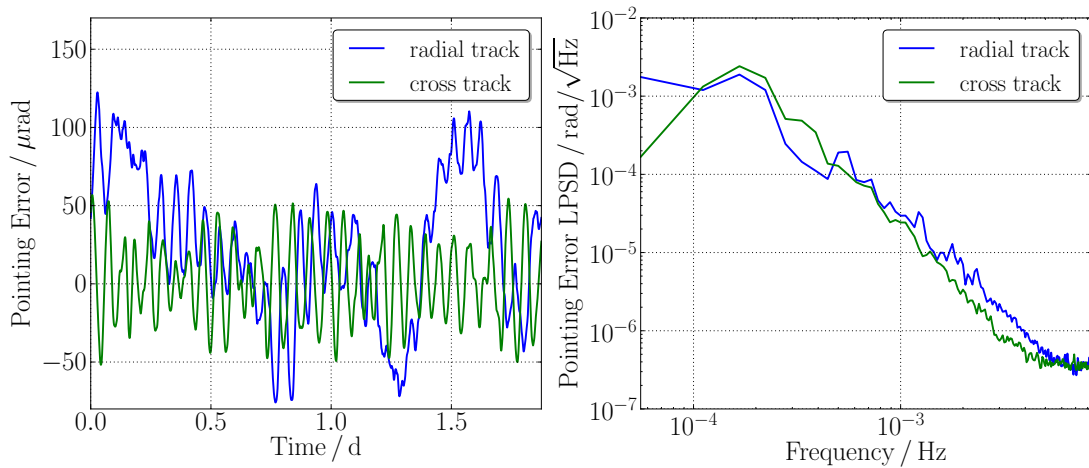


Figure 3.10.: Left: Time series of assumed residual pointing errors due to the orbit propagator on board the GRACE Follow-On satellites. Right: Linear power spectral density of the time series, shown on the left. Processed GRACE data from Feb. 2012 (private communication B. Klipstein, NASA/JPL, 2012).

signal. The frequency response of the FFT is not homogeneous and frequency changes directly couple to the heterodyne amplitude via this mechanism. An analysis of this is postponed to the corresponding chapter.

Pointing noise enters through the heterodyne efficiency and the received power into the photocurrent measurement. The time scale on which the different processes vary can be grouped into three types based on time scales important for acquisition. The initial unknown misalignment biases due to launch misalignments, or sensor biases are static errors which do not change considerably later. These biases determine the initial spatial uncertainty cone that has to be scanned.

Then there are *dynamic biases* which vary on time scales of minutes to hours. The duration of spatial scans over the initial uncertainty cone will have similar length and thus the dynamic biases will not significantly distort the scan pattern, but will change the location of the scan area for each spatial scan. If an acquisition scheme is used that uses an initial LOS calibration and an autonomous link acquisition later over remaining uncertainties, the pointing changes due to dynamic biases add to the uncertainties for a successive laser link acquisition. The dominant noise source for this time scale is the orbit prediction error that changes on periods similar to the orbital revolution period.

Each of the GRACE satellites have an orbit predictor running on board that predicts the angular position of the remote spacecraft based on orbit ephemeris uploaded to the satellite. For a successor mission like GRACE Follow-On the assumed residual pointing

error due to the orbit predictor is shown in Figures 3.10, where a time series is shown on the left and a spectrum computed from the time series on the right. The time series is generated from GRACE data of Feb. 2012 (private communication B. Klipstein, NASA/JPL, 2012) and is shown for the radial and cross track directions. The residual pointing error has a large periodic component of the period of one orbit revolution. The maximum error is about $120 \mu\text{rad}$ in radial direction and $50 \mu\text{rad}$ in cross-track direction. For scans longer than the orbital time, the orbit prediction error adds to the uncertainty, while for fast scans of some minutes it is negligible.

The last group, *jitter*, are changes over time scales smaller than the time for a single spatial scan of the satellites. These will distort the spatial scan pattern and have to be taken into account when setting the resolution of the spatial scan. The only considered process on these times scales is star-camera assembly (SCA) noise. The star-camera assembly estimates the attitude of the spacecraft in the inertial reference frame. See for example [DBF⁺03]. The pointing noise due to the SCA is assumed to be $10 \mu\text{rad}$ (1σ) in pitch and yaw, based on performance specification for GRACE [DBF⁺03]. The specification in roll is given as $80 \mu\text{rad}$ which only adds a negligible additional error in the important directions for acquisition, yaw and pitch, and will be neglected for this analysis. Here, additionally the noise is assumed to be Gaussian distributed.

As long as the DWS signal is not used to automatically align the beam axis, the SCA noise is added every 0.1 s to the current FSM position which will distort a running scanning pattern or lead to signal loss in certain stages of an autonomous link acquisition.

3.5. Beatnote Frequencies

The beatnote frequency of the heterodyne signal is equal to the frequency difference between the frequency of the local oscillator (LO) and the received beam (RX) which was derived in equation (2.1.7). The frequency of the received beam is Doppler shifted to the frequency of the transmitted beam, as the two spacecraft move relative to each other. Figure 3.11 shows how the beatnote frequencies are composed.

With the relative velocity, v_{rel} , and the absolute frequency of the transmitted light, f_{TX} , the Doppler shift is given by

$$f_{\text{D}} = -\frac{v_{\text{rel}}}{c} f_{\text{TX}}. \quad (3.5.1)$$

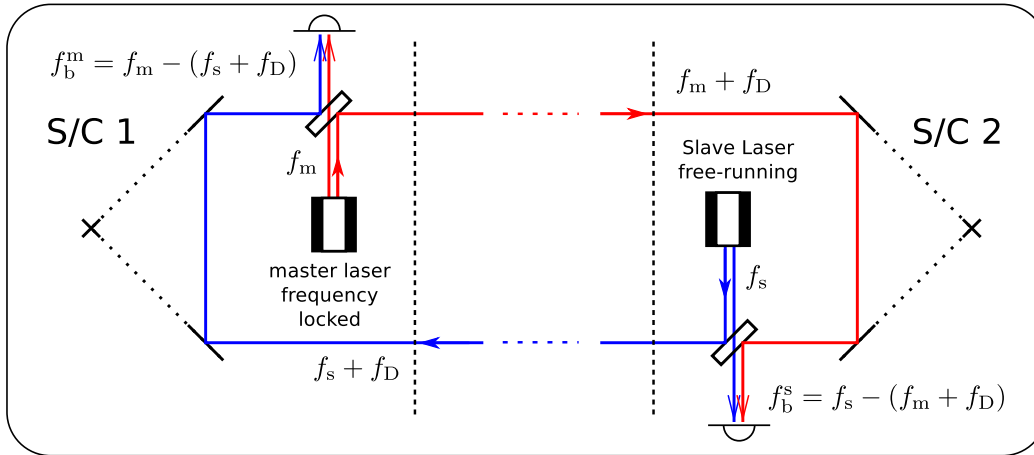


Figure 3.11.: The Doppler shift f_D results in different beatnote frequencies on the two spacecraft. The difference in the beatnote frequencies is twice the Doppler shift.

The frequency of the received light, f_{RX} , is thus,

$$f_{RX} = f_{TX} + f_D. \quad (3.5.2)$$

The frequency of the transmitted light is the absolute frequency of the lasers of the two spacecraft, which will here be denoted as f_m and f_s for the master and the slave laser respectively. With this, the beatnote frequency measured on the master spacecraft f_b^m and the slave spacecraft f_b^s can be calculated by

$$f_b^m = f_m - (f_s + f_D) \quad \text{and} \quad (3.5.3)$$

$$f_b^s = f_s - (f_m + f_D). \quad (3.5.4)$$

The sign of the frequencies is not measurable and hence, what the phasemeter really sees is the modulus of the above frequencies,

$$|f_b^m| = |f_m - (f_s + f_D)| \quad \text{and} \quad (3.5.5)$$

$$|f_b^s| = |f_s - (f_m + f_D)|. \quad (3.5.6)$$

The difference in the absolute value of the beatnote frequencies of the master and the slave spacecraft is thus, twice the one-way Doppler shift. The relative speed between the satellites is, based on GRACE data, assumed to be $|v_{rel}| \leq 2.5 \text{ m s}^{-1}$, resulting in one-way Doppler shifts of maximally $f_D = \pm 2.35 \text{ MHz}$. The difference in the beatnote frequencies due to the Doppler shift might reach up to 4.7 MHz which is more than a

fourth of the complete photodiode bandwidth.

Hence, large Doppler shifts might lead to situations during an acquisition scan, where the beatnote on one of the spacecraft is well within the photodiode bandwidth but is out of band on the other spacecraft, prohibiting a detection.

3.6. Acquisition Schemes

Starting from a large initial uncertainty, different acquisition strategies are possible. On the one hand, a direct acquisition approach, where the scans over the spatial and frequency uncertainty space is stopped as soon as a detection was made. Starting from the frequency and beam alignment at the time of the detection, the satellites try to lock.

On the other hand, an initial line-of-sight calibration scan can be performed which is used to scan the total uncertainty space for the maximum occurring heterodyne signal amplitude and use the angular position and frequency at which the maximum occurred as best estimates. A subsequent autonomous laser link acquisition is done over a much smaller uncertainty space to subsequently lock the satellites.

The principal advantage of the direct link acquisition is the possibility that the scan can be stopped once a signal has been detected. On average, the time until a detection is made and the satellites acquire is half the time for a scan over the complete uncertainty space. An initial line-of-sight calibration scan always scans the full uncertainty space and the average time is equal to the worst case time of the direct acquisition approach.

Ales et al. [AGJB13] studied guidance algorithms and acquisition algorithm sequences for a GRACE Follow-On type laser ranging interferometer, where they investigate a direct link acquisition. However, a line-of-sight calibration scan is generally thought of as being more robust, as the satellites scan their uncertainty space independently of the other satellite. In a direct link acquisition the satellites need to stop the scan once a detection was made without the certainty that the other spacecraft will ever detect a signal. Situations in which only one spacecraft will detect a signal include large Doppler shifts, as mentioned in the previous section, but also large differences in the heterodyne signal amplitude for local and remote beam axis tilts. Additionally, the TMA coalignment error might steer the beam out of the field-of-view of the remote spacecraft, though locally a detection was made.

In this thesis laser link acquisition is studied for an initial line-of-sight calibration scan over the complete uncertainty space. The steering-mirror position and frequency at the time the maximum occurred are used as best estimates for a subsequent autonomous laser link acquisition. A successful experimental demonstration of such an acquisition

scheme was carried out by D. Wuchenich et al. [WMS⁺on] in which the authors modelled the LRIs of the two spacecraft and the inter-satellite link in a bench top experiment. The design of the experiment was partly based on the analysis that is presented in this thesis.

3.7. Conclusions

In this section the absence of dedicated acquisition hardware was identified as the main difference between laser link acquisition for GRACE Follow-On and laser link acquisition as studied in the past. Such dedicated hardware are for example, beam shaping mechanisms or wide field-of-view detectors that decouple the sensor output from the alignment of the beam that is transmitted to the distant spacecraft.

After this, the laser ranging interferometer for the GRACE Follow-On mission is presented with a focus on the subsystems important for acquisition. These are, for example, the fine-steering mirror, the triple-mirror assembly and the photodiodes. Subsequently, the heterodyne signal as the sensor signal that is used for acquisition was introduced for the case of a hot-redundant pair of quadrant photodiodes. In the following, the dependence of the heterodyne signal amplitude on misalignments of the beam axes is investigated. For this case, the effective received power was introduced as the product of the power passing through the receive aperture, the power loss in the receive path and the heterodyne efficiency. The effective received power depends on the alignment of the beam transmitted by the distant spacecraft via the received power. At the same time it depends on the alignment of the local oscillator with respect to the received beam, due to the heterodyne efficiency.

Thereafter, the most important additive and non-additive noise sources are reviewed. For the additive noise sources which are electronic noise, laser shot noise and laser intensity noise, the dependence on the local oscillator power was given. Some values for the RMS of the noise in terms of the effective received power over bandwidths corresponding to FFTs of 512 to 8192 points are given.

As the most important non-additive noise sources, pointing noise and frequency noise are presented. The most important sources of pointing noise are the star-camera assembly attitude jitter, varying on frequencies of 10 Hz and the orbit prediction error that varies on time scales of the orbital period. Finally, some acquisition schemes were discussed. Among those, the combination of an initial line-of-sight calibration scan with a pick-max search and a subsequent autonomous laser link acquisition over reduced uncertainties was chosen as the baseline for the analysis presented in the following chapters.

4. Detection Algorithm, Signal- and Noise Distributions

In this chapter, an algorithm will be introduced for estimating the frequency and amplitude of the measured heterodyne signal. The detection algorithm is based on the computation of fast Fourier transforms (FFT) of sequential non-overlapping chunks of data. The maximum value in a power spectrum will be used as an estimate for the heterodyne amplitude, whereas the index of the frequency bin is an estimate of the heterodyne frequency.

The four data channels from the quadrant photodiodes can be combined to yield higher signal-to-noise ratios. Two distinctly different combinations, the coherent and incoherent sum of the channels, are presented. Based on the design of the algorithm, the distributions of the returned estimates are derived.

At first, the distribution of the power in a single frequency bin of the discrete Fourier transform for a heterodyne signal of constant amplitude and frequency is presented. Initially the distribution is given for a single data channel and after this the result is generalised to the case of the coherent and incoherent sum. Thereafter, the distribution of the maximum value in the power spectrum is given. This is the distribution of the output of the detector.

Furthermore, in a pick-max scan during the initial line-of-sight calibration, the maximum output of the detector over a complete acquisition scan is determined. For both data combinations an estimate of the maximum detector output for the case of no signal at the input of the detector is given, depending on the number of computed estimates. The obtained result will eventually allow to set lower limits on the resolution of the spatial scan.

In the last part of this chapter, the influence of frequency noise and a constant rate frequency sweep on the distribution of the detector output is investigated by means of numerical simulations.

4.1. Detection Algorithm

The signal to be detected is a sinusoid in additive, white, stationary Gaussian noise. For the definition of stationarity, the reader is referred to [WZ71] or similar literature.

However, the exact parameters of the signal, i.e. the amplitude, phase, frequency and arrival time, are unknown. The detector that is used to decide whether the signal is present or not should accommodate this lack of knowledge and still perform close to optimal, i.e. maximising the probability of detection for a fixed probability of false alarm.

An approximately optimal estimator for the initial line-of-sight calibration scan is deduced from the maximum likelihood estimator (MLE) of the arrival time, while a nearly optimum detector can be realised with the *generalised likelihood ratio test*. The derivation of the MLE and optimal detector is outlined in many books about detection or estimation theory and is rather standard, see for example [Kay09, WZ71, Kay93] or [KPK81]. The basic approach is based on the work of Neyman and Pearson from the year 1928 [NP28a, NP28b] or a subsequent article published in 1933 [NP33]. The Neyman-Pearson approach is chosen because no prior information on the value of any of the unknown parameters is given. The following sections will give a short introduction to the detection theory to give enough background to motivate the decision for the chosen detector implementation. For a deeper insight the reader is referred to the corresponding literature. The following derivation is adapted from [Kay09, Kay93].

4.1.1. Maximum Likelihood Estimator for the Heterodyne Signal Parameters

In this section the maximum likelihood estimator for the heterodyne amplitude and the heterodyne frequency are given. In order to simplify the derivation, the amplitude and frequency of the heterodyne signal are assumed to be constant and only the heterodyne signal of a single data channel is considered.

The heterodyne signal, measured in a single channel, was defined in equation (3.3.4) as the coherent sum of two photodiode segments. If the amplitude of the heterodyne signal is denoted by A_c , the beatnote frequency by f_b , and the phase by ϕ_c , then the heterodyne signal, sampled at the discrete times $t_n = n/f_s$, can be written as

$$s_c(t_n) = A_c \cos(2\pi f_b t_n + \phi_c) + I_c(t_n) \quad (4.1.1)$$

$$= A_c \cos(\phi_c) \cos(2\pi f_b t_n) - A_c \sin(\phi_c) \sin(2\pi f_b t_n) + I_c(t_n). \quad (4.1.2)$$

Here, $I_c(t_n)$ is the noise in a single channel measured at time t_n . In Section 3.4.1, the power spectral density of the noise in a channel was defined by the coherent sum of the noises of a single photodiode segment. The most dominant noise sources were given by shot noise, detector electronic noise and laser intensity noise. The noise is treated as white Gaussian noise, for which samples $I(t_m)$ and $I(t_n)$ at different times t_m and t_n are *identical and independently distributed* (IID) normal random variables with constant variance σ_c^2 , i.e. $I_c(t_n) \sim \mathcal{N}(0, \sigma_c^2)$. With the one-sided power spectral density of the combined noise sources in a single channel, \tilde{S}_c^2 , which was given in equation (3.4.6), one can compute the noise variance in the single channel by equation (3.4.7) as

$$\sigma_c^2 = \frac{f_s}{2} \tilde{S}_c^2. \quad (4.1.3)$$

The probability distribution function (PDF) $p(x; \mu, \sigma)$ of the normal distributed random variable $X \sim \mathcal{N}(\mu, \sigma^2)$ with mean μ and variance σ^2 is defined as [Gut09]

$$p(x; \mu, \sigma) = \frac{1}{\sqrt{2\pi} \sigma} \exp\left(-\frac{x^2}{2\sigma^2}\right). \quad (4.1.4)$$

Hence, if the noise is distributed with a Gaussian distribution of zero mean, the probability density function $p(s; A_c, \phi_c, f_b)$ for a given realisation of the data plus noise is given by

$$p(s_c; A_c, \phi_c, f_b) = \frac{1}{(2\pi\sigma_c^2)^{N/2}} \exp\left(-\frac{1}{2\sigma_c^2} \sum_{n=0}^N (s_c(t_n) - A_c \cos(2\pi[f_b/f_s]n + \phi_c))^2\right). \quad (4.1.5)$$

The PDF for a fixed realisation of the data as a function of the signal parameters A_c , ϕ_c and f_b is called the *likelihood function*. The maximum likelihood estimator \hat{A}_c , $\hat{\phi}_c$ or \hat{f}_b , for a signal parameter maximises the PDF of the data, as a function of the parameter. For the case considered here, it can be shown that the MLE of the signal parameters are unbiased estimators for which the variance is equal to the Cramer-Rao bound [Kay93, Cra74]. The Cramer-Rao bound is a lower bound on the variance of any unbiased estimator for a parameter of a deterministic signal.

Rigorous analysis shows [Kay93], that the maximum likelihood estimator for the amplitude \hat{A}_c , of a sinusoidal signal in white Gaussian noise is the absolute value of the discrete Fourier transform of the data at the signal frequency. The MLE of the phase, $\hat{\phi}_c$, is the argument of the discrete Fourier transform. If additionally to the amplitude and phase, the frequency of the signal is unknown, the MLE of the signal frequency, \hat{f}_b , has

to be determined by calculating the DFT for different frequencies until the maximum is found. Due to limited computational power, it is impossible to compute the DFT of all possible frequencies, and hence the MLE is generally not found.

However, fast-Fourier transforms (FFT) [CT65] provide good coverage of a limited frequency band and are computationally efficient. In order to determine the arrival time of the signal, FFTs of sequential non-overlapping chunks of data can be computed. The time of the FFT, for which the maximum amplitude within a spectrum is found, is an estimate for the arrival time of the signal.

In this thesis, the DFT of size N_{DFT} of a time domain input signal, $s(t)$, sampled at times $t_n = n / f_s$, with $n = 0, \dots, N_{\text{DFT}} - 1$, is defined as

$$\mathcal{F}[s](k) := \frac{\sqrt{2}}{N_{\text{DFT}}} \sum_{n=0}^{N_{\text{DFT}}-1} s(t_n) \exp\left(-2\pi i \frac{k}{N_{\text{DFT}}} n\right). \quad (4.1.6)$$

To ease notation the shorthand, $\tilde{s}(k) := \mathcal{F}[s](k)$, will be used in the following. Here, $k = 0, \dots, N_{\text{DFT}} - 1$ is the frequency bin index of the DFT and the central frequencies of the frequency bins are given by

$$f_k = k \frac{f_s}{N_{\text{DFT}}}. \quad (4.1.7)$$

Generally, it is assumed that the DFT is normalised by $\sqrt{2}/N_{\text{DFT}}$. Provided that the frequency of the heterodyne signal is equal to one of the central bin frequencies, $f_b = f_k$, the amplitude of the k -th frequency bin in the spectrum is equal to the root-mean square value of the input signal and it is independent of the number of samples, N_{DFT} .

4.1.2. Detector for the Heterodyne Signal

In 1928/33, Neyman and Pearson laid the foundations for the modern detection theory in their publications [NP28a, NP28b, NP33]. Good discussion of the detection problem can be found in [Kay09, WZ71], while additional information on parameter estimation are given in [Kay93, WZ71]. The detector specified here, is a general detector for a sinusoidal signal in white Gaussian noise with unknown amplitude, phase, frequency and arrival time. This system is widely used in signal detection of all sorts, [KPK81, Hol93].

Prior knowledge of the signal parameters is limited and restricted to the size of the spatial uncertainty cone and frequency uncertainty interval. The probability density function for the parameters in their uncertainty regions is assumed to be flat. This is why the Neyman-Pearson approach is favoured over the Bayesian approach [WZ71, Kay93].

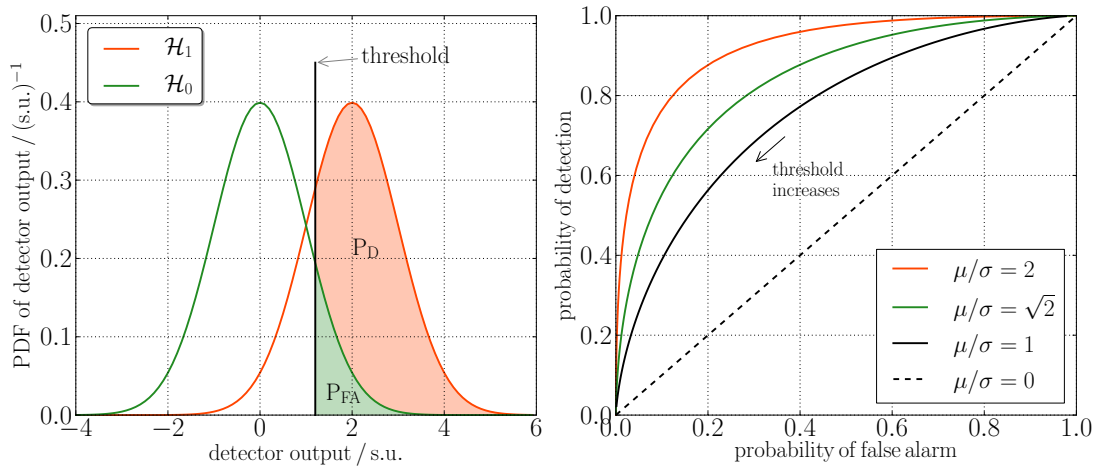


Figure 4.1.: Explanation of some of the important quantities for a detection problem. Left: Two normal PDFs representing the PDF for a random variable under test for the case of two hypotheses, \mathcal{H}_0 and \mathcal{H}_1 . The probabilities of detection, P_D , and false alarm, P_{FA} , depend on the chosen detection threshold. Right: For a given PDF of the test statistic, the P_D as a function of P_{FA} will give a performance estimate of the detector. This plot is called *receiver operating characteristic*. It is shown on the right for different variances of the test statistic. The higher the detection probability for a given false alarm probability, the stronger curved the plot and the better the detector. The dashed diagonal line is for a detector that just guesses with 50% chance for a correct answer.

The detection problem consists of deciding on whether the measured data consists of only noise or the sum of noise and the heterodyne signal. It can be stated mathematically as

$$\begin{aligned} \mathcal{H}_0 : s_c(t_n) &= I(t_n) \\ \mathcal{H}_1 : s_c(t_n) &= A_c \cos(2\pi f_b t_n + \phi_c) + I(t_n), \\ &\text{for, } n = 0, \dots, N_{\text{DFT}} - 1, \quad \text{and } c = 1, \dots, n_c \end{aligned} \quad (4.1.8)$$

with the two hypothesis \mathcal{H}_0 , if only noise is present (*null hypothesis*) or \mathcal{H}_1 , if the signal is also present in the data (*alternative hypothesis*). In the following it is assumed that if the signal is present, it is present in all n_c data channels simultaneously.

In analogy to the last section, a combination of data samples is sought that in some way optimises the decision process between the two hypotheses. This combination is called the *detector* in the following and the output of the detector will be denoted by \mathcal{D} . Due to the noise, each of the measured data samples is a random variable, and has a certain probability distribution function. Also, the detector output, \mathcal{D} , will be a random

variable but with a different PDF.

The PDF of the detector will differ for the two hypotheses, \mathcal{H}_0 and \mathcal{H}_1 . Figure (4.1) shows a simple example of such a change in the PDF due to the change of the mean of a normal random variable. This corresponds, for example, to the detection of a DC offset in white Gaussian noise, for the case that the test statistic is only a single measurement.

The plot on the left shows two normal PDF with variance $\sigma^2 = 1$ and mean values $\mu = 0$ if no signal is present and $\mu = 2$ if a signal is present. It is natural to introduce a threshold and decide for \mathcal{H}_0 if the detector output for the measured data is below the threshold and for \mathcal{H}_1 if it exceeds the threshold. Two types of errors can be made in the detection which is a *false alarm* if \mathcal{D} exceeds the threshold, though no heterodyne signal is present at the input of the detector, and a *false dismissal* if a signal is present but the detector output is smaller than the threshold. The probability of a false alarm, P_{FA} , and a false dismissal, $P_{FD} = 1 - P_D$, depend on the threshold and the PDF of the data under test. Here, P_D is the probability of detection.

The right plot in Figure 4.1 shows the *receiver operating characteristic* (ROC). The ROC is a plot of the detection probability as a function of the false alarm probability. The curve is parametrised by the threshold used to decide on a detection. ROCs strongly depend on the PDF of the detector output which is clear from the above plots. The stronger curved the ROC is, the higher is the probability of detection for a given false alarm probability and the better is the used detector. A straight diagonal line corresponds to a detector that has equal probability of deciding \mathcal{H}_0 or \mathcal{H}_1 , independent of the chosen threshold. This is equivalent to guessing. The ROC thus gives a performance estimate of a given detector.

The great advantage of the Neyman-Pearson approach to signal detection is that it gives a rule, how to find the best combination of the measured data to achieve the highest probability of detection for a given false alarm probability, independent of the threshold. The ROC for this detector will be the one with the strongest curvature and lies above all other detectors, for all false alarm probabilities. However, this is only true for the case that all signal parameters are known and is only asymptotically true for $N \rightarrow \infty$, for the case of unknown parameters.

The Neyman-Pearson theorem now says that for a deterministic signal with unknown parameters in noise, the maximum detection probability, P_D , for a given false-alarm probability, P_{FA} , is achieved, if a detection is claimed when:

$$L(\mathbf{s}) = \frac{p(\mathbf{s}; \hat{A}_q, \hat{\phi}_q, \hat{f}_b, \hat{n}_0, \mathcal{H}_1)}{p(\mathbf{s}; \mathcal{H}_0)} \geq G. \quad (4.1.9)$$

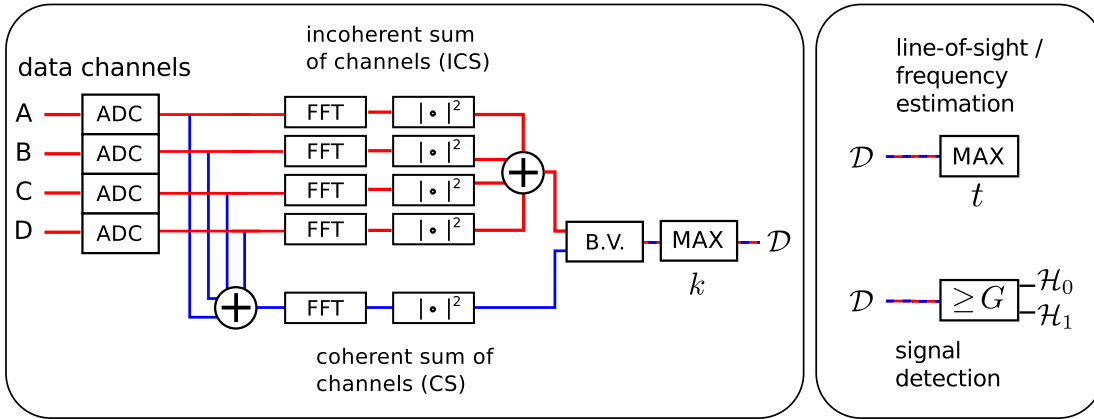


Figure 4.2.: Proposed implementation of the algorithm for detecting the heterodyne signal. The power spectrum of the heterodyne signal is computed and the maximum value in any of the frequency bins, indexed by k , is determined. Frequency bins containing excess noise are vetoed (B.V.). To increase the signal to noise ratio, the coherent sum and incoherent sum of the data channels are formed. Right: Further processing of the detector output \mathcal{D} . For the case of a line-of-sight calibration scan, the maximum detector output over the time, t , of the complete calibration scan is determined, whereas for an autonomous laser link acquisition the detector output is compared against a threshold G .

where $L(s)$ is called the *generalised likelihood ratio*, $p(s; \hat{A}_q, \hat{\phi}_q, \hat{f}_b, \hat{n}_0, \mathcal{H}_1)$ is the likelihood of the data under the hypothesis \mathcal{H}_1 (the signal is present) and $p(s; \mathcal{H}_0)$ is the likelihood of the data if no signal is present. The likelihood for the case considered here, was defined in equation (4.1.5). The signal parameters, i.e. the amplitude, phase, frequency and arrival, are replaced by their MLEs. This test is generally referred to as the generalised likelihood ratio test. The threshold G is determined by the desired false alarm probability and the PDF of the detector.

It can be shown that the optimal detector for the case of a sinusoidal signal in additive, white Gaussian noise is the absolute value of the discrete Fourier transform of the data. In theory, the optimum threshold is determined by the desired false-alarm probability, though for the analysis in this thesis the detection threshold is set based on a minimum required power of the heterodyne signal. This is further discussed in Chapter 7.

The left panel in Figure 4.2 summarises the previous discussion and shows a schematic of the proposed implementation of the detection algorithm which is extended to include combinations of the four available data channels. The data from the quadrant photodiodes (QPD) is first digitised by analogue-to-digital converters (ADC) before it is further processed. To increase the signal-to-noise ratio two combinations of the data can be formed which are denoted the *coherent sum* (CS) and the *incoherent sum* (ICS)

in Figure 4.2. For the case of the CS the data channels are summed up and afterwards a power spectrum is computed by means of a FFT. For the case of the ICS a power spectrum is computed from the data of each channel before the individual power spectra are added. Frequency bins of the power spectra that are known to contain high noise powers are vetoed (B.V.) before the maximum value contained in any of the frequency bins is determined. Following are mathematical definitions of the detector outputs for a single channel \mathcal{D}_c , the coherent sum \mathcal{D}_{CS} and the incoherent sum \mathcal{D}_{ICS} :

$$\mathcal{D}_c = \max_k |\tilde{s}_c(k)|^2, \quad (4.1.10)$$

$$\mathcal{D}_{CS} = \max_k \left| \sum_{c=0}^{n_c} \tilde{s}_c(k) \right|^2, \quad (4.1.11)$$

$$\mathcal{D}_{ICS} = \max_k \sum_{c=0}^{n_c} |\tilde{s}_c(k)|^2, \quad (4.1.12)$$

where the frequency bin index k runs over all non-vetoed frequency bins. The right panel in Figure 4.2 shows the subsequent processing of the output of the detection algorithm. For the initial line-of-sight calibration, the maximum detector output over the time of the complete calibration scan is determined, whereas for the autonomous laser link acquisition the detector output is compared against the threshold G .

4.2. Signal and Noise Distributions

In this section, the distribution of the detector output, \mathcal{D} , is derived. At first, the distribution of the power in a single frequency bin of the power spectrum is given for the case of a single data channel. Subsequently, the result is generalised for the case of the coherent and incoherent sum of the data channels. The final step is the derivation of the distribution of the detector output, \mathcal{D} , which is the maximum value in the frequency bins found in the power spectrum.

For the purpose of this section it is assumed that the beatnote frequency, f_b , of the heterodyne signal is equal to the central frequency, f_j , of the j -th frequency bin, with $j = 0, \dots, N_{\text{DFT}}/2 - 1$. The central bin frequencies were given in equation (4.1.7) as $f_k = kf_s/N_{\text{DFT}}$. Furthermore, the amplitude and phase of the heterodyne signal are assumed to be constant.

4.2.1. Distribution of a Single Channel

If the heterodyne signal of a single data channel can be approximated by a sinusoidal signal with constant amplitude and frequency, the DFT of the input signal can easily be calculated analytically. The time series of the heterodyne signal photocurrent $s_c(t_n)$ in a single channel was given in equation (4.1.1). If the beatnote frequency is set to the central frequency of the j -th frequency bin with help of equation (4.1.7) and $t_n = n/f_s$, it can be given as

$$s_c(n) = A_c \cos\left(2\pi \frac{j}{N_{\text{DFT}}}n + \phi_c\right) + I_c(n). \quad (4.2.1)$$

Here, A_c and ϕ_c are the amplitude and phase of the heterodyne signal photocurrent and I_c is the time series of the noise in the channel. If the DFT as defined in equation (4.1.6), is applied to the time domain signal, $s_c(n)$, and the linearity of the DFT is exploited, the frequency content from the signal and the noise can be treated separately:

$$\tilde{s}_c(k) = A_c \mathcal{F}\left[\cos\left(2\pi \frac{j}{N_{\text{DFT}}}n + \phi_c\right)\right](k) + \mathcal{F}[I_c](k). \quad (4.2.2)$$

The DFT of a sinusoidal input signal with constant amplitude and frequency can be computed analytically by using the following relation:

$$\mathcal{F}\left[\cos\left(2\pi \frac{j}{N_{\text{DFT}}}n + \phi_c\right)\right](k) = \frac{e^{i\phi_c}}{\sqrt{2}} \delta_{j,k} + \frac{e^{-i\phi_c}}{\sqrt{2}} \delta_{N_{\text{DFT}}-j,k}. \quad (4.2.3)$$

Here, $\delta_{j,k}$ is the Kronecker delta defined by

$$\delta_{j,k} = \begin{cases} 1, & \text{if } i = j, \\ 0, & \text{if } i \neq j. \end{cases} \quad (4.2.4)$$

Hence, the DFT of a constant amplitude sinusoidal input signal with frequency f_j has a peak at $j = k$ and has zero response in any other frequency bin. The amplitude of the signal in the frequency bin is given by the RMS amplitude of the input signal. The phase is equal to the phase of the input signal ϕ_c . The second peak at $k = N_{\text{DFT}} - j$ in equation (4.2.3) is due to the symmetry of the DFT for a real valued input signal. As the upper half of the DFT bins does not contain any additional information, they will be omitted from now on.

The second term in equation (4.2.2) can be solved by statistical means. The distribution is given in many text books on detection theory, for example in [Kay09]. The

result is, that the real and imaginary parts of the DFT of additive, white Gaussian noise with variance σ_c^2 , are normal distributed random variables with zero mean and variance $\sigma_c^2/N_{\text{DFT}}$. If the DFT of the time series of the noise in the channel is denoted by $\tilde{I}_c(k)$ for any $k = 0, \dots, N_{\text{DFT}} - 1$, the real and imaginary parts can be given by

$$\mathcal{R}(\tilde{I}_c(k)) \sim \mathcal{N}(0, \sigma_c^2/N_{\text{DFT}}) \quad \text{and} \quad \mathcal{I}(\tilde{I}_c(k)) \sim \mathcal{N}(0, \sigma_c^2/N_{\text{DFT}}). \quad (4.2.5)$$

The functions $\mathcal{R}(x)$ and $\mathcal{I}(x)$ return the real and the imaginary part of the complex variable x . With equation (4.2.2) the amplitude in a single frequency bin can be formulated by

$$\tilde{s}_c(k) = \begin{cases} A_c \cos \phi_c / \sqrt{2} + \mathcal{R}(\tilde{I}_c(k)) \\ \quad + i [A_c \sin \phi_c / \sqrt{2} + \mathcal{I}(\tilde{I}_c(k))] & \text{if } k = j, \\ \mathcal{R}(\tilde{I}(k)) + i \mathcal{I}(\tilde{I}(k)) & \text{if } k \neq j. \end{cases} \quad (4.2.6)$$

The distributions of the real and imaginary part can be given in terms of the heterodyne signal amplitude and phase, the noise variance and the sample size of the DFT. For the case that the bin frequency corresponds to the signal frequency, $k = j$, the real and imaginary parts are normally distributed:

$$\mathcal{R}(\tilde{s}_c(k)) \sim \mathcal{N}\left(\frac{A_c}{\sqrt{2}} \cos \phi_c, \frac{\sigma_c^2}{N_{\text{DFT}}}\right) \quad \text{and} \quad \mathcal{I}(\tilde{s}_c(k)) \sim \mathcal{N}\left(\frac{A_c}{\sqrt{2}} \sin \phi_c, \frac{\sigma_c^2}{N_{\text{DFT}}}\right). \quad (4.2.7)$$

If the signal frequency is not equal to the DFT bin frequency, $k \neq j$, the mean value is zero and the distribution is that of the DFT of noise alone which was already written down in equations (4.2.5).

In the following, the distribution of the frequency bins in the power spectrum is presented. The power spectrum $|\tilde{s}_c(k)|^2$ is calculated from the DFT output by simply taking the modulus squared of each frequency bin. Calculating the power spectrum from equation (4.2.6) yields:

$$|\tilde{s}_c(k)|^2 = \begin{cases} \left(\frac{A_c}{\sqrt{2}} \cos \phi_c + \mathcal{R}(\tilde{I}(k))\right)^2 + \left(\frac{A_c}{\sqrt{2}} \sin \phi_c + \mathcal{I}(\tilde{I}(k))\right)^2 & \text{if } k = j, \\ \mathcal{R}(\tilde{I}(k))^2 + \mathcal{I}(\tilde{I}(k))^2 & \text{if } k \neq j. \end{cases} \quad (4.2.8)$$

Looking at equation (4.2.8), one notices that for both cases, $k = j$ and $k \neq j$, the content

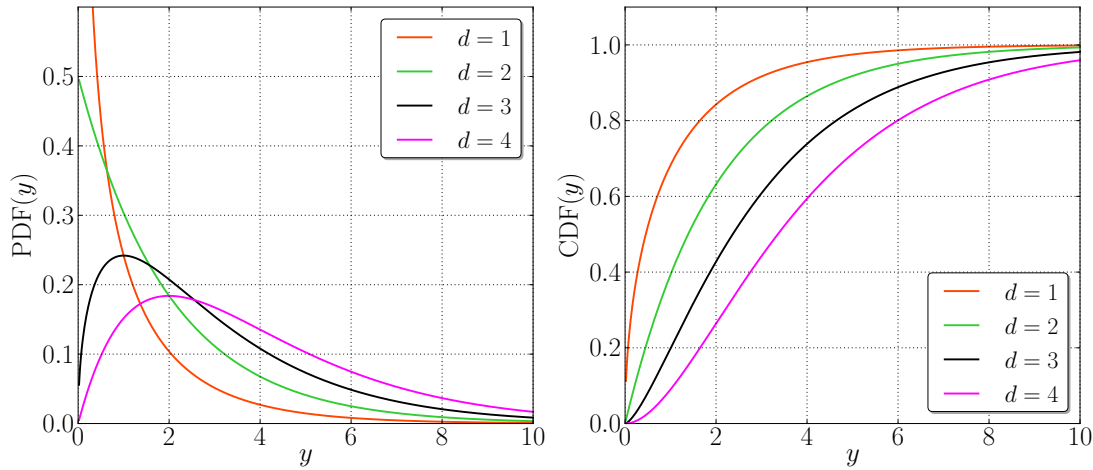


Figure 4.3.: Probability density function and cumulative distribution function of the χ^2 -distribution with $d = 1, 2, 3, 4$ degrees of freedom as defined by equation (4.2.9).

of the frequency bin is of the form $X^2 + Y^2$, where X and Y are normal random variables. For the case that $k \neq j$, the mean of the Gaussian normal distribution is zero, whereas for $k = j$, the mean values μ_1 and μ_2 equal $\mu_1 = A_c \cos \phi_c / \sqrt{2}$ and $\mu_2 = A_c \sin \phi_c / \sqrt{2}$.

For both cases, the distribution of X^2 , respectively Y^2 , is well known and some details can be found for example in [Kay09]. If $X \sim \mathcal{N}(0, \sigma^2)$ with zero mean, the resulting distribution of $Z = X^2 / \sigma^2$ is a χ^2 -distribution with one degree of freedom or short $Z \sim \chi^2(1)$. The PDF $p(z; d)$ of the χ^2 -distribution with d -degrees of freedom is given by:

$$p(z; d) = \frac{z^{d/2-1} e^{-z/2}}{2^{d/2} \Gamma(d/2)}, \quad \text{if } z \geq 0 \quad \text{and} \quad p(z; d) = 0, \quad \text{if } z < 0, \quad (4.2.9)$$

where Γ is the well known Gamma function.

An interesting feature of the χ^2 -distribution is that the sum of two IID χ^2 random variables Z_1 and Z_2 with d_1 and d_2 degrees of freedom is also χ^2 -distributed with $d = d_1 + d_2$ degrees of freedom. Figure 4.3 shows the PDF and the cumulative distribution function (CDF) of the χ^2 -distribution for different degrees of freedom.

However, the above PDF is only valid for the square of a standard normal distributed random variable and needs to be transformed to the more general case of a normal distributed variable with variance $\sigma^2 \neq 1$. The transformation can formally be described by a transformation of the random variable, Z , to a new random variable $Y = \sigma^2 Z$. After the variable transformation the PDF needs to be scaled such that the total probability

is conserved. For this case, the probability density function $p(y; d, \sigma^2)$ of the sum of squared IID normal random variables $Y = \sum_{i=1}^d X_i^2$, where the $X_i \sim \mathcal{N}(0, \sigma^2)$ is given by:

$$p(y; d, \sigma^2) = \frac{1}{\sigma^2} \frac{\left(\frac{y}{\sigma^2}\right)^{d/2-1} e^{-y/(2\sigma^2)}}{2^{d/2} \Gamma(d/2)}, \quad \text{for } y \geq 0 \quad \text{and} \quad p(z; d, \sigma^2) = 0, \quad \text{for } y < 0. \quad (4.2.10)$$

To denote that a random variable Y is distributed according to the PDF given in equation (4.2.10), $Y \sim \chi^2(d, \sigma^2)$ will be written in the following.

The power in a frequency bin of the power spectrum of a single data channel for the case of $k \neq j$, was given in equation (4.2.5). Using the result for the general case of the *scaled* χ^2 -distribution of equation (4.2.10), the PDF of the power in a frequency bin $|\tilde{s}_c(k)|^2$ is $\chi^2(2, \sigma_c^2/N_{\text{DFT}})$ -distributed and the PDF is given explicitly by

$$p(y; 2, \sigma_c^2/N_{\text{DFT}}) = \begin{cases} \frac{N_{\text{DFT}}}{2\sigma_c^2} \exp\left(-\frac{N_{\text{DFT}}}{2\sigma_c^2} y\right) & \text{if } y \geq 0, \\ 0 & \text{if } y < 0. \end{cases} \quad (4.2.11)$$

This type of distribution is also known as *exponential distribution*.

The derivation of the PDF for the case of the frequency bin containing the signal power, $k = j$, follows the same pattern such that redundant steps are left out. As mentioned before, the content of the signal bin is the sum of two squared normal random variables $Z = X^2 + Y^2$, where $X \sim \mathcal{N}(\mu_1, \sigma^2)$ and $Y \sim \mathcal{N}(\mu_2, \sigma^2)$.

If $X_i \sim \mathcal{N}(\mu_i, \sigma^2)$ are IID normal random variables with mean μ_i and variance σ^2 the distribution of the sum of the scaled variables $\hat{Z} = \sum_{i=1}^d X_i^2/\sigma^2$ is known as *non-central χ^2 -distribution* with d degrees of freedom and *noncentrality parameter* λ . The distribution will be denoted by $\hat{\chi}^2(d, \lambda)$ and the noncentrality parameter will be defined as

$$\lambda = \sqrt{\sum_{i=1}^d \left(\frac{\mu_i}{\sigma}\right)^2}. \quad (4.2.12)$$

The PDF $p(z; d, \lambda)$ of a noncentral χ^2 -distributed variable $\hat{Z} \sim \hat{\chi}^2(d, \lambda)$ is defined as:

$$p(z; d, \lambda) = \begin{cases} \frac{1}{2} e^{-(z+\lambda^2)/2} \left(\frac{z}{\lambda^2}\right)^{(d-2)/4} I_{d/2-1}(\lambda\sqrt{z}) & \text{if } z \geq 0, \\ 0 & \text{if } z < 0, \end{cases} \quad (4.2.13)$$

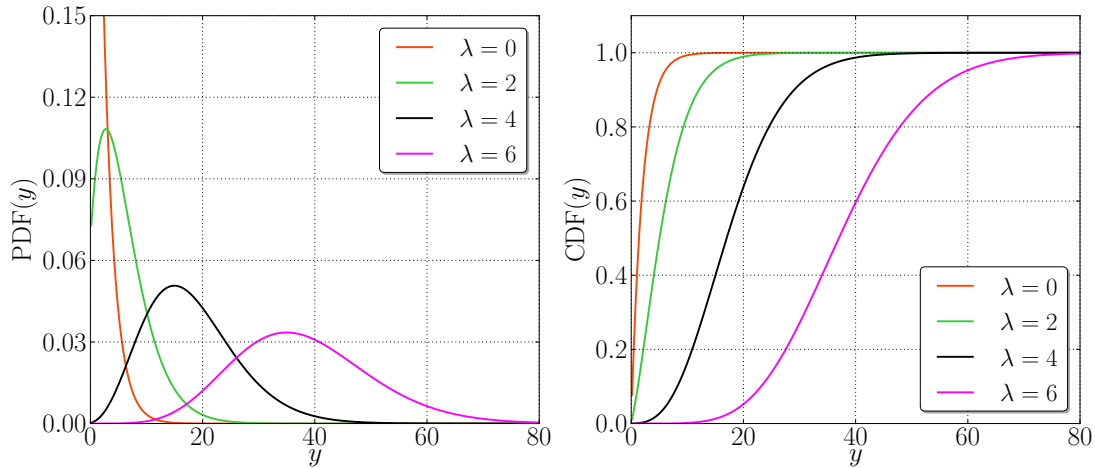


Figure 4.4.: Left: Probability density function of the noncentral χ^2 -distribution with $d = 2$ degrees of freedom and noncentrality parameter $\lambda = 0, 2, 4$ and 6 as defined by equation (4.2.13). Right: The corresponding cumulative distribution functions.

where $I_n(x)$ is the *modified Bessel function of the first kind* of order n [AS64]. For $\lambda \rightarrow 0$, the noncentral χ^2 -distribution approaches the central χ^2 -distribution, as expected. Figure 4.4 shows the PDF and the CDF of the non-central χ^2 -distribution of $d = 2$ degrees of freedom for different non-centrality parameter.

The variable transformation $z = y/\sigma^2$ carried out to parametrise the PDF by also the variance of the Gaussian noise σ^2 , works exactly the same as for the case of the χ^2 -distribution, such that the general PDF for a *scaled* noncentral χ^2 -distributed random variable $\hat{Y} \sim \hat{\chi}^2(d, \lambda, \sigma^2)$ with d degrees of freedom and noncentrality parameter λ is equal to:

$$p(y; d, \lambda, \sigma^2) = \begin{cases} \frac{1}{2\sigma^2} e^{-(y/\sigma^2 + \lambda^2)/2} \left(\frac{y}{\sigma^2 \lambda^2}\right)^{(d-2)/4} I_{d/2-1}\left(\frac{\lambda}{\sigma} \sqrt{y}\right) & \text{if } y \geq 0, \\ 0 & \text{if } y < 0. \end{cases} \quad (4.2.14)$$

In order to get the specific distribution of the power in a frequency bin, containing the heterodyne signal and the noise for a single channel, the PDF is re-parametrised.

Obviously, the distribution has two degrees of freedom, $d = 2$. The noncentrality parameter can be simplified and in fact is simply the signal-to-noise ratio of the heterodyne signal in a frequency bin. This can be seen by inserting the previously defined mean values μ_1 and μ_2 and variance as given in equation (4.2.7) into the definition of

the noncentrality parameter of equation (4.2.12):

$$\lambda = \sqrt{\frac{\mu_1^2}{\sigma_c^2/N_{\text{DFT}}} + \frac{\mu_2^2}{\sigma_c^2/N_{\text{DFT}}}} = \frac{\sqrt{N_{\text{DFT}}}}{\sigma_c} \frac{|A_c|}{\sqrt{2}}. \quad (4.2.15)$$

The result of the above equation is nothing else than the RMS of the heterodyne signal amplitude $|A_c|/\sqrt{2}$ divided by the standard deviation of the noise in the frequency bin of the DFT. This is equal to the signal-to-noise ratio (SNR) of the measured signal over the bandwidth of the FFT. Hence:

$$\lambda = \text{SNR}. \quad (4.2.16)$$

Inserting everything into equation (4.2.14) the following result for the probability density function $p(y; d, \lambda, \sigma_c^2)$ of the power in a single channel, $|\tilde{s}_c(k)|^2 \sim \hat{\chi}^2(d, \lambda, \sigma_c^2/N_{\text{DFT}})$, in the frequency bin containing the heterodyne signal is obtained:

$$p(y; 2, \lambda, \sigma_c^2/N_{\text{DFT}}) = \begin{cases} \frac{N_{\text{DFT}}}{2\sigma_c^2} \exp\left(-\frac{yN_{\text{DFT}}/\sigma_c^2 + \lambda^2}{2}\right) \\ \quad \cdot I_0\left(\sqrt{\frac{yN_{\text{DFT}}}{\sigma_c^2}} \lambda\right) & \text{if } y \geq 0, \\ 0 & \text{if } y < 0. \end{cases} \quad (4.2.17)$$

The mean value, $E[|\tilde{s}_c(k)|^2]$, can be easily derived from the mean of the non-central χ^2 -distribution. The result for the scaled noncentral χ^2 -distribution is:

$$\begin{aligned} E[\tilde{s}_c^2(k)] &= \frac{\sigma_c^2}{N_{\text{DFT}}} (2 + \lambda^2) \\ &= 2\frac{\sigma_c^2}{N_{\text{DFT}}} + \frac{|A_c|^2}{2}. \end{aligned} \quad (4.2.18)$$

For signal to noise ratios $\text{SNR} \gg 1$, the mean is approximately given by the square of the root mean square of the heterodyne signal amplitude.

4.2.2. Distributions of the Coherent Sum of Photodiode Segments

In this section, the previously derived distributions for the case of a single data channel are generalised to the coherent sum of the channels. The data of the coherently combined channels, $s_{\text{CS}}(t_n)$, is just the sum of the data in the individual channels which was given

in equation (4.2.1). It can be given as

$$s_{\text{CS}}(n) = \sum_{c=1}^{n_c} s_c(n) = \sum_{c=1}^{n_c} \left[A_c \cos \left(2\pi \frac{j}{N_{\text{DFT}}} n + \phi_c \right) + I_c(n) \right]. \quad (4.2.19)$$

The linearity of the DFT eases the computation of the power spectrum of the coherently added segments, as the results from the last sections can be reused. With equations (4.2.3) and (4.2.5) this gives:

$$\tilde{s}_{\text{CS}}(k) = \sum_{c=1}^{n_c} \mathcal{F}[s_c](k) = \sum_{c=1}^{n_c} \left(\frac{A_c e^{i\phi_c}}{\sqrt{2}} \delta_{j,k} + \tilde{I}_c(k) \right) \quad (4.2.20)$$

$$= \frac{A_{\text{CS}}}{\sqrt{2}} \delta_{j,k} + \tilde{I}_{\text{CS}}(k). \quad (4.2.21)$$

Here, the coherent sum amplitude, A_{CS} , and the coherent sum of the noise of the individual channels, \tilde{I}_{CS} , are defined as

$$A_{\text{CS}} = \sum_{c=1}^{n_c} A_c e^{i\phi_c}, \quad \text{and} \quad \tilde{I}_{\text{CS}}(k) = \sum_{c=1}^{n_c} \tilde{I}_c(k). \quad (4.2.22)$$

The power spectral density of the noise in the coherent sum of n_c photodiode channels can be given with equation (3.4.5) for the coherent sum of photodiode segments, by using that a channel is made up out of the coherent sum of two segments. It reads:

$$\tilde{S}_{\text{CS}} = \sqrt{2n_c(\tilde{S}_{e,q}^2 + \tilde{S}_{s,q}^2) + 4n_c^2 \tilde{S}_{i,q}^2}. \quad (4.2.23)$$

Here, the one-sided power spectral densities of the shot noise $\tilde{S}_{s,q}$, the detector electronic $\tilde{S}_{e,q}$ noise and the laser intensity noise $\tilde{S}_{i,q}$ were used. They are defined in equations (3.4.2), (3.4.1) and (3.4.3). The variance, σ_{CS}^2 , of the coherent sum of the noises in the frequency bin of the power spectrum can be computed with help of equation (3.4.7) by multiplying the power spectral density with the sampling frequency, f_s , as

$$\sigma_{\text{CS}}^2 = \frac{f_s}{2} \tilde{S}_{\text{CS}}^2 \quad (4.2.24)$$

Hence, the power spectrum of the CS follows the same distribution, as the single channel signal. Only the effective amplitude of the CS and its variance, which were calculated in equations (4.2.22) and (4.2.24), need to be taken into account. The mean value of the

power in the power spectrum of the CS can be given, in analogy to equation (4.2.18) by

$$\mathbb{E}[\tilde{s}_{\text{CS}}^2(k)] = 2 \frac{\sigma_{\text{CS}}^2}{N_{\text{DFT}}} + \delta_{j,k} \frac{|A_{\text{CS}}|^2}{2}. \quad (4.2.25)$$

4.2.3. Distribution of Incoherently Summed Channels

While the distribution of the coherently combined data streams was shown to be normal distributed with a combined variance, this is not true for the distribution of the incoherent sum. Instead, the resulting random variable, which is the incoherent sum, will be a quadratic form of correlated Gaussian random variables. A closed form expression for the PDF could not be found, though there are a closed form solutions for the *moment generating function* and the *characteristic function* from which the PDF can in theory be calculated by taking its Fourier transform. An expression for the mean of the distribution exists and is given at the end of this section. A comprehensive treatment of quadratic forms in random variables can be found in [MP92].

In order to derive expressions for the incoherent sum of the channels the correlation of the noise sources between different channels has to be considered correctly. For the case of the noise sources considered here, shot noise and electronic noise are uncorrelated between the channels but laser intensity noise is fully correlated. In order to simplify the following derivation, the uncorrelated noise sources will be combined into the variable

$$(4.2.26)$$

where $I_{e,c}(n)$ and $I_{s,c}(n)$ are the shot noise and the electronic noise samples in channel c that are measured at time $t_n = n/f_s$. They are the coherent sums of the noise samples of the two hot redundant segments of a single channel. The one-sided power spectral density of $I_{\text{ucor},c}$ can be given in terms of the power spectral densities of the single segment electronic noise $\tilde{S}_{e,q}^2$ and shot noise, $\tilde{S}_{s,q}^2$, by

$$\tilde{S}_{\text{ucor},c}^2 = 2(\tilde{S}_{e,q}^2 + \tilde{S}_{s,q}^2). \quad (4.2.27)$$

Additionally, the coherent sum of the laser intensity noise for the two segments of a channel is defined as, $I_{i,c}$ which has a on-sided power spectral density of

$$\tilde{S}_{i,c}^2 = 4 \tilde{S}_{i,q}^2. \quad (4.2.28)$$

The single channel heterodyne signal using the above terminology is then

$$s_c(n) = A_c \cos\left(2\pi \frac{j}{N_{\text{DFT}}} n + \phi_c\right) + I_{\text{uCor},c}(n) + I_{i,c}(n). \quad (4.2.29)$$

Here again, as in the previous sections, A_c is the constant amplitude of the heterodyne signal, $f_j = j f_s / N_{\text{DFT}}$ with $j = 0, \dots, N_{\text{DFT}}/2 - 1$, ϕ_c is a constant phase. t_n are the times at which the signal is sampled $t_n = n/f_s$, with $n = 0, \dots, N_{\text{DFT}} - 1$. From the definition of the incoherent sum detector that was given in equation (4.1.12) one can define the incoherent sum of the channels (ICS) by

$$\tilde{s}_{\text{ICS}}^2(k) = \sum_{c=1}^{n_c} |\tilde{s}_c(k)|^2 = \sum_{c=1}^{n_c} \left| \frac{A_c e^{i\phi_c}}{\sqrt{2}} \delta_{j,k} + \tilde{I}_{\text{uCor},c}(k) + \tilde{I}_{i,c}(k) \right|^2. \quad (4.2.30)$$

To simplify the notation, the real and imaginary parts of the single channel heterodyne signal $\tilde{s}_c(k) = x_c(k) + i y_c(k)$ will be treated as separate normal random variables. The real part $x_c(k)$ and the imaginary part $y_c(k)$ are uncorrelated. The incoherent sum can then be written as

$$\tilde{s}_{\text{ICS}}^2(k) = \sum_{c=1}^{n_c} |x_c(k)|^2 + |y_c(k)|^2 = \mathbf{x}^t(k) \mathbf{\Lambda} \mathbf{x}(k) + \mathbf{y}^t(k) \mathbf{\Lambda} \mathbf{y}(k), \quad (4.2.31)$$

with $\mathbf{\Lambda} = \mathbf{1}_{n_c}$ being the $(n_c \times n_c)$ -identity matrix and $\mathbf{x}(k) = (x_1(k), \dots, x_{n_c}(k))^t$ as well as $\mathbf{y}(k) = (y_1(k), \dots, y_{n_c}(k))^t$ being the vectors of the real and imaginary parts of the Fourier transformed heterodyne signal in the channels.

The term on the left is a sum of two quadratic forms in the normal random variables $x_c(k)$ and $y_c(k)$ which could be combined into a single quadratic form. A closed form PDF is not available. However, the joined probability distribution function of the random vectors can be given as a multivariate normal distribution with mean vectors $\boldsymbol{\mu}_{x/y}(k) = (\mu_{x/y,1}(k), \dots, \mu_{x/y,n_c}(k))$ and variance-covariance matrices $\boldsymbol{\Sigma}_{x/y}$. The mean of a quadratic form in random variables can generally be given as [MP92]

$$\mathbb{E}[\mathbf{x}^t \mathbf{\Lambda} \mathbf{x}] = \text{tr}(\mathbf{\Lambda} \boldsymbol{\Sigma}_x) + \boldsymbol{\mu}_x^t \mathbf{\Lambda} \boldsymbol{\mu}_x. \quad (4.2.32)$$

The variance-covariance matrices, $\boldsymbol{\Sigma}_{x/y}$, are identical for the real and the imaginary part, such that here the definition for the real part is given as an example. The element in the c_1 -th row and c_2 -th column of the variance-covariance matrix for the random vector

\mathbf{x} is defined as

$$(\boldsymbol{\Sigma}_x)_{c_1, c_2} = \text{Cov}[x_{c_1}, x_{c_2}] = \text{E}[(x_{c_1} - \mu_{x, c_1})(x_{c_2} - \mu_{x, c_2})]. \quad (4.2.33)$$

Inserting the definitions of equations (4.2.29) and (4.2.26), one can easily calculate the variance-covariance matrix to be

$$(\boldsymbol{\sigma}_{x/y})_{c_1, c_2} = \frac{1}{N_{\text{DFT}}} (\sigma_{\text{ucor}, c}^2 \delta_{c_1, c_2} + \sigma_{i, c}^2). \quad (4.2.34)$$

Here, δ is the Kronecker delta and the variances of the uncorrelated noise sources, $\sigma_{\text{ucor}, c}^2$, and of the laser intensity noise, $\sigma_{i, c}$, are defined in analogy to equation (4.2.24) by

$$\sigma_{\text{ucor}, c}^2 = \frac{f_s}{2} \tilde{S}_{\text{ucor}, c}^2 \quad \text{and} \quad \sigma_{i, c}^2 = \frac{f_s}{2} \tilde{S}_{i, c}^2. \quad (4.2.35)$$

Finally, the mean of the incoherent sum can be formulated with the above calculations

$$\text{E}[\tilde{s}_{\text{ICS}}^2(k)] = \text{E}[\mathbf{x}^t(k) \boldsymbol{\Lambda} \mathbf{x}(k) + \mathbf{y}^t(k) \boldsymbol{\Lambda} \mathbf{y}(k)] \quad (4.2.36)$$

$$= \text{tr}(\boldsymbol{\Sigma}_x) + \text{tr}(\boldsymbol{\Sigma}_y) + |\boldsymbol{\mu}_x|^2 + |\boldsymbol{\mu}_y|^2 \quad (4.2.37)$$

$$= \frac{2 n_c}{N_{\text{DFT}}} (\sigma_{\text{ucor}, c}^2 + \sigma_{\text{cor}, c}^2) + \delta_{j, k} \frac{1}{2} \sum_{c=1}^{n_c} |A_c|^2. \quad (4.2.38)$$

The lack of the actual form of the PDF makes it difficult to actually comment on the detection and false alarm probability of the incoherent sum of the channels. However, for high SNR the mean value of the power in a frequency bin for the ICS combination of the channels is approximated by

$$\text{E}[\tilde{s}_{\text{ICS}}^2(k)] \stackrel{\text{SNR} \gg 1}{\approx} \delta_{j, k} \frac{A_{\text{ICS}}^2}{2}. \quad (4.2.39)$$

The amplitude of the ICS combination, A_{ICS} , that is used in the last line, was defined by

$$A_{\text{ICS}} = \sqrt{\sum_{c=1}^{n_c} |A_c|^2}. \quad (4.2.40)$$

4.3. Distribution of the Detector Output

In the first part of this section, the probability distribution for the detector output, \mathcal{D} , is derived. An analytical expressions for the case of the detector that uses the coherent sum of the channels, \mathcal{D}_{CS} , is given. For the detector output of the incoherent sum \mathcal{D}_{ICS} no analytical distribution could be found. The expressions for the detector output were defined in equations (4.1.11) and (4.1.12).

In the second part of this section, the noise root mean square (RMS) of the detector output is derived, for the case of the coherent and incoherent sum. This, at the same time, yields the noise RMS of the maximum of the detector output over a complete line-of-sight calibration scan.

In this section it is assumed that only the lower half of the frequency bins are considered, as the DFT of length N_{DFT} of a real valued time series, has the following symmetry:

$$\tilde{s}(k) = \tilde{s}^*(N_{\text{DFT}} - k), \quad (4.3.1)$$

where $\tilde{s}^*(k)$ is the complex conjugate of $\tilde{s}(k)$. Hence, the upper half of the DFT of a real input signal does not contain additional information.

Furthermore, the veto of certain frequency bins has to be taken into account. However, in this thesis the frequency response of the photodiode is assumed to be flat and the noise sources were introduced as white such that the signal amplitude and the noise power in the DFT are independent of the index of the frequency bin. The results derived in the following section will only depend on the number of the frequency bins that are not vetoed. The number of non-vetoed frequency bins will be denoted by N_{b} .

4.3.1. Probability Distribution of the Detector Output

In this section the general form of the PDF of the detector output is given and subsequently the expression for the case of the coherent sum of the channels is derived. The value of the detector output \mathcal{D} is the maximum power in any of the non-vetoed N_{b} frequency bins for which expressions are given in equations (4.1.10) to (4.1.12). Hence, the PDF of the detector output is the PDF of the maximum power in these N_{b} frequency bins. A general expression for the PDF of the detector output $p_{\mathcal{D}}(y)$ can be derived from its CDF, $P_{\mathcal{D}}(y)$, by

$$p_{\mathcal{D}}(y) = \frac{d}{dy} P_{\mathcal{D}}(y). \quad (4.3.2)$$

The CDF of the detector output $P_{\mathcal{D}}(y)$, is the probability that the value of the detector output is less than or equal to y ,

$$P_{\mathcal{D}}(y) = P(\mathcal{D} \leq y). \quad (4.3.3)$$

For the case considered here, this is equal to the probability that the power in all frequency bins of the power spectrum is less than or equal to y , i.e.

$$P_{\mathcal{D}}(y) = P(\tilde{s}^2(k_1) \leq y \wedge \tilde{s}^2(k_2) \leq y \wedge \cdots \wedge \tilde{s}^2(k_{N_b}) \leq y), \quad (4.3.4)$$

where $\tilde{s}^2(k_i)$ is the k_i -th frequency bin of the power spectrum of either the single channel, the coherent sum or the incoherent sum and i indexes the non-vetoed frequency bins. As it was assumed that the noise in the frequency bins is independently distributed, the joined probability which is defined in equation (4.3.4) can be written as a product of the CDFs of the individual frequency bins as

$$P_{\mathcal{D}}(y) = \prod_{i=1}^{N_b} P(\tilde{s}^2(k_i) \leq y). \quad (4.3.5)$$

The general result of the CDF of the detector output as defined by equation (4.3.5) can be used to determine the CDF of the detector for the case of the two hypotheses, \mathcal{H}_0 and \mathcal{H}_1 . The two hypotheses were defined in equation (4.1.8).

At first, the distribution of the detector under the null hypothesis, \mathcal{H}_0 , is derived. As it was assumed that the noise sources are identical and independently distributed, equation (4.3.5) can be simplified to

$$P_{\mathcal{D}}(y; \mathcal{H}_0) = P_n(\tilde{s}^2(k) \leq y)^{N_b}. \quad (4.3.6)$$

Here $P_n(\tilde{s}^2(k) \leq y)$ is the cumulative distribution function of the k -th frequency bin, while k just stands representative for any of the N_b frequency bins. The subscript n is used to indicate that the frequency bin contains only noise.

If equation (4.3.6) is inserted into equation (4.3.2) the PDF for the detector output is obtained with the the PDF of the power in a single frequency bin, $p_n(y)$, as

$$p_{\mathcal{D}}(y; \mathcal{H}_0) = \frac{d}{dy} P_n(\tilde{s}^2(k) \leq y)^{N_b} = N_b p_n(y) P_n(\tilde{s}^2(k) \leq y)^{N_b-1}. \quad (4.3.7)$$

Equation (4.3.7) is valid for any of the signal combinations. However, for the case of the incoherent sum an analytic expression for the PDF of a single frequency could not be

found. For the coherent sum of the channels the solution can be given explicitly with the PDF presented in equation (4.2.11) and the variance of the coherent sum of the channels that was defined in equation (4.2.24).

The CDF of the power in the single channel of the coherent sum of the channels for the case of negligible heterodyne amplitude can be computed by

$$P_{\text{CS},n}(y) = \int_0^y p_{\text{CS},n}(y) dy = 1 - \exp\left(-\frac{N_{\text{DFT}}}{2\sigma_{\text{CS}}^2} y\right). \quad (4.3.8)$$

And the distribution of the detector output for the case of the coherent sum of the channels for negligible heterodyne amplitude can be given as

$$p_{\mathcal{D}_{\text{CS}}}(y; \mathcal{H}_0) = N_b \frac{N_{\text{DFT}}}{2\sigma_{\text{CS}}^2} \exp\left(-\frac{N_{\text{DFT}}}{2\sigma_{\text{CS}}^2} y\right) \left[1 - \exp\left(-\frac{N_{\text{DFT}}}{2\sigma_{\text{CS}}^2} y\right)\right]^{N_b-1}. \quad (4.3.9)$$

The PDF of the detector output for the case of the alternative hypothesis, \mathcal{H}_1 , can be derived in analogy to equation (4.3.4). The difference now is that one of the frequency bins additionally contains the heterodyne signal and thus the power in the frequency bin is distributed according to a noncentral χ^2 -distribution. The PDF for the case of the single channel was given in equation (4.2.17). If the heterodyne amplitude and noise variance for the single channel are exchanged for the heterodyne amplitude and noise variance of the coherent sum, which were given in equations (4.2.22) and (4.2.24), the noncentrality parameter, as defined by equation (4.2.15), can be defined for the CS by

$$\lambda_{\text{CS}} = \frac{\sqrt{N_{\text{DFT}}}}{\sigma_{\text{CS}}} \frac{|A_{\text{CS}}|}{\sqrt{2}}. \quad (4.3.10)$$

The CDF of the power in a single frequency bin of the coherent sum of the channels is then given by

$$P_{\text{CS},s}(y) := \int_0^y p(y; 2, \lambda_{\text{CS}}, \sigma_{\text{CS}}^2/N_{\text{DFT}}) dy. \quad (4.3.11)$$

And with this the CDF of the output of the coherent sum detector for the case of a heterodyne signal in one frequency bin, can be given as

$$P_{\mathcal{D}_{\text{CS}}}(y; \mathcal{H}_1) = P_{\text{CS},s}(y) P_{\text{CS},n}(y)^{N_b-1}. \quad (4.3.12)$$

The PDF of the detector output can be computed with help of equation (4.3.2) and the

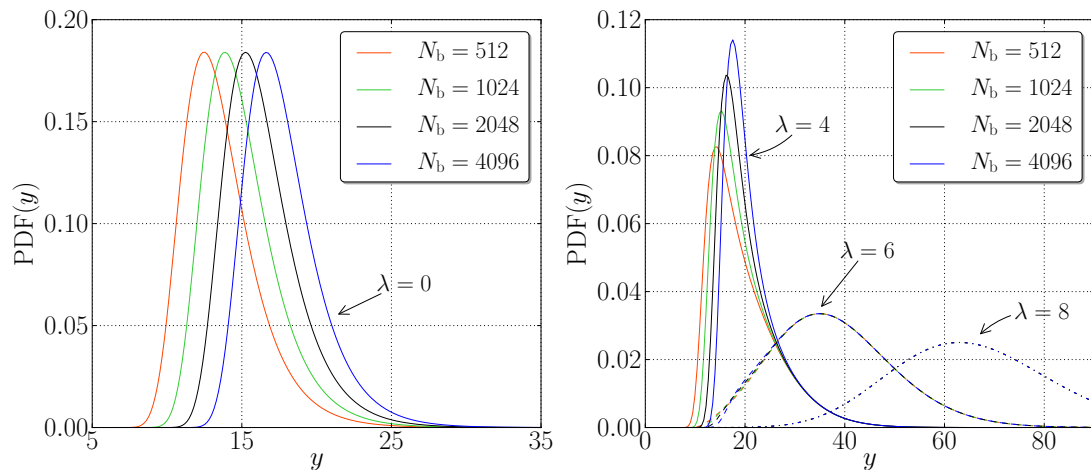


Figure 4.5.: Left: PDF of the maximum found in N_b frequency bins if the amplitude of the heterodyne signal is zero, \mathcal{H}_0 , for the case of the coherent sum or incoherent sum detector. The distribution is given in equation (4.3.9). Right: PDF of the maximum found in N_b frequency bins for the case of a heterodyne signal in one of the frequency bins, \mathcal{H}_1 . The distribution in the frequency bin is shown for different noncentrality parameters of $\lambda = 4, 6, 8$. It is determined by equation (4.3.14). For both plots $\sigma^2/N_{\text{DFT}} = 1$.

PDF of the CS detector output $p_{\text{CS},s}(y) = p(y; 2, \lambda_{\text{CS}}, \sigma_{\text{CS}}^2/N_{\text{DFT}})$, as

$$p_{\mathcal{D}_{\text{CS}}}(y; \mathcal{H}_1) = \frac{d}{dy} [P_{\text{CS},s}(y) P_{\text{CS},n}(y)^{N_b-1}] \quad (4.3.13)$$

$$= p_{\text{CS},s}(y) P_{\text{CS},n}(y)^{N_b-1} + (N_b - 1) p_{\text{CS},n}(y) P_{\text{CS},s}(y) P_{\text{CS},n}(y)^{N_b-2}. \quad (4.3.14)$$

All of the terms occurring in the PDF of the detector output above are already known except for the CDF for the frequency bin containing the heterodyne signal, $P_{\text{CS},s}(y)$. The integral over the PDF cannot be solved by elementary functions, but it can be defined in terms of the Marcum Q-function which is given in the appendix in equation (B.1.6), as

$$P_{\text{CS},s}(y) = 1 - \frac{N_{\text{DFT}}}{\sigma_{\text{CS}}^2} Q_1 \left(\lambda_{\text{CS}}, \sqrt{\frac{N_{\text{DFT}}}{\sigma_{\text{CS}}^2} y} \right). \quad (4.3.15)$$

The left plot in Figure 4.5 shows the PDF of the detector output for different values of N_b , for the case that the input signal only consists of noise. The right plot in Figure 4.5 compares the PDF of the detector output for the case that a heterodyne signal is present

in one of the frequency bins. The PDF is shown for different values of the noncentrality parameter and the number of non-vetoed frequency bins, N_b . While the peak value of the distribution for the case of \mathcal{H}_0 shifts to higher values if the number of non-vetoed frequency bins is increased, it is constant for the case of \mathcal{H}_1 and a high SNR or λ , respectively.

The distributions here were derived for the case of the coherent sum detector. However, for the case of a heterodyne signal with high SNR, the detector output for the ICS will likely be drawn from the frequency bin that contains the heterodyne signal. The general observation that the signal distribution is constant for high SNR input signals is thus also true for the ICS of the channels.

4.3.2. Noise RMS of the Detector Output

During the initial line-of-sight calibration scan, the maximum detector output that occurs over the course of a complete scan is used to estimate the initial alignment and the frequency bias. The detector output is generated at a rate of $\delta f_{\text{DFT}} = f_s/N_{\text{DFT}}$ which is the time that is necessary to sample the data for a complete FFT. If the subsequent detector outputs during the line-of-sight calibration scan are denoted by \mathcal{D}_i , where $i = 1, \dots, N_e$ with the maximum number of estimates of N_e , then the maximum detector output $\hat{\mathcal{D}}$ can be defined as

$$\hat{\mathcal{D}} := \max(\mathcal{D}_1, \mathcal{D}_2, \dots, \mathcal{D}_{N_e}). \quad (4.3.16)$$

In this section, expressions for the RMS of $\hat{\mathcal{D}}$ under the null hypothesis are given. At first, an analytical expression for the case of the CS is derived. The detector returns the maximum power of N_b computed frequency bins and during the line-of-sight calibration the maximum of N_e detector outputs is determined. Under the assumption that the noise is identically and independently distributed during the complete line-of-sight calibration scan, the PDF of $\hat{\mathcal{D}}$ is equivalent to the PDF of the detector output under the null hypothesis $p_{\mathcal{D}}(y; \mathcal{H}_0)$, which was given in equation (4.3.7). The only difference is that the number of frequency bins over which the maximum is determined is equal to $N_t = N_e N_b$ such that the PDF of the maximum detector output for the case of the coherent sum, $\hat{\mathcal{D}}_{\text{CS}}$, can be given as

$$p_{\hat{\mathcal{D}}_{\text{CS}}}(y, N_t; \mathcal{H}_0) = N_t \frac{N_{\text{DFT}}}{2\sigma_{\text{CS}}^2} \exp\left(-\frac{N_{\text{DFT}}}{2\sigma_{\text{CS}}^2} y\right) \left[1 - \exp\left(-\frac{N_{\text{DFT}}}{2\sigma_{\text{CS}}^2} y\right)\right]^{N_t-1}. \quad (4.3.17)$$

The RMS of the detector output under, \mathcal{H}_0 , can be defined as the square root of the second raw moment of the above PDF,

$$\text{RMS}[\hat{\mathcal{D}}_{\text{CS}}](N_t) = \left[\int_0^\infty y^2 p_{\hat{\mathcal{D}}_{\text{CS}}}(y, N_t; \mathcal{H}_0) dy \right]^{1/2}. \quad (4.3.18)$$

The integral in equation (4.3.18) can be calculated explicitly. For $N_t \gg 1$ a simple approximation can be given that is suitable for calculating the RMS of the maximum detector output for arbitrary N_t . Introducing the definition

$$\tilde{\sigma}_{\text{CS}}^2 = \frac{\sigma_{\text{CS}}^2}{N_{\text{DFT}}}, \quad (4.3.19)$$

the noise RMS of the maximum detector output can be given by

$$\text{RMS}[\hat{\mathcal{D}}_{\text{CS}}](N_t) \approx \tilde{\sigma}_{\text{CS}}^2 \left[\frac{2}{3} \pi^2 + 4(\gamma + \ln N_t)^2 \right]^{\frac{1}{2}} \quad (4.3.20)$$

Here, γ is the *Euler-Mascheroni constant*. The first few digits can be given by $\gamma \approx 0.57722$.

Figure 4.6 shows a comparison between the approximation given in equation (4.3.20) and numerically computed results for some values of N_t and $\tilde{\sigma}_{\text{CS}}^2 = 1$. The numerical results have been computed from pseudo-random numbers generated by the MT19937 algorithm of the GSL library [MN98]. The agreement between the analytical formula and the numerical values is excellent over the whole range of considered values of N_t . For the case of the ICS of the channels the power in a single frequency bin is distributed according to a quadratic form in correlated Gaussian random variables and an explicit form of the PDF could not be found.

In order to, nevertheless, deduce a functional dependence between N_t and the RMS of the maximum detector output, the expression that was obtained for the CS, was fitted to numerically computed data from generated pseudo-random numbers. To carry out the fit, a specific ratio of the covariance to the variance has to be assumed. Here, a hot redundant pair of QPDs is assumed and the ratio between the covariance and variance in a single channel was chosen to,

$$\frac{\tilde{\sigma}_{i,c}^2}{\tilde{\sigma}_{i,c}^2 + \tilde{\sigma}_{\text{ucor},c}^2} = 0.30.$$

This corresponds to the case of GRACE Follow-On with the current estimates of noise levels. The result is plotted in Figure 4.6 which shows a comparison between the fit and

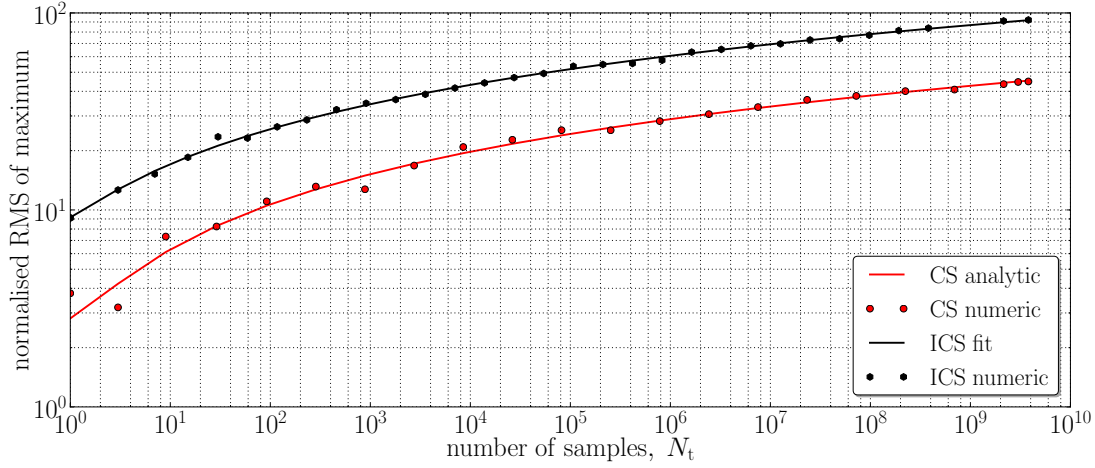


Figure 4.6.: Normalised noise RMS of the maximum of N_t noise samples of the CS and ICS of four channels. The ICS RMS is normalised by the variance of the real part of the noise in a frequency bin of the amplitude spectrum of a single channel. It is assumed that the ratio of the covariance between the noise of two different channels and the variance is equal to 0.30. The CS RMS is normalised to $\tilde{\sigma}_{CS}^2$ which is given in equation (4.3.19). The analytic expression and the fit are given in equations (4.3.20) and (4.3.22). The numerical RMS values are calculated by generating pseudo-random numbers with the MT19937 algorithm [MN98].

numerically computed data of the normalised noise RMS of the detector output, for the case of the incoherent sum combination. The RMS is normalised by the variance in a single channel

$$\tilde{\sigma}_c^2 = \frac{\tilde{\sigma}_c^2}{N_{\text{DFT}}} = \frac{\sigma_{\text{uor},c}^2 + \sigma_{\text{i},c}^2}{N_{\text{DFT}}}. \quad (4.3.21)$$

The fit function is given by

$$\text{RMS}[\hat{\mathcal{D}}_{\text{ICS}}](N_t) \approx \tilde{\sigma}_c^2 \left([5.89 + 14.6(\gamma + \ln N_t)^2]^{\frac{1}{2}} + 5.90 \right). \quad (4.3.22)$$

The analytic expressions for the RMS of the returned maximum can be used to find the RMS of the detector for an initial line-of-sight calibration scan. The time for a complete calibration scan is given by the time for a complete scan of the four dimensional spatial uncertainty space, T_S , multiplied by the number of scan points in the frequency scan, N_f . The rate at which new detector outputs are generated is equal to the FFT bandwidth $\delta f_{\text{DFT}} = f_s/N_{\text{DFT}}$, such that the total number of calculated detector outputs, N_e , is

given by

$$N_e = T_S N_f \frac{f_s}{N_{\text{DFT}}}. \quad (4.3.23)$$

The total number of processed frequency bins, from which the maximum is found is given by $N_t = N_b N_e$. For the following example a sampling frequency of $f_s = 38$ MHz, a DFT size of $N_{\text{DFT}} = 4096$ is assumed and only the lower half of the frequency bins are used $N_b = 2048$. If a complete four-dimensional spatial scan takes about $T_S = 200$ s, then for a single spatial scan, $N_f = 1$, the number of processed DFT frequency bins is $N_t = 3.8 \cdot 10^9$. This corresponds to the last calculated value in the plot of Figure 4.6.

The brute force computation of the random numbers for the ICS combination took about 3.3 h on a 16 core Intel Xeon E5620 for the CS combination about 0.5 h for the case of $N_t = 3.8 \cdot 10^9$. Since the computation time is linear in N_t , calculating the RMS for the complete calibration with 100 frequency scan points is impractical. However, with help of the analytical expressions for the two cases the RMS can be computed. Table 4.1 shows the normalised values computed with equation (4.3.20) and (4.3.22). In order to compute the specific RMS for given noise sources, the normalised values in Table 4.1 have to be multiplied by the variance of the coherent sum $\tilde{\sigma}_{\text{CS}}^2$ defined by equation (4.3.19) or respectively the variance of the noise in a channel $\tilde{\sigma}_c^2$, which was defined in equation (4.1.3), if the ICS noise RMS should be computed.

Table 4.1.: Normalised noise RMS of the maximum detector output, \hat{D} , for the case of the CS and ICS of the channels. The total number of processed DFT bins, N_t , is computed from the total scan time with equation (4.3.23) under the assumption that $f_s = 38$ MHz, $N_{\text{DFT}} = 4096$ and $N_b = 2048$.

Item			
Sum Type	Total Scan Time, $N_f T_S / \text{s}$	N_t	normalised RMS
CS	20 000	$3.8 \cdot 10^{11}$	54.5
	200	$3.8 \cdot 10^9$	45.3
	$108 \cdot 10^{-6}$	2 048	16.6
	$53.9 \cdot 10^{-6}$	1 024	15.2
ICS	20 000	$3.8 \cdot 10^{11}$	109
	200	$3.8 \cdot 10^9$	91.9
	$108 \cdot 10^{-6}$	2 048	37.3
	$53.9 \cdot 10^{-6}$	1 024	34.6

4.4. Distribution of the Detector Output for Time Dependent Frequency

In the last sections, rigid assumptions were imposed on the signal frequency to simplify the derivation of the distributions of the detector output. Here, the frequency will be freely varied within the bandwidth of the FFT. The results that are presented in this section are obtained by means of numerical computations of power spectra.

At first the frequency will be assumed to be constant. Thereafter, the effect of frequency noise on the distribution of the detector output will be investigated. Finally, the effect of a constant rate frequency sweep on the detector distribution will be discussed. The analysis is carried out for the distribution of the CS detector output, though the general conclusions are valid for the ICS combination as well.

4.4.1. Constant Arbitrary Frequency

In general, the frequency will not be constant but vary due to frequency noise or a linear frequency sweep that is used to scan the frequency over the frequency uncertainty interval. If, however, the variation of the frequency over one FFT is small compared to the FFT bin width, the frequency can be treated as constant. The difference to the former sections is, that the frequency can have an arbitrary offset from one of the central bin frequencies of the FFT. This case will be studied here in more detail.

If the frequency of the heterodyne signal is not fixed to one of the central bin frequencies, but is allowed to have any value within the considered frequency band, part of the signal power will be distributed over the complete FFT bandwidth, however, most of the power will be shared between two neighbouring bins. Thus, the signal power in a single frequency bin will decrease if the signal frequency is different from one of the central bin frequencies. This effect is called *scalping loss* [Har78]. The size of the scalping loss is depending on the window function applied to the data before calculating the spectrum [SCMC99]. For the following analysis, a rectangular window is assumed. In the following, the frequency of the heterodyne signal will be written as

$$f_b = (j + \delta b) \frac{f_s}{N_{\text{DFT}}}, \quad (4.4.1)$$

where j is the index of one of the frequency bins and δb is the offset of the signal frequency from the central frequency of the j -th bin in terms of the bin width. The width of the frequency bin in the FFT is given by the ratio between the sampling frequency f_s and the size of the FFT, N_{DFT} . The n -th sample of the time series of the coherent sum

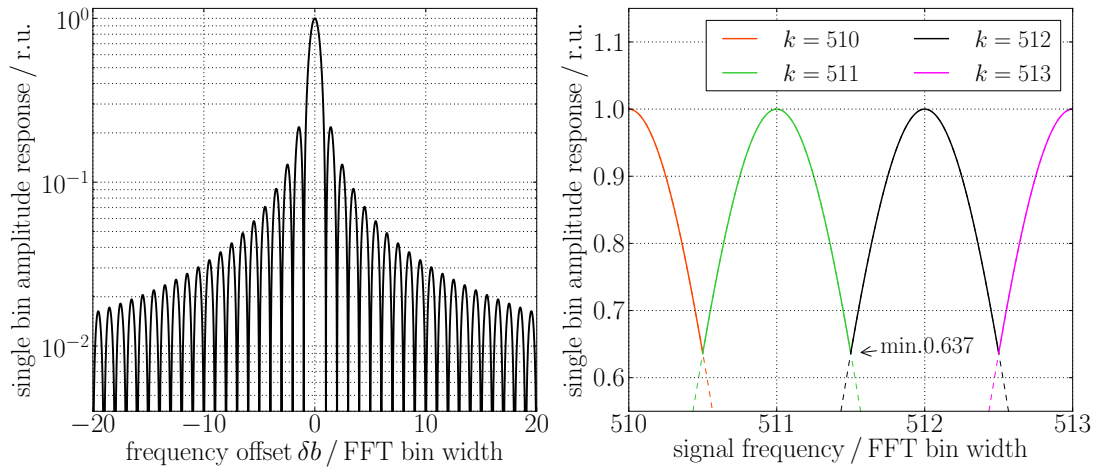


Figure 4.7.: Left: Normalised amplitude response of a DFT as a function of the offset from the central frequency, δb . The normalised amplitude response was defined in equation (4.4.4). Right: Normalised amplitude response of adjacent frequency bins. The envelop of the joined response of the frequency bins gives the amplitude response for an arbitrary frequency of the heterodyne signal. The minimum amplitude response occurs if the signal frequency is halfway between two bins. Here the amplitude is only about 64 % of the maximum amplitude.

signal $s_{CS}(n)$ can then be written as

$$s_{CS}(n) = \sum_{c=1}^{n_c} A_{CS} \cos \left(2\pi \frac{j + \delta b}{N_{DFT}} n + \phi_c \right) + I_{CS}(n). \quad (4.4.2)$$

The DFT of a sinusoidal signal with frequency, $f_b = (j + \delta b)f_s/N_{DFT}$, can be calculated analytically. Moreover, it is possible to define a scaling function $l(k, j + \delta b, N_{DFT})$, that describes the response of a DFT of size N_{DFT} to that sinusoidal signal, as a function of the frequency bin index k . For the case of $\delta b = 0$, the DFT of the coherent sum was given in equation (4.2.21). However, for the case of $\delta b \neq 0$ the DFT yields

$$\tilde{s}_{CS}(k) \approx \frac{A_{CS}}{\sqrt{2}} l(k, j + \delta b, N_{DFT}) + \tilde{I}_{CS}(k). \quad (4.4.3)$$

It is safe to assume that the frequency bin index k is not close to the DC bin, $k = 0$, or the Nyquist bin, $k = N_{DFT}/2$, as those bins will be vetoed in the detection algorithm. For this case the scaling function can be approximated by

$$l(k, j + \delta b, N_{DFT}) \approx \frac{1}{N_{DFT}} \left(\frac{e^{-2\pi i(k-(j+\delta b))} - 1}{e^{2\pi i(k-(j+\delta b))/N_{DFT}} - 1} \right). \quad (4.4.4)$$

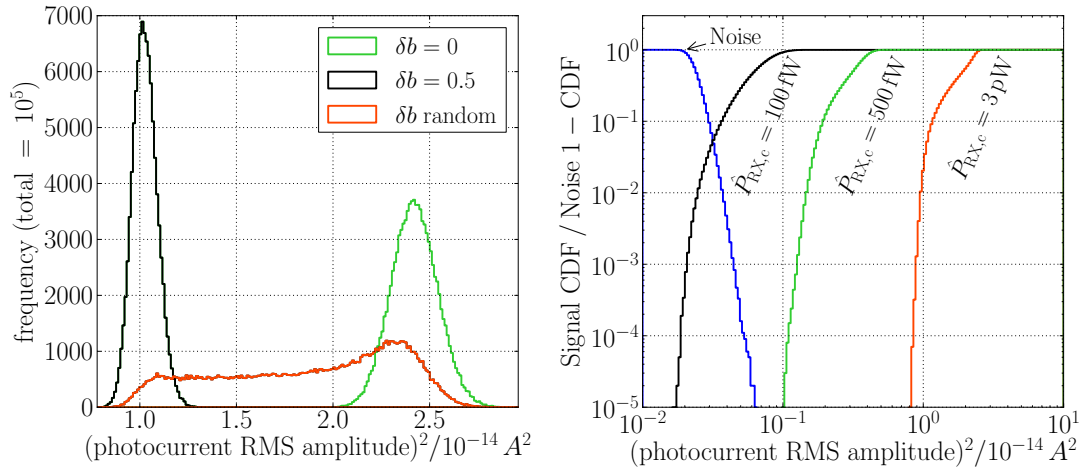


Figure 4.8.: Left: Histogram of the coherent sum detector output, \mathcal{D}_{CS} , for the case that the frequency of the signal is chosen randomly for each DFT. As a comparison the distributions for fixed frequencies with zero offset from the bin centre and with $\delta b = 0.5$ are shown. Right: CDF of the detector output under the hypothesis of a present heterodyne signal, \mathcal{H}_1 , for three values of the effective received power per a channel. Additionally, the right tail probability of the detector output under the null hypothesis \mathcal{H}_0 , i.e. the signal amplitude is zero, is shown. The distributions are well separated for 3 pW per channel effective received power. The other parameters that were used to compute the distributions are: $N_{\text{DFT}} = 4096$, $N_b = 2048$, $P_{\text{LO},c} = 700 \mu\text{W}$.

The left plot in Figure 4.7 shows the scaling function, or *normalised amplitude response*, of the DFT as a function of the frequency offset from the central bin frequency. The amplitude response is maximal for zero frequency offset from the central frequency and drops quickly for increasing offset. The right plot in Figure 4.7, shows the overlapping response of adjacent frequency bins. The envelop of the response of all frequency bins determines the amplitude response of the DFT for a given frequency.

For the case that the frequency is in the middle between two bins, $\delta b = 1/2$, the response is minimal and the two neighbouring bins will contain equal power. Hence, the detector output will vary For a constant amplitude signal that varies in frequency.

The left plot in Figure 4.8 shows numerically computed histograms of the maximum power in an FFT if the signal frequency is drawn from a uniform distribution over the considered frequency band. The resulting distribution is compared to the distribution for a frequency fixed to the centre of a bin and in the middle between two bins. The distribution of the maximum power is much wider if the frequency of the signal is varied than for the case of a fixed frequency. The difference between the highest and lowest sample in the histogram is approximately equal to the scalloping loss, that can be seen

in the right plot of Figure 4.7.

The right plot in Figure 4.8 shows the CDF of the coherent sum detector output for three values of the effective received power in a channel. The effective received power was defined in equation (3.3.11) as the product of the received power that reaches the photodiodes and the heterodyne efficiency. This is compared to the right tail probability (RTP) of the distribution of the detector output for the case of negligible heterodyne amplitude, \mathcal{H}_0 . The RTP is defined by $\text{RTP}(x) = 1 - \text{CDF}(x)$.

The CDF of the detector output under \mathcal{H}_1 can be interpreted as the probability of missed detections if the horizontal axis is interpreted as the threshold above which a detection is claimed. The RTP of the detector output under \mathcal{H}_0 is the probability of false alarm if the horizontal axis is the detection threshold.

For the case of only $\hat{P}_{\text{RX},c} = 100$ fW effective received power per channel, a compromise has to be made by either accepting false alarms with high probability or sacrificing some of the possible detections. For example if the threshold is set at $4 \cdot 10^{-16} \text{ A}^2$ the false alarm probability is still around 1 % but the probability to miss a detection is already 10 %. For the case of $\hat{P}_{\text{RX},c} = 3$ pW effective received power per channel, the distributions are well separated and it is possible to reduce false alarms to a negligible amount, whereas the probability of detection is kept at almost 100 %.

4.4.2. Distribution of the Detector Output with Frequency Noise

The last section discussed the distribution of the coherent sum detector output for the case of a constant arbitrary frequency. This assumption holds if the frequency variations over a DFT are smaller than the width of the frequency bin $\delta f_{\text{DFT}} = f_s/N_{\text{DFT}}$. If the variations are larger, e.g. due to frequency noise of the free-running laser or a frequency sweep, this assumption does not hold anymore.

This section discusses the change of the distributions for different FFT lengths, N_{DFT} , if the beatnote frequency varies due to frequency noise. Increasing the length of the DFT decreases the width of the frequency bins, δf_{DFT} , as can be seen by

$$\delta f_{\text{DFT}} = \frac{f_s}{N_{\text{DFT}}}. \quad (4.4.5)$$

On the one hand, decreasing the frequency bin width increases the SNR for a heterodyne signal for the case of a constant frequency, as the variance of the noise $\tilde{\sigma}_{\text{CS}}^2$ in the frequency bins is proportional to δf_{DFT} . This is generally true but here given explicitly

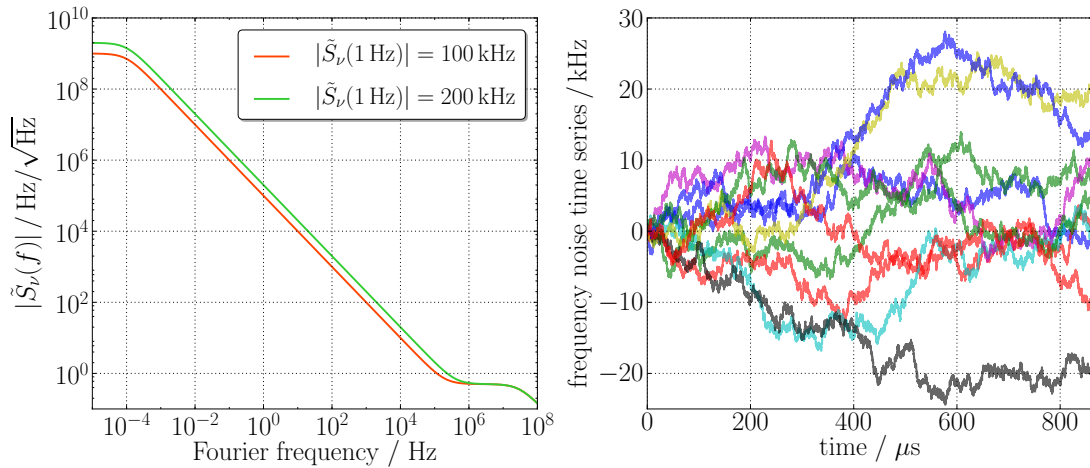


Figure 4.9.: Left: Amplitude spectral density of the frequency noise with shape defined by equation (4.4.7) for two different amplitudes at 1 Hz. Right: A set of computed time series, for the case of $|\tilde{S}_\nu(1 \text{ Hz})| = 200 \text{ kHz}$.

for the coherent sum of the channels. Hence,

$$\tilde{\sigma}_{\text{CS}}^2 = \frac{\delta f_{\text{DFT}}}{2} \tilde{S}_{\text{CS}}^2 = \frac{f_s \tilde{S}_{\text{CS}}^2}{2N_{\text{DFT}}}, \quad (4.4.6)$$

where \tilde{S}_{CS}^2 is the one-sided power spectral density of the noise in the coherent sum of the channels, which was defined in equation (4.2.23). On the other hand, the SNR is decreased, if the bin width is smaller than the variation of the beatnote frequency due to frequency noise which would distribute the signal power over several frequency bins.

The actual shape of the frequency noise power spectral density will strongly depend on the type of laser used. However, the requirements set on the laser performance in terms of frequency and amplitude noise, as well as its applicability in space missions limits the range of possible laser types. The most promising candidate for a mission in the near future is a Nd:YAG *non-planar ring oscillator* (NPRO) [KB85]. The Nd:YAG NPRO has been extensively studied as light source for the Laser Interferometer Space Antenna (LISA) by Troebs et. al. [TeF05, TeF⁺06, TBM⁺09] and for the use in ground based gravitational wave detectors such as *GEO600*, *Laser Interferometer Gravitational-Wave Observatory* (LIGO) by Willke, Heurs and others [WBD⁺00, HQW⁺04]. Numata et al. investigated the noise behaviour of several laser types that can be used in laser interferometer space missions [NCKS10, NC12].

The frequency noise of the Nd:YAG NPRO approximately follows a $1/f$ -slope for a range of frequencies which is here assumed from $100 \mu\text{Hz}$ up to frequencies of about

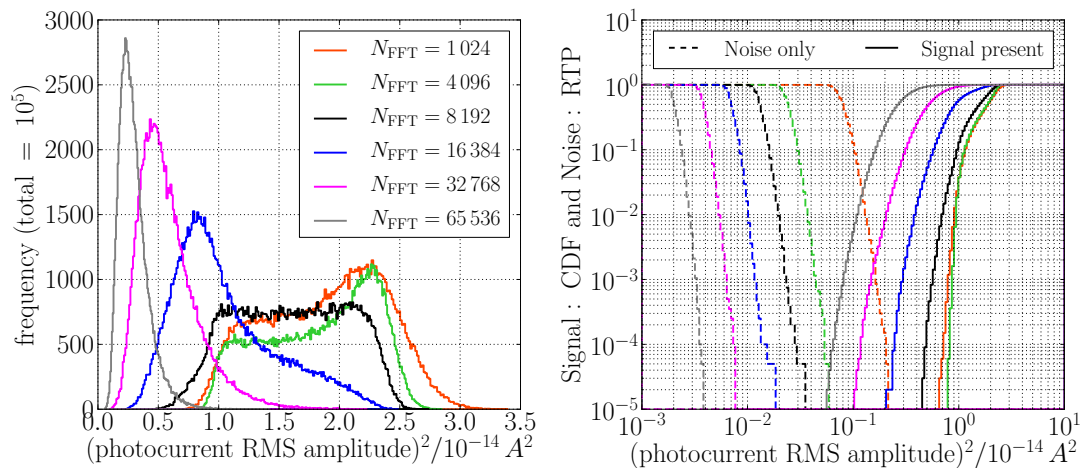


Figure 4.10.: Left: Histogram of the detector output for a heterodyne signal with effective received power of $\hat{P}_{\text{RX}} = 3$ pW per channel. The distribution is compared for different sample sizes of the DFT. Right: Cumulative distribution function of the distribution of the detector output under hypothesis \mathcal{H}_1 , compared to the right tail probability of the distribution for the case of only noise, \mathcal{H}_0 . Here frequency noise with $|\tilde{S}_\nu(f = 1 \text{ Hz})| = 200$ kHz was used.

100 kHz. Measurements by Kullmann [Kul12] show that the frequency noise flattens out at a level of $0.5 \text{ Hz}/\sqrt{\text{Hz}}$ for frequencies above 100 kHz, up to the end of the measurement band of 20 MHz. However, to allow for some margin on the performance the frequency noise level in the following analysis is assumed to have a worst case amplitude spectral density. The amplitude spectral density of the measured frequency noise $\tilde{S}_\nu(f)$ is assumed to have the following shape:

$$|\tilde{S}_\nu(f)| = c \sqrt{\left(1 + \frac{f^2}{f_1^2}\right)^{-1} \left(1 + \frac{f^2}{f_2^2}\right) \left(1 + \frac{f^2}{f_3^2}\right)^{-1}} \quad (4.4.7)$$

where the pole frequencies are $f_1 = 100 \mu\text{Hz}$ and $f_3 = 30 \text{ MHz}$. The frequency of the zero, f_2 , is chosen such that for a given factor c , a noise floor of $0.5 \text{ Hz}/\sqrt{\text{Hz}}$ is created, as was measured in [Kul12]. The factor c is adapted to get $|\tilde{S}_\nu(f = 1 \text{ Hz})| = 200$ kHz for the first and $|\tilde{S}_\nu(f = 1 \text{ Hz})| = 100$ kHz for the second case. The two resulting curves are shown in the left plot of Figure 4.9.

To quantitatively estimate the effect of the frequency noise on the distribution of the detector output a numerical signal generator was developed that computes the signal

with realistic amplitudes and noise sources as defined by:

$$s_{\text{CS}}(n) = A_{\text{CS}} \cos \left(2\pi \frac{f_{\text{b}}}{f_{\text{s}}} n + \frac{2\pi}{f_{\text{s}}} \sum_{i=0}^n \delta f(i) + \phi_{\text{CS}} \right) + I_{\text{CS}}(n), \quad (4.4.8)$$

where A_{CS} is the amplitude and ϕ_{CS} the phase of the coherent sum heterodyne signal, f_{b} is the beatnote frequency and $\delta f(n)$ is the time series of the frequency noise. The time series of the additive noise source is $I_{\text{CS}}(n)$. The time series of the frequency noise was generated by a random number generator that produces random numbers with the spectra defined by equation (4.4.7). The noise generator was created by LISO [Hei99].

From the computed time series of the coherent sum heterodyne photocurrent, as given by equation (4.4.8), the power spectrum was calculated and the maximum power in any of the frequency bins was determined. The distribution of the found maxima is shown in Figure 4.10 for different DFT lengths. For the computations the frequency noise with the larger spectral density was used, $|\tilde{S}_{\nu}(f = 1 \text{ Hz})| = 200 \text{ kHz}$. The results for the case of $|\tilde{S}_{\nu}(f = 1 \text{ Hz})| = 100 \text{ kHz}$ were found to be not significantly different. They are not additionally plotted here.

The decrease of the overall power for larger FFT sample sizes is apparent from the left plot in Figure 4.10 which shows a histogram of the found maxima. However, increasing the FFT size from 1024 to 4096 points reduces the width of the distribution, whereas starting from 8192 upwards the values of the found maxima decrease drastically. The FFT length of $N_{\text{DFT}} = 4096$ points seems to be an optimum for the assumed frequency noise levels. In the right plot of Figure 4.10 the right tail probability for the case of negligible heterodyne amplitude, \mathcal{H}_0 , is shown in comparison to the CDF for the case of \mathcal{H}_1 . The peak value of the distribution of the detector output for the case of only noise decreases while increasing the number of samples in the FFT. This is due to the reduction in the width of the frequency bin which was given in equation (4.4.5).

Increasing the sample size to 4096 points gives a big improvement over the case of 1024 points, as the noise variance decreases by a factor of 4. If the DFT sample size is further increased, the separation between the signal and noise distribution stays approximately constant. Hence, increasing the number of samples above 4096 points results in no further improvement of the detection probability compared to the false alarm probability. This can be understood by looking at the time series of the frequency noise shown in Figure 4.9. For an FFT of 4096 points which corresponds to $108 \mu\text{s}$ the maximum variation in the noise is less than the DFT bin width $\delta f_{\text{DFT}} = f_{\text{s}}/N_{\text{DFT}}$ that is $\delta f_{\text{DFT}} = 9.28 \text{ kHz}$ for 4096 points sampled at 38 MHz. For 8192 samples the DFT bin width is $\delta f_{\text{DFT}} = 4.64 \text{ kHz}$ but the frequency variation reaches up to 10 kHz over the

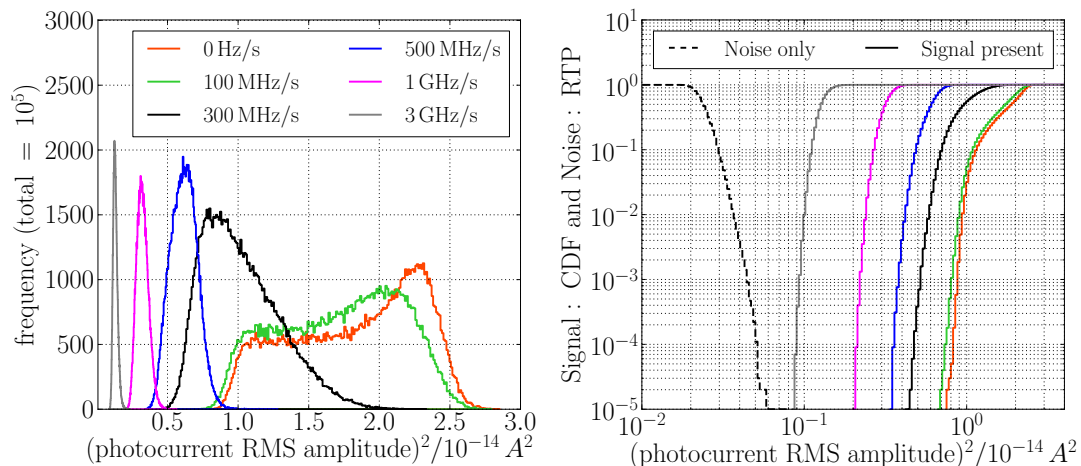


Figure 4.11.: Left: Histograms of the distribution of the detector output for different frequency sweep rates v_s . The DFT size is $N_{\text{DFT}} = 4096$ for each of the computed distributions and the effective received power of the heterodyne signal was set to $\hat{P}_{\text{RX},c} = 3 \text{ pW}$ per channel. Additionally frequency noise with $|\tilde{S}_\nu(f = 1 \text{ Hz})| = 200 \text{ kHz}$ was introduced. Right: RTP function of the distribution of the detector output for the case of only noise, \mathcal{H}_0 , and the CDF of the distribution under \mathcal{H}_1 for the same sweep rates. The LO power per QPD is $350 \text{ }\mu\text{W}$.

time the data for the DFT is sampled.

The signal power is thus distributed over several frequency bins which reduces the maximum power found in one bin. For smaller frequency noise levels, larger DFT sample sizes can be realised before the signal power per bin is reduced.

4.4.3. Distribution of the Detector Output with a Linear Frequency Sweep

In this section, the distribution of the detector output will be discussed for the case of a linear frequency sweep. During the calibration scan and the autonomous acquisition the frequency needs to be scanned, since unknown frequency offsets in the reference cavity or the free-running laser results in an unknown beatnote frequency. To estimate the scan speed for which significant loss of SNR has to be expected, power spectra of the heterodyne signal with frequency noise and an additional frequency sweep with a constant sweep rate v_s were computed. From the maximum values, histograms were calculated to estimate the distribution of the detector output \mathcal{D}_{CS} .

For the analysis in this section, the FFT length is fixed to 4096 points, and frequency noise with $|\tilde{S}_\nu(f = 1 \text{ Hz})| = 200 \text{ kHz}$ was used for the generation of the heterodyne signal time series. For the additive noise sources, the LO power was set to $700 \text{ }\mu\text{W}$ per channel,

whereas the effective received power per channel was set to $\hat{P}_{\text{RX},c} = 3 \text{ pW}$. The initial frequency prior to the sweep was varied in side the measurement band but it was assured that the signal frequency stays within the frequency band for the complete FFT. The mathematical expression of the signal with frequency noise and a constant rate frequency sweep can be given by:

$$s_{\text{CS}}(n) = A_{\text{CS}} \cos \left(2\pi \frac{f_b}{f_s} n + \pi \frac{v_s}{f_s^2} n^2 + \frac{2\pi}{f_s} \sum_{i=0}^n \delta f(i) + \phi_{\text{CS}} \right) + I_{\text{CS}}(n), \quad (4.4.9)$$

where the variables have the same meaning as in the previous sections. The results are shown in Figure 4.11 for different frequency sweep rates. For $v_s \leq 100 \text{ MHz}$ the distribution does not change significantly for the used FFT size. This corresponds to a frequency change of roughly 10.8 kHz during one FFT, which is about one frequency bin width

$$\delta f_{\text{DFT}} = \frac{f_s}{N_{\text{DFT}}}. \quad (4.4.10)$$

For higher sweep rates the frequency sweeps over more than one FFT bin and hence, the power of the signal will be distributed over several frequency bins, decreasing the maximum possible SNR.

The maximum scan rate for which the frequency does not sweep over more than a frequency bin during one DFT can be calculated by

$$\hat{v}_s = \frac{\delta f_{\text{DFT}}}{t_{\text{FFT}}} = \delta f_{\text{DFT}}^2. \quad (4.4.11)$$

However, even for sweep rates of 1 GHz/s the separation between the distribution of \mathcal{D}_{CS} for the case of only noise and the case of a present signal is sufficient to guarantee small false alarm probabilities, while the detection probability remains close to 100%.

Table 4.2 lists the maximum scan speeds for different DFT lengths and a sampling frequency of $f_s = 38 \text{ MHz}$, computed by equation (4.4.11). The maximum scan speed calculated by equation (4.4.11) for the case plotted in Figure 4.11 is $\hat{v}_s \approx 86 \text{ MHz/s}$ while the plot shows that for 100 MHz/s the distribution only slight changes. The margin on the value of the maximum scan speed as computed by equation (4.4.11) seems rather large.

4.5. Conclusions

In this chapter, an algorithm for estimating the frequency and heterodyne amplitude was presented. The algorithm is based on sequentially computed discrete-Fourier transforms of non-overlapping chunks of data. In order to enhance the signal-to-noise ratio, the coherent and incoherent sum combinations were presented.

At first, the distribution of the power in a single frequency bin of the power spectrum was given. Initially, the distribution is given for the case that only a single data channel is used as input to the detector. Subsequently, the result is generalised to the case of the coherent sum of the channels. For the incoherent sum combination no analytical distribution could be found, but an expression for the mean value is given.

Henceforth, for the case of the coherent sum of the data channels, the distribution of the detector output was derived which is the maximum power in any of the frequency bins of the power spectrum. Thereafter, the obtained distribution of the detector output for the coherent sum combination is used to derive an analytical expression for the maximum detector output depending on the number of returned estimates. For the case of the incoherent sum the expression for the coherent sum could be fitted to numerically computed values, yielding excellent agreement.

Finally, the distribution of the detector output for the case of a single channel is investigated for the case of a time dependent signal frequency. At first, the effect of frequency noise is investigated for different sample sizes of the discrete Fourier transform. After that a constant rate frequency sweep is added to the frequency noise, and the effect on the distribution of the detector output for different sweep rates is investigated.

The main results of this chapter are the expressions of the mean value of the detector distribution for the cases of the coherent and incoherent sum of the data channels. These are given in equations (4.2.22) and (4.2.40). Also, the analytical expressions for the root-mean square value of the maximum detector output for the two signal com-

Table 4.2.: Bin width, δf_{DFT} , sampling time, t_{FFT} , and maximum frequency sweep rate, \hat{v}_s , for FFTs of different size, N_{DFT} . The sampling frequency is fixed to $f_s = 38$ MHz.

N_{DFT}	$\delta f_{\text{DFT}} / \text{kHz}$	$t_{\text{FFT}} / \mu\text{s}$	$\hat{v}_s / \text{MHz/s}$
512	74.23	13.47	5510
1024	37.11	26.95	1380
2048	18.56	53.90	344.3
4096	9.277	107.8	86.07
8192	4.639	215.6	21.52

binations are important results. The derived expressions are later on used to estimate the minimum spatial scan resolution for an initial line-of-sight calibration. These expressions are given in equations (4.3.20) and (4.3.22) and some selected values are given in Table 4.1. They are especially useful as the generation of numerical estimates is computationally expensive.

The numerically simulated detector outputs for random frequencies show that the scalloping loss introduced due to the rectangular windowed discrete Fourier transform broadens the distribution as compared to the case for a fixed frequency. The width of the distribution is roughly equal to the scalloping loss, which reaches up to 60%. However, for the noise variance assumed here 500 pW effective received power in a single data channel are sufficient to reduce false alarm rates to a negligible level.

If frequency noise is present, the distribution of the detector output depends on the sample size N_{DFT} of the discrete Fourier transform. The signal-to-noise ratio is reduced if the width of the frequency bin $\delta f_{\text{DFT}} = f_s/N_{\text{DFT}}$ is smaller than the change of the frequency, during the time data is taken for the Fourier transform. For the frequency noise spectral density of $\tilde{S}_\nu(f = 1 \text{ Hz}) = 200 \text{ kHz}/\sqrt{\text{Hz}}$ which was used to generate the spectra the optimal sample size was found to be $N_{\text{DFT}} = 4096$ samples.

A frequency sweep also reduces the signal-to-noise ratio, if the change of the frequency is larger than the width of the frequency bins. Table 4.2 lists frequency sweep rates that correspond to frequency changes of one frequency bin during a Fourier transform. For sample sizes of $N_{\text{DFT}} = 4096$ and 2048 samples the maximum sweep rates are of the order of 100 MHz s^{-1} .

5. High-Fidelity Simulation of the GRACE Follow-On Laser Ranging Interferometer

In the previous chapters, the current design of the laser ranging interferometer for GRACE Follow-On, the expected signal and noise models and a data processing chain to detect the heterodyne signal were discussed. In order to test acquisition strategies, such as an initial line-of-sight (LOS) calibration and an autonomous laser link acquisition, a computer simulation was developed that includes the discussed signal and noise models, as well as a model of the detection algorithm. Additionally, realistic dynamics of the fine-steering mirror (FSM), laser frequency and a differential wavefront sensing (DWS) signal based control loop for the FSM were implemented. A simple model for a phasemeter was used to decide whether DWS is available to enable the control loop.

An important goal of the simulation was to gather statistics about the calibration accuracies and about success and failure rates, as well as timing of an autonomous acquisition, for a broad range of parameters. In order to achieve this goal multiple instances of the simulation code were run in parallel on the ATLAS computing cluster in the scope of a detailed parameter study.

In this chapter, an overview of the concepts used in the simulation is given, which is followed by a presentation of the models for the laser, the FSM and phasemeter, as well as the FSM-DWS control loop. Subsequently, the heterodyne signal computation is explained and finally the implementation of a model for the detection algorithm is discussed.

5.1. Overview

The simulation is realised as a discrete time-domain simulation. In Figure 5.1 a schematic overview is given of the components and dependences that need to be accounted for in the model, in order to achieve a sufficient degree of realism. These components are: the laser, the FSM, the measurement of the heterodyne signal at the quadrant photodiodes (QPD) and the phasemeter. Also, feed-back of the DWS signal and feed-forward of the line-of sight estimate and spatial scan coordinates to the FSM need to be included.

The heterodyne signal needs to be continuously computed for the current alignment

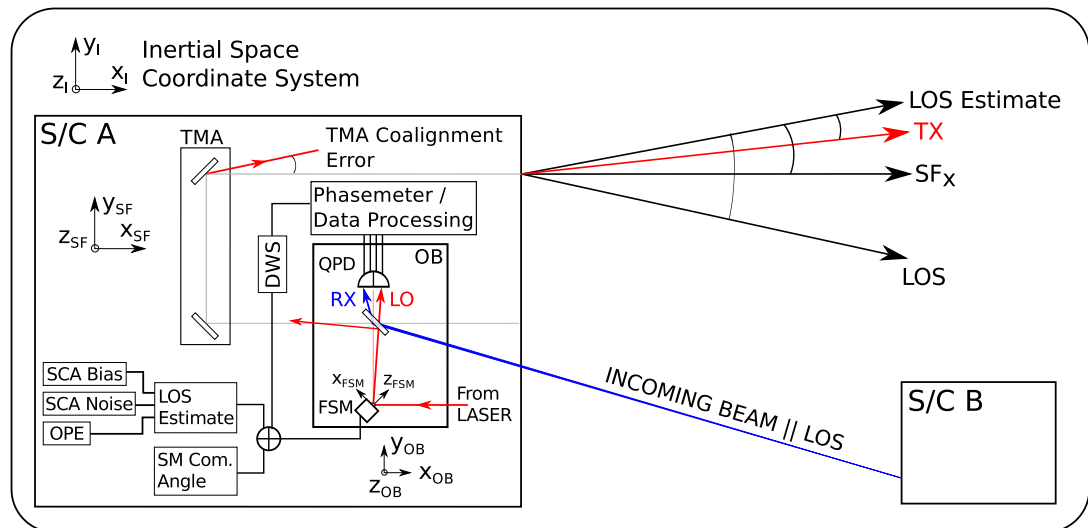


Figure 5.1.: Overview of the alignment angles of the transmitted (TX) and received (RX) beam, the coordinate systems, and fine-steering mirror alignment commands. Redundancy of the QPDs is implemented into the simulation, but not shown here.

of the involved beams. Additionally, a model of the complete data processing chain that is used to detect the heterodyne signal needs to be implemented, taking realistic noise models into account.

At each time step, the laser frequencies and subsequently the beatnote frequencies for the two spacecraft are updated. After this, the new steering mirror alignment is set and the beams are retraced through the optical bench based on the new steering mirror position. Based on the updated frequency and alignment of the beams, the heterodyne amplitudes and phases are calculated for each channel. From the calculated amplitude and phase the power spectrum is derived for the predefined summation mode, i.e. coherent or incoherent sum, also taking the additive noises into account.

This approach, however, assumes that the variation of the amplitude is small enough, such that the amplitude during one FFT can be considered constant. Additionally, a second method following a different approach was implemented. This alternative method is based on the computation of the FSM and beam alignment, as well as the corresponding heterodyne signal at additional, i.e. intermediate times. The additional samples of the heterodyne signal are used to enhance the quality of the power spectrum estimate, at the expense of increased computational effort.

In the following sections, the implemented models for the mentioned components are explained and the algorithm designed to simulate the detection algorithm is discussed.

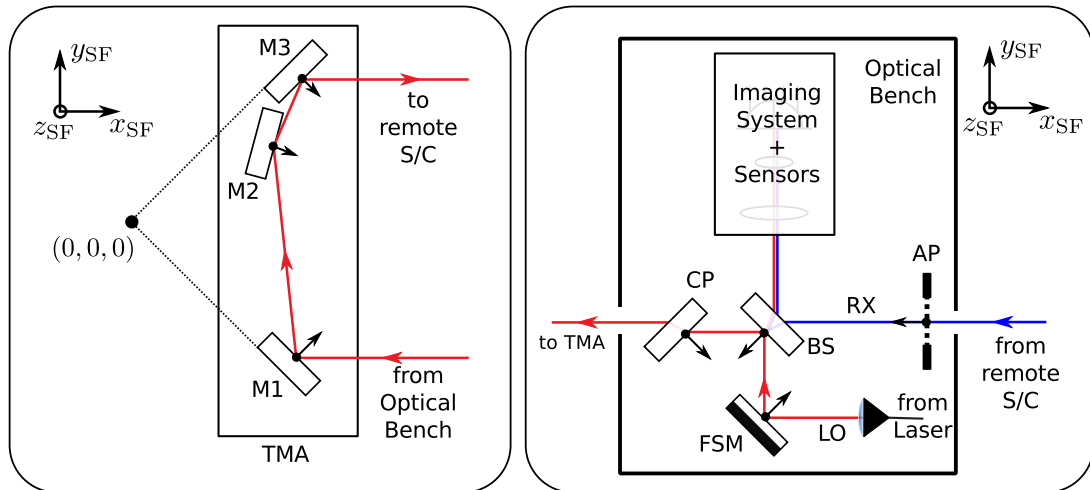


Figure 5.2.: Optical bench layout implemented into the discrete-time simulation. Left: Triple-Mirror Assembly (TMA) and origin of spacecraft coordinate system. Right: Optical bench with fine-steering mirror (FSM), beamsplitter (BS), compensation plate (CP), receive aperture (AP), local oscillator beam (LO) and nominal received beam (RX). The exact coordinates and normal vectors, in the spacecraft coordinate system, are given in Table 5.1, while the reference position and direction of the normal vectors are marked by the dot respectively the arrow at each component.

5.2. Model of the Laser Ranging Interferometer

In this section the model of the laser ranging interferometer (LRI) and its subsystems is presented. This includes the layout of the optical bench, the fine-steering mirror, the laser, the phasemeter, the FSM DWS loop, as well as a model of the frequency response of the quadrant photodiodes.

5.2.1. Optical Bench Layout

The optical bench layout, modelled with the discrete-time simulation, is shown in Figure 5.2. The coordinates of the components' reference points and normal vectors as given in the spacecraft reference frame are summarised in Table 5.1. The reference points and normal vectors are marked by the black dots and arrows in Figure 5.2. The origin of the coordinate system coincides with the vertex of the mirrors' surface planes of the perfectly aligned triple-mirror assembly (TMA).

The layout of the optical bench slightly differs from the layout shown in Figure 3.2, for which the location of the fibre injector and the photodiodes are swapped. This introduces a change of sign of the angle of the incoming beam at the photodiode, whereas the sign

for a tilt of the steering mirror is the same. The presented optical layout has been implemented as an IfoCad [WHK⁺12] model and the beam axes of the local oscillator and the received beam are determined by ray tracing.

However, neither the imaging system nor the photodiodes were included into the ray tracing model. The ray tracing model is used to compute the angles of the transmitted beam after passing through the TMA, to calculate the power received by the remote spacecraft and it is furthermore used to compute the angles of the local oscillator and the received beam at the beamsplitter. These angles are then handed over to the signal calculation procedure, which calculates the heterodyne signals for a redundant pair of QPDs and a perfect imaging system which matches the size of the imaged received beam to the radius of the active area of the QPDs. It is further assumed that the imaging system is designed such that the plane through the rotation point of the steering mirror perpendicular to the beam axis is imaged perfectly onto the QPD detector surface. Also, the plane of the receive aperture is imaged onto the detector surface, such that a pure tilt of the wavefront across the imaged planes is transformed into a pure tilt at the QPD surface. The signal calculation is discussed in more detail in Section 5.3.

5.2.2. Fine-Steering Mirror

The fine-steering mirror on the optical bench serves to track the incoming signal in nominal operation to zero the wavefront tilt between the local oscillator and the received

Table 5.1.: List of the main optical components of the optical bench model that is implemented into the simulation. The reference positions and normal vectors are given in spacecraft coordinates. The reference point for each component is marked by a black dot in Figure 5.2.

Item		Centre Coords.			Normal Vector Coords.		
Description	Abbr.	x_{SF}	y_{SF}	z_{SF}	x_{SF}	y_{SF}	z_{SF}
Fine-Steering Mirror	SM	500	-330.662	24	$1/\sqrt{2}$	$1/\sqrt{2}$	0
Beamsplitter	BS	500	-302.184	24	$-1/\sqrt{2}$	$-1/\sqrt{2}$	0
Compensation Plate	CP	480	-302.184	24	$1/\sqrt{2}$	$-1/\sqrt{2}$	0
TMA Mirror 1	M1	300	-300	24	$1/\sqrt{2}$	$1/\sqrt{2}$	0
TMA Mirror 2	M2	300	266.059	24	$1/2$	$-1/2$	$-1/\sqrt{2}$
TMA Mirror 3	M3	333.941	300	-24	$1/2$	$-1/2$	$1/\sqrt{2}$
Receive Aperture	AP	532.564	-300	24	-1	0	0
Local Oscillator	LO	550	-330.662	24	-1	0	0
Nominal RX Beam	RX	532.564	-300	24	-1	0	0

beam. This is achieved via closed loop control of using DWS signal. During acquisition the FSM is used for steering the local oscillator (LO) and simultaneously the transmitted beam (TX) according to the desired scan pattern. Additionally, the attitude and orbit control system (AOCS) actuates on the FSM using a feed-forward of the current line-of-sight estimate which is based on star camera data and orbit predictions. See Figure 5.1 for a schematic overview of the steering mirror input.

The attitude estimates of the AOCS are assumed to be given in spacecraft coordinates thus they are equivalent to the alignment of the estimated line-of-sight LOS relative to the nominal local oscillator beam axis for zero FSM tilt. The scan pattern is also defined in terms of the LO beam angles. The DWS signal depends on the relative tilt between the local oscillator and the received beam at the photodiode. See Section 2.1.2 for details on DWS. Hence, corrections computed from the DWS signal are also given as angles in the spacecraft frame, or *optical angles*.

The following equations for the desired horizontal and vertical alignment of the local oscillator beam in spacecraft coordinates, α_{op} and β_{op} , summarises the above:

$$\alpha_{op} = \alpha_0 + \alpha_{scan} + \alpha_{AOCS} + \alpha_{DWS} \quad (5.2.1)$$

$$\beta_{op} = \beta_0 + \beta_{scan} + \beta_{AOCS} + \beta_{DWS}, \quad (5.2.2)$$

where α_0 and β_0 are constant offsets from the estimated LOS, α_{scan} and β_{scan} are the current coordinates of the spatial scan and α_{AOCS} and β_{AOCS} are the alignment angles of the estimated LOS. They are the sum of the star-camera assembly (SCA) noise and the initial alignment bias, α_{BIAS} and β_{BIAS} , which are attempted to be determined by the acquisition procedure:

$$\alpha_{AOCS} = \alpha_{SCA} + \alpha_{BIAS} \quad (5.2.3)$$

$$\beta_{AOCS} = \beta_{SCA} + \beta_{BIAS}. \quad (5.2.4)$$

The angles α_{DWS} and β_{DWS} are corrections to the local oscillator alignment based on the DWS signal of the phasemeter.

The local oscillator beam, coming from the fiber outcoupler, is reflected off the fine-steering mirror under 45° incidence. Thus, the desired optical angles have to be converted to tilt angles of the steering mirror. The transformation up to second order in the optical

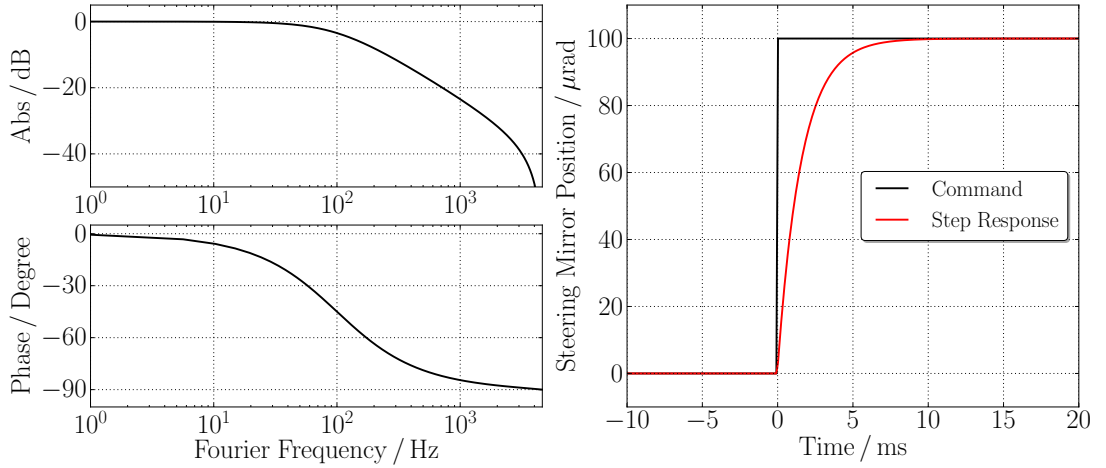


Figure 5.3.: Left: Bode plot of the fine-steering mirror transfer function implementation as IIR filter, one-pole 100 Hz low pass. Right: Step response of the steering mirror in one dimension, for a step of 100 μrad .

angles can be expressed by

$$\beta_{\text{FSM,com}} = -\frac{\beta_{\text{op}}}{\sqrt{2}} \quad (5.2.5)$$

$$\alpha_{\text{FSM,com}} = \frac{\alpha_{\text{op}}}{2} - \frac{\beta_{\text{op}}^2}{4}. \quad (5.2.6)$$

These angles represent the new desired orientation of the FSM. However, the response of the steering mirror's real alignment angles, $\beta_{\text{FSM}}(t_n)$ and $\alpha_{\text{FSM}}(t_n)$, at time, t_n , to a change in the commanded angle is not instantaneous but subject to a transfer function, TF,

$$\beta_{\text{FSM}}(t_{n+1}) = \text{TF}(\beta_{\text{FSM,com}}(t_n), \beta_{\text{FSM}}(t_n)) \quad (5.2.7)$$

$$\alpha_{\text{FSM}}(t_{n+1}) = \text{TF}(\alpha_{\text{FSM,com}}(t_n), \alpha_{\text{FSM}}(t_n)). \quad (5.2.8)$$

The transfer function, assumed for the analysis in this thesis is a simple one-pole low pass, with a pole frequency of $f_{\text{pole}} = 100 \text{ Hz}$. Figure 5.3 shows the Bode plot of the single-pole transfer function on the left, and the step response, for a step of 100 μrad of the steering-mirror command, in the right plot. Typically, the new desired alignment of the FSM is reached after 10 ms.

The settling time of the steering mirror, from here on denoted by τ_{FSM} , is used as a parameter to control the behaviour of the algorithm in the simulation. For example, ev-

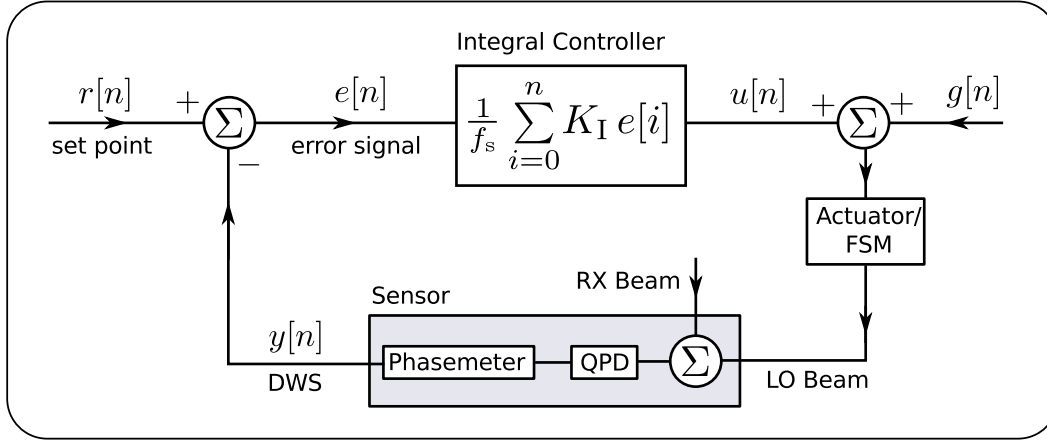


Figure 5.4.: Block diagram of the implemented control loop, to control the beam alignment using the differential wavefront sensing signal from the phasemeter as error signal to the fine-steering mirror. The *set point* is $r[n] = 0$ and the gain of the integrator is set to $K_I = 1.5 \cdot 10^{-2}$. The AOCS correction to the LOS estimates are forwarded to the steering-mirror via the additional correction factor $g[n]$.

every time the steering-mirror is stepped, e.g. in a discretely stepped spatial scan pattern, a flag is set for a time of τ_{FSM} , indicating that the FSM position is invalid. While this flag is set, a possible detection, claimed by the detection algorithm (see Figure 4.2 or 6.11), will not be considered and the timer for controlling the spatial scan is stopped. This is done to ensure that a detection is made only if the FSM is in a well-defined state.

5.2.3. FSM DWS Control Loop

Once the effective received power of the heterodyne signal is large enough, the internal phasemeter phase-locked loops (PLL), can lock to the incoming signal and the DWS signal is made available.

Figure 5.4 shows the block diagram of the implemented control loop using an integral controller to compute the control signal, which is fed to the steering-mirror. Additionally, the AOCS correction, $g[n]$, is added to the correction signal applied to the FSM. The fine-steering mirror actuates on the alignment of the local oscillator beam whose angle is sensed by the QPD, relative to the received beam. The phasemeter computes the phase, ϕ_c , of the heterodyne signal channel and the horizontal and vertical DWS signal is calculated by subtracting the signals one from another as given in equation (2.1.17).

In the simulation, however, the phase of the heterodyne signal is computed from the overlap integral which was given in equation (3.3.6). Also, the DWS signal can, likewise, be defined in terms of the overlap integral. Here at least two definitions are possible

which are given below. First, it can be defined as

$$\text{DWS}_{\text{hor}} = \arg \left[\frac{\mathcal{O}_A \mathcal{O}_C}{\mathcal{O}_B \mathcal{O}_D} \right] \quad (5.2.9)$$

$$\text{DWS}_{\text{ver}} = \arg \left[\frac{\mathcal{O}_A \mathcal{O}_B}{\mathcal{O}_C \mathcal{O}_D} \right], \quad (5.2.10)$$

where \mathcal{O}_q is the overlap integral between the local oscillator and the received beam on the QPD segment q which is the same for the two corresponding segments of a channel. The other possible definition is equivalent to the definition before in equation (2.1.17). It reads:

$$\text{DWS}_{\text{hor}} = \arg \mathcal{O}_A + \arg \mathcal{O}_C - (\arg \mathcal{O}_B + \arg \mathcal{O}_D), \quad (5.2.11)$$

$$\text{DWS}_{\text{ver}} = \arg \mathcal{O}_A + \arg \mathcal{O}_B - (\arg \mathcal{O}_C + \arg \mathcal{O}_D). \quad (5.2.12)$$

The DWS signal computed from the overlap integral of a tophat beam and a Gaussian local oscillator is shown in Figure 5.5. The first method of equations (5.2.9) and (5.2.10) suffers from wrapping at tilt angles of $\pm 100 \mu\text{rad}$ and additional zero crossings occur in the DWS signal at $\pm 220 \mu\text{rad}$. The control loop cannot distinguish between these zero crossings and the zero crossing at zero tilt angle and will eventually lock to the false zero crossings if the loop is closed for tilt angles above $100 \mu\text{rad}$.

In the simulation, however, the second method given in equations (5.2.11) and (5.2.12) is used which does not suffer from phase jumps, as can be seen in the left plot of Figure 5.5. The top left plot of Figure 5.5 shows the time evolution of the steering-mirror position, the steering-mirror command as well as the control signal, $u[n]$, if the control loop is closed at $t = 0$ s. The DWS signal approaches zero, as can be seen in the bottom left plot. Here, a DWS signal of zero does not correspond to the steering-mirror being aligned to its nominal position, because the incoming beam is tilted by roughly $70 \mu\text{rad}$ due to a misalignment of the spacecraft. Additionally, the SCA noise accounts for about $30 \mu\text{rad}$ in the opposite direction.

The control loop, implemented in the simulation, settles after about 10 ms to 15 ms.

5.2.4. Laser

The laser model provides the current absolute frequency of the laser light and the far-field intensity distribution of the beam transmitted to the distant spacecraft. It is also used to store all parameters that characterise the laser such as the local oscillator power at the photodiode, the power transmitted to the remote spacecraft, the laser frequency

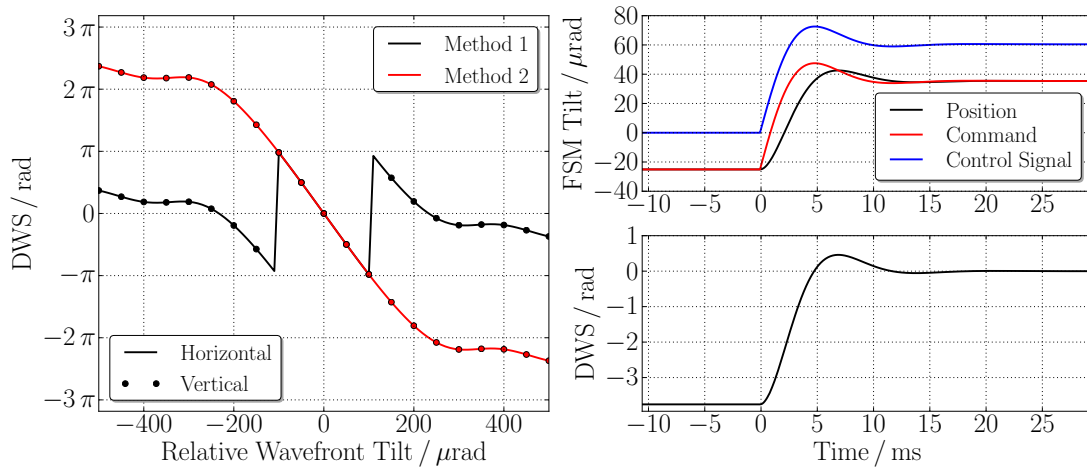


Figure 5.5.: Left: DWS signal computed from the overlap integral between a Gaussian local oscillator and a tophat beam. The DWS signal is computed with the two methods given in equations (5.2.9) and (5.2.10) denoted by *Method 1*, and equations (5.2.11) and (5.2.12) denoted by *Method 2*. Right: Time series of the horizontal FSM position, the commanded position and the control signal at the top and the DWS signal at the bottom. The control loop is closed at $t = 0$ s.

scan rate, as well as the lower and upper bound of the frequency scan.

The momentary absolute frequency is used as the frequency of the local oscillator and as the frequency of the beam transmitted to the remote spacecraft. The current frequency of the laser, ν_i , with $i = m, s$, consists of the nominal laser frequency, $\nu_0 = c/\lambda$, the momentary realisation of frequency noise, δf_i , and a laser frequency tuning, f_i , which is the output of a filter function modelling the thermal actuator of the laser.

Here, c is the vacuum speed of light and λ the nominal laser wavelength, $\lambda = 1\,064$ nm. Hence, the frequency of the laser in the simulation is

$$\nu_i = \nu_0 + \delta f_i + f_i. \quad (5.2.13)$$

Since only the difference of the frequencies is measured in a heterodyne setup $f_b = \pm(\nu_m - \nu_s)$, the constant, nominal laser frequency, ν_0 , is set to zero, and only deviations from ν_0 are considered.

The frequency noise, δf_i , is computed by a noise generator that provides random numbers with a given spectral density. The source code for the noise generator was generated by LISO [Hei99]. The spectral density assumed for the frequency noise, which was used for the analysis in this thesis, is presented in Section 4.4.2 and the corresponding pole-zero model is given in equation (4.4.7). The spectral density, as

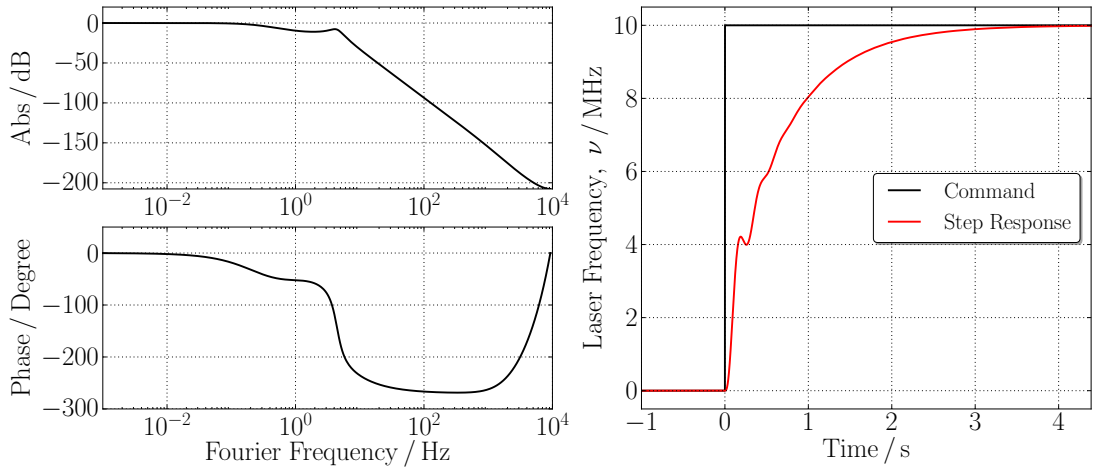


Figure 5.6.: Left: Bode plot of the thermal actuator frequency response. Right: Step response of the thermal actuator model. The pole-zero model of the frequency response is given in Table 5.2.

well as several time series of the produced frequency noise, are shown in the plots in Figure 4.9.

The frequency tuning, f_i , is used to simulate dynamic changes of the laser frequency which are assumed to be controlled by the thermal actuator on the laser crystal. Thus, the frequency tuning is the output of a filter that models the evolution of the laser frequency in the time domain, which depends on a commanded frequency, f_{com} , and the current internal state of the thermal actuator,

$$f_i = f_i(f_{\text{com}}). \quad (5.2.14)$$

The commanded frequency is the desired frequency of the laser. The change of the laser frequency due to a commanded frequency scan or discontinuous changes in the desired frequency are modelled with f_i . A discontinuous change happens for example during an autonomous laser link acquisition, when the beatnote frequency on the slave spacecraft is moved into the centre of the frequency band, once a signal has been detected. Another reason for a discontinuous frequency change is the initialisation of the frequency sweep, where the laser frequency of the free running slave laser is set to the lower boundary of the frequency uncertainty interval.

The pole-zero model of the used thermal actuator is listed in Table 5.2. It is implemented in the simulation as an infinite-impulse response filter (IIR) which was also generated with the aid of LISO [Hei99]. Figure 5.6 shows a Bode plot on the left and

the step response for a 10 MHz step of the frequency command on the right. After a time of $t = 2$ s after the step input, the desired frequency is reached within an error of approximately 5%. Therefore, in the analysis of an autonomous laser link acquisition given in Chapter 7, the laser settling time is defined as $\tau_L = 2$ s.

The models of the far-field intensity of the transmitted beam, provided by the *laser* data structure, are the Gaussian beam with beam quality factor, $M^2 \geq 1$, as defined in equation (3.3.17), and the propagated fibre mode defined by equation (2.5.18).

5.2.5. Phasemeter

A simple model of a four-channel phasemeter is implemented into the simulation, to decide whether the DWS signal is available and whether the steering-mirror control can be handed over to the DWS control loop. The state diagram of the model is shown in Figure 5.7.

Each phasemeter contains four PLLs, one for each channel. The state diagram of a PLL is shown in the left panel of Figure 5.7. The state machine representing each of the PLL consists of four states, i.e. the `Default` state, represented by the black circle, a `Not Locked` state as well as the `Locking` and `Locked` states.

The phase-locked loop makes the transition from `Not Locked` to `Locking` once the effective received power in the channels is above a set threshold of 3 pW. On entry into the `Locking` state a timer is started that counts the elapsed time since entering the state. If the time spent in the `Locking` state exceeds 1 ms and the effective received power in the channel does not drop below 2 pW, the phase-lock loop transitions to the `Locked` state or else back to `Not Locked`. If the effective received power in a channel is less than 1 pW while the phase-lock loop of the channel is locked, the state machine transitions back to the `Not Locked` state.

The phasemeter has three states, which are the `Default` state and the ones labelled: `DWS Not Available` and `DWS Available`. The phasemeter starts in the state where

Table 5.2.: List of the poles and zeros of the model for the thermal actuator of the lasers, used in the simulation, (private communication G. Heinzl, AEI, 2013)

Type	Frequency / Hz	Q-Value
Pole	0.25	∞
Zero	1.15	∞
Pole	4.42	2.33
Pole	5	∞

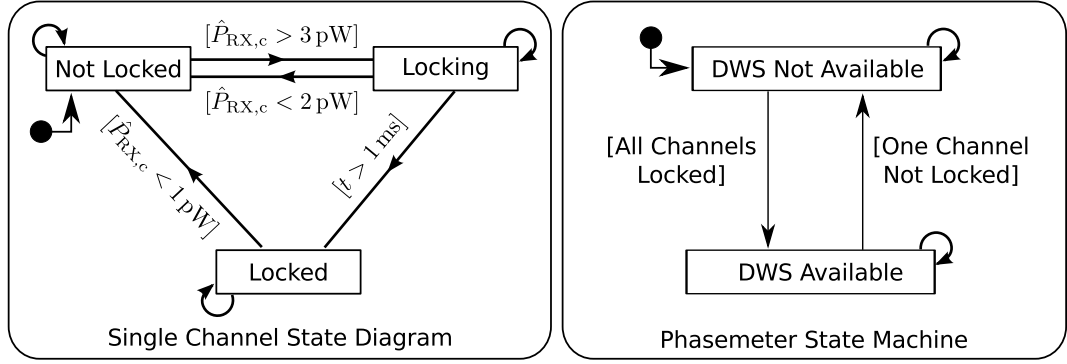


Figure 5.7.: Left: State diagram of a phase-lock loop of a single phasemeter channel. Right: State diagram of the complete phasemeter, showing the two important states for acquisition, signalling if DWS signal is available or not. The two states are composite states, each containing the state machines of four single channels, shown on the left.

DWS is not available and transitions to the state **DWS Available**, if the PLLs of all channels are in the **Locked** state. The phasemeter on each spacecraft is assumed to have four channels, corresponding to the four segments of a QPD. See Figure 3.4 for an overview of the segment and channel labelling of a QPD. If the phasemeter is in the state **DWS Available**, the FSM DWS control loop can be closed. The control loop is automatically opened if one of the PLLs of the phasemeter transitions out of the **Locked** state. The phasemeter then returns to **DWS Not Available**.

5.2.6. Frequency Response of the Quadrant Photodiodes

The frequency response of the quadrant photodiodes, $g(f_b)$, is assumed to be limited by a lower bound, f_{low} , and an upper bound, f_{up} , where the upper bound is smaller than the Nyquist frequency, $f_s/2$, in order to prevent aliasing of the heterodyne signal into the photodiode bandwidth. The functional form of, $g(f_b)$, is chosen as

$$g(f_b) = \begin{cases} \exp\left(-\frac{(f_b^2 - f_{up}^2)^2}{2w^2}\right) & \text{if } f_b \geq f_{up}, \\ 1 & \text{if } f_{low} < f_b < f_{up}, \\ \exp\left(-\frac{(f_b^2 - f_{low}^2)^2}{2w^2}\right) & \text{if } f_b \leq f_{low}. \end{cases} \quad (5.2.15)$$

The frequency response is thus, flat and equal to 1 for all frequencies between f_{low} and f_{up} . It drops with a Gaussian profile to zero for frequencies above f_{up} and below f_{low} . The width of the transition region is determined by the parameter w which is chosen as $w = 1 \text{ MHz}$ for the analysis in this thesis.

5.3. Signal Calculation

The important signals that need to be computed in the simulation are the amplitudes and phases of the heterodyne signal in the four channels of the redundant photodiode pair.

Expressions for the heterodyne signal in a single channel were given in equation (3.3.4) provided that the received power is the same for each QPD segment of a single channel and that no additional phase offsets are introduced before adding the signals of the two corresponding segments. The amplitude of the heterodyne signal in a channel denoted by A_c , is just twice the single segment amplitude, A_q , and the phase is the same for the combined heterodyne signal ϕ_c and the individual segments ϕ_q ,

$$\begin{aligned} s_c(t) &= 2 s_q(t) \\ &= 2 A_q \cos(2\pi f_b t + \phi_q) \\ &= A_c \cos(2\pi f_b t + \phi_c). \end{aligned} \quad (5.3.1)$$

This also implies that the heterodyne efficiency for the sum of the two corresponding segments, η_c , is equal to the heterodyne efficiency of a single segment, η_q . Hence,

$$A_c = 2A_q, \quad \phi_c = \phi_q, \quad \text{and} \quad \eta_c = \eta_q. \quad (5.3.2)$$

The amplitude of the single channel heterodyne signal, A_c , depends on the received power P_{RX} , the heterodyne efficiency η_c , and the beatnote frequency f_b . It is calculated similar to equation (3.3.9) by

$$A_c = \frac{2 \rho_{PD} g(f_b)}{n_c} \sqrt{P_{LO} P_{RX} \eta_c}. \quad (5.3.3)$$

The beatnote frequencies for each spacecraft are computed using the formulas given in equations (3.5.4). With the indices m for the master spacecraft and s for the slave spacecraft, they are repeated here as follows:

$$f_b^m = f_m - (f_s + f_D) \quad \text{and} \quad (5.3.4)$$

$$f_b^s = f_s - (f_m + f_D). \quad (5.3.5)$$

See equation (5.2.13) for how the laser frequencies, f_m and f_s , are computed. The Doppler shift, f_D , is randomly chosen and constant for a complete simulation run.

The power received by the distant spacecraft is computed from equation (3.3.16) for

either the far-field intensity of the Gaussian beam with quality factor, M^2 , from equation (3.3.17) or the propagated fiber mode defined by equation (2.5.18). The spacecraft separation is fixed at the start of the simulation. The tilt of the remote beam is computed from the angles of the transmitted beam after passing the TMA and adding the TMA coalignment error to the beam axis alignment computed by ray tracing. After that, the direction of the TX beam is transformed from spacecraft coordinates into the inertial reference frame.

In order to compute the heterodyne efficiency, η_c , and the phase of the heterodyne signal, ϕ_c , as a function of the relative misalignment of the local oscillator and received beam, the normalised overlap integral, \mathcal{O}_q from equation (2.1.8), has to be calculated each time the alignment of the beams changes. Alignment fluctuations during a spatial scan or just due to SCA noise may require re-computing the alignment for each simulated time step. Hence, directly integrating the electric field at the photodiode will be computationally too expensive.

The beam parameters, however, are assumed to be fixed and for this reason the overlap integral is precomputed on a grid of relative alignment angles with a side length of 2 mrad and a resolution of 5 μ rad. Points in between are interpolated, using bilinear interpolation. For angles greater than 1 mrad the overlap integral is set to zero. The heterodyne efficiency is then computed as $\eta_c = |\mathcal{O}_q|^2$ and the phase as $\phi_c = \arg \mathcal{O}_q$.

The relative misalignment between the local oscillator and the received beam is computed from the alignment angles of the local oscillator transmitted through the beamsplitter and the received beam reflected off the beamsplitter. The definitions of the horizontal and vertical alignment angles in the photodiode's reference frame are shown in the left panel of Figure 3.5. For each beam the angles with the (x, z) and (y, z) -planes are calculated at the beamsplitter from which the relative misalignment angles are computed as the difference of the angles in the two orthogonal directions. These two angles are then passed to the interpolation function, which returns the phase and heterodyne efficiency for this particular misalignment.

5.4. Detection Algorithm

The detection algorithm proposed before, computes fast Fourier transforms (FFT) of the heterodyne signal, measured with a sampling frequency of $f_s = 38$ MHz. Computing the full time series of the data and calculating the FFTs is too expensive. Based on the results obtained in Chapter 4 a model of the output of the algorithm was developed.

At each simulated time step a power spectrum of the noisy heterodyne signal, for

either the coherent or incoherent sum, is computed and the maximum power in any of the non-vetoed frequency bins, as well as the index of the frequency bin containing the maximum, is returned. The maximum power is used as an estimate of the received power and the bin index is used as an estimate of the beatnote frequency.

5.4.1. Detection Algorithm for Constant Amplitude

In Chapter 4 the probability distributions for the power in a single frequency bin is given for a heterodyne signal of constant amplitude and frequency, as well as for a frequency bin containing only noise. For a heterodyne signal of constant amplitude and frequency, the power spectrum can be simulated by drawing random numbers from these distributions for each frequency bin that is not vetoed.

If the beatnote frequency, f_b , is not equal to one of the central bin frequencies of the FFT, i.e. $f_b \neq j f_s / N_{\text{DFT}}$ with $j = 0, \dots, N_{\text{DFT}} - 1$, the power in the heterodyne signal is distributed over two neighbouring bins and hence two signal bins exist. The lower index, j_1 , and the higher index, j_2 , of the signal bins are computed from the sampling frequency, f_s , the sample size of the FFT, N_{DFT} , and the beatnote frequency as

$$j_1 = \left\lfloor \frac{f_b}{f_s} N_{\text{DFT}} \right\rfloor \quad (5.4.1)$$

$$j_2 = j_1 + 1, \quad (5.4.2)$$

where $\lfloor x \rfloor$ is the *floor* operation, returning the largest integer value smaller than x , or x if x is an integer. If any of the two bin indices is vetoed it is not considered in the search for the maximum.

The amplitude of the heterodyne signal in the two signal bins was given in equation (4.4.3). The power in the frequency bins for the the coherent sum can be given in analogy, with the coherent sum amplitude, A_{CS} , defined by equation (4.2.22) or equivalently by

$$A_{\text{CS}} = \left| \sum_{c=1}^{n_c} A_c e^{i\phi_c} \right|, \quad (5.4.3)$$

which is implemented in the simulation using the computation of the single channel amplitudes from equation (5.3.2). The power in the signal bins, $\tilde{s}_{\text{CS}}^2(j_i)$, can then be

computed by

$$\tilde{s}_{\text{CS}}^2(j_i) \approx \frac{A_{\text{CS}}^2}{2} |l(j_i, j_1 + \delta b, N_{\text{DFT}})|^2. \quad (5.4.4)$$

The scaling function, $l(k, j + \delta b, N_{\text{DFT}})$, is given in equation (4.4.4), where the offset of the beatnote frequency from the central bin frequency in FFT bin widths, δb , is computed by

$$\delta b = \frac{f_{\text{b}}}{f_{\text{s}}} N_{\text{DFT}} - j_1. \quad (5.4.5)$$

The power in the frequency bin is distributed according to a noncentral χ^2 -distribution with two degrees of freedom, as given by equation (4.2.17). For the case of the coherent sum detector the parameters used for the distribution of the lower and upper signal bin are, with $i = 1, 2$,

$$\lambda_i = \frac{\sqrt{N_{\text{DFT}}}}{\sigma_{\text{CS}}} \frac{A_{\text{CS}} |l(j_i, j_1 + \delta b, N_{\text{DFT}})|}{\sqrt{2}}, \quad \text{and} \quad \sigma^2 = \sigma_{\text{CS}}^2. \quad (5.4.6)$$

For the definition of the variance of the coherent sum, σ_{CS}^2 , see equation (4.2.24). The remaining frequency bins are assumed to contain only noise and hence, for all frequency bins with indices between k_{low} and k_{up} which are no signal bins, a random number is drawn from the χ^2 -distribution with two degrees of freedom, given in equation (4.2.11). Here again, the variance used has to be the coherent sum variance, σ_{CS}^2 , given above.

For the generation of χ^2 -distributed random variates the MT19937 algorithm [MN98] is used which is part of the GNU Scientific Library [GDT⁺03]. The generation of non-central χ^2 -distributed random variates, Z , with two degrees of freedom can be done by making use of the addition rule for non-central χ^2 -distributed variables by defining

$$Z_i = X_i^2 + Y, \quad (5.4.7)$$

where X_i is Gaussian distributed with mean λ_i and variance 1, $X_i \sim \mathcal{N}(\lambda_i, 1)$ and Y is χ^2 -distributed with one degree of freedom. The random variate for the power in the signal bin with index j_i is then

$$\tilde{s}_{\text{CS}}^2(j_i) = \frac{\sigma_{\text{CS}}^2}{N_{\text{DFT}}} Z_i. \quad (5.4.8)$$

To generate the power spectrum of the heterodyne signal of the coherent sum, only a single call to the χ^2 random number generator has to be made for the frequency bins

that contain only noise, and only one call to the χ^2 and one additional to a Gaussian random number generator, for each of the two signal bins.

For the incoherent sum of the channels, no analytic distribution was found. In order to simulate the power spectrum for the ICS, the power spectrum of the individual channels is computed using the approach presented above, whereas the coherent sum amplitude and variance are exchanged for the amplitude and variance in the individual channels, A_c and σ_c^2 , given in equations (3.3.9) and (3.4.7). The spectra generated for the channels are then summed up to get the spectrum of the incoherent sum.

5.4.2. Detection Algorithm for Varying Amplitude

If the amplitude of the heterodyne signal over the course of an FFT is not constant, the simplified approach has to be modified. The DFT of the heterodyne signal with varying amplitude can be written in terms of a discrete circular convolution, \star , between the DFT of the time varying amplitude and the DFT of the *cosine-term* by making use of the convolution theorem. It reads:

$$\mathcal{F}[s_c(t_n)](k) = \mathcal{F}[A_c(t_n) \cos(2\pi f_b t_n + \phi_c)](k) \quad (5.4.9)$$

$$= (\mathcal{F}[A_c(t_n)] \star \mathcal{F}[\cos(2\pi f_b t_n + \phi_c)])(k). \quad (5.4.10)$$

It is assumed that the beatnote frequency is of the form $f_b = (j_1 + \delta b) f_s / N_{\text{DFT}}$, with j_1 being the index of the lower signal bin and $0 \leq \delta b \leq 1$ being the frequency offset from the centre frequency of the j_1 -th frequency bin. The DFT of the *cosine-term* is then the scaling function $l(k, j_1 + \delta b, N_{\text{DFT}})$ which was already given in equation (4.4.4). By writing \tilde{A}_c instead of $\mathcal{F}[A_c(t_n)]$ the convolution can be given by

$$\begin{aligned} \mathcal{F}[s_c(t_n)](k) = & \sum_{\kappa=0}^k \tilde{A}_c(\kappa) l(k - \kappa, j_1 + \delta b, N_{\text{DFT}}) \\ & + \sum_{\kappa=k+1}^{N_{\text{DFT}}-1} \tilde{A}_c(\kappa) l(N_{\text{DFT}} + k - \kappa, j_1 + \delta b, N_{\text{DFT}}). \end{aligned} \quad (5.4.11)$$

The dependence of the scaling function on the frequency offset from a fixed frequency bin is shown in Figure 4.7. It can be seen that it is strongly localised around the signal bin. The DFT of the time varying amplitude will be localised around the DC bin, $k = 0$, for all amplitude variations encountered during acquisition. For the signal bin with index

$k = j_1$, the above equation can be rewritten as

$$\begin{aligned} \mathcal{F}[s_c(t_n)](k) &= \sum_{\kappa=0}^{j_1} \tilde{A}_c(\kappa) l(j_1 - \kappa, j_1 + \delta b, N_{\text{DFT}}) \\ &\quad + \sum_{\kappa=1}^{N_{\text{DFT}}-j_1-1} \tilde{A}_c(N_{\text{DFT}} - \kappa) l(j_1 + \kappa, j_1 + \delta b, N_{\text{DFT}}). \end{aligned} \quad (5.4.12)$$

Here, the DFT of the amplitude time series around the DC bin, is multiplied by the DFT response to the cosine-term around the signal bin, j_1 . As was said before, these terms are strongly localised, such that the terms for large κ do not contribute, significantly, to the result and hence, the sum can be limited to a few n_b terms. This gives

$$\begin{aligned} \mathcal{F}[s_c(t_n)](k) &\approx \sum_{\kappa=0}^{n_b} \tilde{A}_c(\kappa) l(j_1 - \kappa, j_1 + \delta b, N_{\text{DFT}}) \\ &\quad + \sum_{\kappa=1}^{n_b} \tilde{A}_c(N_{\text{DFT}} - \kappa) l(j_1 + \kappa, j_1 + \delta b, N_{\text{DFT}}). \end{aligned} \quad (5.4.13)$$

Still, this assumes an FFT of an amplitude time series that is sampled with the full sampling frequency of 38 MHz and would be expensive to compute. The frequency bin width of an FFT, $\delta f_{\text{DFT}} = f_s/N_{\text{DFT}}$, however, is invariant under a simultaneous scaling of the sampling frequency f_s and the number of samples N_{DFT} by a factor a . This is equivalent to leaving the sampling time for a single FFT constant. Hence, for such a scaling the central bin frequencies for bins of the same index are identical. Thus, the number of samples of the amplitude time series, that are taken to calculate its spectrum can be reduced to $N' = a N_{\text{DFT}}$

The new number of samples N' should not be chosen too small, as aliasing will increase due to the reduced sampling frequency. The N' -point Discrete Fourier transform of the amplitude time series is

$$\tilde{A}'_c(k) = \frac{\sqrt{2}}{N'} \sum_{n=0}^{N'-1} A_c(t_n) \exp\left(-2\pi i \frac{k}{N'} n\right). \quad (5.4.14)$$

The amplitude time series consists of real numbers and hence,

$$[\tilde{A}'_c(k)]^* = \tilde{A}'_c(N' - k). \quad (5.4.15)$$

The approximation of the DFT given in equation (5.4.13) can now be rewritten with the

DFT of the amplitude time series for the reduced sampling rate by

$$\begin{aligned} \mathcal{F}[s_c(t_n)](k) \approx & \sum_{\kappa=0}^{n_b} \tilde{A}'_c(\kappa) l(j_1 - \kappa, j_1 + \delta b, N_{\text{DFT}}) \\ & + \sum_{\kappa=1}^{n_b} [\tilde{A}'_c(\kappa)]^* l(j_1 + \kappa, j_1 + \delta b, N_{\text{DFT}}). \end{aligned} \quad (5.4.16)$$

This approximation is used in the simulation to compute the FFT, if amplitude variations over a single FFT should be considered. In the above equation it was implicitly assumed that,

$$\tilde{A}'_c(N' - \kappa) \approx [\tilde{A}'_c(\kappa)]^*, \quad (5.4.17)$$

which is true as can be seen by plugging in the indices $N' - \kappa$ and $N_{\text{DFT}} - \kappa$, into the definition of the DFT. See equation (4.1.6) and (5.4.14) and using equation (5.4.15),

$$\tilde{A}'_c(N' - \kappa) = \tilde{A}'_c(-\kappa) = [\tilde{A}'_c(\kappa)]^* \quad (5.4.18)$$

$$\tilde{A}_c(N_{\text{DFT}} - \kappa) = \tilde{A}_c(-\kappa) = [\tilde{A}_c(\kappa)]^*. \quad (5.4.19)$$

In order to find appropriate values for N' and n_b , numerical simulations were made using possible sweep rates for the spatial scan, as well as realistic signal and noise levels, see next chapter. The amplitude time series was computed for a given sampling frequency of 38 MHz for a fixed number of samples of N_{DFT} , and the maximum power in the spectrum was compared against the approximation given in equation (5.4.16) for various N' and n_b .

It was found that for the considered cases, the maximum in the power spectrum of the fully sampled DFT and the approximation deviates by less than 3% for $N' = 64$ and $n_b = 6$. For most cases, the difference in the value of the maximum deviates by less than 1%. It is important to mention, that the maxima computed with the approximation, are always smaller than the maximum computed with the fully sampled DFT. For this reason, the level of accuracy is assumed to be sufficient.

5.5. Conclusions

The simulation that was described in this chapter, implements realistic models of the subsystems that are important for acquisition such as the optical bench, the laser, the fine-steering mirror, the DWS control loop as well as the photodiodes. Moreover, realistic

beam models to compute the far-field intensity are implemented as well as functions yielding accurate values of the heterodyne efficiency depending on the current alignment of the laser beams.

The included noise sources constitute an assumed worst case spectral density which is assumed to be white over the bandwidth of the photodiode. The implemented simulation of the detection algorithm, efficiently computes random variates of the expected distribution of the detector output depending on the frequency, phase and amplitude. Also, time variations of the amplitude over a single FFT can be approximated with high accuracy.

In the following the methods provided by the simulation are used to study the initial line-of-sight calibration, as well as to test a proposed algorithm for an autonomous laser link acquisition.

6. Initial Line-of-Sight Calibration

In this chapter an initial *line-of-sight (LOS) calibration* scan is analysed for the case of the GRACE Follow-On laser ranging interferometer (LRI). The initial LOS calibration is a scan over the complete uncertainty space during which the optimal alignment of the beam axis and tuning of the laser frequency is estimated from the time when the maximum detector output was recorded.

In the first section, possible scan patterns are presented and their properties are evaluated with respect to uncertainty cone coverage and applicable scan speeds. Subsequently, the frequency scan is discussed and the order of the scans is reviewed. The final result of this section is an estimate of the total time of the line-of-sight calibration scan depending on the scan resolution.

This is followed by a review of the coherent and incoherent sum combinations of the detection algorithm and an investigation of their tilt dependence. Furthermore, variations of the tilt dependence for changes of the beam width, additional phasefront curvature errors or different photodiode slit widths are determined.

The obtained results are henceforth used to estimate the allowable simultaneous misalignment of the transmitted beam with respect to the line-of-sight and of the local oscillator beam with respect to the received beam, in order to guarantee a signal that is large enough to be unambiguously above the noise.

In the last section of this chapter, the spatial distribution of line-of-sight estimates are computed with help of the high-fidelity simulation that was discussed in the previous chapter.

6.1. Spatial Scan Patterns for the Initial LOS Calibration

In this section, suitable scan patterns to cover the spatial uncertainty cones of the master and the slave spacecraft are discussed. As the speed of the scans will be significantly different on both spacecraft, the scan pattern does not necessarily have to be the same. The following analysis assumes a special order of the scans which has the frequency scan as the slowest scan and the spatial scan of the master spacecraft as the fastest scan:

<i>Slow Scan</i>	<i>Intermediate Scan</i>	<i>Fast Scan</i>
Frequency scan	→ Slave Spatial scan	→ Master Spatial scan

The reason for this particular order is given in a separate section once estimates for the spatial scan times are obtained. In principle, the total spatial scan over the spatial uncertainty space of both spacecraft is a search in four dimensions. In the following a scan of the four dimensional uncertainty space is called a *complete spatial scan*. The full spatial uncertainty space is covered, if the slow spatial scan on the slave spacecraft dwells on a single scan point at least as long as the fast scan needs to completely cover its uncertainty cone. The scan time for the fast scan will be denoted by T_1 , whereas the number of scan points in the slow spatial scan will be denoted by N_2 . The total time for a complete spatial scan, T_S , is then given by

$$T_S = N_2 t_d \geq N_2 T_1. \quad (6.1.1)$$

Here, t_d is the dwell time of the slave spacecraft on a single scan point. The notion of a *scan point* is clear for a discretely stepped scan, such as the hexagonal scan which is discussed below, but it needs some clarification for a continuous scan pattern. However, this is done later in Section 6.1.4.

The spatial scan has to be carried out multiple times for each of the scan points in the frequency scan. Hence, it is obvious that some analysis of the scan patterns that are applied to search the spatial uncertainty cone, is valuable to find efficient patterns, given the restrictions imposed by the instrument. These restrictions are for example, a limited scan speed and finite control loop bandwidth of the fine-steering mirror (FSM) as well as a limited detector field-of-view.

This section will start with presenting and discussing a small list of possible scan patterns; all having different properties. It will continue with a discussion of scan patterns for the slow scan and for the fast scan. Eventually, the frequency scan is discussed and the scan sequence is reviewed. A summary of the discussion with estimates of the total spatial scan time is given at the end.

6.1.1. Scan Patterns

The following section discusses scan patterns that are considered for implementation in the GRACE Follow-On satellites, though there are others discussed in the context of inter-satellite laser communication or constellation control of micro-satellites [SKA01].

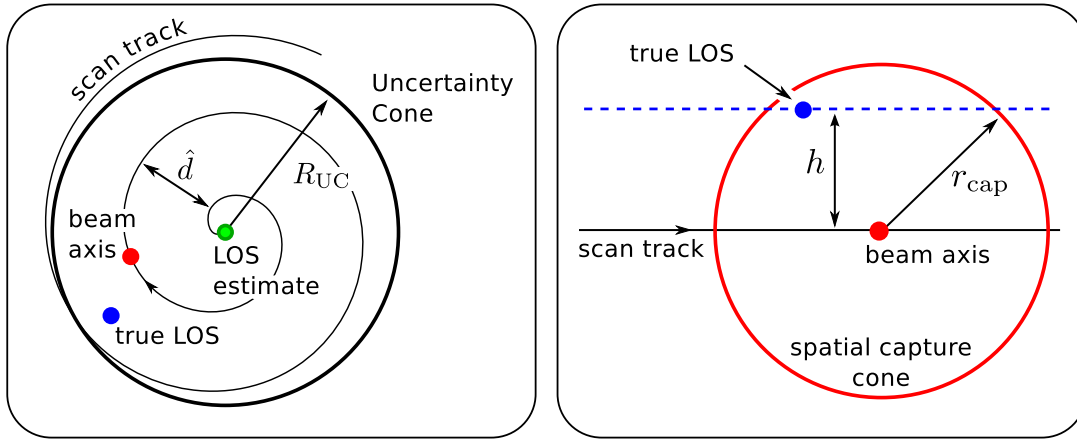


Figure 6.1.: Left: *Uncertainty cone* of radius R_{uc} around the estimated LOS. The true LOS is expected to be located at a random position within the uncertainty cone. The spatial scan determines the *scan track* on which the beam axis is swept over the uncertainty cone. The maximum separation between two neighbouring parts of the scan track is denoted by \hat{d} . Right: Close up around the beam axis. The LOS penetrates the spatial capture cone at the *LOS-to-scan-track separation*, h . The *spatial capture cone radius*, r_{cap} , is determined by the desired minimum signal power that the recorded maximum should have.

Here, scan patterns based on a hexagonal grid, an Archimedean spiral and Lissajous figures are being discussed.

The type of scan pattern can drastically decrease or increase the time needed for a complete spatial scan of the whole uncertainty cone. On the one hand, the scan pattern itself can be more efficient in covering the uncertainty cone with less overlap between neighbouring scan points. On the other hand, the scan has to be carried out by the FSM that is mounted on the optical bench of the LRI. The finite bandwidth of the FSM control-loop limits the time, the FSM needs to settle to a commanded position and its transfer function introduces deviations of the real steering mirror position from the commanded value. Hence, when talking about a suitable scan pattern, the properties of the scan pattern and the restrictions imposed by the instrument have to be taken into account.

In analysing spatial scan patterns, some quantities are of interest which are explained in Figure 6.1. The left panel shows the *uncertainty cone* of radius R_{uc} around the *estimated line-of-sight*. The beam axis is swept along the *scan track* in order to scan the complete uncertainty cone, in which the *true line-of-sight* is located at an unknown, random position; this is where the other spacecraft is. The separation between two adjacent parts of the scan track is denoted by d and the maximum separation occurring

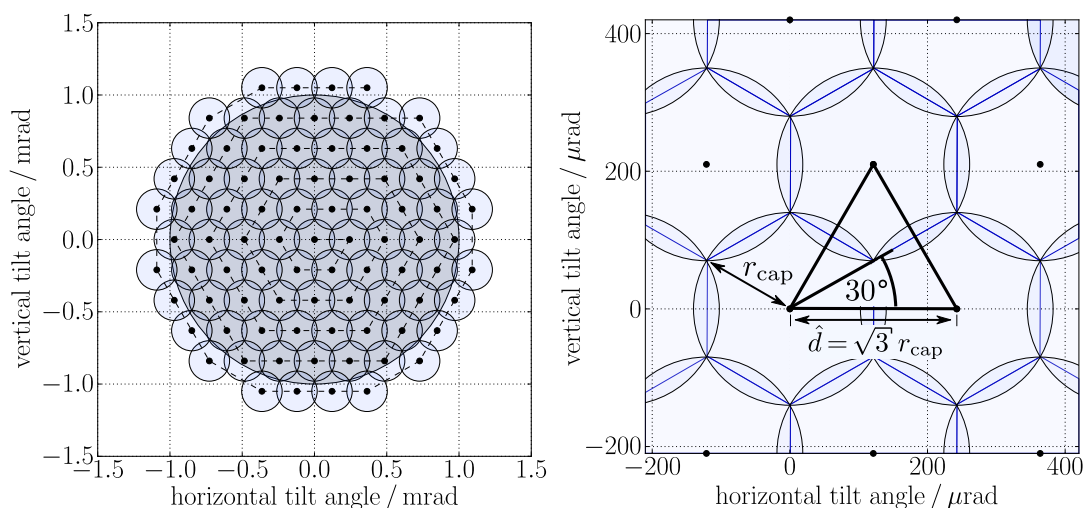


Figure 6.2.: Left: Hexagonal scan pattern for an uncertainty cone of radius $R_{uc} = 1$ mrad. The desired capture range is $r_{cap} = 140 \mu\text{rad}$. Right: Zoomed in version of the scan pattern. The scan points are distributed on vertices of equilateral triangles with side lengths of $\hat{d} = \sqrt{3} r_{cap}$, whereas the intersection points of the scan points form hexagons.

for any point along the scan track by \hat{d} .

The right panel in Figure 6.1 shows a close up of the region around the beam axis, with the *spatial capture cone* drawn around it. The radius of the spatial capture cone r_{cap} is determined by the minimum signal power that is desired for the maximum recorded signal during the pick-max scan. It is also called the *spatial capture range*. Hence, the spatial scan should be set up such that the LOS remains within the *spatial capture cone* for at least the required dwell time t_d . Generally, r_{cap} is not required to be the same for the master and the slave spacecraft, though this is assumed for the analysis in this chapter, because it significantly reduces the complexity of the acquisition algorithm. In the following section three types of scan patterns are introduced which are a hexagonal scan, an Archimedean spiral scan and a Lissajous raster scan.

Hexagonal Scan

The most efficient coverage of the plane with circles uses a hexagonal pattern, where every scan point lies in the centre of a hexagon. The hexagonal scan is a discretely stepped scan for which the *scan track* consists of individual, separated points. The separation between any two points is identical, $d = \hat{d}$. The maximum deviation of the true LOS from the closest scan point is equal to $\hat{d}/\sqrt{3}$. Thus, for a desired capture

range of r_{cap} , the scan point separation should be chosen such that

$$\hat{d} = \sqrt{3} r_{\text{cap}}. \quad (6.1.2)$$

This allows for the least overlap between neighbouring scan points. The scan points can be visited in a kind of spiral pattern starting from the centre and continuing outwards, until the whole uncertainty cone is covered. Reinitialisation requires either reverting the scan or jumping back to the central starting point. To fully exploit the optimality of the hexagonal scan a discrete stepping has to be applied.

The left plot in Figure 6.2 shows an example of an uncertainty cone of radius $R_{\text{uc}} = 1$ mrad, covered by a hexagonal scan with a desired capture range of $r_{\text{cap}} = 140 \mu\text{rad}$ that uses 85 scan points. The right plot shows a close up of the central region to highlight that the scan points are located at the vertices of equilateral triangles with a side length of $\sqrt{3} r_{\text{cap}}$. Also shown are the hexagons around the centre of a scan point which are formed by the intersection points of the capture cones of neighbouring scan points. Scan points for which all of the vertices of the surrounding hexagon lie outside the uncertainty cone are excluded, as they either redundantly cover parts of the uncertainty cone or have no intersection region with it at all.

Archimedean Spiral Scan

A continuous spiral scan can be realised by scanning the uncertainty cone with an Archimedean spiral, starting also from the centre of the uncertainty cone and spiralling outwards until it is fully covered. The Archimedean spiral is special in the way that the spiral arm separation, d , and the angular sweep rate are constant, except for a small period at the centre where the angular accelerations are much larger. The coordinates for the scan track can be computed by the following formula:

$$\mathbf{r}(t) = \frac{d}{2\pi} \phi(t) \begin{pmatrix} \cos \phi(t) \\ \sin \phi(t) \end{pmatrix}, \text{ where } \phi(t) = 2\pi \frac{r_{\text{max}}}{d} \sqrt{\frac{t}{T}}. \quad (6.1.3)$$

Here, T is the scan time for a complete coverage and r_{max} is the maximum radius of the spiral. The maximum scan track separation is equal to the arm separation, $\hat{d} = d$, as the arm separation is constant. The true LOS is farthest away from any point on the scan track if it lies directly in between two adjacent spiral arms. Hence, the maximum possible separation between the LOS and the scan track is $\hat{h} = d/2$. The spiral arm

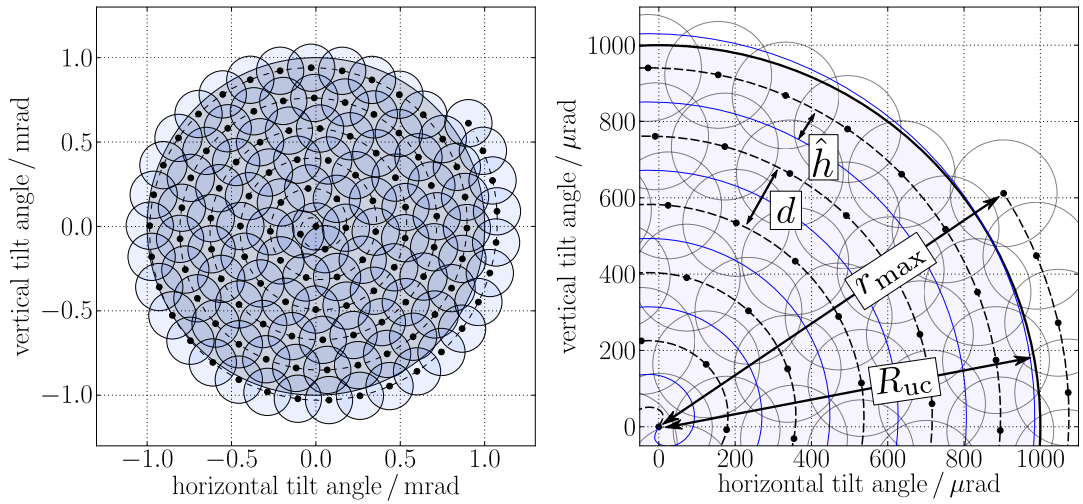


Figure 6.3.: Left: Archimedean scan pattern for an uncertainty cone of $R_{uc} = 1$ mrad and a desired capture range of $r_{cap} = 140 \mu\text{rad}$ that is indicated by the drawn circles. Right: Zoomed in version of the scan pattern that shows the geometric length scales of the Archimedean spiral.

separation, d , should generally be chosen such that

$$\hat{h} = \frac{d}{2} < r_{cap}, \quad (6.1.4)$$

due to the continuous movement of the beam axis along the scan track. The details on this are given in Section 6.1.2. The left plot in Figure 6.3 shows an example of an Archimedean spiral scan for an uncertainty cone of radius $R_{uc} = 1$ mrad and a desired capture range of $r_{cap} = 140 \mu\text{rad}$. The right plot shows the introduced quantities, such as the arm separation, d , the maximum LOS-to-scan-track separation, \hat{h} , and the maximum scan radius r_{max} . The maximum scan radius, $r_{max} = R_{uc} + d/2$, is chosen larger than the uncertainty cone radius by half the arm separation to achieve full coverage of the uncertainty cone.

The scan speed of the Archimedean spiral is large at the centre but rapidly approaches a nearly constant sweep rate which can be given in terms of the maximum scan radius, the arm separation and scan time as follows:

$$v_{arch} = \frac{r_{max}}{2dT} \sqrt{4\pi^2 r_{max}^2 + d^2 \frac{T}{t}} \stackrel{t \rightarrow \infty}{\approx} \frac{\pi}{T} \frac{r_{max}^2}{d}. \quad (6.1.5)$$

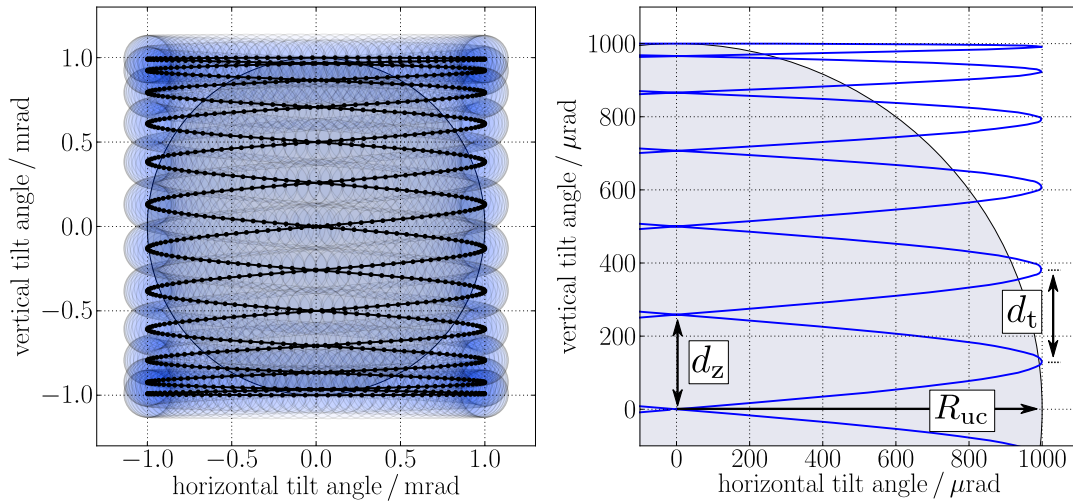


Figure 6.4.: Left: Lissajous raster scan for an uncertainty cone radius of $R_{uc} = 1$ mrad and a frequency ratio of $n = 12$, resulting in a worst case misalignment of $\hat{h} = 129$ μ rad. Right: Close up of the Lissajous figure shown in the left plot, showing the distance between the central zero-crossings, d_z , and the central turning points, d_t .

Lissajous Scan

Also a Lissajous raster scan can be performed, for which the two orthogonal axes of the steering mirror are driven by sinusoidal signals with constant frequencies. A raster scan implies a higher frequency, \hat{f} , in one of the axis and a lower frequency, \check{f} , in the other direction to scan over the two dimensional uncertainty cone. An important quantity to characterise Lissajous patterns is the frequency ratio

$$n = \hat{f}/\check{f}. \quad (6.1.6)$$

The scan pattern is equal to a closed Lissajous figure if the ratio of the frequencies in the two axes is a rational number, $n \in \mathbb{Q}$. Then the scan is periodic with a period of

$$T = \check{f}^{-1} = n \hat{f}^{-1}. \quad (6.1.7)$$

However, here the discussion is restricted to integer frequency ratios. The coordinates of the scan track can be calculated with help of the following formula:

$$\mathbf{r}(t) = R_{uc} \begin{pmatrix} \sin(2\pi\hat{f}t + \phi_n) \\ \sin(2\pi(\hat{f}/n)t) \end{pmatrix}, \quad \text{with } \phi_n = \begin{cases} 0 & , \text{ if } n \text{ is even,} \\ \pi/2 & , \text{ if } n \text{ is odd.} \end{cases} \quad (6.1.8)$$

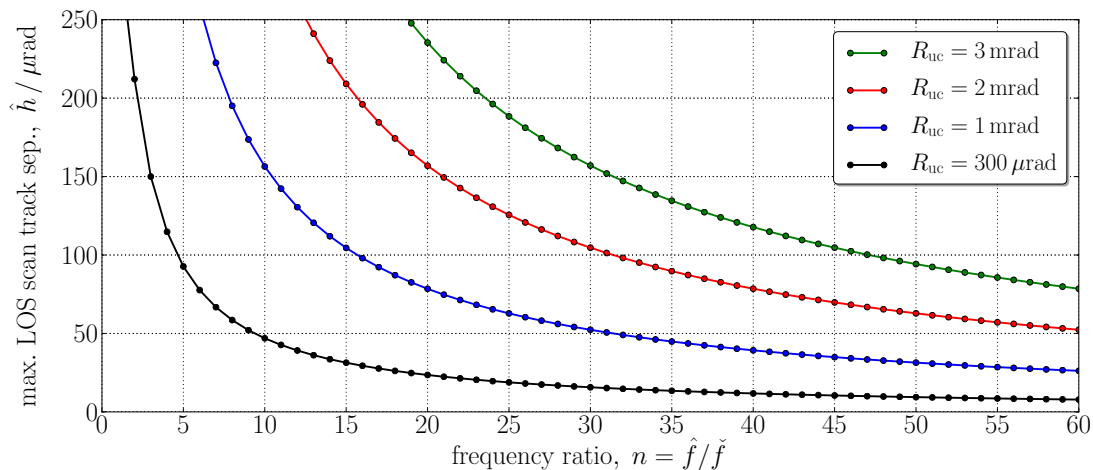


Figure 6.5.: Maximum LOS-to-scan-track separation, \hat{h} , during a Lissajous scan, as a function of the frequency ratio n , for different uncertainty cone radii, R_{uc} . Computed using equations (6.1.11) and (6.1.9).

R_{uc} is again the radius of the uncertainty cone. The additional phase shift, ϕ_n , is necessary to avoid patterns which repeat after a time $t = 1/(2\check{f})$ and have a coarser uncertainty cone coverage.

Figure 6.4 shows a Lissajous raster scan with a frequency ratio of $n = 12$ which results in a maximum scan track separation of $\hat{h} = 129 \mu\text{rad}$, for an uncertainty cone radius of $R_{uc} = 1 \text{ mrad}$. For integer frequency ratios the maximum scan track separation during a Lissajous scan occurs either between the central zero crossings in the centre of the uncertainty cone or at the central turning points at the edge of the uncertainty cone. The right plot in Figure 6.4 shows the location of the maximum scan track separation for a Lissajous scan with even frequency ratio. The separation between the central zero crossings, d_z , or the turning points, d_t , can be calculated by

$$\begin{aligned} \text{for odd } n: d_t(n) &= R_{uc} |\sin \pi/n| & \text{for even } n: d_t(n) &= 2R_{uc} |\sin \pi/2n| \\ d_z(n) &= 2R_{uc} |\sin \pi/2n| & d_z(n) &= R_{uc} |\sin \pi/n|. \end{aligned} \quad (6.1.9)$$

And the maximum scan track separation is approximately the maximum of d_t and d_z :

$$\hat{d} \approx \max(d_t, d_z). \quad (6.1.10)$$

The point right between the two central zero-crossings or turning points is the one which has maximum separation to the scan track, for any point in the uncertainty cone. Hence,

the maximum separation between the LOS and the point on the scan track that closest approaches the LOS is half the maximum scan track separation, $\hat{h} = \hat{d}/2$. For a desired capture range of r_{cap} and uncertainty cone radius, the frequency ratio of the Lissajous scan should be chosen such that

$$\hat{h}(n, R_{\text{uc}}) \approx \frac{1}{2} \max [d_t(n, R_{\text{uc}}), d_z(n, R_{\text{uc}})] < r_{\text{cap}}. \quad (6.1.11)$$

Figure 6.5 shows the maximum LOS-to-scan-track separation computed from equation (6.1.11) as a function of the frequency ratio, n , for four different uncertainty cone radii R_{uc} . The sweep rates during the Lissajous scan vary periodically between the turning points and the zero crossing of the fast scan axis. The maximum sweep rate, \hat{v}_{lis} , can be approximated if the fast axis frequency is larger than the slow axis frequency which is the case for all scan patterns discussed for the calibration scan. It can be given as

$$\hat{v}_{\text{lis}} \approx 2\pi R_{\text{uc}} \hat{f} = \frac{2\pi}{T} n R_{\text{uc}}. \quad (6.1.12)$$

Table 6.1 lists the maximum scan speeds of the Lissajous scan for different uncertainty cone radii and a fast axis frequency of $\hat{f} = 100$ Hz.

6.1.2. Synchronising the Spatial Scans

An important limit to the time necessary for total acquisition arises from the need to synchronise the spatial scans on both satellites such that the full four dimensional search space is covered. In particular, this sets the time, T_2 , of the slow scan, depending on the time, T_1 , to complete the fast spatial scan on the other satellite. Figure 6.6 visualises the argument applied in the following section.

Table 6.1.: Maximum scan speeds of the Lissajous scan, \hat{v}_{lis} , for different uncertainty cone radii and corresponding maximum angular range swept over during a single FFT, $r_d = \hat{v}_{\text{lis}} t_{\text{FFT}}$, where $t_{\text{FFT}} = N_{\text{DFT}}/f_s$. The fast axis frequency is set to $\hat{f} = 100$ Hz and the sampling frequency is assumed to be $f_s = 38$ MHz.

$R_{\text{uc}} / \text{mrad}$	$\hat{v}_{\text{lis}} / \text{rad s}^{-1}$	$r_d / \mu\text{rad}$		
N_{DFT}		4096	2048	1024
0.3	0.19	20.5	10.2	5.1
1	0.63	67.9	34.0	17.0
2	1.3	140.1	70.1	35.0
3	1.9	204.8	102.4	51.2

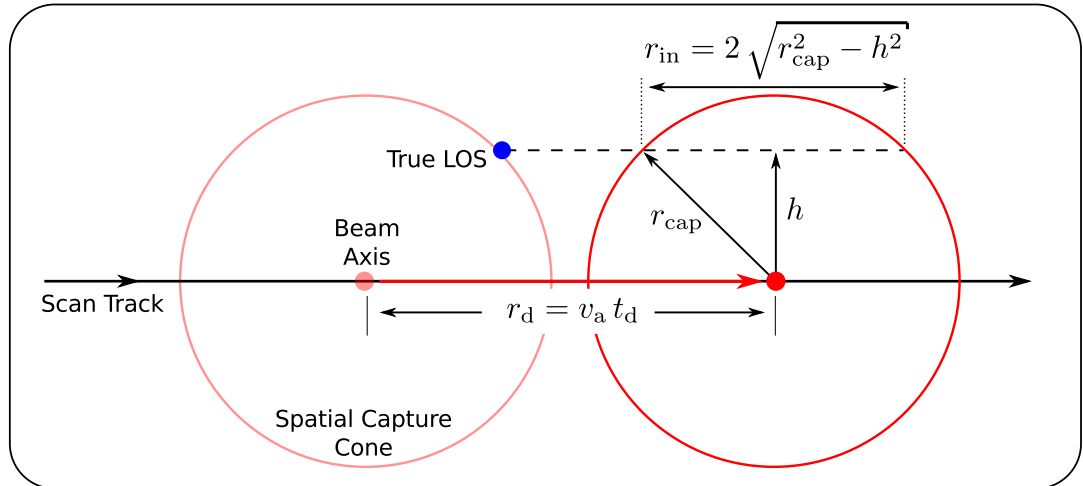


Figure 6.6.: Geometric relation between the spatial capture range, r_{cap} , the separation between the LOS and the scan track, h , as well as the angular scan rate, v_a . r_{in} is the distance the line-of-sight will stay in the spatial capture cone if the beam is swept along the scan track by r_d , with a rate of v_a during the dwell time t_d . If the LOS should remain within the spatial capture cone for a complete FFT, the beam axis has to be swept by no more than r_{in} during the dwell time.

The beam axis is swept along the scan track which is determined by the chosen scan pattern. In the figure, the scan track is locally approximated by a straight line. If the scan pattern is dense enough, every point within the uncertainty cone will be covered by the spatial capture cone around the beam axis. Hence, the LOS (blue dot in Figure 6.6) will penetrate the spatial capture cone at a certain separation, h , from the scan track. The length of the track, the LOS will propagate inside the spatial capture cone, is the chord of the circle at separation h from the centre of the circle. The length of the chord is easily computed by

$$r_{\text{in}} = 2\sqrt{r_{\text{cap}}^2 - h^2}. \quad (6.1.13)$$

The time the LOS will stay inside the worst case misalignment cone is the ratio of the length of the chord and the angular sweep rate, v_a , of the beam axis at the considered part of the scan pattern:

$$t_{\text{in}} = \frac{r_{\text{in}}}{v_a}. \quad (6.1.14)$$

Generally, t_{in} will be different for different points along the scan track. By choosing the worst possible misalignment of the LOS to the scan track for each point of the scan

track and calculating the sweep rate of the scan at this point, the minimum time that the LOS will stay inside the worst case misalignment cone can be estimated. This time should be chosen as the dwell time for the search and the scan speed should be adapted if the fast scan cannot be finished during the dwell time of the slow scan.

6.1.3. Fast Spatial Scan

Given the different scan patterns above, following is a discussion on their suitability for the fast scan on the master spacecraft. As said before, the hexagonal scan pattern has the most efficient coverage of the uncertainty cone because it minimises the overlap between neighbouring scan points. Despite the fact that it needs the least number of points, it is not suitable to be used as the scan pattern for the fast spatial scan on the master spacecraft.

This is due to the discrete stepping between scan points and the finite bandwidth of the FSM control loop which results in a finite settling time, τ_{FSM} , onto a commanded scan point. The full transition between scan points will take some time of the order of some milliseconds, depending on the actual implementation of the controller. The dwell time for each scan point of the fast scan would then compute to

$$t_d = t_{\text{FFT}} + \tau_{\text{FSM}} = t_{\text{FFT}} \left(1 + \frac{\tau_{\text{FSM}}}{t_{\text{FFT}}} \right), \quad (6.1.15)$$

where t_{FFT} is the time necessary to take data for a single FFT, $t_{\text{FFT}} = N_{\text{DFT}}/f_s$. The time for total acquisition is thus increased by a factor of $a = (1 + \tau_{\text{FSM}}/t_{\text{FFT}})$. In the previous chapter, FFTs of length 2048 or 4096 point were found to be suitable in order to achieve high enough SNR. The time for a single FFT of 4096 points sampled at $f_s = 38 \text{ MHz}$ is of the order of $100 \mu\text{s}$.

In Figure 5.3, the step response of the steering mirror was shown for a single-pole low pass filter with a pole frequency of $f_{\text{pole}} = 100 \text{ Hz}$. The resulting settling time can be seen to be $\tau_{\text{FSM}} \approx 10 \text{ ms}$ which results in a factor of $a \approx 101$. This adds unacceptable overhead which rules out the hexagonal scan for the fast scan.

The Archimedean scan is a continuous scan pattern. It also has an efficient coverage of the uncertainty cone, compared to the Lissajous scan. However, continuous scans will be distorted by the steering mirror response function such that a complete coverage of the uncertainty cone can only be guaranteed if the scan track separation is reduced to increase the overlap of the spatial capture cone. For the Archimedean spiral this problem mainly occurs at the centre of the spiral where the accelerations are highest. Decreasing the arm separation, however, will increase the scan time.

Another possibility is to measure the steering mirror response function and invert the effect of the distortion by precomputing a spiral pattern that, when distorted by the FSM response function, will give the desired Archimedean spiral. Though the transformation is straightforward, it needs to be computed each time the speed of the scan, the uncertainty cone or spiral arm separation is changed.

The last scan pattern remaining in the list is the Lissajous scan pattern. Though the FSM frequency response will also effect the Lissajous scan, the change is much simpler to compute, because it only changes the amplitude and phase of the sinusoidal signal supplied to the steering mirror by the gain and phase of the FSM's transfer function at the frequency of the input signal. The following corrections to the amplitude and phase should be applied

$$\mathbf{r}(t) = R_{uc} \begin{pmatrix} |\hat{c}_{yaw}|^{-1} \sin(2\pi \hat{f}t + \phi_n + \arg \hat{c}_{yaw}) \\ |\check{c}_{pitch}|^{-1} \sin(2\pi \check{f}t + \arg \check{c}_{pitch}) \end{pmatrix}, \quad (6.1.16)$$

where the correction factors are computed from the transfer function, $\tilde{H}_{FSM,i}$ with $i = \text{yaw, pitch}$, function by

$$\hat{c}_i = \tilde{H}_{FSM,i}(\hat{f}), \quad \text{and} \quad \check{c}_i = \tilde{H}_{FSM,i}(\check{f}). \quad (6.1.17)$$

This simple correction that involves only simple scalar correction factors is a big advantage of the Lissajous raster scan. In the following, an estimate for the time needed by a Lissajous raster scan is given, depending on the maximum LOS-to-scan-track separation, \hat{h} . This is a necessary intermediate result, to estimate the total time needed for the whole calibration process.

Equation (6.1.11) gives the maximum LOS-to-scan-track separation, \hat{h} , of the Lissajous scan, given the uncertainty cone radius, R_{uc} , and the frequency ratio, n . Since the time for a full scan is given by $T = 1/\check{f} = n/\hat{f}$, finding the smallest frequency ratio for which the maximum LOS-to-scan-track separation is smaller than the desired spatial capture range

$$\hat{h}(n, R_{uc}) < r_{cap}, \quad (6.1.18)$$

gives the minimum scan time for the chosen r_{cap} and uncertainty cone radius. \hat{h} as a function of the frequency ratio was given in Figure 6.5.

Figure 6.7 shows the minimum scan time for a Lissajous scan for different uncertainty cone radii, depending on the desired spatial capture range, if the above rule of

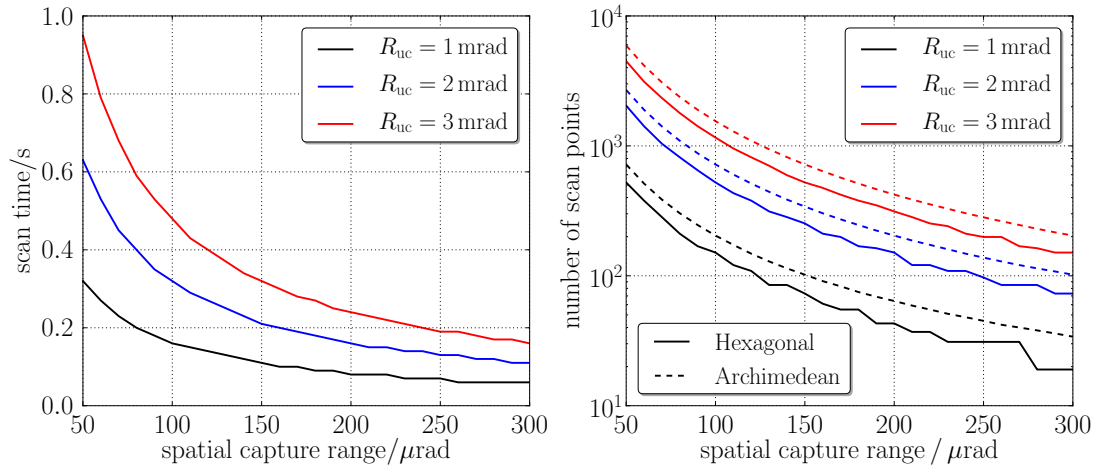


Figure 6.7.: Left: Scan time for a Lissajous raster scan with a fast axis frequency of $\hat{f} = 100$ Hz, depending on the desired spatial capture range, r_{cap} , and different uncertainty cone radii, R_{uc} , using equation (6.1.18). Right: Number of scan points needed by the hexagonal and Archimedean scan to cover the whole uncertainty cone, depending on a desired spatial capture range, r_{cap} , for different uncertainty cone radii. The number of scan points needed by the Archimedean scan is calculated by minimising equation (6.1.22). The Archimedean scan roughly needs about 30% more scan points than the hexagonal scan.

equations (6.1.18) or (6.1.11) is used.

6.1.4. Slow Spatial Scan

Now the scan patterns which are usable for the slow spatial scan are discussed and an estimate of the number of scan points necessary to cover the uncertainty cone is given, depending on the desired capture range. As said in the last section, the hexagonal scan pattern covers the uncertainty cone most efficiently by minimising the overlap between neighbouring scan points. The left plot in Figure 6.7 shows the number of scan points that are necessary to fully cover the uncertainty cone, as a function of the desired spatial capture range and for three different uncertainty cone radii. For small scan point radii the number of points is proportional to the square of the uncertainty cone radius, as expected.

In contrast to the fast scan, here, the dwell time on each scan point of the slow scan is not equal to t_{FFT} , but it is equal to the scan time of the fast scan, T_1 . Hence, replacing t_{FFT} by T_1 in equation (6.1.15) and comparing the settling time to the scan time of the

master spacecraft

$$t_d = T_1 \left(1 + \frac{\tau_{\text{FSM}}}{T_1} \right), \quad (6.1.19)$$

shows that for the slow scan the additional time penalty, τ_{FSM} , is small for all realistic scan times of the master spacecraft. For example, from Figure 6.7 the scan time, T_1 , for an uncertainty cone of radius $R_{\text{uc}} = 1 \text{ mrad}$ and a desired spatial capture range of $r_{\text{cap}} = 300 \text{ } \mu\text{rad}$, can be found to be $T_1 \approx 50 \text{ ms}$. For this case, the dwell time is computed to $t_d = 1.2 T_1$, which adds a 20% overhead to the dwell time, compared to the scan time of the fast scan. However, for a more realistic case of an uncertainty cone radius of $R_{\text{uc}} = 3 \text{ mrad}$ and a desired capture range of $r_{\text{cap}} = 150 \text{ } \mu\text{rad}$, the scan time for the fast scan is $T_1 = 0.32 \text{ s}$ which results in a dwell time of $t_d = 1.03 T_1$.

Turning now to the Archimedean spiral scan, the first thing to do is to get an equivalent for the number of scan points in the spiral scan. This will make it possible to compare the hexagonal scan with the Archimedean spiral. In order to get complete coverage of the uncertainty cone for the case of the slow scan, the LOS has to remain within the spatial capture cone while the fast scanning spacecraft finishes one complete scan. Starting from the centre of the spiral this will give a partition of the scan track which is depending on the uncertainty cone radius, the desired spatial capture range and the chosen arm separation.

The explanation is given in Figure 6.6. The arm separation, d , will set the maximum separation between the LOS and the scan track to $\hat{h} = d/2$, because adjacent spiral arms are all separated by the same distance. The worst case is if the LOS exactly lies in the middle between two spiral arms at a distance of \hat{h} from the scan track. For this case the chord through the spatial capture cone of radius r_{cap} at a height of \hat{h} will give the maximum range the scan is allowed to advance such that the LOS will stay inside the spatial capture cone. Since the sweep rate of the Archimedean spiral is approximately constant after a short initial period, shown in equation (6.1.5), this can be used to partition the scan track into sections of equal length. These sections are henceforth called *scan points of the archimedean spiral* or just *scan points*. The number of scan points can then easily be calculated from the length of the complete spiral divided by the length of the sections. A derivation of the number of scan points follows. The length of the spiral, from the centre to the end point, can be given in terms of the spiral arm separation, d , and the maximum deviation from the centre, r_{max} , by

$$L(d, r_{\text{max}}) = \frac{d}{4\pi} \left(\phi_{\text{max}} \sqrt{\phi_{\text{max}} + 1} + \ln(\phi_{\text{max}} + \sqrt{\phi_{\text{max}} + 1}) \right), \quad (6.1.20)$$

where ϕ_{\max} is defined as

$$\phi_{\max} = 2\pi \left(\frac{1}{2} + \frac{r_{\max}}{d} \right). \quad (6.1.21)$$

The number of scan points, N_2 , necessary to cover the complete uncertainty cone, is then given by the length of the spiral, divided by the length of the chord, r_{in} , through the spatial capture cone at a height of $\hat{h} = d/2$. The maximum radius of the spiral necessary to completely cover the uncertainty cone, is chosen as $r_{\max} = R_{\text{uc}} + \hat{h}$ which is shown in Figure 6.3. The number of scan points can then be calculated by the ratio between the length of the spiral and the length of the chord, r_{in} , through the worst case misalignment cone, given in equation (6.1.13) as

$$N_2 = \frac{L(2\hat{h}, R_{\text{uc}} + \hat{h})}{2\sqrt{r_{\text{cap}}^2 - \hat{h}^2}}. \quad (6.1.22)$$

For smaller \hat{h} , hence, smaller spiral arm separation, the length of the spiral increases, whereas r_{in} is bound by the diameter of the spatial capture cone and thus, the number of scan points increases. On the other hand, increasing \hat{h} decreases the spiral length while also r_{in} decreases. It is equal to zero if $\hat{h} = r_{\text{cap}}$, because for this case the chord through the circle is equal to the tangent to the circle and the number of scan points approaches infinity. However, it is clear that in between these two extremal points, there must be a minimum number of scan points, necessary for complete uncertainty cone coverage. Due to the transcendental nature of the equation, only numerical methods can be used to find the optimum number of points for N_2 . In the left plot of Figure 6.7, the minimum number of points for the Archimedean spiral is compared to the number of points needed for a hexagonal scan. Shown is the dependence of the number of scan points for a fixed uncertainty cone radius, but for a varying capture range. The comparison yields that the Archimedean scan roughly needs about 30% to 50% percent more points than the hexagonal scan.

Now, putting everything together, the time for the four dimensional spatial scan can be estimated using equation (6.1.1) and assuming that the fast scan is done with a Lissajous raster scan and the slow scan with either a hexagonal or Archimedean spiral scan. Figure 6.8 shows the necessary time for a complete spatial scan depending on the desired capture range, uncertainty cone radius and scan pattern, if the dwell time, t_{d} , is set to the scan time of the master spacecraft. For a scan of a 3 mrad uncertainty cone with a desired capture range of 150 μrad , the scan time is roughly 180 s for a

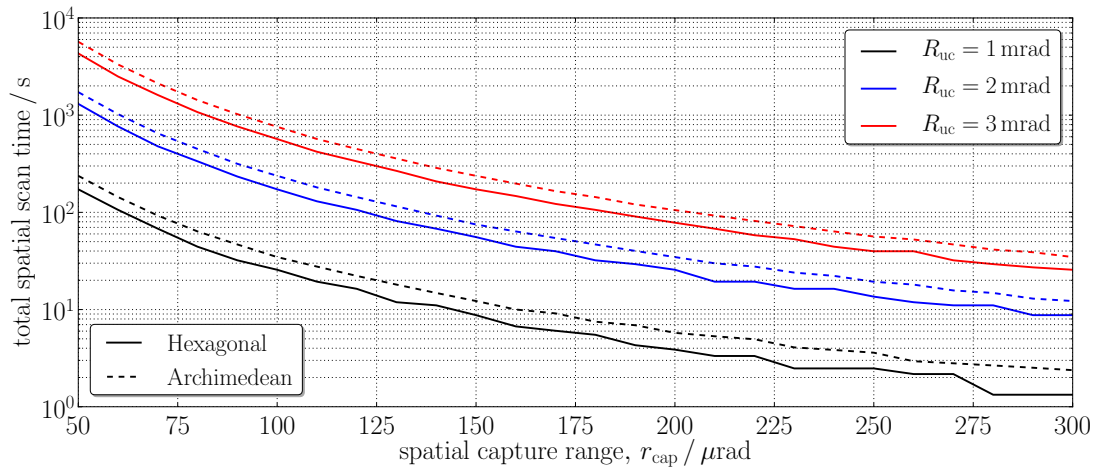


Figure 6.8.: Total scan time for a complete four dimensional spatial scan estimated using equation (6.1.1) and assuming that the fast scan is done with a Lissajous raster scan and the slow scan with either a hexagonal or Archimedean spiral scan. This plot combines the results shown in Figure 6.7.

hexagonal scan and 250 s for an Archimedean spiral scan. The 30 % increased scan time of the Archimedean spiral scan, due to the increased number of scan points, needs to be compared to the increase in scan time of the hexagonal scan due to the additional settling time of the steering-mirror, τ_{FSM} , that needs to be considered. With equation (6.1.19) the time penalty of the hexagonal scan was estimated to be at most 20 %, for the case of an uncertainty cone of radius $R_{\text{uc}} = 1$ mrad and capture range of $r_{\text{cap}} = 300 \mu\text{rad}$. This is still less than the time needed, if an Archimedean spiral scan is used.

6.2. Frequency Scan, Scan Order and Total Acquisition Time

During the initial LOS calibration scan, the spatial uncertainty cone and also the unknown frequency interval have to be scanned. For a fixed, desired total scan time for the initial LOS calibration scan, the position of the frequency scan in the order of the scans determines the frequency sweep rate. The following three orders are discussed here where the slave spacecraft always performs the slow spatial scan and the master the fast spatial scan:

<i>Slow Scan</i>	<i>Intermediate Scan</i>	<i>Fast Scan</i>
(1) Frequency scan	→ Slave Spatial scan	→ Master Spatial scan
(2) Slave Spatial scan	→ Frequency scan	→ Master Spatial scan
(3) Slave Spatial scan	→ Master Spatial scan	→ Frequency scan

In the following, expressions for the total scan time and the frequency sweep rate are derived for the first of the three cases which is the case assumed so far. The frequency sweep rates and total acquisition times for some representative cases are given.

At the end, sweep rates and scan times are computed for the two remaining scan orders, (2) and (3), and compared to the results obtained for the first case. The frequency scan is assumed to be a linear ramp with a constant *scan rate* or *sweep rate*, v_s , starting from a lower bound, f_{low} . The momentary frequency during the scan is computed by

$$f_{\text{sweep}}(t) = v_s t + f_{\text{low}}. \quad (6.2.1)$$

Also the number of frequency scan points can be defined with the frequency uncertainty interval, F_{uc} , and the usable photodiode bandwidth, F_{PD} , by

$$N_f = \frac{F_{\text{uc}}}{F_{\text{PD}}}. \quad (6.2.2)$$

At first, a slow frequency scan, an intermediate spatial scan on the slave spacecraft and a fast spatial scan on the master spacecraft is assumed:

<i>Slow Scan</i>	<i>Intermediate Scan</i>	<i>Fast Scan</i>
(1) Frequency scan	→ Slave Spatial scan	→ Master Spatial scan

In this order, a complete scan of the four dimensional spatial scan is performed while the frequency scan advances by at most the usable frequency band of the photodiode, F_{PD} . The full scan time, T , for the initial LOS calibration scan is then given by the time for a complete four-dimensional spatial scan, T_S , and the number of frequency scan points calculated from equation (6.2.2) by

$$T = N_f T_S. \quad (6.2.3)$$

For this case the maximum frequency sweep rate, v_s , that needs to be applied can be computed from the time for a complete spatial scan, T_S , and the width of the usable

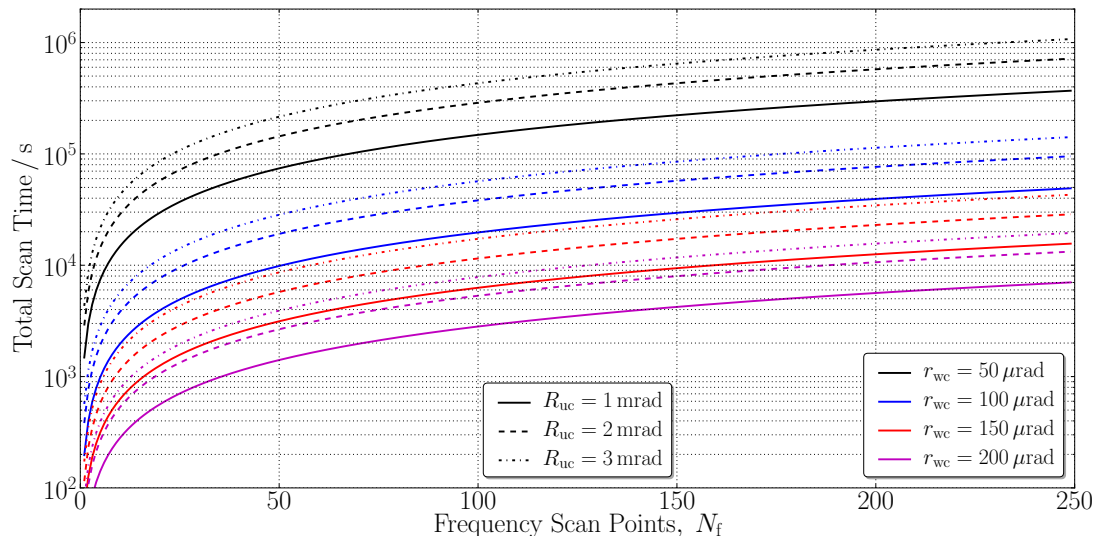


Figure 6.9.: Total scan time for a five-dimensional LOS calibration scan, as a function of the number of frequency scan points N_f . For spatial scan times of Figure 6.8.

frequency band of the photodiode, F_{PD} by

$$v_s = \frac{F_{PD}}{T_S}. \quad (6.2.4)$$

This assumes that the beatnote frequency sweeps over the full photodiode bandwidth once for each performed spatial scan.

The complete time for an initial LOS calibration scan can be computed from the times for a complete spatial scan given in Figure 6.8. Choosing some representative values for the desired spatial capture range, r_{cap} , and the three uncertainty cone radii, the total time, T , can be computed. Figure 6.9 shows T for some representative combinations of R_{uc} and r_{cap} as a function of the number of frequency scan points. In Figure 6.10 the frequency sweep rates for a photodiode bandwidth of $F_{PD} = 15$ MHz are shown.

For example, with $F_{PD} = 15$ MHz and $F_{uc} = 2$ GHz, the number of frequency scan points is $N_f = 133$. If for the fast spatial scan a Lissajous scan and for the slower spatial scan a hexagonal scan is used, with an uncertainty cone radius of $R_{uc} = 3$ mrad and a desired capture range of $r_{cap} = 150$ μ rad, the complete spatial scan time is $T_2 = 167$ s. The total time to cover the five-dimensional uncertainty space then results in, $T = 133 \cdot 180$ s = 22 211 s = 6.2 h. The plot in Figure 6.10 shows the sweep rates for the scan times computed in the section about the spatial scan and shown in Figure 6.8. These frequency sweep rates of less than 2 MHz s⁻¹ are small enough such that no reduction in

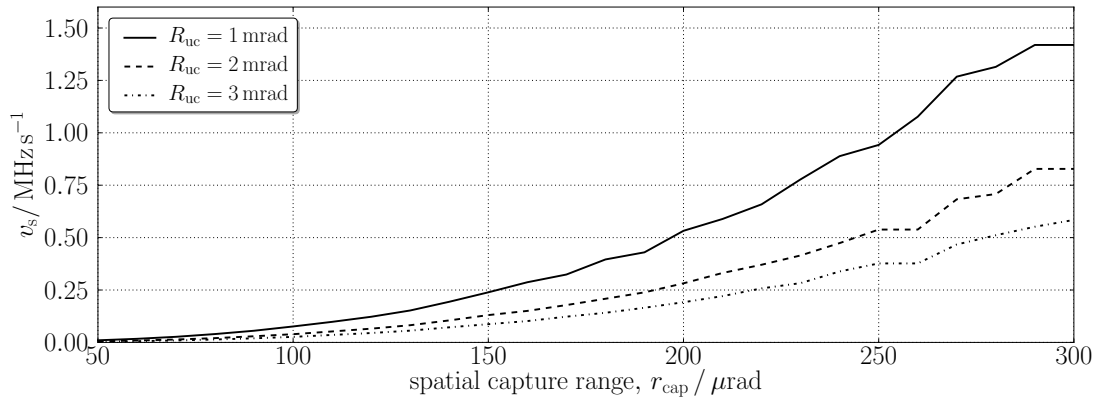


Figure 6.10.: Frequency sweep rates computed with equation (6.2.4) for the spatial scan times shown in Figure 6.8 and a photodiode bandwidth of $F_{\text{PD}} = 15 \text{ MHz}$. The spatial scan on the slave spacecraft is assumed to be a hexagonal scan, whereas the master spacecraft performs a Lissajous raster scan.

signal-to-noise ratio, due to the finite frequency bin width of the FFT is expected. See Figure 4.11 and Table 4.2 for maximum sweep rates for a given FFT length.

In order to show that the first scan sequence is already a good choice, the total acquisition time and the frequency sweep rates for the two remaining sequences are computed. The following numbers represent a scan over a large uncertainty cone and are used for the comparison: $R_{\text{uc}} = 3 \text{ mrad}$, $r_{\text{cap}} = 150 \mu\text{rad}$, $F_{\text{PD}} = 15 \text{ MHz}$ and $F_{\text{uc}} = 2 \text{ GHz}$. At first, sequence (3) is investigated which has the frequency scan as the fastest scan and the spatial scans as the slower scans:

$$\begin{array}{ccc}
 \textit{Slow Scan} & & \textit{Intermediate Scan} & & \textit{Fast Scan} \\
 (3) \text{ Slave Spatial scan} & \rightarrow & \text{Master Spatial scan} & \rightarrow & \mathbf{\text{Frequency scan}}
 \end{array}$$

The scan pattern of the master spacecraft can now also be chosen as a hexagonal scan, because for this case the dwell time on each scan point is the time for a complete frequency scan, and therefore longer than the fine-steering mirror settling time, τ_{FSM} . The number of scan points in the hexagonal scan is here denoted by N . The total acquisition time is then given by

$$T = N^2 T_f, \quad (6.2.5)$$

if the frequency scan time is denoted by T_f . For the case considered here, the number of scan points in the hexagonal scan is $N = 523$. In order to achieve the same total

acquisition time of $T \approx 22\,000$ s, the frequency scan time has to be $T_f \approx 80$ ms which, however, results in a frequency scan rate of $v_s \approx 25$ GHz s⁻¹ which leads to a strongly reduced SNR. The last option is to scan the frequency as the intermediate scan:

$$\begin{array}{ccc}
 \textit{Slow Scan} & & \textit{Intermediate Scan} & & \textit{Fast Scan} \\
 (2) \quad \text{Slave Spatial scan} & \rightarrow & \mathbf{\text{Frequency scan}} & \rightarrow & \text{Master Spatial scan}
 \end{array}$$

The total time for the LOS calibration for this case is given as the product of the number of scan points in the hexagonal scan, N_2 , the number of frequency scan points, N_f , and the time for the fast spatial scan on the master by

$$T = N_2 N_f T_1. \quad (6.2.6)$$

Again, using the example from above and using a Lissajous scan on the master with a scan time of $T_1 = 0.32$ s and a hexagonal scan on the slave spacecraft with $N_2 = 523$ scan points. The total acquisition time, T , is then equal to $T = 22\,000$ s if the frequency scan scans over one usable photodiode bandwidth each time the fast scan is completed. The necessary frequency sweep rate computes to $v_s = F_{PD}/T_1 \approx 48$ MHz s⁻¹. For FFT lengths of less than 8192 points no reduction in SNR is expected for this sweep rate. However, one has to consider that the time for the slow spatial scan on the slave spacecraft is the total calibration time of here $T_2 = T = 22\,000$ s. On these time scales the orbit prediction error will affect the scan pattern. In the worst case, the pointing noise will shift the current scan position by up to 100 μ rad, potentially leading to gaps in the uncertainty cone coverage.

To accommodate this huge worst case pointing noise, the separation between neighbouring scan points has to be strongly reduced to increase the overlap of the spatial capture cones. However, this also increases the scan time by increasing the number of necessary scan points. Hence, also this scan sequence seems to have some disadvantages, though further research is necessary.

6.3. Detector Signals for the Initial LOS Calibration

In Chapter 4, an algorithm was proposed to find the maximum heterodyne signal power during a complete scan, based on an approximation to the maximum likelihood estimator for the heterodyne amplitude. The data-flow diagram of the resulting algorithm is again depicted in Figure 6.11.

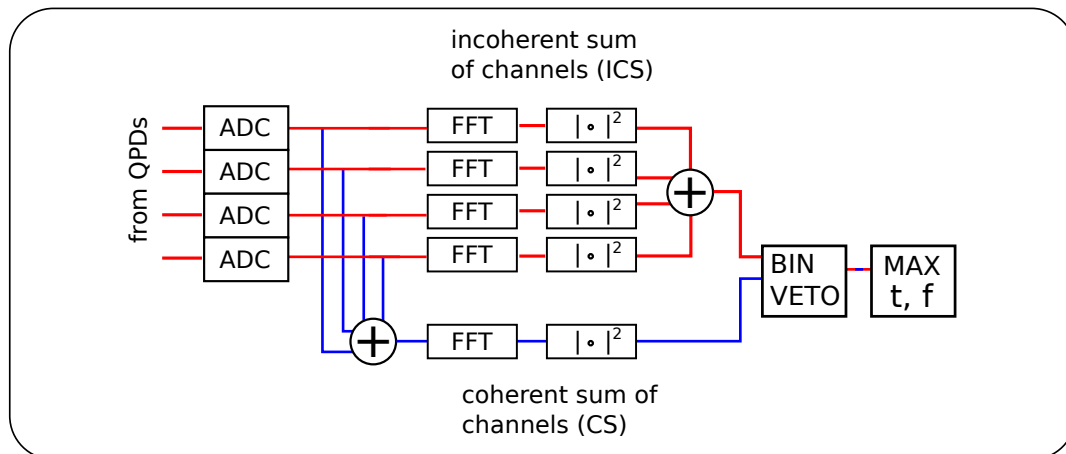


Figure 6.11.: Shows the data processing chain used to estimate the frequency and arrival time of the signal, also showing the coherent (CS) and incoherent (ICS) sums of the channels.

The basic principle of the estimation algorithm is to continuously compute fast Fourier transforms (FFT) of sequential, non-overlapping chunks of data, consisting of N_{DFT} samples, during which the fine-steering mirror (FSM) is scanning the spatial uncertainty cone and the laser frequency is swept over the frequency uncertainty interval. For each computed FFT the highest power occurring in any of the frequency bins is picked and compared against previously found maxima. The time when the overall maximum was found, yields an estimate of when the beam alignment and frequency were closest to their optimal values.

The data streams of the individual channels can be combined either coherently (CS), by adding the channels before the FFT is computed or incoherently (ICS), by summing up the power spectra of the individual channels. In this section, the tilt dependence of the CS and ICS signal combinations are determined. In order to do so, effective heterodyne efficiencies are defined and in analogy to the approach taken in Section 3.3.2, the effective received power is defined for the case of the coherent and incoherent sum combinations. In the last part of this section, the coherent and incoherent sum heterodyne efficiencies are investigated for additional wavefront errors or a change in the waist radius of the local oscillator beam, as well as for different widths of the insensitive slits of the photodiode.

6.3.1. Effective Heterodyne Efficiency for the CS and ICS

To estimate the response of the detection algorithm for the coherent and incoherent sum of the channels, an effective heterodyne efficiency can be defined for each case. In Section 4.3.1 it was shown that the distribution of the maximum, found in the power

spectrum of the heterodyne signal, approaches the distribution of the signal bin for high signal-to-noise ratios. In Sections 4.2.2 and 4.2.3 the expected power of the signal distributions for the CS and ICS were given in equations (4.2.25) and (4.2.39). For the case of high SNR the mean value of the frequency bins containing the signal with a frequency of $f_b = j f_s / N_{\text{DFT}}$ are given by

$$\mathbb{E}[\tilde{s}_{\text{CS}}^2(j)] \stackrel{\text{SNR} \gg 1}{\approx} \frac{|A_{\text{CS}}|^2}{2} \quad (6.3.1)$$

$$\mathbb{E}[\tilde{s}_{\text{ICS}}^2(j)] \stackrel{\text{SNR} \gg 1}{\approx} \frac{|A_{\text{ICS}}|^2}{2}. \quad (6.3.2)$$

Where $\tilde{s}_{\text{CS}}^2(k)$ and $\tilde{s}_{\text{ICS}}^2(k)$ are the power spectra of the coherent sum and the incoherent sum of the channels and $\mathbb{E}[x]$ is the expected value of x . Their signal amplitudes, A_{CS} and A_{ICS} , were defined by

$$A_{\text{CS}} = \left| \sum_{c=1}^{n_c} A_c \exp(i\phi_c) \right| \quad \text{and} \quad A_{\text{ICS}} = \sqrt{\sum_{c=1}^{n_c} |A_c|^2}, \quad (6.3.3)$$

with the phase of the single channel heterodyne signal, ϕ_c . The amplitudes can be cast into a form similar to the single channel heterodyne signal, whereas an effective heterodyne efficiency can be defined that encapsulates the dependence on the local misalignment. The single channel heterodyne amplitude, A_c , was defined in equation (3.3.9) as

$$A_c = 2 \rho_{\text{PD}} g(f_b) \sqrt{P_{\text{LO},c} P_{\text{RX},c} \eta_c}, \quad (6.3.4)$$

with the photodiode responsivity, ρ_{PD} , the photodiode frequency response, $g(f_b)$, the local oscillator and received beam powers, $P_{\text{LO},c}$ and $P_{\text{RX},c}$, falling onto the photodiode segments the channel is made up of, and the heterodyne efficiency, η_c , for the interference on each segment of the channel. With these definitions the amplitude of the coherent sum combination can be reformulated, given equations (6.3.3) and (6.3.4), as follows:

$$|A_{\text{CS}}|^2 = \left| \sum_{c=1}^{n_c} 2 \rho_{\text{PD}} g(f_b) \sqrt{P_{\text{LO},c} \rho_{\text{BS}} P_{\text{RX},c} \eta_c} \exp(i\phi_c) \right|^2 \quad (6.3.5)$$

$$= \left| 2 \rho_{\text{PD}} g(f_b) \sqrt{P_{\text{LO}} \rho_{\text{BS}} P_{\text{RX}}} \right|^2 \left| \frac{1}{n_c} \sum_{c=1}^{n_c} \sqrt{\eta_c} \exp(i\phi_c) \right|^2 \quad (6.3.6)$$

$$= \left| 2 \rho_{\text{PD}} g(f_b) \sqrt{P_{\text{LO}} \rho_{\text{BS}} P_{\text{RX}} \eta_{\text{CS}}} \right|^2. \quad (6.3.7)$$

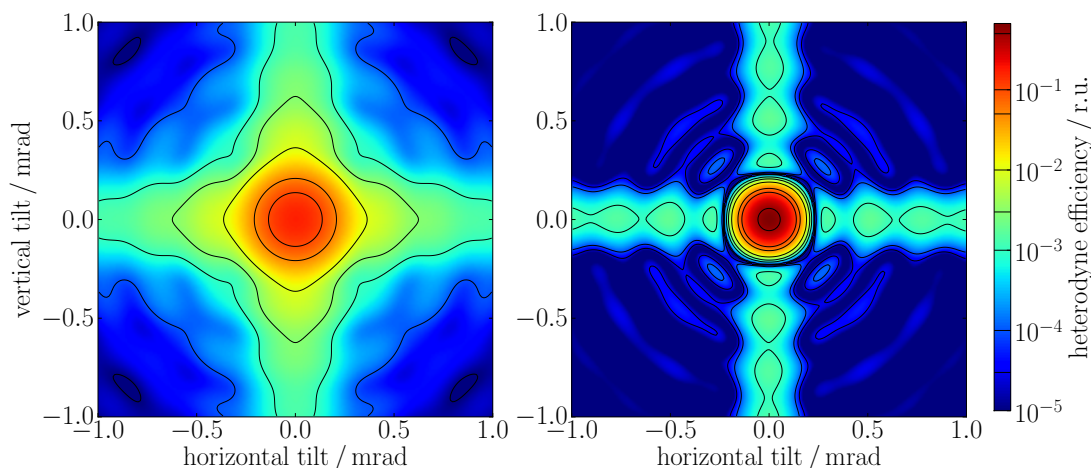


Figure 6.12.: Left: Effective heterodyne efficiency of the incoherent sum of the channels. Right: Effective heterodyne efficiency of the coherent sum of the channels. Both are shown as a function of vertical and horizontal relative angular misalignment of the RX and LO beam axis. The heterodyne efficiencies are defined in equations (6.3.12) and (6.3.8). The LO beam waist radius is $w_0 = 2.5$ mm and the waist position is at the QPD, the RX beam is a perfect tophat beam with flat amplitude and phase profile. The width of the inactive slits of the QPD is $30 \mu\text{m}$. The contour lines are also shown in the colour bar on the left.

In going from equation (6.3.5) to equation (6.3.6) it was assumed that the same power falls onto each segment, i.e. $P_{\text{LO},c} = P_{\text{LO}}/n_c$ and $P_{\text{RX},c} = P_{\text{RX}}/n_c$. The purpose of the imaging system on the optical bench is to ensure exactly this. It is designed to image a wavefront tilt at the image plane into a pure wavefront tilt with no beam walk at the photodiode. If the beams are aligned to the centre of the QPD and the two object planes of the imaging system coincide with the receive aperture plane and the centre of rotation of the FSM, there will be no beam walk on the photodiode, and each segment will receive the same power, both from the local oscillator as well as the weak signal beam.

Now, in order to get to the last line of equation (6.3.7), the following definition of the *coherent sum heterodyne efficiency* η_{CS} is introduced:

$$\eta_{\text{CS}} = \frac{1}{n_c^2} \left| \sum_{c=1}^{n_c} \sqrt{\eta_c} \exp(i\phi_c) \right|^2. \quad (6.3.8)$$

For zero slit width, this is equal to the heterodyne efficiency of a single-element diode. The right plot in Figure 6.12 shows the dependence of the CS heterodyne efficiency on local beam axis misalignments. The plus shape, originating from the insensitive slit, can

be easily spotted. Comparison with the single segment heterodyne efficiency shows a more symmetric and faster drop for increasing tilt.

Similarly, with equations (6.3.3) and (6.3.4), one can formulate the ICS signal amplitude with an effective *incoherent sum heterodyne efficiency*, η_{ICS} , by

$$|A_{\text{ICS}}|^2 = \sum_{c=1}^{n_c} \left| 2\rho_{\text{PD}}g(f_b) \sqrt{P_{\text{LO},c}\rho_{\text{BS}}P_{\text{RX},c}\eta_c} \exp(i\phi_c) \right|^2 \quad (6.3.9)$$

$$= \left| 2\rho_{\text{PD}}g(f_b) \sqrt{P_{\text{LO}}\rho_{\text{BS}}P_{\text{RX}}} \right|^2 \frac{1}{n_c^2} \sum_{c=1}^{n_c} \eta_c \quad (6.3.10)$$

$$= \left| 2\rho_{\text{PD}}g(f_b) \sqrt{P_{\text{LO}}\rho_{\text{BS}}P_{\text{RX}}\eta_{\text{ICS}}} \right|^2. \quad (6.3.11)$$

In going from equation (6.3.9) to equation (6.3.10), it is assumed that $P_{\text{RX},c} = P_{\text{RX}}/n_c$ and $P_{\text{LO},c} = P_{\text{LO}}/n_c$. For the last equality in the above derivation, the following definition for the heterodyne efficiency of the incoherent sum, η_{ICS} , is used:

$$\eta_{\text{ICS}} = \frac{1}{n_c^2} \sum_{c=1}^{n_c} \eta_c. \quad (6.3.12)$$

The left plot in Figure 6.12 shows the tilt dependence of the ICS heterodyne efficiency on the left. Compared to the coherent sum heterodyne efficiency, η_{CS} , the drop for increasing tilt is much slower in any direction. Also, the wings for only horizontal and vertical tilt are much more pronounced. However, the maximum value of the heterodyne efficiency for zero tilt is reduced by a factor equal to the number of the segments, as compared to the CS heterodyne efficiency, due to the exchanged order of summing and squaring. Summarising the above and making the connection to the detection/estimation problem: The patterns shown are analogous to the field-of-view (FOV) of the acquisition detector for local beam axis misalignments. Hence, the radius of the FOV for local beam misalignments of the acquisition detector, using the ICS is by about a factor of two larger, than the FOV using the CS detector. However, this comes at a price, for the coherent sum combination can be computed using only a single FFT, whereas the ICS uses four FFTs to compute the spectra of all channels individually and thus, only smaller FFT sizes could be used with the ICS for the case of limited computing resources.

Figure 6.13 shows a comparison of the heterodyne efficiencies, as computed for the plots in Figure 6.12 for a pure horizontal or vertical tilt as well as a diagonal tilt. The slower drop of the ICS is clearly visible, nearly doubling the possible misalignment in vertical and horizontal direction before the heterodyne efficiency drops to 10^{-2} . In diagonal direction, still 50% larger misalignments are possible. Again, the difference in

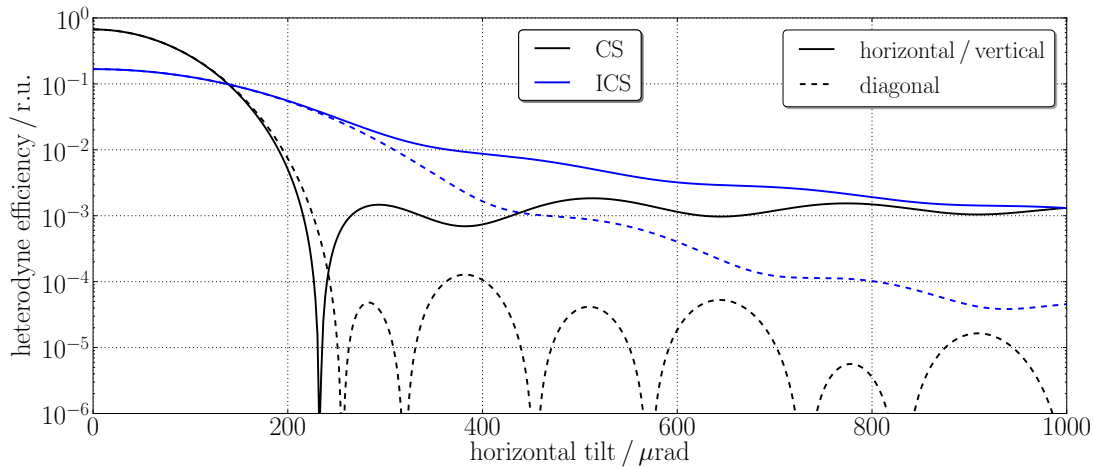


Figure 6.13.: Cross-sectional plot of the coherent and incoherent sum heterodyne efficiencies for interference of a tophat and a Gaussian beam on a single photodetector, as a function of the relative wavefront tilt. Shown are plots for pure horizontal or vertical tilts as well as a tilt in the diagonal direction. The beam and photodiode parameters are the same as were used for the generation of the plots in Figure (6.12).

the maximum value for zero tilt is due to the exchanged order of squaring and summing, which is a property of the detection algorithm itself and not an artefact of the definition of the CS and ICS heterodyne efficiencies.

6.3.2. Effective Received Power for the CS and ICS

The definition of the effective heterodyne efficiencies, together with the heterodyne amplitudes of the CS and ICS of the channels, can be used to define an effective received power similar to the case of the effective received power for a single channel which was given in equations (3.3.10) and (3.3.11).

For this, the two satellites are again labelled by $i, j = 1, 2$, with $i \neq j$. For the misalignment angles the following is agreed upon: if α_i and β_i are arguments to the heterodyne efficiency, they are the local beam misalignments on spacecraft i , i.e. the relative beam axis misalignment between the local oscillator and the received beam. On the other hand, α_i and β_i are the misalignment angles relative to the LOS of the beam transmitted by spacecraft i if they are arguments to the received power. Misalignments of the transmitted beam on spacecraft i , lead to a loss in effective received power in the other spacecraft, j . See Figure 6.14 for the definition of these angles.

The effective received power for the coherent sum of the channels, $\hat{P}_{\text{RX,CS}}$, is defined with the power loss in the receive path, ρ_{rx} , and the total received beam power in the

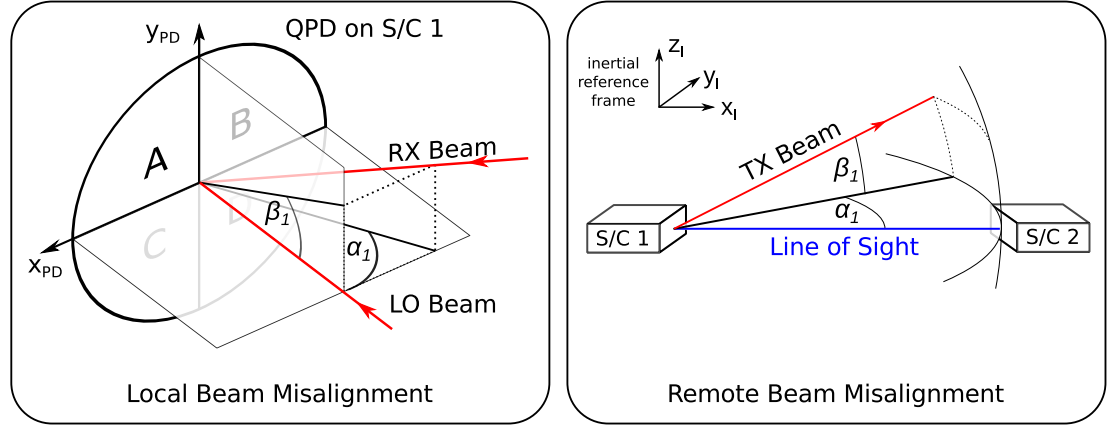


Figure 6.14.: Left: Local misalignment angles as the relative beam axis tilt in QPD coordinates of spacecraft 1. Right: Transmit beam misalignment of spacecraft 1 in inertial frame.

receive aperture, P_{RX} , as

$$\hat{P}_{\text{RX,CS}}(\alpha_i, \beta_i, \alpha_j, \beta_j) := \rho_{\text{rx}} P_{\text{RX}}(\alpha_j, \beta_j) \eta_{\text{CS}}(\alpha_i, \beta_i). \quad (6.3.13)$$

Plugging in the definition of η_{CS} from equation (6.3.8), the maximum effective received power is obtained for zero tilt and no relative phase between the channels, i.e. $\phi_c = \phi_d$ and also $\eta_c = \eta_d$ for all $c, d = 1, \dots, n_c$. For this case the maximum effective received power is equal to the sum of the single channel received power, as can be seen by

$$\begin{aligned} \hat{P}_{\text{RX,CS}} &= \rho_{\text{rx}} P_{\text{RX}} \frac{1}{n_c^2} \left| \sum_{c=1}^{n_c} \sqrt{\eta_c} \exp(i\phi_c) \right|^2 \\ &\leq \rho_{\text{rx}} n_c P_{\text{RX},c} \eta_c \\ &= n_c \hat{P}_{\text{RX},c}. \end{aligned} \quad (6.3.14)$$

Here, $\hat{P}_{\text{RX},c}$ is the single channel effective received power. On the other hand, the effective received power for the ICS, $\hat{P}_{\text{RX,ICS}}$, is defined by

$$\hat{P}_{\text{RX,ICS}}(\alpha_i, \beta_i, \alpha_j, \beta_j) := \rho_{\text{rx}} P_{\text{RX}}(\alpha_j, \beta_j) \eta_{\text{ICS}}(\alpha_i, \beta_i). \quad (6.3.15)$$

It can be estimated to be roughly equal to the single channel effective received power $\hat{P}_{\text{RX},c}$. This can be seen by plugging in the definition of η_{ICS} from equation (6.3.12) into

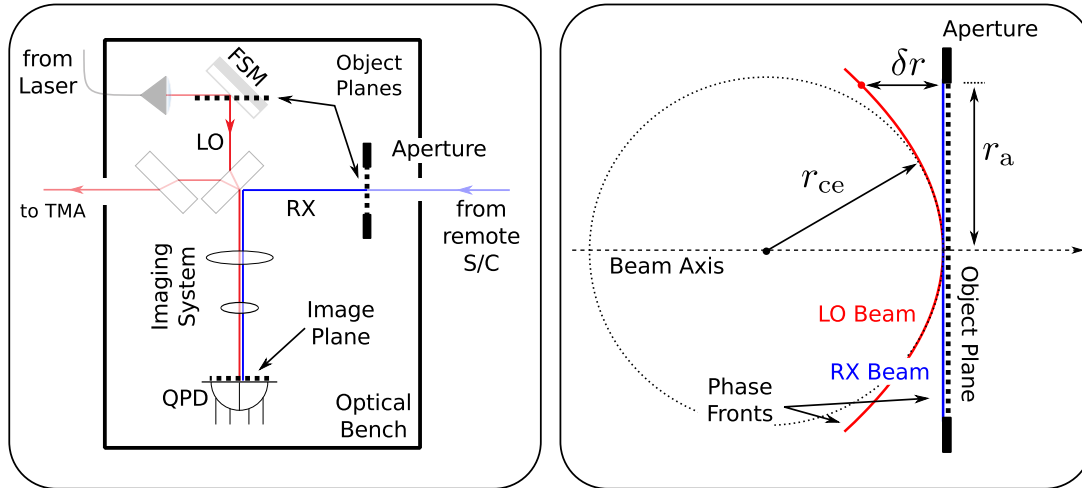


Figure 6.15.: Left: Object and imaging planes of the imaging system on the optical bench. The receive aperture plane and a plane through the FSM rotation point are imaged onto the QPD. Right: Visualises the quantities used to define a curvature error in the wave front of the LO beam at the object plane of the imaging system.

equation (6.3.15):

$$\begin{aligned}
 \hat{P}_{\text{RX,ICS}} &= \rho_{\text{rx}} P_{\text{RX}} \frac{1}{n_c^2} \sum_{c=1}^{n_c} \eta_c \\
 &= \rho_{\text{rx}} P_{\text{RX},c} \frac{1}{n_c} \sum_{c=1}^{n_c} \eta_c \\
 &= \rho_{\text{rx}} P_{\text{RX},c} \bar{\eta}_c.
 \end{aligned} \tag{6.3.16}$$

Here, the mean heterodyne efficiency over all channels was defined by $\bar{\eta}_c = \sum_{c=1}^{n_c} \eta_c$. Nevertheless, there is a gain in the SNR for the ICS combination as the heterodyne amplitude is proportional to the square-root of the product of the effective received power and the power of the local oscillator. For the ICS sum of the segments the local oscillator is n_c times the single channel local oscillator power.

6.3.3. Variation of the Heterodyne Efficiency

The heterodyne efficiency limits the FOV of the detector for local beam misalignments. Hence, variations of the heterodyne efficiency due to different photodiode slit widths, curvature errors or different waist radii of the Gaussian beam will have an effect on the detector performance. The Figures 6.16, 6.17 and 6.18 show the change of the heterodyne

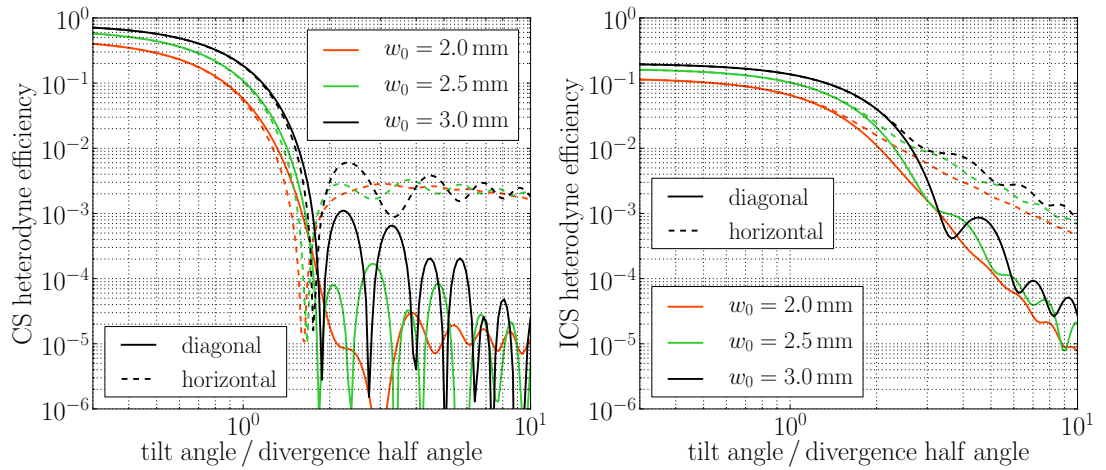


Figure 6.16.: Left: For three different waist radii of the Gaussian LO beam, shows the CS heterodyne efficiency for tilts in the vertical / horizontal direction, as well as diagonal direction, in QPD coordinates. Right: For the same waist radii shows the ICS heterodyne efficiency. The tophat beam's radius is equal to the photodiode radius and the Gaussian beam waist position is located at the photodiode. The QPD slit width is $\delta s = 30 \mu\text{m}$.

efficiency for variations of these parameters, for interference of a Gaussian LO with a tophat beam on a quadrant photodiode as a function of the relative tilt angle. Here again only cross-sections for tilts in purely horizontal or vertical direction as well as for a tilt in diagonal direction are compared. The heterodyne efficiency was calculated by computing the overlap integral, defined in equation (2.1.8), over the electric fields of the local oscillator (LO) and the received beam (RX) in the object planes of the imaging system. The integration boundaries corresponding to the individual segments are mapped to the object planes by scaling the radius of the active area, as well as the slit width by the inverse of the imaging system's magnification factor. In the left panel of Figure 6.15, the optical bench is shown together with the object and image planes of the imaging system. The imaging system is designed such that the receive aperture plane and the plane through the rotation point of the FSM are imaged onto the QPD, in a way that a tilt in the object plane is mapped to a tilt in the image plane without beam walk.

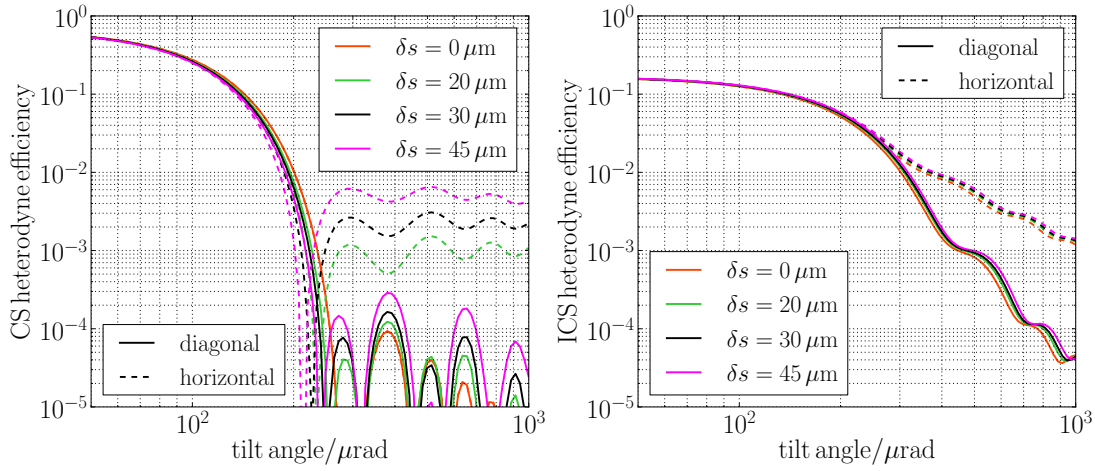


Figure 6.17.: Left: CS heterodyne efficiency for different QPD slit widths, δs , as a function of the relative wavefront tilt, between the Gaussian LO and tophat beam. Right: Incoherent sum heterodyne efficiency for the same slit widths. The tophat beam's radius is equal to the photodiode radius and the Gaussian beam waist radius is $w_0 = 2.5$ mm and located at the QPD.

The electric field amplitudes of the LO and RX beam are assumed to be defined by equation (3.3.14) which is repeated here as follows:

$$E_{\text{RX}} = \sqrt{\frac{1}{\pi}} \frac{1}{r_a} \exp(-ikx\alpha -iky\beta), \quad \text{and} \quad (6.3.17)$$

$$E_{\text{LO}} = \sqrt{\frac{2}{\pi}} \frac{1}{w_0} \exp\left(-\frac{x^2 + y^2}{w_0^2}\right). \quad (6.3.18)$$

The assumption is that the magnification of the imaging system is $m = R_{\text{PD}}/r_a$, where R_{PD} is the QPD radius and r_a is the receive aperture radius, so that the receive aperture is perfectly mapped to the active area of the photodiode. Only the slit width of the QPD has to be scaled by the inverse of the magnification factor of the imaging system.

Figure 6.16 shows the change of the CS and ICS heterodyne efficiency for a change in the waist radius of the Gaussian local oscillator. Changing the waist size of the Gaussian beam, whereas the tophat beam and photodiode radius are held constant, has a huge impact on the maximally achievable heterodyne efficiency for zero wavefront tilt. For 2 mm, 2.5 mm and 3 mm waist radius the maximum values of the heterodyne efficiency for the coherent sum are $\eta_{\text{CS}} = 0.48, 0.67$ and 0.80 and for the incoherent sum, $\eta_{\text{ICS}} = 0.12, 0.17, 0.20$, respectively. This is caused by the fact that for larger waist radii the Gaussian beam's amplitude distribution on the QPD surface approaches that of a

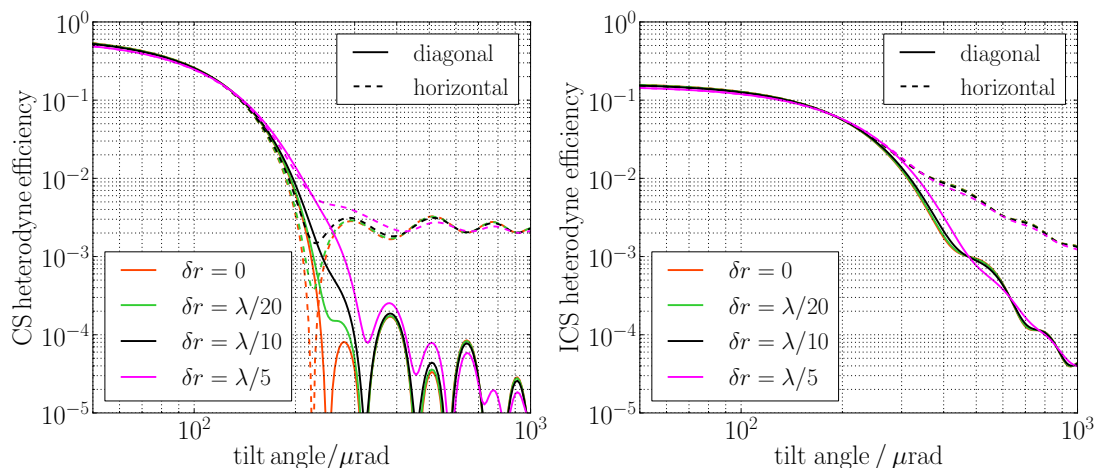


Figure 6.18.: Left: CS heterodyne efficiency for different wavefront curvature errors of the local oscillator beam, as a function of the relative wavefront tilt between the LO and RX tophat beam. Right: Incoherent sum heterodyne efficiency for the same curvature errors. The tophat beam's radius is equal to the photodiode radius and the Gaussian beam waist radius is $w_0 = 2.5$ mm and located at the QPD.

plane wave and hence, better overlap with the perfect tophat beam is achieved.

The horizontal axis of the plot is normalised to the divergence half angle of the Gaussian beam which is $\theta_0 = \lambda/(\pi w_0)$, with the wavelength λ . For the three considered cases of waist radii, $w_0 = 2$ mm, 2.5 mm and 3 mm, the divergence half angles are $\theta_0 = 169$ μ rad, 136 μ rad and 113 μ rad. The bend of the curve starts at about θ_0 for the coherent sum combination and at about $2\theta_0$ for the incoherent sum combination. Increasing the divergence will hence increase the field-of-view of the detector to local beam axis misalignments, but it also increases the width of the Gaussian beam in the far field by roughly the same amount.

Figure 6.17 shows the change of the heterodyne efficiency if the width of the insensitive slit that separates the individual segments is changed. The maximum achievable heterodyne efficiency slightly increases with wider slit width which is not visible from the plots due to the thickness of the lines. The field-of-view slightly decreases for increasing slit width and the plateau height at misalignments > 300 μ rad, for the case of pure horizontal/vertical tilt, for the CS increases with increasing slit width. The ICS combination is not altered noticeably. The curvature error in the plots of Figure 6.18 was generated by multiplying the electric field of the Gaussian LO beam by the following

quadratic phase function in the radial distance r from the beam centre

$$\delta E(r) = \exp\left(-2\pi i \frac{\delta r}{\lambda} \frac{r^2}{r_a^2}\right),$$

where δr is the deviation of the phase due to the curvature error at a distance of r_a in transversal direction from the beam axis. r_a is the radius of the tophat beam or the receive aperture radius. The right panel in Figure 6.15 gives an explanation of the used quantities. The radius of curvature, r_{ce} , of the wavefront error is then just given by $r_{ce} = r_a / \sqrt{4\pi \delta r / \lambda}$.

For the case of the CS of the channels, an increasing curvature error will decrease the heterodyne efficiency for zero tilt, from about $\eta_{CS} = 0.67$ if no curvature error is present to $\eta_{CS} = 0.61$ for a curvature error of $\delta r = \lambda/5$, which is a loss of roughly 9%. The ICS drops by the same ratio. However, the change is more prominent for higher tilt angles and is bigger for the CS than for the ICS. For example at $\alpha = 200 \mu\text{rad}$ misalignment the CS heterodyne efficiency with curvature error of $\delta r = \lambda/5$ is about 5 times higher than for the case of no curvature error. Also, the dip of η_{CS} at a bit more than $200 \mu\text{rad}$ misalignment vanishes for higher curvature errors. The ICS heterodyne efficiency is nearly unchanged.

Summarising the results, the ICS sum combination is nearly invariant under a change in the QPD slit width or an additional curvature error of the interfering beams. Generally, the field-of-view of the ICS is larger than that of the CS detector for all three examined waist sizes of the Gaussian beam. The CS combination however, roughly limits the field-of-view of the detector for local misalignments to the divergence half angle of the Gaussian beam. The divergence angle limits the FOV of the detector for remote beam axis tilts if the beam propagation factor, M^2 , is close to 1. An additional curvature error will increase the FOV of CS detector for local beam misalignments while an increase in the QPD slit width will slightly decrease the field-of-view.

6.4. Maximum LOS-to-Scan Track Separation

The aim of this section is to estimate the maximum allowable, simultaneous misalignment on both spacecraft such that the maximum returned by the detection algorithm over the complete calibration scan is most likely not due to noise alone. If it would be, the resulting alignment calibration is likely to yield an arbitrary alignment, because for this case the time, when the maximum was returned, is not correlated to the alignment of the beam axes relative to the LOS.

For the analysis in this section it is assumed, that the master spacecraft runs a fast Lissajous raster scan while the slave spacecraft dwells on a fixed scan point. So far, effects due to amplitude variations during an FFT were not considered. However, for the large uncertainty cones, as expected for the initial LOS calibration, scan speeds are high and variations of the heterodyne amplitude during an FFT will affect the power spectrum. In order to analyse the worst case, the maximum scan speed of the Lissajous scan is assumed in the following analysis.

The results obtained in Section 4.3.2 about the detector noise RMS, the heterodyne efficiency of the CS and ICS of the channels of Section 6.3.1, but also some results of the spatial scan section, can now be used to estimate the maximum allowable misalignment during the initial LOS calibration scan. The basic approach taken here is to compare the maximum in a computed power spectrum of the heterodyne signal to the noise RMS of the detector, over the complete time of the calibration scan. The alignment angles for which the maximum in the power spectrum is equal to the noise RMS of the

Table 6.2.: List of the default parameters used in the simulation to produce the maximum allowable misalignment. Variations of parameters are done while keeping all other parameters fixed to their default values.

Item			
Parameter	Symbol	Value	Unit
S/C separation	$D_{S/C}$	270	km
Transmitted laser power	P_{TX}	13.7	mW
Usable LO power (sum of segments)	P_{LO}	1.2	mW
Beam quality factor	M^2	1.05	r.u.
Beam waist size (radius)	w_0	2.5	mm
QPD responsivity	ρ_{PD}	0.6	$A W^{-1}$
QPD slit width	δ_s	30	μm
Number of QPD segments	n_{seg}	8 (hot redundancy)	number
Power loss in receive beam path	ρ_{rx}	0.795	r.u.
Samples in FFT	N_{DFFT}	2048	number
Sampling frequency	f_s	38	MHz
Lissajous fast axis frequency	\hat{f}	100	Hz
Uncertainty cone radius	R_{uc}	3	mrad
Receive aperture radius	r_a	4	mm
Noise equivalent current	NEI	5	pA/\sqrt{Hz}
Relative intensity noise	RIN	$3 \cdot 10^{-8}$	$1/\sqrt{Hz}$
Total number of computed frequency bins	N_b	$3.8 \cdot 10^9$	number

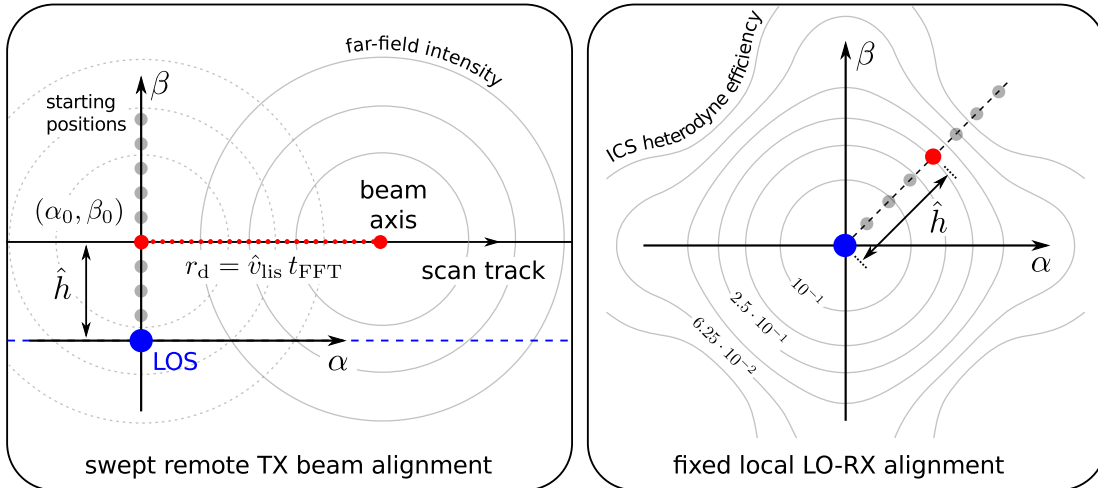


Figure 6.19.: Explanation of the calculations done to find the maximum simultaneous scan track separation, \hat{h} , for both spacecraft, here, exemplary for the heterodyne signal measured by the slow scanning slave spacecraft. Left: For a given initial alignment of $(\alpha_0, \beta_0) = (0, \hat{h})$, a fixed FFT of size N_{DFT} and a given maximum scan speed of \hat{v}_{lis} , a time series of the received power is generated for a scan of the remote spacecraft in horizontal direction. Right: The relative misalignment between the LO and RX beam on the local spacecraft is kept fixed at a position in diagonal direction at a distance from the LOS that corresponds to the vertical remote misalignment of \hat{h} . This determines the heterodyne efficiency for the measurement on the local spacecraft. From the time series of the received power and the heterodyne efficiency, time series of the heterodyne signal are calculated and Fourier transformed. Then the maximum value in the power spectrum is returned for a comparison against the noise RMS.

detector, is the maximum allowable simultaneous misalignment. If the two spacecraft run spatial scans with identical maximum scan track separations, \hat{h} , the found maximum simultaneous misalignment is also the maximum scan track separation that is usable for the calibration scans.

In principle, the maximum scan track separation, \hat{h} , computed for the two spacecraft are slightly different, due to the different tilt dependence of the received power and of the heterodyne efficiency. In the first case, considered in Figure 6.19, the signal is measured on the slave spacecraft and the received power varies while the heterodyne efficiency is constant over the course of an FFT. For the second case, the signal is measured on the master spacecraft and the heterodyne efficiency varies while the received power is constant. Both cases will be considered and discussed here.

Figure 6.19 explains the concept of the computation, exemplary for the case of a sweep of the remote spacecraft which here, corresponds to the signal measured by the slave

spacecraft. The initial scan position, $(\alpha_0, \beta_0) = (0, \hat{h})$, is varied in vertical direction only. The initial position for horizontal alignment is fixed to $\alpha_0 = 0$, as this corresponds to the situation for which the least signal power is collected in a single FFT. The range of vertical locations for the starting position, β_0 , was chosen from $0 \mu\text{rad}$ to $500 \mu\text{rad}$ with a resolution of $5 \mu\text{rad}$. The results were interpolated for intermediate values by cubic interpolation.

From the initial position the horizontal alignment angles, α_n , of the TX beam axis of the master spacecraft are computed for each sample of the FFT of size N_{DFT} , under the assumption of a constant sweep rate, $\hat{v} = 2\pi\hat{f}R_{\text{uc}}$, and sampling frequency, f_s , by

$$\alpha_n = \alpha_0 + \hat{v} \frac{n}{f_s}, \quad \text{with } n = 0, \dots, N_{\text{DFT}} - 1, \quad (6.4.1)$$

while the vertical alignment is kept constant, i.e. $\beta_n = \hat{h}$. As said before, the assumption is that the beam axis alignment of only one spacecraft varies over the course of an FFT, such that here the local alignment of the local oscillator beam axis is held constant.

Misalignments between the local oscillator and the received beam enter into the signal amplitude through the change of the heterodyne efficiency. In Figure 6.12 it was shown that the drop of the heterodyne efficiency for tilt in horizontal or vertical direction was much slower than a drop in the diagonal direction. In order to take this asymmetry into account and only compute the worst case maximum allowable misalignment, the misalignment between the LO and RX beams is varied along the diagonal direction, see the right panel of Figure 6.19. The relative angular misalignment between the LO and RX is chosen as $(\alpha, \beta) = (\hat{h}/\sqrt{2}, \hat{h}/\sqrt{2})$, where \hat{h} is the maximum LOS-to-scan-track separation of the remote spacecraft's spatial scan, as indicated in the figure.

The reason for these particular choices is that a Lissajous scan is assumed which, close to the centre of the spatial uncertainty cone, scans horizontally. Choosing $\alpha_0 = 0$ considers the worst possible starting position for a single FFT as the least signal power is collected in the FFT. For the other satellite, which keeps its scan position constant over the time of an FFT, a worst case position for the alignment is chosen. The heterodyne amplitude time series for the FFT was then calculated according to the formula given in equation (2.1.14)

$$s_c(n) = 2 s_q(n) = \frac{4 \rho_{\text{PD}} g(f_b)}{n_{\text{seg}}} \sqrt{P_{\text{LO}} \rho_{\text{rx}} P_{\text{RX}}(\alpha_n, \beta_0) \eta_q(\beta_0/\sqrt{2}, \beta_0/\sqrt{2})} \quad (6.4.2)$$

$$\cdot \cos(2\pi n f_b / f_s + \phi_q). \quad (6.4.3)$$

The beatnote frequency was set both to a value in the centre of the frequency band, and also right between two frequency bins, in order to find the worst case results for maximum scalloping loss. The heterodyne signals of the channels, s_c , were then used as input for the CS respectively the ICS detectors of Figure 4.2. The detector output was calculated for various LOS-to-scan-track separations. Now, the computed detector output for a pure signal input without noise, was compared against the RMS value of the maximum returned by the detector over a complete spatial scan of 200 s, if only noise is present during the whole scan.

The value of the noise RMS of the maximum, for the coherent and incoherent sum, depending on the total number of frequency bins, N_b , over which the maximum is searched, was derived in Section 4.3.2. Analytical formulas to compute the values also for a longer scan were given in equations (4.3.20) and (4.3.22). The difference between the noise RMS for a scan of 200 s and a scan of 20 000 s were given in Table 4.1 and only differ by roughly 20 %. Here, the noise RMS for a scan of 200 s is chosen, where half of the FFT bins are searched over. Thus, the number of frequency bins in which the maximum is searched over is $N_b = 3.8 \cdot 10^9$. The values for the incoherent and coherent sum noise RMS are listed in the table as $\text{RMS}_{\text{CS}} = 45.3 \tilde{\sigma}_{\text{CS}}^2$, and $\text{RMS}_{\text{ICS}} = 91.9 \tilde{\sigma}_c^2$. The variances of the noise in a frequency bin of a single channel, $\tilde{\sigma}_c^2$, and of the coherent sum of all channels, $\tilde{\sigma}_{\text{CS}}^2$, were defined by equations (3.4.7) and (4.2.24). In order to also compare the maximum LOS-to-scan-track separation for higher noise levels, it is additionally computed for RMS values which are 5 and 10 times higher.

This calculation was done for varying some parameters from their default values, so that their influence on the worst case misalignment can be estimated. The parameters that were varied are the scan speed, the FFT length, the spacecraft separation and the transmitted power, the beam propagation factor of the transmitted Gaussian beam (TX), the waist radius of the TX beam, the slit width of the quadrant photodiode and the amplitude of a possible wavefront curvature error.

The plots in Figure 6.20 show the maximum allowable LOS-to-scan-track separation, \hat{h} , of the spatial scans as a function of the spacecraft separation, $D_{\text{S/C}}$, on the left and as a function of the total transmitted power, P_{TX} , on the right. In both plots the results are shown for the CS and ICS detector, for a sweep of the remote TX beam and the local RX to LO alignment, as well as for the three different noise levels given before.

The first thing to note is that \hat{h} for the ICS is significantly larger than for the CS, by roughly 30 %, which is no surprise given the results for the effective heterodyne efficiencies η_{CS} and η_{ICS} of Section 6.3.1. The maximum simultaneous misalignment for the case of the CS varies between 185 μrad and 200 μrad for the default noise level, while

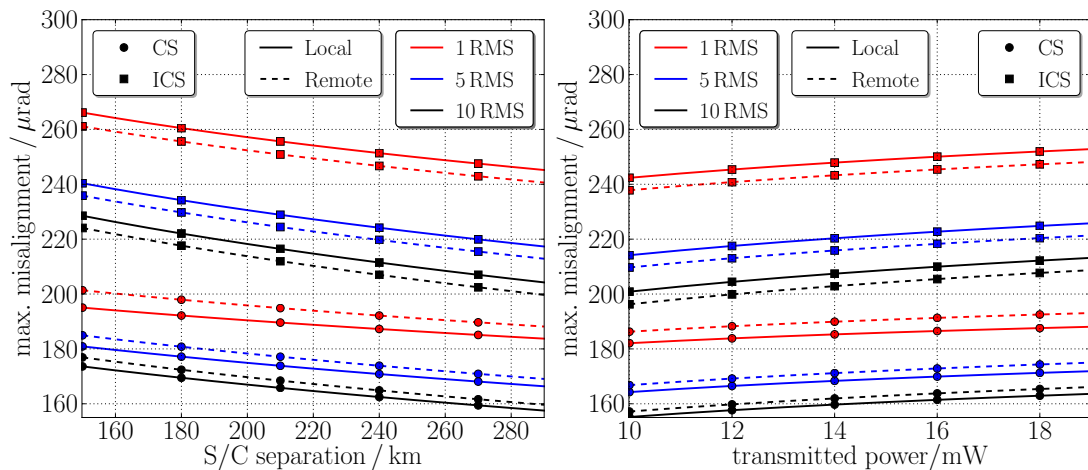


Figure 6.20.: Left: Maximum allowable LOS-to-scan-track separation, \hat{h} , as a function of the spacecraft separation. Right: \hat{h} as a function of the transmitted power, P_{TX} . Results are shown for both spacecraft, the CS and ICS of the channels as well as for three different noise levels. The results labelled *local*, correspond to a measurement on the master spacecraft, for which the local alignment between the LO and RX beam is swept during one FFT. *Remote* stands for a measurement of the slave spacecraft, for which the remote satellites sweeps the TX beam alignment. The noise level labelled $1\times$, corresponds to the default noise parameters given in Table 6.2.

the ICS varies from $240\ \mu\text{rad}$ to $260\ \mu\text{rad}$, as a function of the spacecraft separation. The three different colours encode the noise RMS of the maximum returned by the detector. Increasing the level of the RMS noise by a factor of 10 decreases \hat{h} by roughly 12% to 15% for the case of the ICS and 10% to 15% for the case of the CS.

In the right plot of Figure 6.20, the maximum \hat{h} , is shown for a change of the transmitted power from 10 mW to 20 mW. The maximally allowed simultaneous misalignment is seen to increase by about $10\ \mu\text{rad}$ for doubling the output power for the case of the ICS combination. If the CS combination is used \hat{h} merely changes by $5\ \mu\text{rad}$. The third piece of information given in the plot is the difference between the signals taken by the slave spacecraft, for which the remote spacecraft is sweeping, and the master, for which the local misalignment between the LO and RX beam changes over an FFT. The signal of the master satellite is plotted using the solid line and the signal of the slave is drawn with a dashed line. The difference between the remote and locally varied misalignment is small and in a range of $5\ \mu\text{rad}$.

Interesting is that for the ICS signal, the master spacecraft has a wider field-of-view (FOV) while for the CS it is the slave spacecraft. The reason for this is shown in

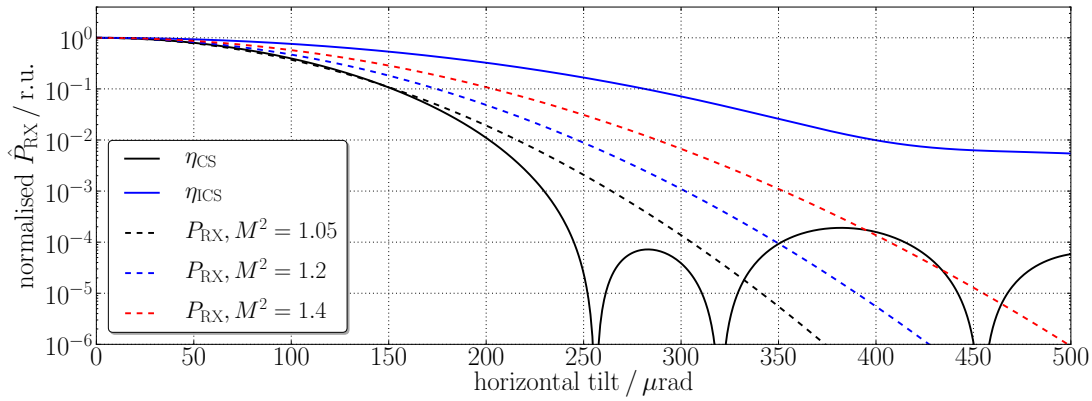


Figure 6.21.: Compares the loss of effective received power \hat{P}_{RX} for a local tilt, due to the heterodyne efficiency, with the loss experienced by the reduction of received power, P_{RX} , due to a TX beam axis tilt at the remote spacecraft.

Figure 6.21 which shows the tilt dependence of the effective received power, \hat{P}_{RX} , as a function of only local misalignments which is due to the heterodyne efficiency, η_{CS} or η_{ICS} , and also for a pure remote misalignment. For this case the reduction in the effective received power is due to the decrease of the received power P_{RX} . The assumed far-field intensity is a Gaussian beam with beam quality factors between $M^2 = 1.05$ and $M^2 = 1.4$.

The faster the effective received power drops, for a fixed scan range, the smaller is the collected power in the FFT and the smaller is the maximum returned by the detection algorithm. Thus, compared to the Gaussian far-field intensity distribution, the CS heterodyne efficiency drops quicker and the maximum allowable simultaneous misalignment, \hat{h} , is smaller for a locally swept alignment scan and larger for increasing M^2 -factor. On the other hand, the ICS sum combination drops slower for a local misalignment than for all considered Gaussian beam far-field intensities, for a varying remote beam axis misalignment, and here the maximum \hat{h} is larger for a local misalignment.

In Figure 6.22, the change of \hat{h} is shown as a function of the beam quality factor, M^2 , of the transmitted Gaussian beam and the speed of the scan, \hat{v} . A change of the M^2 -factor increases the divergence of the Gaussian beam and thus, increases the width of the far-field intensity distribution, as can be seen in Figure 6.21. An increased width of the far-field intensity distribution obviously increases \hat{h} . The incoherent sum combination increases linearly with the M^2 -factor by a factor of about 20% over the considered range of values of M^2 . For the CS instead, the increase flattens out, because of the faster drop of the CS. Remember that \hat{h} is depending on the product of the far-field intensity and

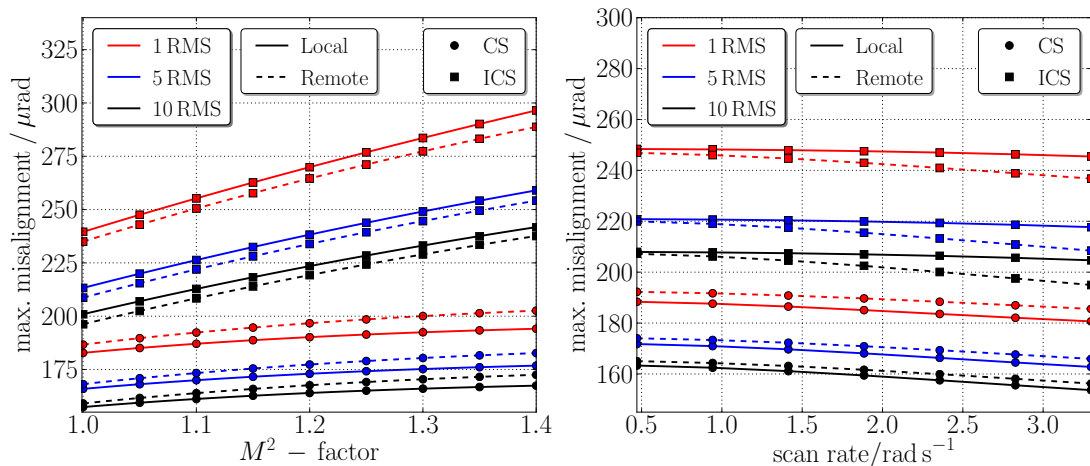


Figure 6.22.: Left: Maximum simultaneous misalignment, \hat{h} , as a function of the Gaussian beam quality factor, M^2 . Right: \hat{h} depending on the angular sweep rate, \hat{v}_{lis} . For further explanations, see Figure 6.20.

the heterodyne efficiency as given by equation (6.3.13) and (6.3.15).

However, the M^2 -factor as it is used in the parametrisation of the Gaussian beam in equation (3.3.17), only scales the divergence angle, whereas the intensity profile remains Gaussian and falls off smoothly for larger misalignments. In general, a large M^2 -factor would also change the shape of the intensity which was not investigated here.

If the scan rate, $\hat{v}_{\text{lis}} = 2\pi\hat{f}R_{\text{uc}}$, is changed, e.g. by varying the uncertainty cone radius, R_{uc} , or the fast axis frequency, \hat{f} , of the Lissajous scan, for the case of the ICS, a different behaviour of \hat{h} can be seen for an alignment variation of the remote and the local spacecraft. A change of the scan rate increases the range, the beam axis is swept over during one FFT, while keeping the number of scan points fixed. For the case of the CS and a sweep of the remote TX beam axis this leads to a loss in collected power during the FFT. For a local scan using the ICS, the heterodyne efficiency drops much slower and the collected power is nearly independent of the scan range, at least for the considered range of scan rates.

Table 6.3 lists the maximum allowable misalignment for variations of the QPD slit width, δ_s , the Gaussian beam waist radius w_0 , wavefront curvature errors, δr , and the sample size of the FFT, N_{FFT} . For the variation of the curvature error the heterodyne efficiencies as shown in the plots of Figure 6.18 are used, while the far-field intensity distribution was not altered. For the variation of the waist radius of the local oscillator beam, the heterodyne efficiencies as shown in Figure 6.16 are used and the far-field intensity distribution is computed using the same waist radius. The change in the slit

width was simulated by using the heterodyne efficiencies shown in Figure 6.17.

The biggest effect can be seen for the change of the local oscillator beam waist radius, w_0 , which is due to the change of the beam divergence in the far-field and the increase of the width of the heterodyne efficiency. The beam divergence half angles θ_0 for the considered cases of $w_0 = 2$ mm, 2.5 mm and 3 mm, are $\theta_0 = 169$ μ rad, 135 μ rad, 113 μ rad. The relative increase of the maximum separation between the LOS and the scan track, \hat{h} , is larger than the relative increase of the divergence angle, which is due to the simultaneous increase of the width in the far-field and of the heterodyne efficiency. For the rest of the varied parameters the change in the maximum allowable simultaneous misalignment is about 5 μ rad for the case of the CS over the range of the parameters for all noise levels. However, for the ICS a change of 15 μ rad can be observed for a change in the FFT length from 512 to 4096 points for the default noise level.

Table 6.3.: List of the maximum allowable, simultaneous misalignment, \hat{h} , for the coherent and incoherent sum combinations, for the default parameters listed in Table 6.2. For the case of the CS, the values for relative LO to RX alignment variations are shown and for the case of the ICS, the values for remote misalignments. The noise levels assumed for the parameters are listed at the bottom of Table 6.2 for a total number of computed frequency bins of $N_b = 3.8 \cdot 10^9$ which corresponds to a 200s spatial scan. For the wavefront error: $\lambda = 1064$ nm.

Item			CS max. \hat{h} / μ rad			ICS max. \hat{h} / μ rad		
Description	Symbol	Value	1	5	10	1	5	10
Noise / \times RMS			1	5	10	1	5	10
QPD slit width	δ_s	20.0 μ m	188	170	161	242	215	202
		30.0 μ m	185	168	159	243	215	202
		45.0 μ m	182	166	157	244	216	203
LO waist radius	w_0	2.0 mm	215	192	180	284	248	230
		2.5 mm	185	168	159	243	215	202
		3.0 mm	166	152	145	214	191	180
wavefront curvature error	δr	0	185	168	159	243	215	202
		$\lambda/20$	185	169	160	243	216	203
		$\lambda/10$	186	170	161	243	216	203
		$\lambda/5$	190	173	164	245	217	203
FFT sample size	N_{DFT}	512	180	162	152	231	200	189
		1024	186	169	161	243	212	199
		2048	185	168	159	243	215	202
		4096	186	169	161	246	219	206

6.5. Distributions of the Found Maxima

The result of the initial line-of-sight (LOS) calibration scan is an estimate of the fine-steering mirror (FSM) position that will align the beam axis of the transmitted beam (TX) parallel to the LOS between the two satellites. Due to random alignment biases, TMA coalignment errors and pointing noise, as well as a finite resolution of the spatial scan, the estimate will not be exact, but subject to residual alignment biases. These biases depend on the chosen scan resolution, the type of the scan and the specific realisation of pointing noise at the very time the maximum heterodyne amplitude was recorded.

In this section the distribution of the residual misalignment of the TX beam axis is investigated for different worst case misalignments of the spatial scan, for the hexagonal and the Lissajous scan. Also the FFT length is varied and the effect of a TMA coalignment error is discussed. In order to determine the distribution of the residual misalignment of the TX beam, relative to the LOS, the high-fidelity simulation presented in

Table 6.4.: List of the default parameters used in the simulation to produce the distribution of the line-of-sight estimates. Deviations from these will be mentioned explicitly.

Item			
Parameter	Symbol	Value	Unit
S/C separation	$D_{S/C}$	290	km
Transmitted laser power	P_{TX}	13.7	mW
Usable LO power (sum of segments)	P_{LO}	1.2	mW
Beam quality factor	M^2	1.2	r.u.
Beam waist size (radius)	w_0	2.5	mm
QPD responsivity	ρ_{PD}	0.6	$A W^{-1}$
QPD slit width	δ_s	30	μm
Number of QPD segments	n_{seg}	8 (hot redundancy)	number
Loss in receive beam path	ρ_{rx}	0.795	r.u.
Samples in FFT	N_{DFT}	2048	number
Sampling frequency	f_s	38	MHz
Lissajous fast axis frequency	\hat{f}	100	Hz
Uncertainty cone radius	R_{uc}	3	mrad
Receive aperture radius	r_a	4	mm
Noise equivalent current	NEI	5	pA/\sqrt{Hz}
Relative intensity noise	RIN	$3 \cdot 10^{-8}$	$1/\sqrt{Hz}$
Total number of computed frequency bins	N_b	$3.8 \cdot 10^9$	number

Section 5 was used. The simulation was run for one complete spatial scan and the state of each spacecraft (S/C), at the time of the maximum occurring FFT bin amplitude, was recorded. This includes the FSM's position and the TX beam alignment. The angular alignment returned as the LOS estimate is the alignment of the TX beam at the last recorded sample for the FFT in which the maximum was found. No additional delays, for example due to the calculation of the FFT, are taken into account.

Table 6.4 lists the default parameters used in these simulation runs. The frequency difference between the lasers of the two spacecraft was randomly chosen from a uniform distribution within the usable photodiode bandwidth, in order to include the effect of frequency variations that enter the measurement through scalloping loss of the rectangular windowed FFT. These frequency variations are for example due to frequency noise, or a slow frequency sweep. However, no Doppler shift and no frequency sweep was directly simulated. The frequency sweep rates for the initial LOS calibration were found to be far less than $v_s = 100 \text{ MHz s}^{-1}$ and thus no significant reduction of SNR due to the frequency sweep is expected. Frequency sweep rates for the initial LOS calibration as a function of the desired capture range, r_{cap} , were given in Figure 6.10. Compare this also to Figure 4.11 and the list of maximum scan speeds given in Table 4.2.

The dominant source of pointing noise, adding on time scales longer than a single spatial scan, is the orbit prediction error which is briefly discussed in Section 3.4.2. It can be considered by adding the uncertainty due to the orbit prediction error on top of the distribution of the LOS estimate that remains after a single spatial scan.

The master satellite runs a Lissajous scan with a fast axis frequency of $\hat{f} = 100 \text{ Hz}$ and the slave spacecraft runs a hexagonal scan. For the following analysis the CS combination of the channels is used. In order to determine the remaining uncertainty after the initial LOS calibration and find the distribution of the TX beam angle, relative to the LOS, the simulation was run a 1000 times with the same parameters. For each simulation run a random initial alignment bias was drawn from a uniform distribution inside the uncertainty cone of radius $R_{\text{uc}} = 3 \text{ mrad}$.

The simulation was run for a complete spatial scan and the TX beam angles relative to the LOS were recorded for the overall occurring maximum detector output. Results are shown in Figures 6.23a to 6.23d for both of the two spacecraft and for different maximum LOS-to-scan-track separations of $\hat{h} = 100 \text{ } \mu\text{rad}$, $145 \text{ } \mu\text{rad}$, $180 \text{ } \mu\text{rad}$ and $250 \text{ } \mu\text{rad}$. The maximum LOS-to-scan-track separation of the Lissajous scan is only adjustable in discrete steps, corresponding to integer frequency ratios $n = \hat{f}/\check{f}$, while \hat{h} for the hexagonal scan is continuously adjustable. The frequency ratio of the Lissajous scan was chosen such that \hat{h} is just smaller than the desired value while for the hexagonal scan it was set

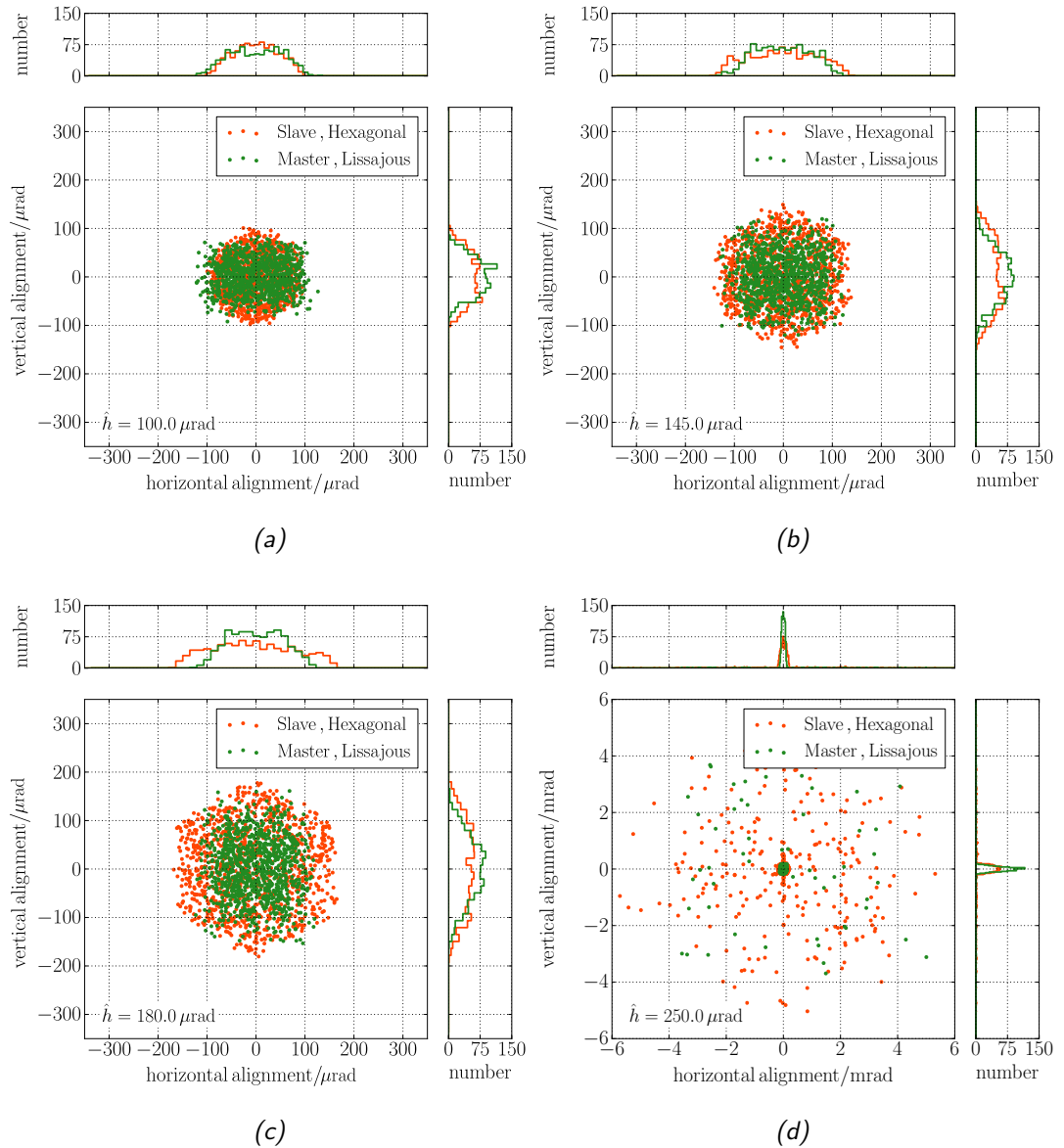


Figure 6.23.: Distribution of the TX beam angles, recorded when the maximum detector output occurred. The TMA coalignment error was set to zero during the simulation runs, to show only the distribution for varying uncertainty biases within the uncertainty cone. For each set of parameters 1000 random alignment biases were drawn from a uniform distribution within the uncertainty cone. For the different plots only the worst case misalignment of the scan pattern were varied, i.e. $\hat{h} = 100 \mu\text{rad}$ and $n = 55$ in 6.23a, $\hat{h} = 145 \mu\text{rad}$ and $n = 35$ in 6.23b, $\hat{h} = 180 \mu\text{rad}$ and $n = 28$ in 6.23c as well as, $\hat{h} = 250 \mu\text{rad}$ and $n = 20$ in 6.23d. The plots show that the width of the distributions follow the desired worst case misalignment up to $\hat{h} = 180 \mu\text{rad}$.

exactly to the desired value. This results in a slightly narrower distribution for the case of the Lissajous scan.

In Figure 6.23a the distribution of the angular misalignment of the TX beam to the LOS, for the maximum recorded signal power over a complete spatial scan, is shown for a maximum LOS-to-scan-track separation of $\hat{h} = 100 \mu\text{rad}$. The frequency ratio of the Lissajous raster scan was set to $n = 55$, resulting in $\hat{h} \leq 85.7 \mu\text{rad}$, which takes the synchronisation requirement of Section 6.1.2 into account. The first obvious thing to note is that the distribution of TX beam alignments is different for the two scan patterns. For the case of the hexagonal scan, the shape of the distribution clearly resembles a hexagon with its diameter equal to the set \hat{h} . This is more pronounced in the plots for larger \hat{h} but can also be seen in the case of $\hat{h} = 100 \mu\text{rad}$.

For the Lissajous scan, however, the width is different in the two axes. In the vertical direction the width is in accordance to the set LOS-scan-track separation of $\hat{h} = 85.7 \mu\text{rad}$, but it is wider in the horizontal direction, having a width of $\approx 100 \mu\text{rad}$. The horizontal alignment is not limited by the LOS-to-scan-track separation but by the maximum range, the FSM sweeps during one FFT. The maximum range swept by the steering mirror \hat{r}_d occurs at the zero-crossing of the fast scan axis and can be computed with equation (6.1.12) to

$$\begin{aligned}\hat{r}_d &= \hat{v}_{\text{lis}} \cdot t_{\text{FFT}} \\ &\approx 2\pi \hat{f} R_{\text{uc}} \cdot t_{\text{FFT}},\end{aligned}\tag{6.5.1}$$

which is shown in Figure 6.6. Plugging in the used parameter values for the fast axis frequency $\hat{f} = 100 \text{Hz}$, the uncertainty cone radius $R_{\text{uc}} = 3 \text{mrad}$ and FFT time, $t_{\text{FFT}} \approx 53.895 \mu\text{s}$, this gives $\hat{r}_d \approx 101.6 \mu\text{rad}$ which fits to the horizontal widths of the distributions of all of the Figures 6.23a to 6.23c. The horizontal width of the distribution of TX angles for the Lissajous raster scans is constant while the width in the vertical direction follows the set LOS-to-scan-track separation, \hat{h} , of the scan.

The results plotted in Figure 6.23d, $\hat{h} = 250 \mu\text{rad}$, suggest that the calibration is likely not successful in that case, as can be seen by the wide spread of the recorded TX angles of up to 6 mrad relative to the LOS. For this case, the maximum separation between the LOS and the scan track is too large such that for some simulation runs the maximum effective received power is below the maximum value produced by noise alone. The found maximum thus occurs at a random time during the spatial scan which yields an arbitrary alignment estimate.

Another interesting figure is the carrier-to-noise density (C/N_0) of the heterodyne

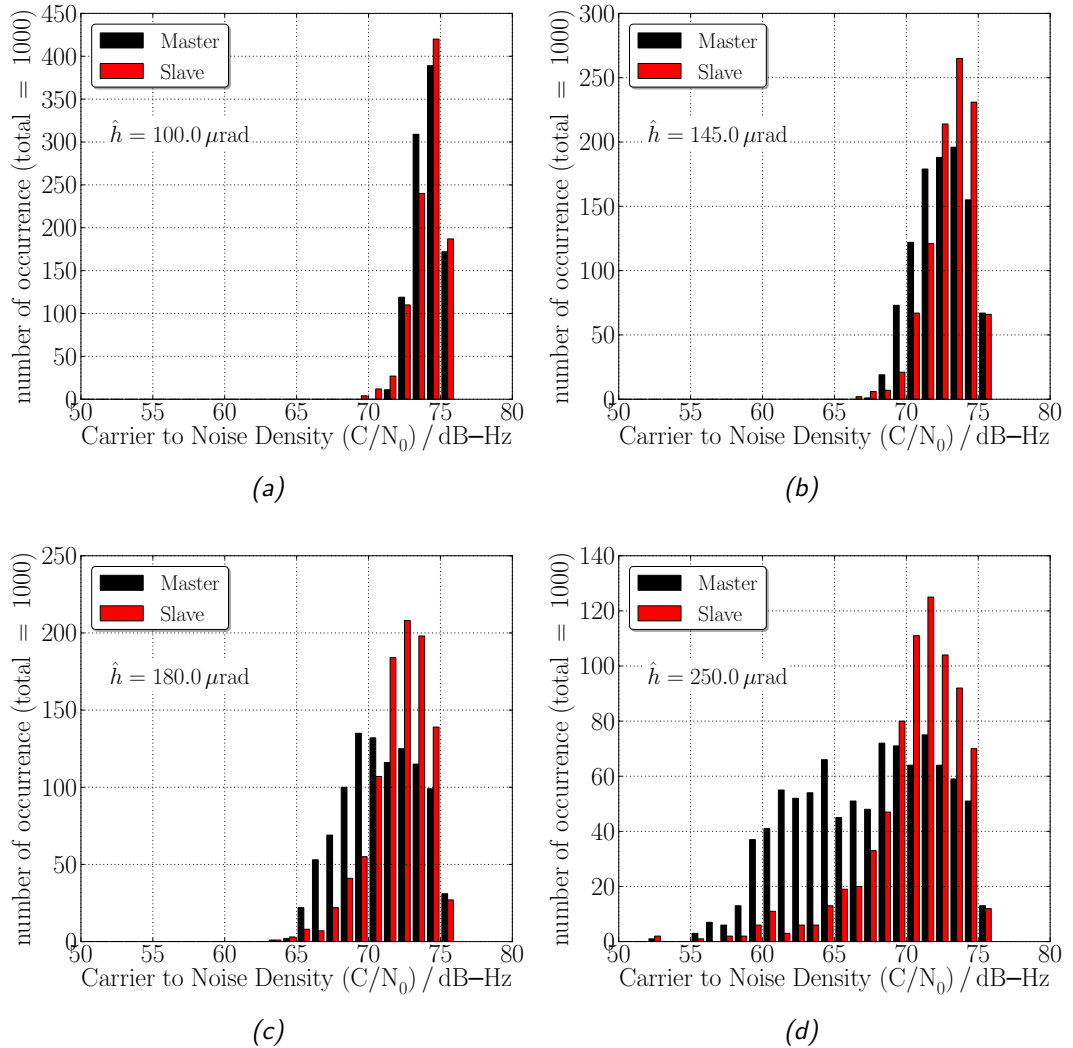


Figure 6.24.: Distribution of the carrier-to-noise density (C/N_0) of the single segment heterodyne signal, recorded at the time the maximum occurred during a pick-max search over an uncertainty cone with radius of $R_{uc} = 3$ mrad. These are the C/N_0 corresponding to the distributions of TX beam angles shown in the plots 6.23a to 6.23d. For the different plots only the LOS-to-scan-track separation, \hat{h} , of the scan pattern were varied, i.e. $\hat{h} = 100 \mu\text{rad}$ in 6.24a, $\hat{h} = 145 \mu\text{rad}$ in 6.24b, $\hat{h} = 180 \mu\text{rad}$ in 6.24c and $\hat{h} = 250 \mu\text{rad}$ in 6.24d. For increasing the maximum separation between the LOS and the scan track, the width of the distribution increases. The maximum value is invariant, corresponding to perfect alignment of both S/C, while the minimum found C/N_0 will decrease for larger separations. Figure 6.24d shows the distribution if \hat{h} is too large and the true LOS is not found with some probability.

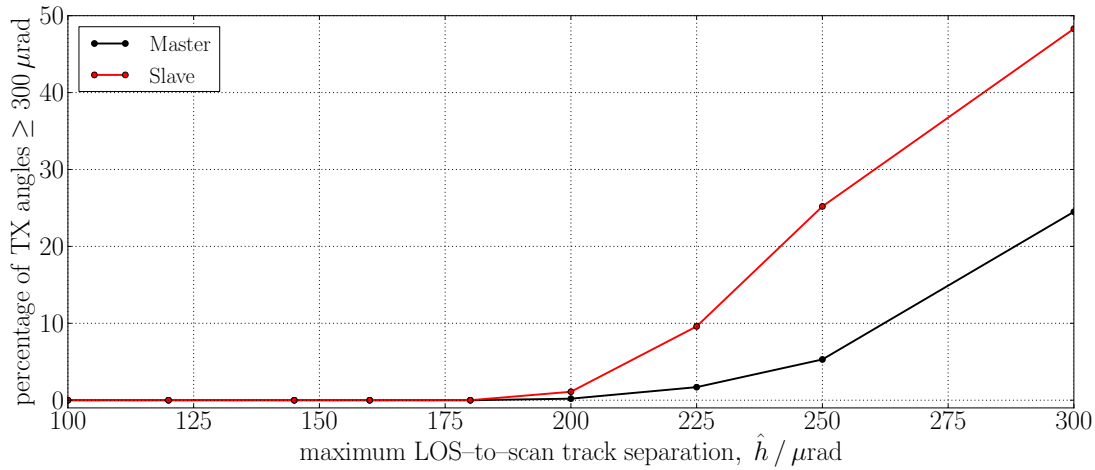


Figure 6.25.: Percentage of simulation runs for which the TX beam angles relative to the LOS that correspond to the found maximum, are larger than $300 \mu\text{rad}$. The effect of bigger worst case misalignment can be seen in Figures 6.23d and 6.24d. The master runs a fast Lissajous raster scan while the slave uses a slow hexagonal scan.

signal in a single channel which is defined as the power of the carrier signal in Watt, divided by the noise spectral density in Watts per Hertz,

$$C/N_0 = \frac{A_c^2/2}{2NEI^2 + 2q_e \rho_{\text{PD}} P_{\text{LO},c} + (\rho_{\text{PD}} P_{\text{LO},c} \text{RIN})^2}. \quad (6.5.2)$$

The unit of C/N_0 is given in Hz. Figures 6.24a to 6.24d show the distribution of the carrier-to-noise density for a single channel that corresponds to the found maximum during the initial LOS calibration scan. The plots correspond to the same simulation runs for which the distribution of the TX beam angles is shown in the Figures 6.23a to 6.23d. The carrier-to-noise density ratio is a direct indicator for the performance of the phasemeter. The left edge of the distribution of the carrier-to-noise density ratio, seen in the plots, is hence a lower limit of the performance of the phasemeter if the beams are aligned to the found calibration estimate.

The plot in Figure 6.25 shows the percentage of simulated spatial scans for which the residual TX beam angle is bigger than $300 \mu\text{rad}$, depending on the maximum LOS-to-scan-track separation of the scan. For a separation larger than $\hat{h} = 190 \mu\text{rad}$, there is a non-negligible probability that the maximum heterodyne signal power is less than the noise power returned by the detection algorithm during the spatial scan. This fits well with the predictions for the maximally allowed misalignment for a spatial scan that was made in the previous section.

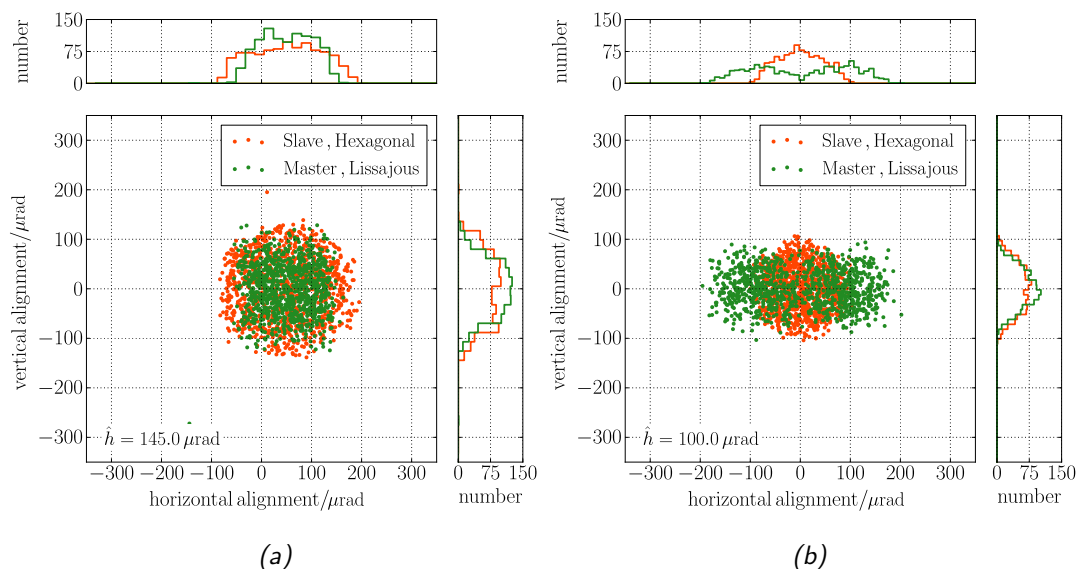


Figure 6.26.: Left: Distribution of the TX beam angles for the maximum occurring detector output for the case of a TMA coalignment error of $\gamma_{\text{TMA}} = 50 \mu\text{rad}$. The chosen maximum separation between the LOS and the scan track is $\hat{h} = 145 \mu\text{rad}$. Right: Distribution of the TX beam angles for the maximum occurring detector output if the FFT size is set to 4096 samples. The chosen \hat{h} for the scan is $\hat{h} = 100 \mu\text{rad}$.

Again, the big difference in the results between the Lissajous scan which is run by the master spacecraft, and hexagonal scan, that is run by the slave spacecraft, originates from the slightly smaller maximum separation between the LOS and the scan track that is chosen for the Lissajous scan to ensure that the LOS will stay within the spatial capture cone for at least a complete FFT. A second reason is that the LOS-to-scan-track separation during a Lissajous raster scan only occurs in the centre of the scan pattern. The scan point density is much higher at the edges of the covered area which increases the mean resolution of the scan.

The former plots that show the calibration accuracy were made using data from simulations with zero TMA coalignment error. This is obvious through the fact, that the distribution of residual beam alignment errors is centred around the true LOS at zero misalignment. The plot in Figure 6.26a shows the distribution for the same scan parameters that were also used in the data generation for Figure 6.23b, i.e. $R_{\text{uc}} = 3 \text{ mrad}$, $\hat{h} = 145 \mu\text{rad}$ for the hexagonal scan, a frequency ratio of $n = 35$ and a fast-axis frequency of $\hat{f} = 100 \text{ Hz}$ for the Lissajous scan. Additionally, a coalignment error of $\gamma_{\text{TMA}} = +50 \mu\text{rad}$ in horizontal direction was set on both spacecraft. It is easy to see

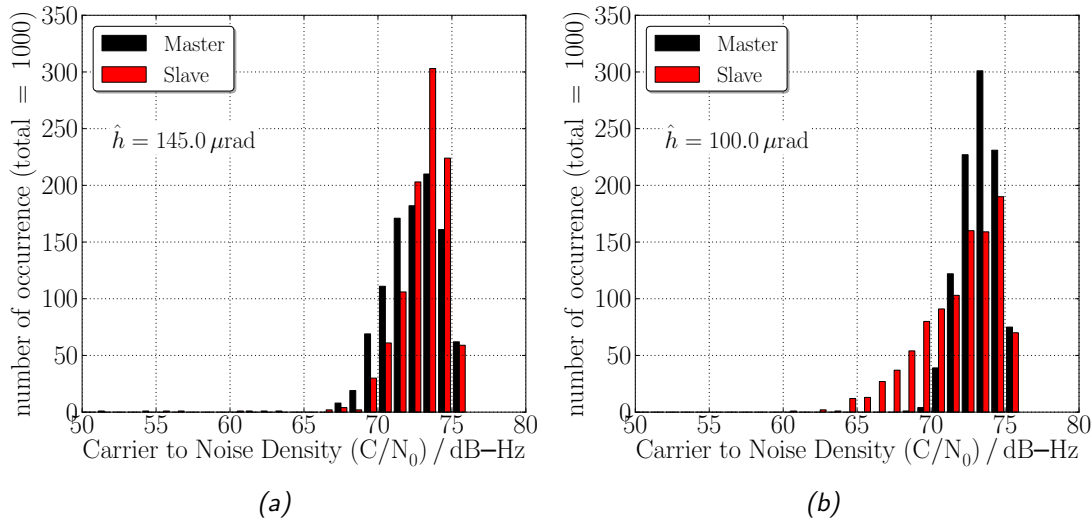


Figure 6.27.: Left: Distribution of the single channel C/N_0 for the maximum occurring detector output for the case of a TMA coalignment error of $\gamma_{\text{TMA}} = 50 \mu\text{rad}$. The chosen LOS-to-scan-track separation for the scan is $\hat{h} = 145 \mu\text{rad}$. Right: Distribution of the single channel C/N_0 for the maximum occurring detector output if the FFT size is set to 4096 samples. The chosen \hat{h} for the scan is $\hat{h} = 100 \mu\text{rad}$.

the horizontal shift of the distribution's mean value by $+50 \mu\text{rad}$.

However, this is due to the additional coalignment error added on transmission through the TMA to the other spacecraft. Figure 6.27a shows the distribution of the corresponding single channel carrier-to-noise density. A comparison with the histogram of Figure 6.23b yields no significant difference to the case of no TMA coalignment error. This shows clearly that the calibration will only be relative to the wavefronts of the incoming beam, which do not depend on the alignment of the transmitted beam of the remote spacecraft, since the arriving waveform is approximately spherical, with the centre of curvature close to the centre of mass of the remote spacecraft. Only when going through the TMA to the other spacecraft is the coalignment error added to the beam alignment. The TMA coalignment error will not be visible from only looking at the FSM position where the maximum occurred but the time of occurrence is necessary to extract that information from where the beam was pointed to.

Another interesting parameter is the FFT length that is used in the detection algorithm, because a larger number of samples in the FFT increases the SNR of the signal inside a frequency bin, as long as the variation of the frequency due to a frequency sweep or frequency noise is small compared to the width of the frequency bin. Figure 6.26b

shows the residual TX beam angles for a scan with maximum LOS-to-scan-track separation of $\hat{h} = 100 \mu\text{rad}$ and an FFT length of $N_{\text{DFT}} = 4096$ points.

The time of the FFT, t_{FFT} , determines the time between two successive LOS estimates. For $N_{\text{DFT}} = 4096$ samples in the FFT, the time between two successive estimates is $t_{\text{FFT}} = N_{\text{DFT}}/f_s \approx 108 \mu\text{s}$. The maximum range the TX beam angle sweeps during this time is $\hat{r}_d = \hat{v}_{\text{lis}} t_{\text{FFT}}$, with the maximum scan rate of the Lissajous scan, \hat{v}_{lis} . For an uncertainty cone radius of 3 mrad and a fast axis frequency of $\hat{f} = 100 \text{ Hz}$, the scan rate is $\hat{v}_{\text{lis}} = 1.9 \text{ rad s}^{-1}$, see Table 6.1 and equation (6.1.12). The range the TX beam axis is swept for this case is $\hat{r}_d = 205 \mu\text{rad}$ which is even larger than the LOS-to-scan-track separation of $\hat{h} = 100 \mu\text{rad}$. The carrier-to-noise density in a single channel for the time the maximum was recorded is shown in the left plot of Figure 6.27b. In comparison to the former case of $N_{\text{DFT}} = 2048$, C/N_0 is slightly reduced, due to the on average larger separation between the LOS and the TX beam alignment when the maximum is recorded.

6.6. Conclusions

In this chapter, an initial line-of-sight calibration scan was analysed as a first step to an autonomous laser link acquisition. The detailed analysis performed in this chapter yielded estimates for the total scan time based on the desired scan resolution. Subsequent analysis of the tilt dependence of the two proposed signal combinations provided estimates of the maximally allowed separation between the LOS and the scan track. Combining both results gives a lower bound for the possible scan times.

In the first part of this chapter, the spatial and frequency scans were investigated. Three types of spatial scan patterns were introduced, namely a discretely stepped hexagonal scan as well as a continuously scanned Archimedean spiral scan and a Lissajous raster scan.

The use of the hexagonal scan was found to be advantageous for the slow scan due to its optimal coverage of the uncertainty cone. The Lissajous scan was instead selected for the fast spatial scan for its simplicity and simple frequency response. Relations between the desired capture range and the maximum separation between the LOS and the scan track were derived and used to estimate the scan time for a complete four dimensional spatial scan.

Subsequently, the frequency scan and the scan sequence were discussed. For the case of a slow frequency scan, the frequency sweep rates and total acquisition times were computed. For a large uncertainty cone radius, alternative scan sequences were

evaluated. It was found that either the resulting frequency sweep rate would have to be chosen too large to give sufficient signal-to-noise ratio or the resolution of the spatial scan would have to be increased due to increased pointing noise due to the orbit prediction on long time scales.

In the second part of this chapter, the coherent and incoherent sum combinations of the detection algorithm were discussed and an effective heterodyne efficiency could be defined for the two cases. The tilt dependence of the two heterodyne efficiencies were investigated for different photodiode slit widths and waist radii of the local oscillator. Also the effect of an additional phasefront curvature error was calculated. A change of the local oscillator's waist radius has a large effect on the tilt dependence for both data combinations, whereas the photodiode slit width and the curvature error change the tilt dependence of the CS. The tilt dependence of the ICS remains nearly unchanged for these cases. The largest change of the CS signal occurs for larger tilt angles of about 200 μrad and more.

This was followed by an estimation of the maximum simultaneous misalignment allowed on both spacecraft such that the signal is large enough to be unambiguously above the noise. It was found that the CS signal limits the allowable misalignment to about 180 μrad to 190 μrad . The biggest change of this limit could be related to the divergence of the transmitted beam which depends on the waist radius or the M^2 -factor of the Gaussian beam. The ICS instead limits the allowed misalignment to about 230 μrad to 270 μrad . The field-of-view of the ICS combination is approximately a factor of $\sqrt{2}$ larger than the field-of-view that is provided by the CS combination.

The maximally allowed simultaneous misalignment can be used as an estimate of the maximum allowable separation between the scan track and the LOS. As the time for a spatial scan is roughly proportional to the square of the LOS-to-scan-track separation, this might be exploited to speed up the calibration scan by about a factor of 2.

In the last section, the distributions of the residual misalignment of the transmitted beam after an initial LOS calibration scan was investigated. For a discretely stepped hexagonal scan the width of the distribution is limited by the maximum separation between the LOS and the scan track. For a Lissajous scan instead, the width of the distribution in the direction of the fast scanning axis is depending on the scan rate and the FFT length. In the direction of the slow scanning axis it only depends on the maximum LOS-to-scan-track separation. For larger FFT lengths, the residual misalignment in horizontal direction might exceed the set separation between the scan track and the LOS.

7. Autonomous Laser Link Acquisition

In this chapter, an algorithm for an autonomous laser link acquisition is proposed. The goal of an autonomous laser link acquisition is to reduce remaining uncertainties in the angular bias and in the frequency difference of the lasers such that finally tracking of the received light can be realised with differential wavefront sensing. An autonomous laser link acquisition is carried out after the initial line-of-sight calibration or at any time when the laser link got interrupted during the mission.

This chapter will start by summarising the assumed parameter values for which the link acquisition algorithm was developed and review some of the challenges that need to be tackled in designing a working and robust algorithm. It will further continue with reviewing the detection signals and show how the detection threshold should be chosen. At the same time, this fixes the allowable simultaneous misalignment of both spacecraft and hence the minimum scan resolution.

Thereafter, the spatial scan pattern for the autonomous laser link acquisition is presented and expressions for the frequency scan rates and total scan times are given. This is followed by the presentation of the proposed algorithm including an explanation of the actual implementation. The results given in the subsequent section show that the algorithm is robust and yields high success rates while keeping the acquisition time at an acceptable level. The chapter concludes with a summary of identified reasons for the few remaining time outs and failures of the algorithm.

7.1. Introduction

After an initial line-of-sight calibration, the uncertainty in the alignment of the laser beams on each spacecraft is reduced from an initial bias of up to 3 mrad down to values of some hundred μ rad. The exact uncertainties depend on the chosen scan resolution during the initial line-of-sight calibration and additional dynamic biases, such as the orbit prediction error as the biggest contributor or thermal effects. Also, the uncertainty in the frequency difference between the master and slave laser is reduced from a possible range of some GHz down to about 100 MHz.

The goal of the autonomous laser link acquisition is to search the remaining uncertainty space to acquire a signal from the remote spacecraft and autonomously, without

communication between the satellites or via ground control, transition to a state where the laser ranging interferometers (LRI) on both spacecraft are tracking the incoming laser light. Pointing control of the fine steering mirrors (FSM) is then handed over to a control loop exploiting differential wavefront sensing (DWS) to automatically align the wavefronts of the local oscillator (LO) beam to the wavefronts of the received laser beam (RX) from the remote spacecraft.

In Chapter 6 estimates of reachable calibration accuracies were given together with necessary scan times. An accuracy of roughly $150 \mu\text{rad}$ was possible for an overall scan time of 5.5 h for the case of 100 frequency scan points. Assuming this number as baseline for the analysis in this chapter, the orbit prediction error adds a conservatively estimated maximum of $100 \mu\text{rad}$ on top. Additionally allowing for some margin, the remaining uncertainty in the alignment of the beam axis on both spacecraft is set to $R_{\text{uc}} = 300 \mu\text{rad}$ for the analysis in this chapter. The frequency uncertainty after the initial line-of-sight calibration is due to drifts of the laser frequency in the time between the detected maximum during a pick-max search and the subsequent autonomous laser link acquisition. It is set here to $F_{\text{uc}} = 100 \text{ MHz}$.

These two values are the main parameters that determine the average and worst case time of an autonomous laser link acquisition. However, there are other parameters which will influence the performance of the acquisition process. These parameters are only specified to be limited to a certain range, for example the triple-mirror assembly (TMA) coalignment error $|\gamma_{\text{TMA}}| \leq 40 \mu\text{rad}$, the one-way Doppler shift $|f_{\text{D}}| \leq 2.35 \text{ MHz}$ which the laser light experiences due to the relative movement of the satellites. Also the clocks of both spacecraft might have some unknown offset assumed to be $|\delta t_0| \leq 500 \mu\text{s}$ which inhibits a perfectly synchronised start of the acquisition process on both satellites. The algorithm developed here needs to successfully lock the LRIs for any value of these variable parameters with high probability.

Another unknown is the exact far-field intensity distribution of the transmitted (TX) laser beam. The simplest model assumes a pure Gaussian beam with quality factor between $M^2 = 1$ and $M^2 = 1.2$, as given in equation (3.3.17). A different model for the far-field intensity distribution was derived by propagating a fundamental fibre mode resulting in the simple model defined by equation (2.5.18). The algorithm that is proposed here is tested for all of these cases in order to investigate its limits.

The main idea of the algorithm which is presented here, is that the uncertainty space is scanned for a signal which exceeds a predefined detection threshold. The algorithm used to detect the heterodyne signal is that of Section 4 which compares the maximum frequency bin value that is found in a power spectrum of the heterodyne signal against

the set threshold. If a signal exceeds the threshold, the scans are stopped. The key point is that a detection should only be claimed if the effective received power in a single phasemeter channel is sufficiently high to directly lock the phasemeter, without the need for additional alignment optimisations. Hence, one of the main concerns is to determine the correct signal combination which provides high enough SNR and at the same time is a sufficient indicator for the power received in a single phasemeter channel.

A somewhat different approach would be a multi-stage process, where the spatial uncertainty cone is initially scanned by a coarse scan to find the correct frequency, and after detecting the signal the uncertainty is gradually decreased until the signal strength is large enough to lock the phasemeter. The gradual decrease can be done by subsequent scans with smaller radius or higher resolution [KS89] while the detection threshold is increased. Another option would be to dither the angular alignment of the laser beams to estimate the direction of the power gradient [GKK⁺04]. However, the additional logic will increase the complexity of the algorithm design and here a simpler approach is evaluated also because the remaining spatial and frequency uncertainties are small and a full search over the complete uncertainty space is done quickly.

The first section of this chapter is thus dedicated to the analysis of the available signal combinations and determination of the correct threshold. This is followed by a discussion of a possible scanning scheme. The proposed algorithm is explained in more detail thereafter. Finally, results of conducted simulation runs which test the algorithm for various parameter values, and the three far-field intensity distributions which were mentioned before, are presented. The acquisition algorithm was also tested for a range of detection thresholds to investigate its sensitivity to this key parameter.

7.2. Signals and Thresholds

The general detection problem was extensively discussed in Chapter 4 and only the main results important for the following analysis will be reviewed. The expected RMS noise in a frequency bin of a 4096 point DFT of a single channel, expressed as equivalent effective received power, was estimated to be $\hat{P}_{RX,c}^{\text{noise}} \approx 3 \text{ fW}_{\text{rms}}$ and for the coherent sum (CS) detector to roughly $\hat{P}_{RX,CS}^{\text{noise}} \approx 40 \text{ fW}_{\text{rms}}$, at a considered local oscillator power of $P_{LO,q} = 150 \mu\text{W}$ per photodiode segment. See Table 3.3 for a list of noise levels for different LO powers and DFT sizes.

Figure 4.8 presents the distribution of the output of the CS detector for different effective received powers per phasemeter channel. It shows a clear distinction between the distribution due to only noise and a present signal for $\hat{P}_{RX,c} \geq 500 \text{ fW}$. Using the

separation of the CS noise and signal distributions as indication for sufficient separation also for the case of the incoherent sum (ICS) one can argue that if the single channel effective received power is larger than 500 fW the false alarm rates due to the additive noise sources are negligible.

The minimum effective received power per channel to which the phasemeter is still able to lock to, is assumed to be $\hat{P}_{RX,c} = 3 \text{ pW}$. Any threshold set for the CS detector which guarantees at least 3 pW per phasemeter channel will thus limit false alarm rates to far less than 1 in 10^6 . However, this is only true for the simple noise models assumed here and does not consider other noise artefacts as glitches, etc.

Choosing the correct threshold is nevertheless essential for a successful acquisition process and not trivial. The data combination used for the detection of the heterodyne signal, either the CS or the ICS for their higher SNRs, have to be used as an indicator for the effective received power in a single channel.

In order to determine a detection threshold for the acquisition process, it is assumed that perfect knowledge about the far-field intensity distribution of the transmitted beam and the dependence of the heterodyne signal on the relative wavefront tilt exist. However, the exact intensity distribution is likely not known beforehand, as the far-field intensity is hard to generate in a laboratory. Also the generation of a nearly perfect tophat beam interfering with the LO on the optical bench is not easily done. However, in studying the threshold selection for different far-field intensity distributions, general rules can be derived that need to be considered. Some knowledge might also be gained during an initial LOS calibration.

The first question to answer is which of the available data combinations is a suitable indicator for the effective received power in a single channel and the second question is how to set the threshold value for the chosen data combinations.

7.2.1. Detector Signal for Autonomous Laser Link Acquisition

The chapter discussing the detection algorithm also proposed two distinctly different ways of combining the signals of different photodiode channels which are denoted the coherent sum (CS) and the incoherent sum (ICS) of the channels. The data flow diagram is shown in Figure 4.2. For the two different combinations, the signal amplitude could be formulated with effective heterodyne efficiencies η_{CS} and η_{ICS} which are defined in equations (6.3.8) and (6.3.12) in a form similar to that of the single channel heterodyne amplitude A_c . The expression is here recapitulated with indices i, j being either 1 or 2

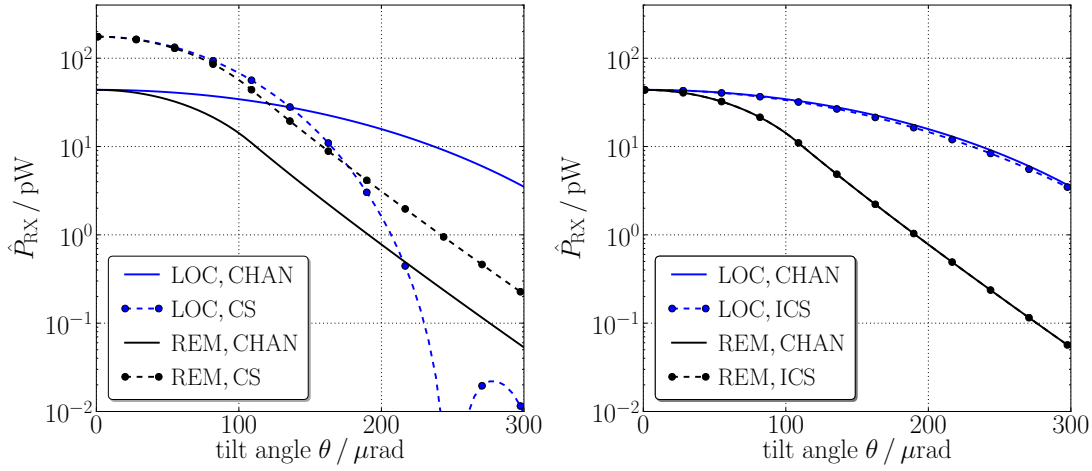


Figure 7.1.: Comparison between the effective received power \hat{P}_{RX} for tilt of the beam axis on one spacecraft for perfect alignment of the other spacecraft for the coherent sum (CS) and incoherent sum (ICS) of the channels as defined by equation (7.2.4), as well as a single channel (CHAN) from equation (7.2.2). The blue curve shows \hat{P}_{RX} for the local spacecraft tilting the beam (LOC) and the black curve shows \hat{P}_{RX} for the remote spacecraft (REM). The tilt is in the diagonal direction yielding the steepest fall-off. The parameters used here are given in Table 7.4.

and $i \neq j$, indexing the two spacecrafts, whereas c indexes one of the n_c data channels:

$$A_c(\alpha_i, \beta_i, \alpha_j, \beta_j, f_b) = 2 \rho_{PD} g(f_b) \sqrt{P_{LO,c} \hat{P}_{RX,c}(\alpha_i, \beta_i, \alpha_j, \beta_j)} \quad (7.2.1)$$

$$\hat{P}_{RX,c}(\alpha_i, \beta_i, \alpha_j, \beta_j) := \rho_{RX} P_{RX,c}(\alpha_j, \beta_j) \eta_c(\alpha_i, \beta_i) \quad (7.2.2)$$

Here α_i, β_i are the horizontal and vertical tilt angles between the LO and the RX beam, and are further on called *local misalignment angles*, α_j, β_j are the misalignment angles between the LOS and the axis of the beam transmitted by the remote spacecraft. As these angles determine the received power due to the tilt of the TX beam axis on the remote spacecraft they will be called *remote misalignment angles*. Figure 3.5 shows a sketch of the local and remote misalignment angles.

The frequency response of the photodiode is denoted by $g(f_b)$ and ρ_{PD} is the photodiode responsivity. The angular dependence of the heterodyne amplitude can be combined in an effective received power \hat{P}_{RX} which is defined by equation (3.3.11) as a function of the heterodyne efficiency η_c of the segments of the channel c . The received power per channel is given by $P_{RX,c} = P_{RX}/n_c$, where P_{RX} is the total power passing through the receive aperture and $P_{LO,c}$ is the total local oscillator power that is collected in a

single channel. It is assumed that the LO power on all segments is equal and that the segments have uniform responsivity over their surface area. The losses in the path of the RX beam are combined in ρ_{rx} . For the CS and ICS combinations the heterodyne amplitude can be given in a similar form by:

$$A_{\text{S},i}(\alpha_i, \beta_i, \alpha_j, \beta_j, f_b) = 2 \rho_{\text{PD}} g(f_b) \sqrt{P_{\text{LO}} \hat{P}_{\text{RX},\text{S}}(\alpha_i, \beta_i, \alpha_j, \beta_j)} \quad (7.2.3)$$

$$\hat{P}_{\text{RX},\text{S}}(\alpha_i, \beta_i, \alpha_j, \beta_j) := \rho_{\text{rx}} P_{\text{RX}}(\alpha_j, \beta_j) \eta_{\text{S}}(\alpha_i, \beta_i) \quad (7.2.4)$$

where S stands for either CS or ICS. The dependence of the heterodyne efficiency for the two combinations on the relative tilt between the wavefronts of the LO and RX beam was also shown in the plots of Figure 6.12, indicating the much smaller change of the ICS combination as compared to the CS combination. The dependence on remote misalignments is the same for the two cases and determined by the far-field intensity pattern of the beam transmitted by the remote spacecraft. The heterodyne efficiencies fall off faster in the diagonal direction than in the horizontal or vertical direction which is also shown in Figure 6.13.

In this chapter only the worst case powers are of importance and hence only misalignments in diagonal direction are considered. A local misalignment by an angle θ_i will be defined by $\alpha_i = \beta_i = \theta_i/\sqrt{2}$. Additionally, the far-field intensity pattern of the TX beam is assumed to be circular symmetric to the beam axis such that the received power only depends on the combined angle $\theta_j \approx \sqrt{\alpha_j^2 + \beta_j^2}$. The following simplified notation will be used for the rest of this chapter:

$$\hat{P}_{\text{RX}}(\theta_i, \theta_j) := \hat{P}_{\text{RX}}\left(\theta_i/\sqrt{2}, \theta_i/\sqrt{2}, \theta_j, 0\right). \quad (7.2.5)$$

In the right plot in Figure 7.1 the effective received power \hat{P}_{RX} for misalignments of one spacecraft is shown for the CS and a single channel (CHAN). The left plot in Figure 7.1 shows the same for the ICS and a single channel (CHAN). For perfect alignment of the distant spacecraft the two plots compare the dependence of the effective received power \hat{P}_{RX} on beam axis misalignments of the local spacecraft.

From the left plot in Figure 7.1 it is obvious that the single channel signal is different in shape to the CS signal which falls off faster. The faster drop is due to relative phase shifts between the channels. However, the important thing to note is that the CS signal has a similar dependence on local and remote misalignments, up to approximately 200 μrad . Tilting a beam on one spacecraft will hence change the signal on both spacecraft approximately by the same amount and the detected signal power on both

spacecraft will cross a set threshold simultaneously for misalignments $\leq 200 \mu\text{rad}$.

The right plot in Figure 7.1 compares the dependence of the ICS to the single channel \hat{P}_{RX} for beam axis tilts on one spacecraft. The response of the ICS signal on local and remote beam axis tilts is vastly different. Most importantly the signal drops much faster for the remote spacecraft than for the local spacecraft. In fact, this makes the ICS unusable for a detection algorithm as implemented here because the local misalignment can be much larger before the signal is lost or a set threshold is crossed than for the remote spacecraft.

This will likely lead to the following situation. In the above plot, setting a definite threshold of for example 10 pW for the incoherent sum effective received power, the local misalignment can be bigger than 300 μrad for perfect alignment of the remote spacecraft and a detection would still be claimed. This would stop the steering mirror scan at these 300 μrad misalignment. Hence, the transmitted beam would be misaligned by 300 μrad from the LOS and the effective received power on the remote spacecraft would be less than 200 fW. A different but more complex implementation might be possible to accommodate these large differences between the local and remote signal but this will not be studied here.

For the reason given above the CS combination of the segments is preferred over the ICS combination for the autonomous laser link acquisition. The following analysis of the proposed acquisition algorithm is done with the CS signal only.

7.2.2. Threshold Selection for the CS Detector

Two types of thresholds are used in the proposed algorithm. The first one is the detection threshold G_{CS} , which is used in the detection algorithm to decide if a signal is present. The other threshold is the *signal-lost* threshold C_{CS} , which in turn is used to decide if the signal is lost again once a detection has been made. The reason for this will be explained later on.

However, both thresholds will be derived from a necessary minimum CS effective received power ξ_{CS} that ensures a minimum signal power in a single phasemeter channel. The selection of a threshold for the signal detection G_{CS} will be defined in terms of the CS effective received power ξ_{CS} for its indicative meaning. However, the detection algorithm compares the threshold G_{CS} against the maximum value in a power spectrum of the heterodyne signal photocurrent. For the case of a present signal, the mean value of the signal bin will be equal to the squared root mean square (RMS) of the heterodyne photocurrent. Therefore, the minimum effective received power ξ_{CS} has to be converted

from effective received power to RMS amplitude squared by

$$\begin{aligned} G_{\text{CS}} &:= \left[\frac{2 \rho_{\text{PD}} \sqrt{P_{\text{LO}} \xi_{\text{CS}}}}{\sqrt{2}} \right]^2 \\ &= 2 \rho_{\text{PD}}^2 P_{\text{LO}} \xi_{\text{CS}}. \end{aligned} \tag{7.2.6}$$

Here the maximum frequency response of the photodiode is assumed to be $g(f_b) \equiv 1$. The threshold ξ_{CS} for the CS effective received power depends on the shape of the far-field intensity pattern and the heterodyne signal. While here only the heterodyne efficiency for interference of a perfect tophat with a perfect Gaussian beam on a detector with 0.5 mm radius and 30 μm slit width was used, as far-field patterns the simple model for the propagated fibre mode, as given in equation (2.5.18), and a Gaussian beam with beam quality factor of $M^2 = 1.0$ and $M^2 = 1.2$ was used to compare the performance of the algorithm for these three cases. An expression to compute the intensity of a Gaussian beam with beam quality factor of M^2 was given in equation (3.3.17).

The change of the heterodyne efficiency for curvature errors and different photodiodes slit widths was discussed in Section 6.3.3. The outcome was that within a range of roughly 200 μrad the tilt dependence will remain approximately the same except for small variations of the maximum heterodyne efficiency for zero tilt which however only slightly decreases the SNR of the signal. The difference of the far-field intensity pattern for the propagated fibre mode and a possible Gaussian beam with $M^2 = 1.2$ however, will have different behaviours for small tilt angles as well, and the on-axis power for the non-perfect Gaussian beam will be reduced by about a third as compared to the simple model of the propagated fibre mode or a perfect Gaussian beam with $M^2 = 1$.

For the threshold selection here it is assumed that the signal level only changes due to misalignments of the beam axes. However, the signal level will also change due to a change in the beatnote frequency because of the frequency response of the photodiode or scalloping loss, see Section 4.4.1. Also the additive noise sources such as shot noise, laser intensity noise and detector electronic noise will change the measured signal and hence the detector output. These changes will be accounted for by defining the signal-lost threshold C_{CS} , which will be derived from the minimum CS effective received power ξ_{CS} ,

by multiplying the heterodyne amplitude with the scalloping loss factor $\rho_{\text{scallop}} \approx 0.637$:

$$\begin{aligned} C_{\text{CS}} &:= \left[\rho_{\text{scallop}} \frac{2 \rho_{\text{PD}} \sqrt{P_{\text{LO}} \xi_{\text{CS}}}}{\sqrt{2}} \right]^2 \\ &= 2 \rho_{\text{scallop}}^2 \rho_{\text{PD}}^2 P_{\text{LO}} \xi_{\text{CS}} \\ &= 2 \rho_{\text{PD}}^2 P_{\text{LO}} \zeta_{\text{CS}}. \end{aligned} \tag{7.2.7}$$

In the last line the signal-lost threshold in terms of the effective received power was defined by:

$$\zeta_{\text{CS}} = \rho_{\text{scallop}}^2 \xi_{\text{CS}}. \tag{7.2.8}$$

Determining the detection threshold for the CS signal here principally means finding the maximum misalignment allowed on both spacecraft before the single channel effective received power will drop below the desired lower limit of ξ_{CHAN} . This will guarantee that a signal will only be detected if the combined misalignment of both spacecraft is such that the photodiode still receives an effective received power of ξ_{CHAN} per channel. The resolution of the spatial scan pattern has to be set according to the found limit on the allowable misalignment in order for the signal to be detectable.

7.2.3. A Naive Approach

At first the threshold selection is done for the case that the far-field intensity pattern is given by the propagated fibre mode of equation (2.5.18). The effective received power for the CS signal and the single channel (CHAN) is shown in the plots of Figure 7.2 for the case of a remote (REM) TX beam misalignment and local RX to LO beam axis misalignment (LOC) at the beamsplitter as well as for a simultaneous (SIM) misalignment on both spacecraft. Two different approaches have been taken to find the correct value for the threshold of which one turned out to be wrong if the single channel effective received power should be limited to a minimum value of ξ_{CHAN} which here is assumed to be $\xi_{\text{CHAN}} = 3 \text{ pW}$. This incorrect method is shown in the plot of Figure 7.2 indicated by the circles. It sets the CS threshold ξ_{CS} based on the single channel effective received power for simultaneous misalignments on both spacecraft. At first the angle θ_{sim} for a simultaneous misalignment is determined for which the single channel effective received power crosses the lower limit. This is marked by the circle numbered (1), and written

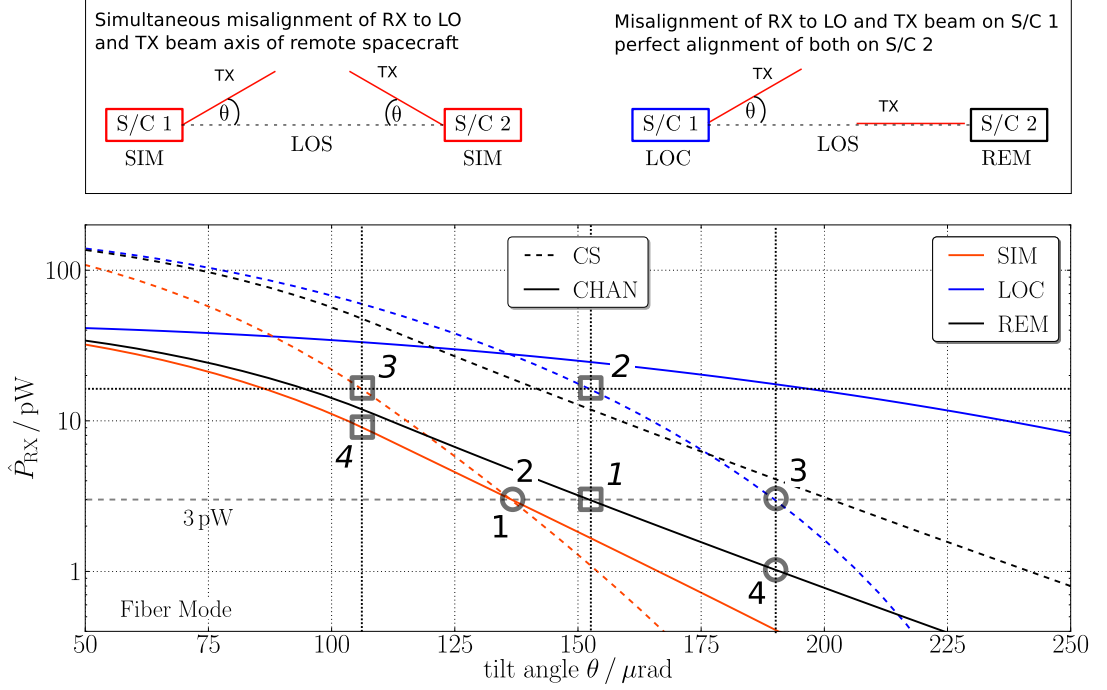


Figure 7.2.: Two methods how two choose the threshold. The curves correspond the single channel (CHAN) and coherent sum (CS) effective received power \hat{P}_{RX} for misalignments of the beam axes. Here, local misalignment (LOC) is the tilt of the LO beam with respect to the RX beam at the beamsplitter, whereas remote misalignment (REM) is the misalignment of the TX beam of the distant spacecraft relative to the LOS. The effective received power is plotted for the case of simultaneous (SIM) local and remote misalignment and for only local misalignment. For this case, the effective received power is shown for the local spacecraft (LOC) as a function of the relative beam axis tilt at the beamsplitter, and for the remote spacecraft (REM) for misalignments of the TX beam of the local spacecraft relative to the LOS. Circles: Procedure for picking the threshold based on the simultaneous misalignment on both spacecraft (1) and (2), which might lead to a detection on both spacecraft (3) though not enough power is received on the photodiode of the remote spacecraft for the phasemeter to lock (4). Squares: Procedure for picking the CS threshold (2) based on the single channel effective received power on the remote spacecraft (1). The allowable simultaneous misalignment (3) is much smaller than for the first method, but if a detection was made the power is guaranteed to exceed the 3 pW threshold for a single channel (4), also (1). For further details see the text. The far-field intensity pattern here is assumed to be the fibre mode far-field of equation (2.5.18) which for the small misalignments considered here is close to the purely Gaussian profile with $M = 1$.

mathematically with the simplified notation of equation (7.2.5) as

$$\hat{P}_{RX,c}(\theta_{sim}, \theta_{sim}) \stackrel{!}{=} \xi_{CHAN}. \quad (7.2.9)$$

The threshold for the CS effective received power is subsequently set as the value of $\hat{P}_{\text{RX,CS}}$ for the same simultaneous misalignment θ_{sim} , marked by circle (2). Hence:

$$\Rightarrow \xi_{\text{CS}} = \hat{P}_{\text{RX,CS}}(\theta_{\text{sim}}, \theta_{\text{sim}}). \quad (7.2.10)$$

However, this is problematic for the case that the remote spacecraft is better aligned than θ_{sim} , as the CS signal level for the local spacecraft increases and allows for a larger local misalignment before the threshold is violated which in turn results in a larger misalignment for the remote spacecraft.

This is depicted in the plot for the extreme case that the remote spacecraft is perfectly aligned to the LOS resulting in the maximum possible received power. For this case the CS on the local spacecraft crosses the threshold at θ_{one} (3) for which the CS signal on the remote spacecraft is also still above the threshold so that it can detect the signal.

In spite of that, the single channel effective received power on the remote spacecraft is below $\xi_{\text{CHAN}} = 3 \text{ pW}$ such that the phasemeter might not be able to lock to the incoming signal. Since a detection was made the information can be used to start a second smaller scan that could be implemented into the algorithm for the autonomous laser link acquisition and would use a second higher threshold to increase the signal level until the single channel effective received power is above ξ_{CHAN} . However, this will increase the complexity of the algorithm and as the baseline here was to keep it as simple as possible a different approach for setting the threshold was chosen which limits the single channel signal to the desired lower limit for all detection events.

7.2.4. An Improved Approach

This second approach is shown in the plot of Figure 7.2, indicated by the squares and italic numbers, for the same parameters. The threshold is chosen for the case of misalignment of only the local spacecraft. At first the misalignment angle θ_{one} is determined for which the single channel effective received power of the remote spacecraft crosses the desired lower limit, square number (1), hence:

$$\hat{P}_{\text{RX},c}(0, \theta_{\text{one}}) \stackrel{!}{=} \xi_{\text{CHAN}}. \quad (7.2.11)$$

The threshold for the CS signal on the local spacecraft is then set to the value of $\hat{P}_{\text{RX,CS}}$ for a misalignment of θ_{one} in diagonal direction in photodiode coordinates and perfect

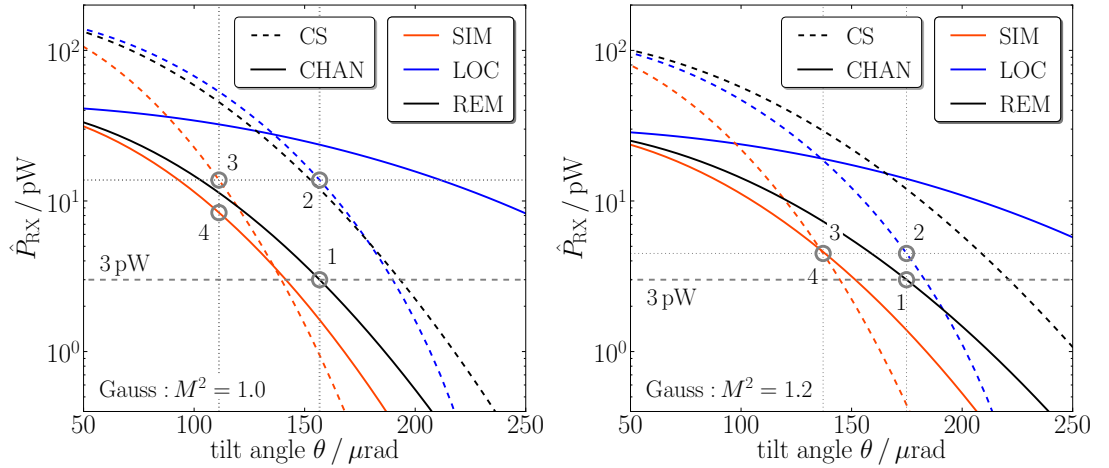


Figure 7.3.: Single channel (CHAN) and coherent sum (CS) effective received power \hat{P}_{RX} for misalignments of the beam axes on both spacecraft simultaneously (SIM) and of only one of the beams on one spacecraft while the other beam axis is perfectly aligned to the LOS. For this case, the effective received power is shown for the local spacecraft (LOC) as a function of the relative wavefront tilt at the photodiode and for the remote spacecraft (REM) for which the power is degraded due to the decrease in the received power. Left: The far-field intensity distribution is assumed to be a Gaussian beam with beam quality factor $M^2 = 1.0$. Right: Here, the far-field intensity is a Gaussian beam with $M^2 = 1.2$. The procedure to set the threshold is the improved approach from the plot in Figure 7.2.

alignment of the other spacecraft, marked by square number (2), in Figure 7.2,

$$\Rightarrow \xi_{CS} = \hat{P}_{RX,CS}(\theta_{\text{one}}, 0). \quad (7.2.12)$$

Setting the threshold to this value will ensure that the single channel received power always exceeds the desired lower limit, if the CS effective received power is above the threshold. The maximum allowable LOS-to-scan-track separation of the spatial scan, can then be found by determining the simultaneous misalignment angle θ_{sim} such that the CS effective received power equals the set threshold:

$$\hat{P}_{RX,CS}(\theta_{\text{sim}}, \theta_{\text{sim}}) \stackrel{!}{=} \xi_{CS}. \quad (7.2.13)$$

However, in the later sections it will be explained that some extra margin between ξ_{CS} and the signal lost threshold ζ_{CS} is advantageous if attitude jitter due to the star-camera assembly (SCA) is present. Here, it is assumed that the SCA attitude corrections add an attitude error of $10 \mu\text{rad}$ (1σ) to the FSM position every 100 ms. In order to consider

a loss in the effective received power due to misalignments as a result of SCA noise one can increase the difference between the detection and signal lost threshold.

The way to do this that is proposed here, is to subtract additional angular margin θ_{mar} from the allowed simultaneous misalignment θ_{sim} and determine a new detection thresholds $\xi_{\text{CS,mar}}$ by:

$$\xi_{\text{CS,mar}} := \hat{P}_{\text{RX,CS}}(\theta_{\text{sim}} - \theta_{\text{mar}}, \theta_{\text{sim}} - \theta_{\text{mar}}). \quad (7.2.14)$$

This way additional attitude jitter by θ_{mar} will not lead to a signal lower than the signal-lost threshold.

7.2.5. Thresholds for the Three Far-Field Distributions

Here now values for the CS thresholds and the corresponding simultaneous misalignments are calculated for the parameters given in Table 7.4. Table 7.1 lists the computed thresholds and simultaneous misalignment angles for the three far-field intensity patterns and different angular margins. It can be seen that the thresholds and simultaneous misalignments are closer together in case of the propagated fibre mode and a far-field distribution corresponding to a Gaussian beam with $M^2 = 1$ than for the Gaussian beam

Table 7.1.: Summarising the maximum simultaneous misalignment, θ_{sim} , and the CS effective received detection thresholds computed for the three different far-field intensities and angular margins. The Gaussian beam waist radius is assumed to be $w_0 = 2.5$ mm, resulting in a divergence half angle for $M^2 = 1$ of $\theta_0 = 136 \mu\text{rad}$. The parameters for the propagated fibre mode correspond to the small core case, given in Table 2.1. A Gaussian beam fitted to the fibre mode at the outcoupler results in a waist radius of also ~ 2.5 mm.

		Item		
Beam Type	$\theta_{\text{sim}} / \mu\text{rad}$	Angular Margin	Symbol	Value / pW
Fiber Mode	106	20 μrad	$\xi_{\text{CS},20}$	40
		10 μrad	$\xi_{\text{CS},10}$	27
		0 μrad	ξ_{CS}	17
Gaussian, $M^2 = 1$	111	20 μrad	$\xi_{\text{CS},20}$	32
		10 μrad	$\xi_{\text{CS},10}$	21
		0 μrad	ξ_{CS}	14
Gaussian, $M^2 = 1.2$	137	20 μrad	$\xi_{\text{CS},20}$	11
		10 μrad	$\xi_{\text{CS},10}$	7.2
		0 μrad	ξ_{CS}	4.5

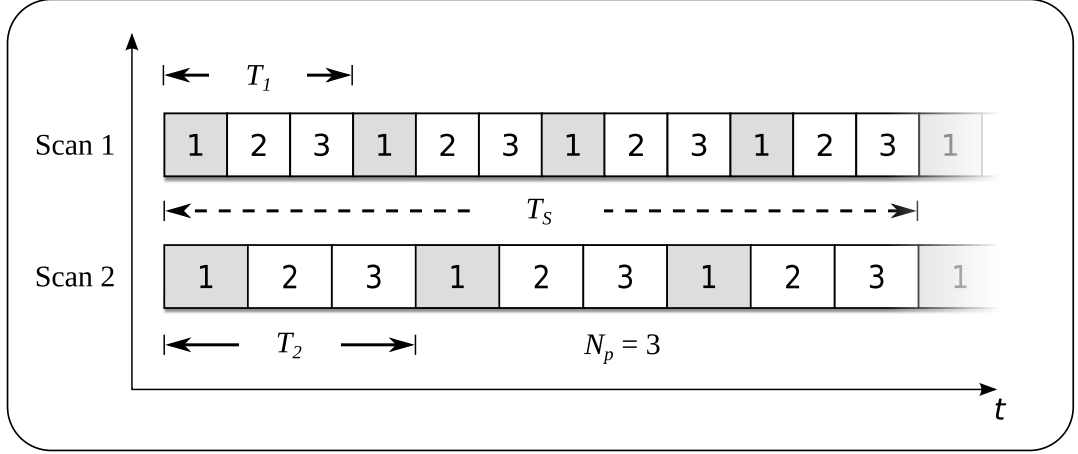


Figure 7.4.: Concept of the slipping scan for a scan space of each $N_p = 3$ points. Shown is the time evolution of the scan points which are indexed 1, 2 and 3 for both scans. The time T_2 of the second slower scan is chosen such that the first faster scan covers $N_p + 1$ points while the second scan covers N_p points. The second scan is thus falling one scan point behind the fast scan each time the slow scan finishes. The relation between the scan times for the two scans is then $T_2 = T_1 (1 + N_p^{-1})$. The total uncertainty space of N_p^2 points is covered in $T_S = (T_1^{-1} - T_2^{-1})^{-1} = (N_p + 1) T_1$.

with $M^2 = 1.2$. The difference in the thresholds is roughly 25 % and the simultaneous misalignment angle, θ_{sim} , only deviates by $5 \mu\text{rad}$. A quality factor of $M^2 \neq 1$ will increase the divergence of the beam by a factor of M^2 while decreasing the on-axis power by a factor of $1/(M^2)^2$. The higher divergence of the Gaussian beam thus results in a larger field-of-view for remote misalignments. The resolution of the spatial scan can potentially be chosen coarser by about $30 \mu\text{rad}$ than is possible for the Gaussian beam with $M^2 = 1$.

However, Figure 7.3 shows that in case of the Gaussian beam with $M^2 = 1.2$ the CS effective received power for a remote beam axis tilt falls off slower than the CS signal for local beam axis tilt. For a given remote beam axis misalignment this slightly increases the maximum possible misalignment of the local spacecraft compared to the case of the fibre mode far-field or the Gaussian beam with $M^2 = 1$. The effect of this for the proposed algorithm is discussed later on in the results section.

7.3. Spatial Scan for the Autonomous Laser Link Acquisition

In principle, the same scan patterns can be used for the autonomous laser link acquisition than were used for the initial LOS calibration. However, the scans used for the initial

LOS calibration were chosen to increase the speed for large uncertainty cones and long scan times. Here the remaining spatial uncertainties are much smaller and the total scan times are expected to be less than the scan times during the initial LOS calibration scans. The initial uncalibrated uncertainty cone radius is assumed to be 3 mrad while the remaining uncertainty cone radius after calibration is assumed to be roughly a factor of ten less, i.e. of the order of 300 μ rad.

If the resolution of the scan remains the same, a speed up of roughly 10 in the time for a single scan can be expected, while the total scan time for covering the four-dimensional spatial uncertainty space shrinks by a factor of 100. Hence, the expected times for covering the total spatial uncertainty space is of the order of seconds. During the initial LOS calibration one satellite is scanning the uncertainty cone as fast as possible while the other satellite dwells on one scan point for the whole scan time of the fast scan and then advances to its next scan point. The total time to cover the four dimensional spatial uncertainty space can then easily be computed by $T_S = N_p T_1$ as the product of the scan time of the fast scan T_1 and the number of scan points of the slow scan N_p .

However, a different approach is possible, where both spatial scans are fast and run at only slightly different rates, so that the slower of the scans will slowly fall behind the fast scan (private communication D. Shaddock, ANU, 2012 / B. Spero, NASA/JPL, 2012). All combinations of scan points of the two scans will be covered if the slow scan slips by the equivalent of at most one scan point during the time of the faster scan.

Letting the spatial scan run with about the same rate is advantageous in an autonomous acquisition as it simplifies and speeds up the signal verification and thus reduces the cost of a false alarm. More detailed information are given when the actual algorithm implementation will be presented. Figure 7.4 shows a schematic of the time evolution of the scan points for two such scans with scan times T_1 and T_2 . The number of scan points in each scan is $N_p = 3$ indexed 1, 2 and 3. The time T_2 of the slower scan is chosen as

$$T_2 = T_1 (1 + N_p^{-1}) \tag{7.3.1}$$

so that the fast scan covers $N_p + 1$ scan points while the slower scan covers N_p points. The slow scan thus slips by one scan point each time it finishes its scan. This can be seen in Figure 7.4 because the first scan point of the second scan is scanned concurrently with scan points of the first scan of increasing index until the first scan points of both scans are scanned again at the same time and the pattern repeats. The second scan is thus repeated N_p times before the scans align again and all combinations of scan points

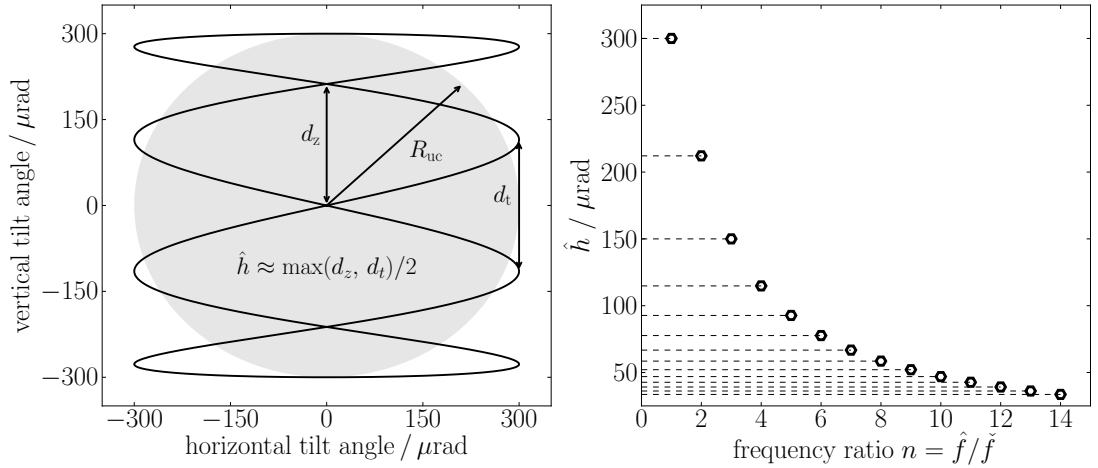


Figure 7.5.: Left: Geometry of the Lissajous scan with frequency ratio $n = 4$ and the two biggest separations of adjacent scan tracks, which occur at the central zero crossings d_z and the central turning points d_t . The maximum separation between the LOS and the scan track, \hat{h} , during the scan can be estimated by $\hat{h} \approx \max(d_t, d_z)/2$. Right: Estimated maximum LOS-to-scan-track separation, \hat{h} , as a function of the frequency ratio of the fast and slow frequency axes for an uncertainty cone radius of $R_{uc} = 300 \mu\text{rad}$.

of the first scan and the second scan have been covered. The total time to cover the combined uncertainty space is then computed with eqn. (7.3.1) to:

$$T_S = N_p T_2 = (N_p + 1) T_1. \quad (7.3.2)$$

For a large number of scan points the total scan times for a slipping scan and the type scan assumed for the calibration scan, which again was given by $T_S = N_p T_1$, can be thought of as approximately the same. During the autonomous laser link acquisition the two scans will run at the maximum speed possible, which will render a scan with discrete stepping impractical for the same reasons it is impractical for the fast scan during an initial LOS calibration. Here again Lissajous raster scans will be used but now on both satellites. Again the maximum separation between the line-of-sight and the scan track during a Lissajous raster scan, \hat{h} , is determined by the uncertainty cone radius, R_{uc} , and the frequency ratio $n_i = \hat{f}_i/\check{f}_i$ between the fast axis frequency \hat{f}_i and the slow axis frequency \check{f}_i of the scan, with $i = 1, 2$ indexing the two spacecraft. An estimate of the maximum LOS-to-scan-track separation \hat{h} for a Lissajous scan as a function of the uncertainty cone radius and the frequency ratio was given in equations (6.1.9) and (6.1.11) as $\hat{h} \approx \max(d_z, d_t)/2$, where d_z and d_t are shown in the left plot of Figure 7.5. \hat{h} as a function of the frequency ratio is shown in the right plot of Figure 7.5 for an

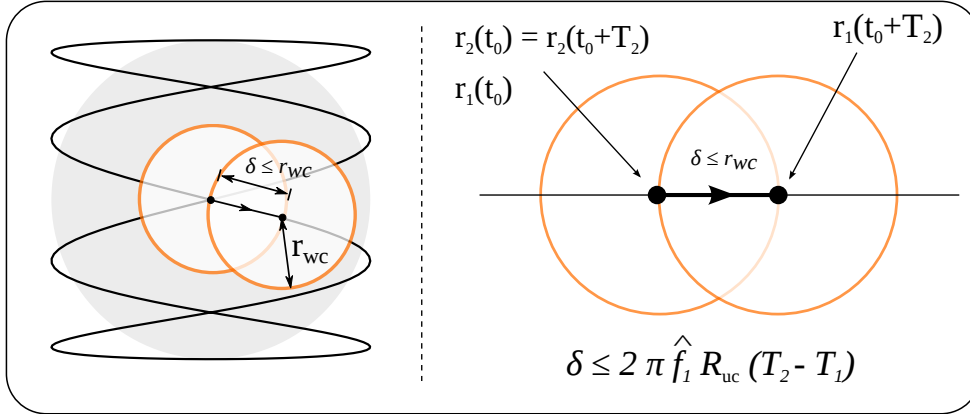


Figure 7.6.: Synchronise the two slipping Lissajous scans.

uncertainty cone radius of $300 \mu\text{rad}$. For the following analysis it is assumed that the scans on both satellites will have the same resolution, i.e. $n_1 = n_2 = n$. The remaining question is how to choose the time of the slower scan such that the complete combined uncertainty space will be covered as no discrete stepping is wanted for the Lissajous scan.

The difference in the scan times, τ , for the Lissajous raster scans can be approximately estimated using the formulas for the scan coordinates of equation (6.1.8). For the Lissajous scan the uncertainty cone is not partitioned into a discrete set of scan points because it is a continuous scan. However, the size of a scan point can be defined as the desired capture range r_{cap} which here should be set equal to the found maximum simultaneous misalignment $r_{\text{cap}} = \theta_{\text{sim}}$.

The scan time difference between the Lissajous scans on the two spacecraft can be found if one restricts the maximum slip of the scans during one spatial scan to the desired capture range r_{cap} . For simplicity the scans are assumed to start at the same position at time t_0 . Hence, if $\mathbf{r}_1(t_0)$ is the position of the faster scan at time t_0 and $\mathbf{r}_2(t_0)$ is the position of the slower scan at time t_0 and $T_2 = T_1 + \tau$ is the scan time of the slower scan, then the following conditions should hold:

$$\begin{aligned}
 \mathbf{r}_1(t_0) = \mathbf{r}_2(t_0) \quad \text{and} \quad \delta &= |\mathbf{r}_1(t_0 + T_2) - \mathbf{r}_2(t_0 + T_2)| \\
 &= |\mathbf{r}_1(t_0 + T_1 + \tau) - \mathbf{r}_2(t_0)| \\
 &= |\mathbf{r}_1(t_0 + \tau) - \mathbf{r}_2(t_0)| \leq \theta_{\text{sim}}.
 \end{aligned} \tag{7.3.3}$$

If the difference in the scan times, τ , is small compared to T_1 and T_2 one can approximate

the slip δ as follows:

$$\begin{aligned}\delta &= |\mathbf{r}_1(t_0 + \tau) - \mathbf{r}_2(t_0)| = R_{\text{uc}} \left| \begin{pmatrix} \sin 2\pi \hat{f}_1(t_0 + \tau) \\ \sin 2\pi \check{f}_1(t_0 + \tau) \end{pmatrix} - \begin{pmatrix} \sin 2\pi \hat{f}_2 t_0 \\ \sin 2\pi \check{f}_2 t_0 \end{pmatrix} \right| \\ &\approx R_{\text{uc}} \sqrt{(2\pi \hat{f}_1 \tau)^2 \cos(2\pi \hat{f}_1 t_0)^2 + (2\pi \check{f}_1 \tau)^2 \cos(2\pi \check{f}_1 t_0)^2}\end{aligned}\quad (7.3.4)$$

In getting to the last line the addition theorem for the sine was used and additionally the following small angle approximations were applied:

$$\begin{aligned}\cos(2\pi \hat{f} \tau) &\approx 1, & \sin(2\pi \hat{f} \tau) &\approx 2\pi \hat{f} \tau, \\ \cos(2\pi \check{f} \tau) &\approx 1, & \sin(2\pi \check{f} \tau) &\approx 2\pi \check{f} \tau.\end{aligned}$$

Equation (7.3.4) can be used to estimate an upper bound on the slip δ for any starting point t_0 . The maximum δ is obtained if both cosine functions attain their maximum value at the same time, which is only true for $t_0 = j T_1$ where j is an integer number. The upper bound on the slip can then be given by:

$$\begin{aligned}\delta &\leq 2\pi R_{\text{uc}} \tau \sqrt{\hat{f}^2 + \check{f}^2} \\ &= 2\pi R_{\text{uc}} \hat{f} \tau \sqrt{1 + 1/n^2} \\ &\approx 2\pi R_{\text{uc}} \hat{f} \tau\end{aligned}\quad (7.3.5)$$

The error in carrying out the last approximation is $\leq 3\%$ for a frequency ratio of $n \geq 4$ and should cause no problems as some margin will be applied to the timing and scan resolution later on. Now, finally the maximum scan time difference can be estimated by requiring that the slip should be less than the desired capture range, $r_{\text{cap}} = \theta_{\text{sim}}$, by:

$$\begin{aligned}\delta &\lesssim 2\pi R_{\text{uc}} \hat{f} \tau \leq \theta_{\text{sim}}, \\ \Rightarrow \tau &\leq \frac{\theta_{\text{sim}}}{2\pi R_{\text{uc}} \hat{f}}.\end{aligned}\quad (7.3.6)$$

The last sentences in this section are devoted to deriving an expression for the total scan time to cover the complete combined uncertainty space of both satellites.

Let's assume the individual scan times are T_1 for the faster scan and T_2 for the slower scan and that the scan time difference is $T_2 - T_1 = \tau$. One can now compare equation (7.3.1) for the time of the discrete scan with the equation $T_2 = T_1 + \tau$ and cast

it into a similar form by:

$$T_2 = T_1 \left(1 + \frac{\tau}{T_1} \right). \quad (7.3.7)$$

Interpreting the fraction within the parentheses as the inverse of an effective number of scan points $\hat{N}_p = T_1/\tau$ the total spatial scan time T_S can be given by:

$$T_S = (\hat{N}_p + 1) T_1 = \left(\frac{T_1}{\tau} + 1 \right) T_1. \quad (7.3.8)$$

That this is indeed the correct answer for the total scan time T_S , which is characterised by the fact that the scans start to repeat from the beginning and the first scan points of each scan align again, can be understood if one inserts $\tau = T_2 - T_1$ into equation (7.3.8). The total scan time T_S can then be reformulated to $T_S = (T_1^{-1} - T_2^{-1})^{-1}$, which is just the inverse of the beat frequency between the slow scanning axes. Actual values for the scan times are shown in the results section for the parameters used during the simulation runs.

7.4. Proposed Algorithm and State Diagram

Here, now the proposed algorithm for an autonomous link acquisition is presented. The emphasis is on describing the current status of the development as well as give insight into some of the design decisions that were taken. The design of the algorithm was mainly driven by the goal to show for once that an autonomous laser link acquisition can work by only using the heterodyne signals of the science photodiodes as acquisition and tracking signals and secondly to give a first more qualitative estimate on the robustness and timing requirements of the autonomous laser link acquisition. The algorithm was designed so that synchronisation between the satellites is of lesser importance and both satellites can carry out their part of the algorithm without the need for communication between the satellites or ground control. Another design goal was to make the algorithm simple, and more complex designs are certainly possible.

Figures 7.8 and 7.9 show the state diagrams of the developed algorithm for the slave and the master spacecraft respectively. As stated earlier the name *master* is used for the spacecraft whose laser is locked to the reference cavity and will not be swept, whereas *slave* names the satellite whose laser is free-running and will be swept to scan the frequency uncertainty region. Handling of the frequency sweep is the only difference in the state diagrams of the two spacecraft, apart from this they are identical.

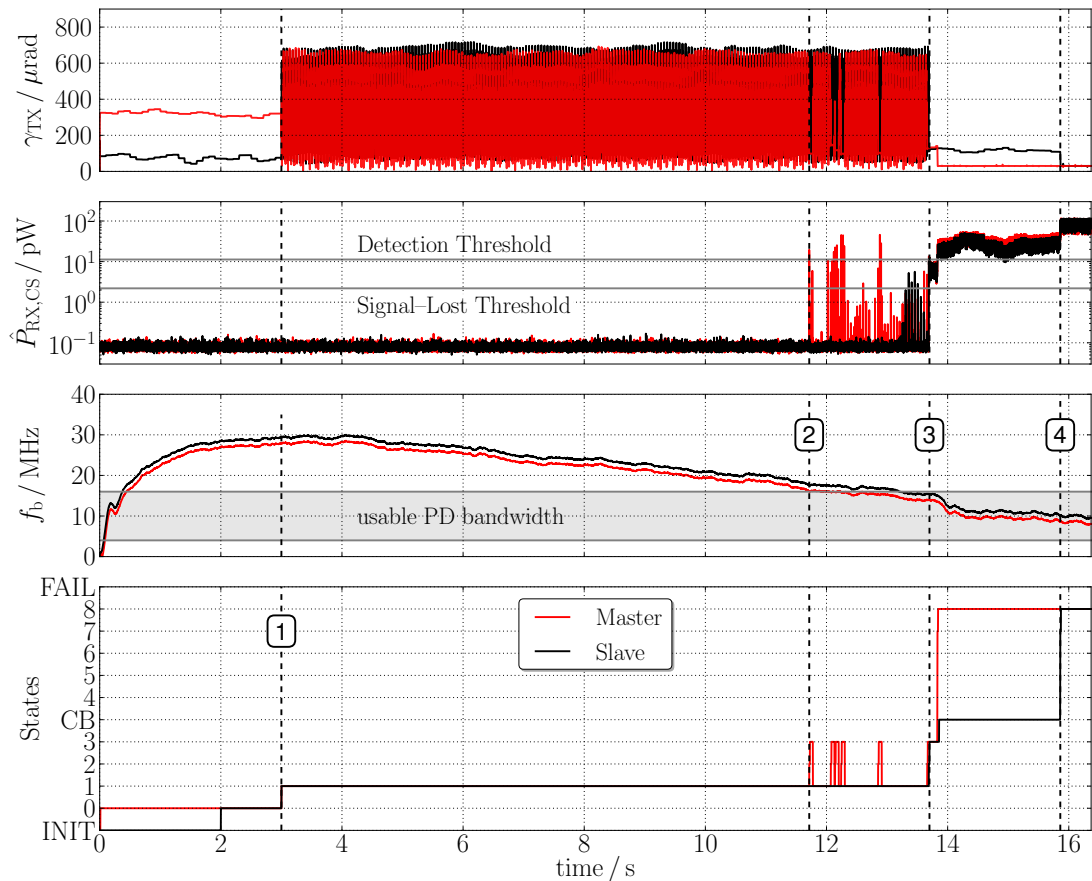


Figure 7.7.: Time series plots of some indicative parameters showing the evolution of the algorithm from an initial phase up to (1), via the scanning phase (1)–(3) and signal verification and frequency settling phase (3)–(4), to the final phase after (4) when both satellites have locked and start tracking the incoming light. The plots show from top to bottom: TX beam angle γ_{TX} relative to the LOS, the CS effective received power $\hat{P}_{\text{RX,CS}}$, the beatnote frequency f_b and the current state of the algorithm. The prefix S or M for the states of the slave and master are omitted in the y-axis labels because the assignment is unambiguous.

The state diagram shows the actions taken when transitioning between states and also the conditions under which a state is left; they are also called *transition guards*. Despite of the details already given in the diagrams the actual actions taken during the execution of the states are not visible. However, this section will go through the states one by one and explain their working. The main tool to do so are plots of misalignment γ_{TX} of the transmitted beam’s (TX) axis relative to the line-of-sight (LOS) in the inertial reference frame, the effective received power for the coherent sum (CS) detector $\hat{P}_{\text{RX,CS}}$ as well as the beatnote frequency f_b of the heterodyne signal. Sometimes also a time series of

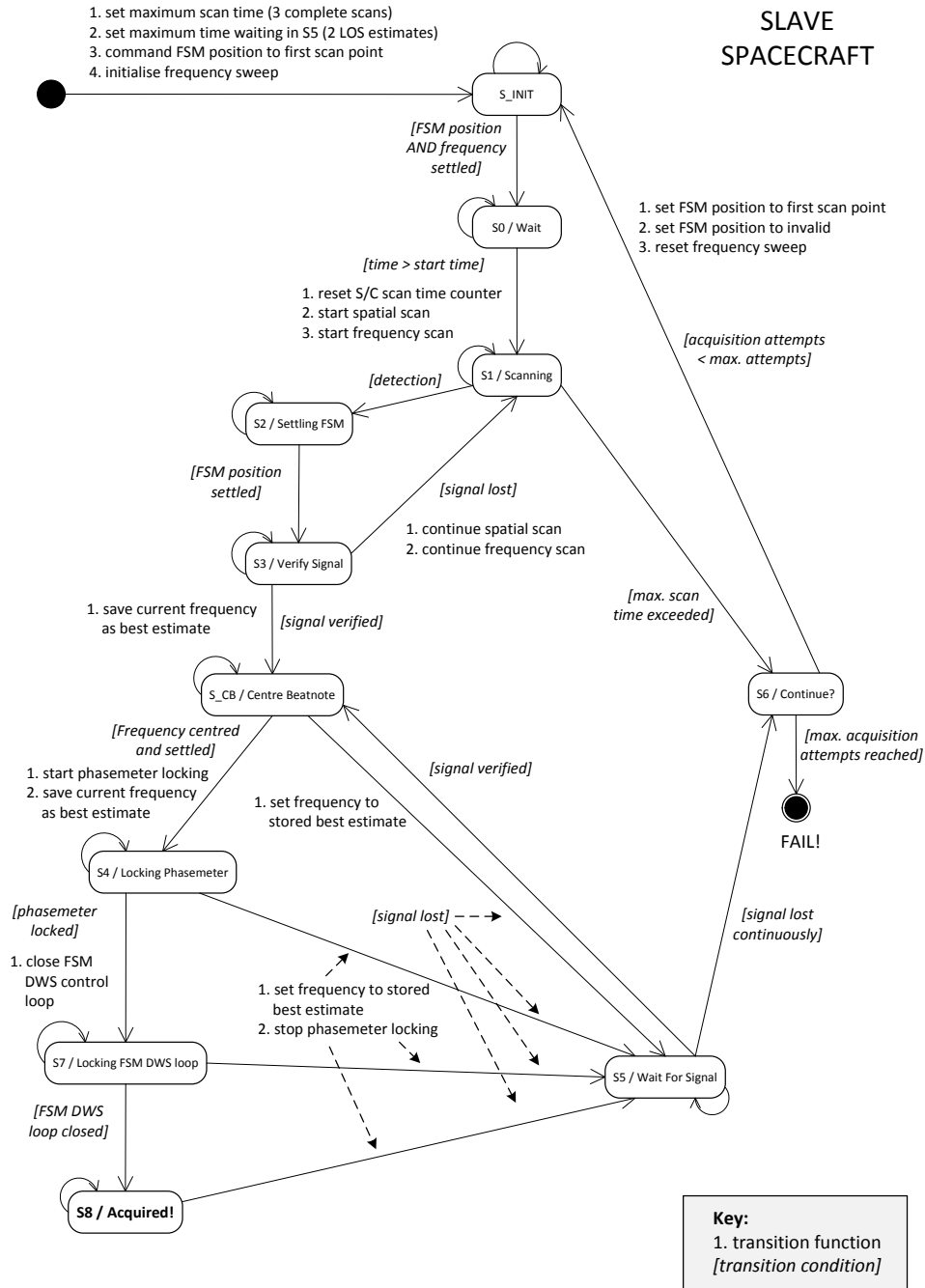


Figure 7.8.: State diagram for the acquisition algorithm of the slave satellite.

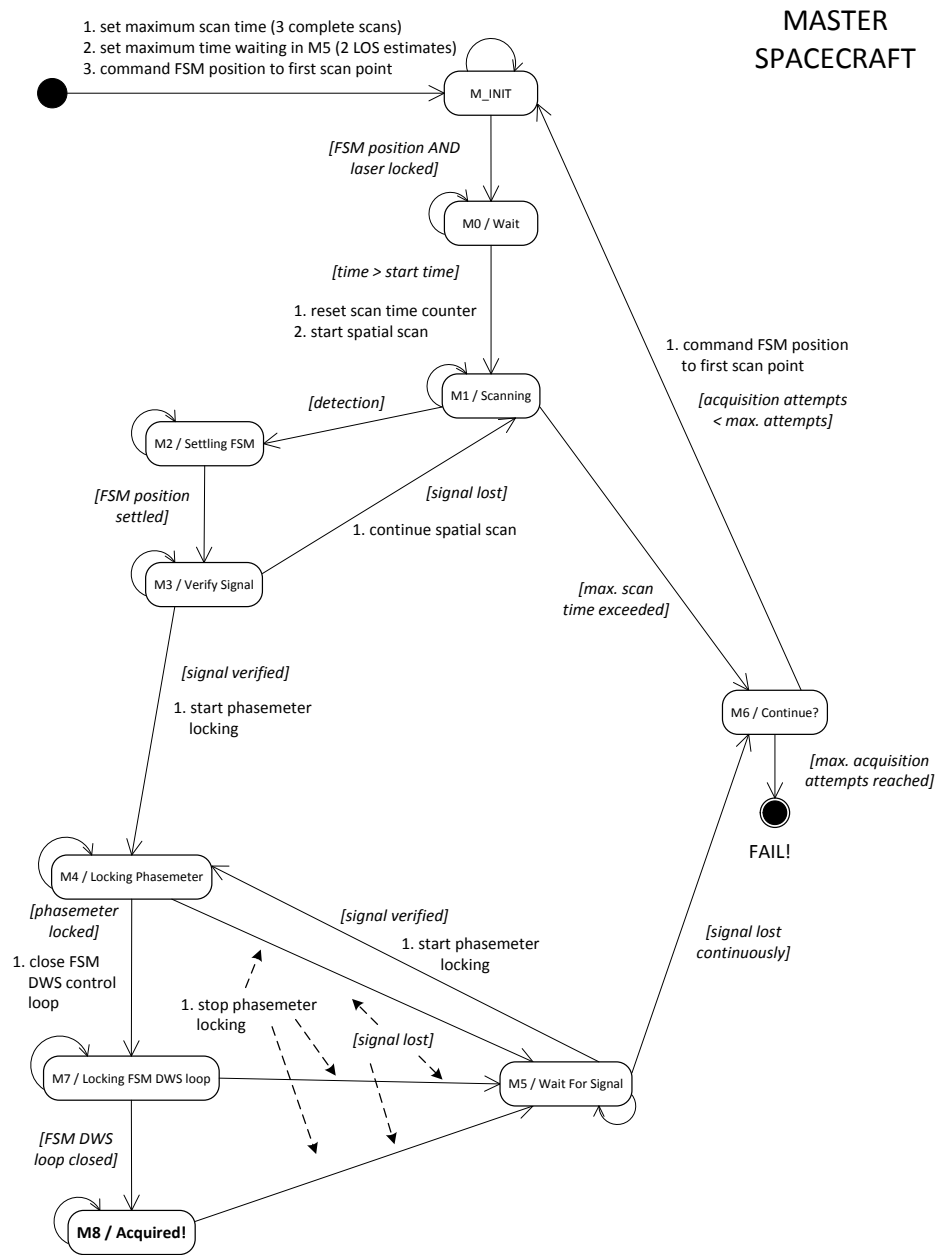


Figure 7.9.: State diagram for the acquisition algorithm of the master satellite.

the evolution of the states is presented to show the reaction of the algorithm to certain events.

An example is shown in Figure 7.7. The upper panel shows the TX beam angles γ_{TX} of both spacecraft relative to the LOS, whereas the middle and bottom panel show the coherent sum effective received power $\hat{P}_{\text{RX,CS}}$ and the beatnote frequency for both spacecraft respectively. The detection threshold ξ_{CS} and the signal-lost threshold ζ_{CS} of equation (7.2.8) are shown in the middle panel for this particular simulation run and in the frequency plot at the bottom the usable photodiode frequency band is shown; it is equal to the non-vetoed region of the FFT in all simulation runs conducted here.

Some special times are marked by annotated vertical lines across all plots. These partition the overall acquisition process in an initialisation phase, before time (1), a scanning phase that is ended at time (3), followed by a signal verification phase in which also the beatnote frequency is centred into the PD bandwidth. Finally both satellites lock at time (4) which is accompanied by a strong increase in the effective received power.

The plots in Figure 7.7 give already a good overview of the process of an acquisition run. Focusing first on the upper plot showing the outgoing beam angles γ_{TX} . Initially, the fine-steering mirror (FSM) position is kept fixed at the best estimate of the LOS. The deviation between the LOS ($\gamma_{\text{TX}} = 0$ rad) and the estimated LOS is due to a remaining initial angular bias and unknown coalignment error of the triple-mirror assembly (TMA). Star-camera assembly (SCA) attitude noise is responsible for the jitter in the outgoing beam angles at a rate of 10 Hz and magnitude of 10 μrad (1σ).

In the frequency plot it can be seen that during the initialisation phase the frequency of the slave laser is set to the lower bound of the frequency scan interval that here is offset from the frequency of the laser on the master spacecraft by 30 MHz. The initialisation period also ensures that the frequency of the slave laser can reach the lower bound of the frequency scan interval before any scans are actually started.

The difference in the beatnote frequencies measured by the master and the slave spacecraft is due to the Doppler shift which was here randomly set to $f_{\text{D}} = 738$ kHz. The magnitude of the difference is equal to $2 \cdot f_{\text{D}}$. The small rebound of the frequency for small t and the slow increase is due to the transfer function of the thermal actuator used to control the laser frequency of the slave laser. See Figure 5.6 in the chapter about the high-fidelity simulation for a plot of the thermal-actuator transfer function and step response.

The commands given to initialise the laser frequency and the steering mirror positions are given during the transition from the default state—black circle in Figures 7.8 and (7.8)—to the states `M_INIT` and `S_INIT` respectively. After the initialisation phase, (1),

the spatial and frequency scans are started which can be seen in the upper plot by the large amplitude signal for the TX beam angles and the slow drift of the beatnote frequencies.

An interesting period starts when the beatnote frequency of the master spacecraft enters the band width of its photodiode (PD), at time (2), while the beatnote frequency of the slave laser is still outside of its photodiode bandwidth. Several gaps in the scan of the master appear at times when the CS signal of the master crosses the detection threshold, ξ_{CS} , and the scan is stopped for a signal verification. As the slave spacecraft keeps scanning, the signal is immediately lost again and after a certain period it resumes its scan from the last scan position. Some seconds later the beatnote frequency measured by the slave spacecraft will also enter the PD bandwidth and the CS effective received power starts to increase on the photodiode of the slave spacecraft. At time (3), the detection threshold is crossed for both spacecraft nearly simultaneously, the scans of both spacecraft are stopped, and the signals are verified. After the successful verification the master spacecraft directly transitions to state M4 while initiating the lock of the phasemeter to the incoming signal. After the lock of all phasemeter channels was successful differential wavefront-sensing (DWS) signals are available, the FSM DWS control loop is closed and the steering mirror position is driven to zero DWS. However, the TMA coalignment error is added to the beam direction after passing the FSM and prevents the TX beam from being centred exactly onto the LOS. Here the TMA coalignment error was randomly set to roughly $30 \mu\text{rad}$.

After the slave spacecraft has detected and verified the signal, it tries to centre the beatnote in the centre of the non-vetoed region of the PD bandwidth, such that for large Doppler shifts the beatnote frequency at both spacecraft will reside in the usable PD bandwidth. Centring the beatnote frequency is initiated upon entering the state S_CB. How this is done exactly is explained in more detail in the corresponding section later. The process of centring the beatnote frequency can be seen in Figure 7.7 shortly after time (3) in the frequency plot, where the frequency rapidly sweeps towards the centre of the PD bandwidth. In order to make sure that the frequency is settled when the phasemeter lock is initiated on the slave spacecraft a period of $\tau_L = 2\text{ s}$ is waited for before the state machine transitions to the next state S4.

Starting from time (4) also the slave spacecraft has initiated the phasemeter lock and shortly thereafter DWS signal is available and the FSM DWS loop on the slave spacecraft is closed which drives the FSM to the position with zero DWS signal. The CS effective received power on both spacecraft now drastically increases due to the better alignment. However, both transmitted laser beams have a residual misalignment to the

LOS of approximately $30 \mu\text{rad}$ which is due to the TMA coalignment error that here is by chance roughly the same for both spacecraft.

The overview of the acquisition process is now complemented by a complete listing, in Sections 7.4.1 to 7.4.6, of the states of the master and slave satellite while states with equal functionality in the master and slave part of the algorithm will be treated together.

7.4.1. Initialisation Phase

Involved States: S_INIT, S0, M_INIT, M0

Commanding the FSM position to the estimated LOS on the master and the slave spacecraft and the frequency of the free-running slave laser to the lower bound of the frequency scan interval is done during all transitions to the INIT state. Concurrently timers are started measuring the elapsed time t_{FSM} and t_{L} since the commands for the FSM and the laser were given. During the INIT state no additional actions are taken but the number of acquisition attempts N_{A} is incremented by 1. The state of the state machine transitions from M_INIT to M0, if

$$t_{\text{FSM}} \geq \tau_{\text{FSM}}, \quad (7.4.1)$$

and for the slave spacecraft from S_INIT to S0, if

$$t_{\text{FSM}} \geq \tau_{\text{FSM}} \quad \text{and} \quad t_{\text{L}} \geq \tau_{\text{L}}. \quad (7.4.2)$$

Table 7.2.: Global constants used to control the algorithm and their default values; T_2 is the time of the slower spatial scan, *dep.* means the value is depending on other parameters. The meaning of the constants is discussed in the description of each state. The timing constants, τ_{FSM} , τ_{L} and τ_{DWS} are derived from the step responses shown in Section 5.2.

Item				
Description	Symbol	Value	Unit	
Maximum number of acquisition attempts	$N_{\text{A,max}}$	4		
FSM settling time	τ_{FSM}	10	ms	
Laser frequency settling time	τ_{L}	2	s	
Time before signal verification	τ_{SV}	T_2		
Number of sequential detection in verification	N_{SD}	1 000		
Time to wait in S5, M5	τ_{wait}	200	ms	
Time FSM is driven to zero in DWS loop	τ_{DWS}	10	ms	
Detection threshold	G_{CS}	dep.	A_{RMS}^2	
Signal-lost threshold	C_{CS}	dep.	A_{RMS}^2	

The values of the predefined constants τ_{FSM} and τ_{L} are given in Table 7.2. The function of the states M0 and S0 is to roughly synchronise the start of the scan once in the beginning, when the whole acquisition process is initiated. It delays the transition to the scanning state up to an agreed point in time t_0 . However, for successive acquisition attempts during one run this state is passed immediately without additional delay. Also random differences in the start time are inserted here by adding a random offset δt_0 to t_0 to test the algorithm for asynchronous starts.

7.4.2. Scanning Phase and Detection

Involved States: S1, S2, M1, M2

During the transition from S0 to S1 and M0 to M1 the counter for counting the total scan time is reset to zero. The spatial scan is started and for the case of the slave spacecraft the frequency sweep is also started. The scanning states S1 or M1 are left to S6 or M6 if a predefined maximum scan time is exceeded during which no detection was made. If the maximum returned by the CS detector exceeds the set detection threshold,

$$\max_k |\tilde{s}_{\text{CS}}(k)|^2 > G_{\text{CS}} \quad \text{with} \quad k = k_{\text{low}}, \dots, k_{\text{up}}, \quad (7.4.3)$$

the spatial and frequency scans are stopped and the state machine transitions to M2 or S2 respectively. For $k < k_{\text{low}}$ and $k > k_{\text{up}}$ the frequency bins are vetoed and not considered for a detection. For a definition of the CS signal $\tilde{s}_{\text{CS}}(k)$ see equation (4.2.21) and for the definition of the threshold G_{CS} see equation (7.2.6). Stopping the spatial scan and commanding the FSM to the position, where the detection occurred might result in overshoot of the steering-mirror. Thus, after stopping the scans, the states M2 and S2 wait for a predefined time τ_{FSM} to allow the steering mirror to settle to the commanded point. The frequency sweep is assumed to be slow enough so that no significant overshoot is expected and no additional settling time for the laser frequency is defined.

7.4.3. Signal Verification Phase

Involved States: S3, M3

The signal verification which happens in the states S3 and M3 on the slave and master is identical and implemented as follows. The main idea here is that due to the similar tilt dependence of the CS effective received power $\hat{P}_{\text{RX,CS}}$ for local and remote measurement, see Figure 7.2 or 7.3, it is likely that, if one spacecraft made a detection and fixes its FSM position to where the detection occurred, the other spacecraft will also detect a signal, if its scan position approaches the LOS. Hence, before the actual signal verification starts,

a certain time τ_{SV} is waited for. It is chosen as the scan time of the slower spatial scan, T_2 , in order to wait for a detection of the remote spacecraft, which will then end its scan and fixes its FSM position which will in turn likely result in a signal at the local spacecraft. Here a wider far-field intensity pattern as compared to the local response which is given by the heterodyne efficiency is advantageous, but not a necessity. This will be discussed further in the results section.

The signal verification is successful if a number of N_{SD} sequential FFTs yield maximum values above the signal-lost threshold C_{CS} ,

$$\max_k |\tilde{s}_{CS}(k)|^2 > C_{CS} \quad \text{with} \quad k = k_{\text{low}}, \dots, k_{\text{up}}. \quad (7.4.4)$$

The number of sequential detections is set as high as $N_{SD} = 1000$ to guarantee a robust signal, which is very unlikely to drop below the signal-lost threshold due to noise and scalloping loss alone. After a successful verification the master transitions to M4 to lock the phasemeter and the state machine on the slave spacecraft transitions to S_CB in which the beatnote frequency is centred in the PD bandwidth.

If at any time the detector output drops below C_{CS} , i.e.

$$\max_k |\tilde{s}_{CS}(k)|^2 \leq C_{CS} \quad \text{with} \quad k = k_{\text{low}}, \dots, k_{\text{up}}, \quad (7.4.5)$$

the signal verification failed and the state machine transitions back to the scanning states M1 or S1, resuming the scans during the transition.

7.4.4. Centring the Beatnote Frequency on the Slave Spacecraft

Involved State: S_CB

During the transition from S3 to S_CB the current frequency command for the laser is stored as backup \hat{f}_L . The laser frequency will be commanded to this backup frequency any time the signal is lost hereafter and the state machine of the slave spacecraft transitions to the buffer state S5.

The relative speed of the satellites as measured during the current GRACE mission is limited to roughly 2.5 m s^{-1} resulting in a one-way Doppler shift of up to $f_D = \pm 2.35 \text{ MHz}$. The difference in the beatnote frequencies is $2 \cdot f_D$ resulting in possible frequency differences of the beatnote on the master and slave spacecraft of up to $\pm 4.7 \text{ MHz}$.

However, a signal verification is only successful if both spacecraft detected a signal and stopped their scans which means that the beatnote frequency is in the measurement band on both spacecraft. Though if the beatnote signal on one of the spacecraft is

close to the edge of the measurement band, frequency noise might push it outside of the measurement band. For this reason the beatnote frequency measured on the slave spacecraft is centred in the measurement band to avoid such a situation. The way this is realised in the simulation is to estimate the beatnote frequency f_b from the FFT bin number k_{\max} the maximum signal was found in, by

$$f_b \approx k_{\max} \frac{f_s}{N_{\text{DFT}}}, \quad (7.4.6)$$

where f_s is the sampling frequency and N_{DFT} is the sample size of the FFT. The offset, f_{off} , from the centre of the measurement band is then calculated with the bin indices of the lower and upper bound of the vetoed frequency band k_{low} and k_{up} by

$$f_{\text{off}} = \left[k_{\max} - \frac{k_{\text{up}} + k_{\text{low}}}{2} \right] \frac{f_s}{N_{\text{DFT}}}. \quad (7.4.7)$$

This offset is added to the current commanded frequency of the slave laser, resulting in the centring of the beatnote frequency. See Figure 7.7 directly after marker (3) for an example.

After commanding the laser frequency to the new value a period of τ_L seconds is waited for the frequency to move to the centre before the transition to S4 is initiated. A check if the beatnote is really centred might be necessary though in the simulation this was not implemented. During the transition to S4 the current, now centred frequency, is stored as new current backup frequency \hat{f}_L .

If the signal drops below the signal-lost threshold C_{CS} , the state machine transitions to the buffer state S5 during which the frequency is set back to the backup frequency \hat{f}_L .

7.4.5. Initiate Tracking

Involved States: S4, S7, S8, M4, M7, M8

At any time during the execution of one of the above listed states, is the detector output checked for a lost signal. This means, that any time,

$$\max_k |\tilde{s}_{\text{CS}}(k)|^2 \leq C_{\text{CS}} \quad \text{with} \quad k = k_{\text{low}}, \dots, k_{\text{up}}, \quad (7.4.8)$$

the state machine restores the state of the frequency and steering mirror as was after the signal verification M3 for the master and after the beatnote centring S_CB for the slave and transitions to M5 respectively S5. It is expected and no additional settling time for the laser frequency is defined.

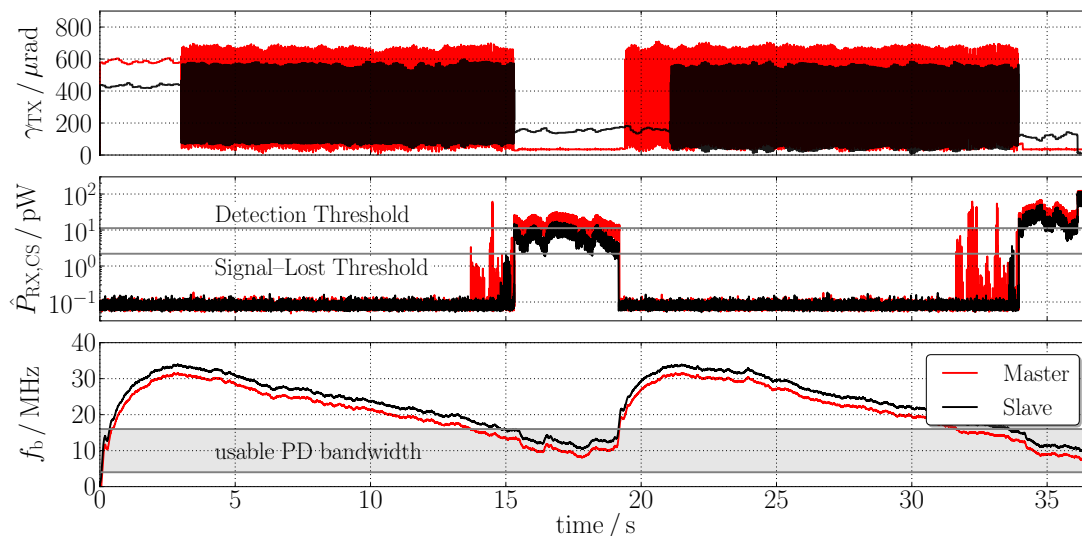


Figure 7.10.: Time series of an acquisition process which needed two attempts. It also motivates the inclusion of the buffer states as the signal drops below the signal-lost threshold after detection and verification. Figure 7.11 shows a close-up of the important region.

For both the master and the slave, the transition from 4 to 8 via 7 is straight-forward if the signal is not lost. Locking the phasemeter to the incoming light is initiated during the transition to S4/M4 from S_CB or M3 and the state machine resides in S4/M4 as long as the DWS signal is not available. If the phasemeter signals successful locking of all channels and DWS is available the state machine transitions to S7/M7 during which it closes the FSM DWS loop.

In states S7/M7 a predefined time of τ_{DWS} , is waited for to allow the control loop to drive the DWS signal to zero after which the transition to the final state S8 or M8 is done.

7.4.6. Buffer State and Decision State

Involved States: S5, S6, M5, M6

The buffer state was introduced as some processes exist which lead to a loss in the signal after the signal has been successfully detected and verified. See Figures 7.10 and 7.11 for an example of an acquisition process which benefits twice from the existence of the buffer state, though the signal is finally lost and the scans are reinitialised. In the shown acquisition process, star-camera assembly (SCA) noise leads to increasing misalignments. The simulated SCA noise has an assumed standard deviation of $10 \mu\text{rad}$ being added every 100 ms to the current FSM position.

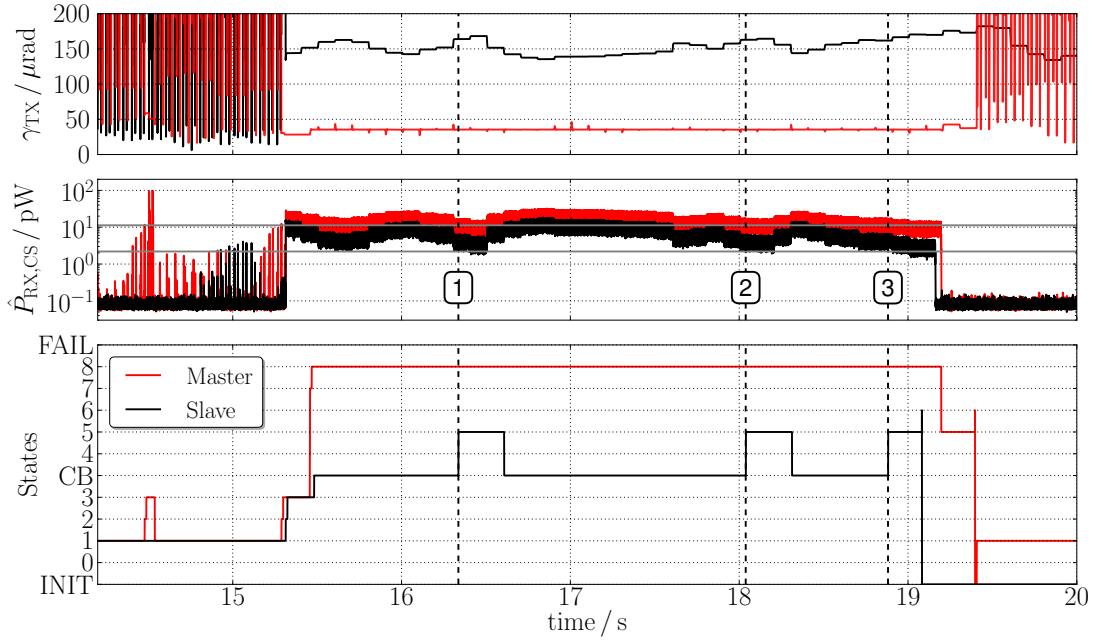


Figure 7.11.: Close-up of Figure 7.10. After signal detection and verification the signal drops below the lower threshold initiating a transitions to S5 which redetects the signal and transitions back to S_CB, (1) and (2). After the third time (3) the signal is lost completely. One reason for this is that the slave waits too long for the frequency to settle, while SCA noise accumulates. Reducing this time, τ_L , is a key to improve the algorithm during this phase.

Also frequency noise might be a cause in case of large Doppler shifts and a limited usable PD measurement band. However, if these noise sources are responsible for the signal loss, the probability exist that the signal will reappear shortly after. The buffer states S5 and M5 try to exploit this in that it is waited for some time τ_{wait} for the signal to reappear. A restart of the scans might then be prevented.

The way the signal is verified is the same as in the signal verification states M3 or S3 by counting the number of sequential FFTs for which the detector output is above C_{CS} . Also the same number N_{SD} of sequential FFTs is required.

However, the difference is that if the signal is below C_{CS} it is checked if the time since entering the state t_5 is longer than τ_{wait} . If not, the number of sequential detections already counted, is reset to zero and counting will restart anew. Only if

$$\max_k |\tilde{s}_{CS}(k)|^2 \leq C_{CS} \quad \text{and} \quad t_5 > \tau_{wait}, \quad (7.4.9)$$

is the signal declared lost completely and the state machine will transition to the decision

state S6 or M6.

The decision state only compares the current number of acquisition attempts N_A carried out, to a predefined maximum number of attempts $N_{A,\max}$. If $N_A \leq N_{A,\max}$ the transition to S_INIT, M_INIT is initiated and the next attempt is started. If however, $N_A > N_{A,\max}$ the state machine transitions to S_FAIL or M_FAIL respectively.

7.5. Results

The presented algorithm for the autonomous laser link acquisition was implemented on top of the high-fidelity simulation to control the underlying dynamics of the LRI components, provided by the lower layer of the simulation. The implementation of the proposed algorithm was tested for the three different far-field intensity patterns discussed earlier and for different thresholds accounting for different margins, to test the sensitivity of the algorithm to this parameter. The thresholds used for the simulation runs are summarised in Table 7.1.

The corresponding signal-lost thresholds ζ_{CS} are computed from the detection threshold with no margin by equation (7.2.8). Determining the thresholds, however, also sets the capture range as the maximally allowed simultaneous misalignment, $r_{\text{cap}} = \theta_{\text{sim}}$, to reach the detection threshold and, hence, the maximum LOS-to-scan-track separation, \hat{h} , of the spatial scan that can be combined with a given threshold. Table 7.3 lists the used scan times for a given threshold, whereas the frequency of the fast-scanning axis is kept fix at $\hat{f} = 100$ Hz. For simulation runs in which the angular margin is reduced from $\theta_{\text{mar}} = 20 \mu\text{rad}$ to $10 \mu\text{rad}$ or $0 \mu\text{rad}$, the parameters of the spatial scan were kept at the values for the case of $\theta_{\text{mar}} = 20 \mu\text{rad}$.

The frequency sweep rate was then computed from the total spatial scan time T_S by requiring that during one complete spatial scan half, the size of the usable PD bandwidth is swept over, meaning:

$$v_s = \frac{F_{\text{PD}}}{2T_S}. \quad (7.5.1)$$

For the usable photodiode bandwidth of $F_{\text{PD}} = 12$ MHz, from 4 MHz to 16 MHz, and the spatial scan times of Table 7.3 the maximum sweep rate computes to $v_s = 1.72 \text{ MHz s}^{-1}$. A loss of SNR due to the frequency sweep is not expected as seen from Figure 4.11. In order to rigorously test the algorithm, 1000 simulations were conducted for a given far-field intensity distribution, detection and signal-lost threshold with random values for the initial angular and frequency bias, for the triple-mirror assembly (TMA) coalignment

error as well as for the Doppler shift. Also an initial random offset for the start time of the algorithm was introduced to test if asynchronous starts effect the algorithm performance. The ranges of the parameters from which random values were drawn from a uniform distribution over the specified interval are listed in Table 7.5.

All simulations were run for the worst case separation of the spacecraft of 270 km and an FFT length of 4096 points. The simulation was thus run at a rate of $f_{\text{sim}} = 38 \text{ MHz}/4096 = 9.277 \text{ kHz}$ simulating one FFT per time step. The one-way light travel time at this distance is $t_{\text{light}} \approx 901 \mu\text{s}$ and was approximated by delaying the received power and frequency of the laser light by 8 samples at the simulation rate, resulting in a time delay of $\tau_{\text{delay}} = 862.3 \mu\text{s}$. All other parameters were fixed and correspond to an assumed low power case for a GRACE Follow-On mission; these are listed in Table 7.4.

For the unknown frequency offset δf_0 before the link acquisition is started, it is assumed that the uncertainty interval is known and the frequency sweep is started from below the lower edge of the uncertainty interval, such that the sign of the frequency change is known. If the sign would not be known a more complicated procedure for centring the beatnote frequency in the centre of the PD bandwidth had to be used which first estimates the correct sign of the offset to be applied.

7.5.1. Fibre Mode Far-Field

At first, the results obtained for using the simple model of the propagated fibre mode far-field as given by equation (2.5.18) are discussed. The single channel (CHAN) and coherent sum (CS) signals for a simultaneous, local and remote misalignment are shown

Table 7.3.: Spatial scan parameters for desired capture range of $r_{\text{cap}} = \theta_{\text{sim}} - \theta_{\text{mar}}$ for the thresholds listed in Table 7.1 for an angular margin of $\theta_{\text{mar}} = 20 \mu\text{rad}$. Also given are the maximum separation between the LOS and the scan track during the scan, \hat{h} , and the corresponding frequency ratio $n = \hat{f}/\check{f}$. With these parameter values the scan time of the faster scan T_1 is calculated assuming a fast axis frequency of $\hat{f} = 100 \text{ Hz}$. The scan time difference τ and the overall spatial scan time T_S are computed with equations (7.3.8) and (7.3.6). For simulation runs using smaller angular margins the spatial scan parameters are kept fix at the values for $\theta_{\text{mar}} = 20 \mu\text{rad}$.

Item						
Beam Type	$r_{\text{cap}} / \mu\text{rad}$	$\hat{h} / \mu\text{rad}$	n	T_1 / ms	$\tau / \mu\text{s}$	T_S / s
Fiber Mode	86	77.7	6	60	456	7.95
Gaussian, $M^2 = 1$	91	77.7	6	60	483	7.52
Gaussian, $M^2 = 1.2$	117	92.7	5	50	621	4.08

in Figure 7.2. Based on these signals the detection and signal-lost thresholds as well as the maximum LOS-to-scan-track separation, \hat{h} , for the spatial scans are chosen with the

Table 7.4.: Default parameters used for the simulations. The noise sources correspond to the default values defined in Table 3.2. The usable photodiode bandwidth F_{PD} is assumed to be located between 4 MHz and 16 MHz.

Item			
Description	Symbol	Value	Unit
Spacecraft separation	$D_{S/C}$	270	km
One-way light travel time	τ_{delay}	862.3	μs
TX beam power	P_{TX}	13.7	mW
LO beam power	P_{LO}	0.6	mW / photodiode
QPD slit width	δ_s	30	μm
QPD radius	R_{PD}	0.5	mm
QPD responsivity	ρ_{PD}	0.6	A/W
QPD segments	n_{seg}	8	(hot redundant) number
Usable photodiode bandwidth	F_{PD}	12	MHz
Receive aperture radius	r_a	4	mm
Power loss in RX beam path	ρ_{rx}	0.795	r.u.
Spatial uncertainty cone radius	R_{uc}	300	μrad
Frequency uncertainty	F_{uc}	100	MHz
Frequency noise	\hat{S}_ν	$200/f$	$\text{kHz}/\sqrt{\text{Hz}}$
FFT size	N_{DFT}	4096	number
Lissajous fast axis frequency	\hat{f}	100	Hz
Gaussian beam waist radius	w_0	2.5	mm
Gaussian beam quality factor	M^2	1.0, 1.2	r.u.
Fibre mode core radius	a	2.54	μm
Fibre mode normalised frequency	V	1.967	r.u.

Table 7.5.: Ranges of the randomised parameters in the simulation runs. For these, variates were drawn from uniform distributions.

Item				
Description	Symbol	Min.	Max.	Unit
Initial frequency offset	δf_0	-100	0	MHz
Initial angular bias	γ_{BIAS}	0	300	μrad
TMA coalignment error	γ_{TMA}	0	40	μrad
Initial start time offset	δt_0	-500	500	μs
Doppler shift	f_{D}	-2.5	2.5	MHz

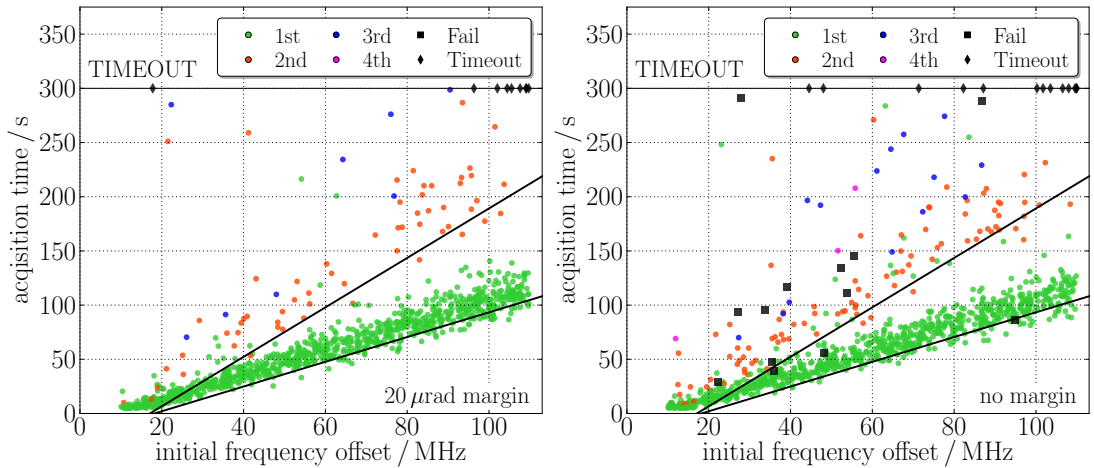


Figure 7.12.: Simulation results for the fibre mode far-field. The figure shows scatter plots of the acquisition time over the initial frequency offset as measured from the lower bound of the frequency sweep interval. The two solid lines correspond to the time of the earliest entry of the beatnote into the measurement band for the used frequency sweep rate, not considering the Doppler shift or frequency noise. The lower one for a first and upper one for a second attempt. The colour encodes the minimum number of attempts any of the two spacecraft needed to acquire. Left: upper CS threshold chosen with $20\ \mu\text{rad}$ margin to the desired capture range $r_{\text{cap}} = \theta_{\text{sim}}$ to guarantee $3\ \text{pW}$ effective received power per channel in case of a detection. Right: upper CS threshold chosen with no margin.

improved method shown in the plot of Figure 7.2.

As was stated in the last section some margin between the detection and signal-lost thresholds should be kept so that additional misalignments due to SCA noise do not immediately reduce the signal power below the signal-lost threshold. However, due to some robustness in the proposed algorithm introduced by the buffer states M5 and S5 a lost signal will not inevitably lead to a reinitialisation of the scans but there is a high probability that the signal reappears.

In order to investigate the performance of the algorithm for different margins three cases were considered, namely margins corresponding to $\theta_{\text{mar}} = 20\ \mu\text{rad}$, $10\ \mu\text{rad}$ and $0\ \mu\text{rad}$. The used thresholds are listed in Table 7.1.

The results for a $20\ \mu\text{rad}$ margin and no margin are compared in Figure 7.12. The plots show the time the two spacecraft needed to acquire as a function of the initial offset of the beatnote frequency, as measured from the lower bound of the frequency sweep interval. The colour of the circles encode the minimum number of attempts needed by any of the two spacecraft to acquire, whereas the maximum number of attempts was set to 4. If one of the spacecraft did not acquire in the fourth attempt the acquisition was

said to be failed.

Failures are marked by black squares in the two plots. The maximum time for the laser link acquisition was set to $t_{\text{TO}} = 300$ s and the simulation was stopped if the acquisition process was not successful after t_{TO} . Simulation runs that timed out are marked by black diamonds. The two solid straight lines mark the time for the earliest entry of the beatnote into the PD bandwidth given the used frequency sweep rate and assuming no frequency noise and Doppler shift. The lower of these two lines marks the time for the first attempt and the upper line for a second attempt.

However, some of the green circles lie below the bottom and some of the orange circles below the upper line indicating an acquisition which succeeded earlier than the perfect limit. Frequency noise or a Doppler shift can reduce the actual frequency offset by chance reducing the time for a successful acquisition. Apart from this the two lines seem to partition the circles nicely into the group of acquisitions that at least needed a single attempt and those that needed more than one by any of the two spacecraft. The most prominent feature in both plots is the, however, expected strong correlation between the acquisition time and the frequency offset, following the lower solid line. More than 90 % of all simulation runs acquired directly in the first attempt for an angular margin of $20 \mu\text{rad}$, no acquisitions failed but 9 timed out.

The number of successful acquisitions with a minimum of one attempt is reduced to 86 % if no angular margin is applied, as can be seen in the right plot of Figure 7.12. The number of failures increased to 13, and also 13 acquisitions timed out, but still the success rate is at 97.4 %. Hence, most of the failed first attempts are successful in a succeeding second or third attempt. The width of the area with the most green circles is determined by the total time of the four-dimensional spatial scan T_S and is mostly due to variations in the angular bias and frequency noise.

7.5.2. Gaussian Beam, $M^2 = 1$

The second series of simulations was carried out using the Gaussian beam with beam quality factor $M^2 = 1$ for the far-field intensity pattern. The single channel (CHAN) and coherent sum (CS) signals for the three types of misalignments were shown in the left plot of Figure 7.3. The CS detection threshold for no margin was found to be 13.7 pW at a simultaneous misalignment of $\theta_{\text{sim}} = 111 \mu\text{rad}$ and from this the signal-lost threshold is defined in analogy to the latter case. The thresholds for $10 \mu\text{rad}$ and $20 \mu\text{rad}$ margin were estimated to be $\xi_{\text{CS},20} = 32$ pW and $\xi_{\text{CS},10} = 21$ pW.

The results for this case are shown in Figure 7.13. The principle pattern is the same as for the fibre mode far-field with 94 % of the acquisitions being successful with a minimum

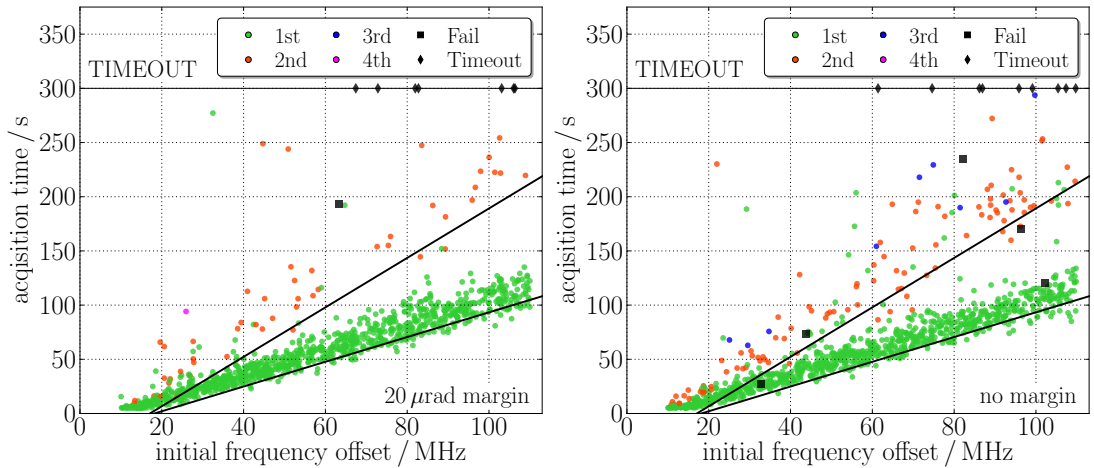


Figure 7.13.: Simulation results for a far-field intensity pattern of a Gaussian beam with beam quality factor $M^2 = 1.0$. Left: upper CS threshold chosen with $20 \mu\text{rad}$ margin to the desired capture range $r_{\text{cap}} = \theta_{\text{sim}}$ to guarantee 3 pW effective received power per channel in case of a detection. Right: upper CS threshold chosen with no margin. For more details see Figure (7.12).

of one attempt, one failed and 7 timed out. Decreasing the margin also increases the number of acquisitions successful only in a second or third attempt and introduces some failures. The overall performance however is slightly better than in the case of the fibre mode far-field which might originate from the larger difference between the remote and local CS signal, whereas the local CS signal falls-off more slowly as compared to the remote CS signal. Compare to Figures 7.2 and 7.3.

7.5.3. Gaussian Beam, $M^2 = 1.2$

The last considered case is for a Gaussian beam with beam quality factor $M^2 = 1.2$ which significantly increases the width of the far-field distribution. The plot of the signals for the single channel (CHAN) and the coherent sum (CS) of the channels, as a function of the beam axis misalignment is shown in the right plot of Figure 7.3. It can be seen that the remote beam misalignment has a much wider response than the local CS signal. The effect of this is obvious from the plots in Figure 7.14. The number of successful acquisitions with a minimum of one attempt with 96% is the highest of all considered cases, while the maximum allowable misalignment is the largest, resulting in a faster spatial scan and frequency sweep. Also, the number of simulations that need a higher number of attempts is less than in the two other cases if no margin is applied to the detection threshold. The detection thresholds used for this case are: $\xi_{\text{CS}} = 4.48 \text{ pW}$,

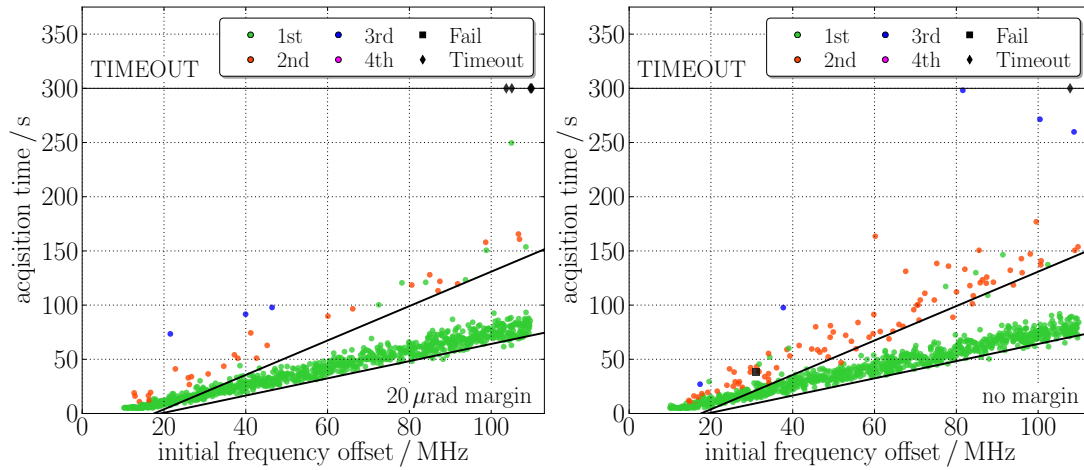


Figure 7.14.: Simulation results for a far-field intensity pattern of a Gaussian beam with beam quality factor $M^2 = 1.2$. Left: upper CS threshold chosen with $20 \mu\text{rad}$ margin to the desired capture range, $r_{\text{cap}} = \theta_{\text{sim}}$, to guarantee 3 pW effective received power per channel in case of a detection. Right: upper CS threshold chosen with no margin. For more details see Figure 7.12.

$\xi_{\text{CS},10} = 7.2 \text{ pW}$ and $\xi_{\text{CS},20} = 11.27 \text{ pW}$, whereas the required capture range for ξ_{CS} is $\theta_{\text{sim}} = 137 \mu\text{rad}$.

7.5.4. Summary of Simulation Runs

All results are again summarised in Table 7.6, showing the number of successful acquisition attempts, the number of failures and time-outs. The successful attempts are additionally broken down into the maximum number of attempts any of the two spacecraft needed. This is in contrast to the plots in Figures 7.12 to 7.14 where the colour encodes the minimum number of attempts needed. The percentage of successful acquisition attempts is above 97% in all considered cases independent of the angular margin used to determine the CS threshold, ξ_{CS} .

Similar results are obtained for the fibre-mode far-field and the Gaussian beam far-field with $M^2 = 1.0$. This is expected because in these two cases the remote and local CS signal have similar shapes, whereas for the Gaussian beam the curves are much closer together, resulting in slightly better performance. Looking at the number of simulations for which both satellites needed only a single attempt to acquire, it can be noticed that decreasing the angular margin between the detection threshold and the signal-lost threshold leads to a higher probability that the first attempt will fail.

It can also be seen that the number of acquisitions successful in the first attempt

increases about linear with the angular margin applied to the threshold. The percentage of acquisitions successful with at most 2 attempts which failed in a first attempt of one of the spacecraft is for all cases of the angular margin in the range of 63% – 69%, while those acquisitions not successful with at most 2 attempts, will acquire with three attempts with 47% – 50% probability. Additionally, one series of simulations was made using the same thresholds for the signal detection and for the decision if a signal is lost by setting the thresholds to the 0 μrad margin and thus, not accounting for scalloping-loss in the FFT. The results are shown in the rows labelled *equal threshold*.

Here, the number of acquisitions successful in the first attempt is reduced significantly to 64% – 66%, whereas the number of failed and timed out acquisitions only increase to roughly 6%. The reason for this can be seen in the high number of runs for which one of the spacecraft is successful in a second attempt. For the simulations using the Gaussian beam with beam quality factor $M^2 = 1.2$ for the far-field intensity pattern the bottom line is, that the increased width of the intensity distribution in the far-field and in particular, the fact that the remote CS signal falls-off much slower than the local CS

Table 7.6.: Outcome of the simulation runs for the three different far-field beam types and angular margins. Additionally, results are shown for simulations in which the two thresholds were chosen identical, i.e. the signal-lost threshold was not reduced to account for scalloping loss and the detection threshold was chosen with 0 μrad margin. The successful acquisitions are here broken down into the maximum number of attempts one of the two spacecraft needed. This is in contrast to the plots in figures 7.12 to 7.14, in which the minimum number of attempts is encoded by the colour.

Item		Acquired	1st	2nd	3rd	4th	Time Out	Fail
Fiber Mode	20 μrad	991	900	69	15	7	9	0
	10 μrad	978	846	99	26	7	20	2
	0 μrad	974	806	120	37	11	13	13
	equal thresholds	937	643	224	55	15	43	20
Gaussian $M^2 = 1$	20 μrad	992	915	69	6	2	7	1
	10 μrad	989	862	108	15	4	8	3
	0 μrad	986	811	132	36	7	9	5
	equal thresholds	943	664	206	58	15	36	20
Gaussian $M^2 = 1.2$	20 μrad	995	933	54	4	4	5	0
	10 μrad	997	891	89	17	0	2	1
	0 μrad	998	854	120	17	7	1	1
	equal thresholds	990	814	140	30	6	6	2

signal, increases the rate of successful acquisitions and reduces the number of sequential attempts needed by the two spacecraft. It can also be seen from the table that the actual value of the threshold does not drastically change the number of timeouts or failures for this case. For equal thresholds and $0 \mu\text{rad}$ margin, the success rate is still 99 % with 81 % of the acquisitions succeed without any of the two spacecraft needing a second attempt.

7.5.5. Time-Outs and Failures

Despite the high success rate of the proposed acquisition algorithm, there are a few time outs and failures for which reasons were identified. Also ways to prevent the failures and time outs are proposed.

Failures only occur, if the total number of subsequent acquisition attempts of any of the two spacecraft exceeds a predefined maximum number $N_{A,\text{max}}$ which was set to $N_{A,\text{max}} = 4$ in all of the simulation runs that are discussed in this section. See Section 7.4.6 for a description of the states involved in the decision process.

On the other hand, *time outs* only occur if the overall time since starting the acquisition exceeds a predefined maximum acquisition time which was set to 300 s.

Time Outs

One reason for time outs is that no simultaneous detections on the two spacecraft occurred and the scan continued until a time out was raised. A reason for this might be that the derivation of the scan time difference τ from equation (7.3.6) is too simplified, in order to guarantee complete coverage of the spatial uncertainty cone for all cases. A more detailed derivation might lead to an improved estimate for the scan time difference.

Also, the amplitude of the sinusoidal motion of the Lissajous scan was set equal to the uncertainty cone radius, and hence no margin for star-camera assembly (SCA) noise was applied. For an initial angular bias close to the edge of the uncertainty cone, SCA noise might lead to a separation between the LOS and the scan track which is larger than desired. An increased scan range should prevent these time out.

Another reason is due to the large frequency noise considered in the simulation and insufficient margin applied to the scan range of the frequency sweep. The frequency noise might accumulate in a way that some of the frequency scan points cannot be reached and the frequency sweep rate is reversed before the beatnote enters the photodiode bandwidth. An increased frequency scan range for large frequency noise will prevent these time outs.

A different mechanism is due to large frequency offsets δf_0 which are close to the

maximal value of $\delta f_0 = -100$ MHz, for which the time before the beatnote enters the photodiode bandwidth reaches 100s and more. This is visible from Figures 7.12 or 7.13, which show the acquisition results for the case of the far-field given by the propagated fibre-mode and the Gaussian beam with $M^2 = 1.0$. The spatial scan times for these cases are nearly equal with $T_S = 7.5$ s to 8 s which are listed in Table 7.3.

If the signal was detected and lost thereafter, the scan will be reinitialised, restarting the spatial and frequency scans. In a second attempt, the earliest entry of the beatnote frequency again occurs about 100s after the scans were restarted, and hence 200s of the allowed 300s are already spent. A third and fourth attempt are unlikely before the acquisition process is stopped due to a time out. In fact, most Time Outs are caused by signal losses in combination with large frequency offsets. For smaller frequency offsets and scan times, these repeated signal losses lead to failures. The reasons for signal losses are described in the following, as far as they could have been identified.

Failures

Failures only occur if at least one of the spacecraft exceeded the maximum number of subsequent acquisition attempts. A running acquisition attempt is interrupted if either the time in the scanning state exceeded the maximum scan time or a signal was lost after the signal verification. See Section 7.4.2 for a description of the scanning state, or Section 7.4.5 for a description of the states involved in initiating tracking after the signal verification. An important mechanism that leads to signal loss is due to a combination of a large Doppler shift and frequency noise. A time series of the signal power and beatnote frequencies is shown in Figure 7.15. The large frequency difference due to the Doppler shift of $2f_D = 4.86$ MHz compared to the bandwidth of the QPD of assumed $F_{PD} = 12$ MHz, from 4 MHz to 16 MHz, results in the master frequency being fixed close to the edge of the frequency band, while the beatnote frequency on the slave spacecraft is fixed to the centre of the photodiode bandwidth. Frequency noise shifts the beatnote frequency outside of the usable photodiode bandwidth, finally resulting in the signal being lost. All failures happening during the simulation runs using the Gaussian beam with $M^2 = 1.2$, as the far-field intensity, are due to this.

A way to mitigate the risk of losing the signal, might be to use the difference of the current and desired frequency bin index of the FFT to compute a correction to the laser frequency and repeatedly correct the frequency if it drifts too far away from the centre of the usable photodiode bandwidth. For smaller frequency noise and larger photodiode bandwidths than assumed here, this problem should vanish.

However, the most important process which gains in importance for smaller angular

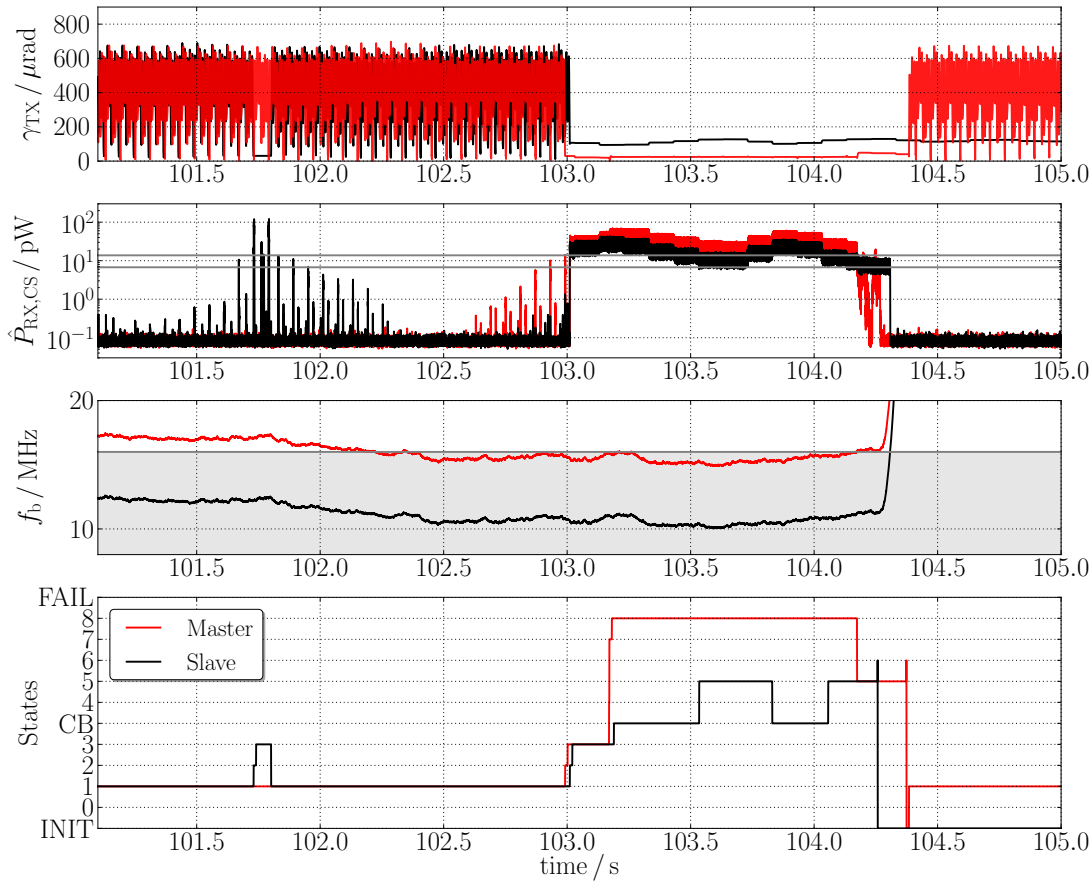


Figure 7.15.: Signal loss during the beatnote centring in state S_{CB} . Due to the large one-way Doppler shift of $f_D = 2.43$ MHz, the difference in the beatnote frequencies is $2f_D = 4.86$ MHz. Fixing the beatnote frequency of the slave to the centre of its PD bandwidth results in a beatnote frequency on the master spacecraft which is close to the edge of its PD bandwidth. Eventually, the frequency noise shifts the beatnote frequency of the master spacecraft out of the PD bandwidth, resulting in signal loss. From top to bottom: Alignment of the transmitted beam relative to the LOS, effective received power returned by the detection algorithm, beatnote frequency and current state of the state machine.

margin between the signal-lost and detection threshold is already being discussed as a motivation for the buffer state S_5 . See Figures 7.10 and Figures 7.11 as well as the explanations given in the description of the buffer state in Section 7.4.6. Here, pointing noise due to the star-camera assembly (SCA) results in increasing misalignments and reduction in the effective received power, during the beatnote centring on the slave spacecraft. For smaller angular margin, smaller pointing errors will already lead to a loss in the signal, increasing the probability for a signal loss. The increase of time outs

and failures for smaller angular margin between the detection and signal-lost thresholds can be seen in Table 7.6.

7.6. Conclusions

In this chapter, an algorithm for an autonomous laser link acquisition for the case of the GRACE Follow-On laser ranging interferometer was presented. In the beginning, the coherent and incoherent sum combinations of the phasemeter channels were evaluated for their usability as indicator for the effective received power in a single phasemeter channel. It was found that for the case of the proposed algorithm, the coherent sum combination is preferable, because the narrower field-of-view for local beam axis misalignments more strongly restricts the transmit beam misalignment. The wider field-of-view for local beam misalignments that is provided by the incoherent sum combinations, allows misalignments of the transmitted beam that may prevent a detection on the distant spacecraft.

Subsequently, it was shown that the detection threshold for the coherent sum detector should be set for perfect alignment of the received beam, based on the effective received power per phasemeter channel on the remote spacecraft. Setting the threshold based on the simultaneous misalignment of both spacecraft, might lead to insufficient signal amplitude in a single phasemeter channel, despite a successful detection.

Thereafter, the spatial scan pattern for the autonomous laser link acquisition was proposed as two Lissajous scans running at nearly equal rates. An expression for the maximum difference in the scan times was derived that depends on the desired capture range.

The presented algorithm yields high success rates of more than 99% for a wide range of considered parameters. The obtained results show that more than 90% of the acquisition runs were successful in a first attempt, if an angular margin of $\theta_{\text{mar}} = 20 \mu\text{rad}$ between the detection and signal-lost thresholds was used. Hence, in at least 90% of the acquisition runs, the acquisition time is less than the time for a complete scan over the five-dimensional uncertainty space. A scan over the complete five-dimensional uncertainty space, that covers the angular and frequency uncertainties, needs approximately 100 s or 105 s for the case of the far-field of a propagated fibre-mode or the Gaussian beam with $M^2 = 1.0$. If the far-field intensity is given by a Gaussian beam with $M^2 = 1.2$, the larger divergence of the beam allows for a coarser scan resolution. For this case, the total scan time reduces to 54.4 s.

8. Summary and Conclusions

In this thesis, a detailed analysis of laser link acquisition for the GRACE Follow-On laser ranging interferometer (LRI) using only heterodyne signals was given. A comprehensive analysis of the interferometer signals, including the simulation of non-Gaussian beams, was carried out. In addition, an algorithm to detect the heterodyne signal in the presence of noise was developed and the distributions of its output were derived. These results were, henceforth, used in combination with realistic models of instrument subsystems to develop a sophisticated simulation of the LRI to extensively test acquisition procedures. Detailed analysis of scan patterns together with the developed high-fidelity simulation were used to investigate an initial line-of-sight calibration scan. For this case, realistic estimates of scan times, limits to the scan resolution and the accuracy of the alignment estimates were obtained. Moreover, an algorithm for an autonomous laser link acquisition was designed and successfully tested with help of the high-fidelity simulation of the LRI. The suitability of the algorithm for the GRACE Follow-On mission could be verified due to its high success rate and limited timing requirements.

In order to simulate non-Gaussian beams such as tophat beams or fibre modes in interferometers, the mode expansion method was implemented in IFOCAD [Hei12], a toolkit to simulate 3D setups of complex interferometers. A comprehensive analysis of the propagation of tophat beams provided simple expressions to estimate the required mode order in the series expansion, as a function of the desired propagation distance, transversal range and tophat radius. For smaller aperture sizes the calculated electric field is accurate close to the aperture even for moderately high mode orders used in the mode decomposition. However, the dependence of the required mode order on the square of the aperture radius renders the mode expansion of the tophat beam computationally expensive for the case of larger aperture radii. The study of the propagation and transformation of the fundamental fibre mode yielded the far-field intensity pattern for GRACE Follow-On taking clipping at the exit aperture into account. The results show that clipping is negligible for aperture radii larger than twice the mode radius of the propagated fibre mode. In the case of negligible clipping an analytical model for the far-field intensity distribution could be obtained that provided important input for the following study on laser link acquisition.

The mode expansion method as is, proved extremely useful as it greatly extended the

type of beams that can be simulated in the framework of IFOCAD. However, for the investigation of the far-field intensity pattern of the fundamental fibre mode, the actually aspheric surface of the fibre outcoupler had to be approximated by a parabolic surface. For the future it would be highly valuable to be able to simulate aspheric surfaces in combination with the mode expansion method. Also, in the decomposition of the tophat beam an effect generally known as Gibbs phenomenon could be observed that originates due to the discontinuous boundary of the electric field amplitude at the edge of the tophat beam. Here, techniques such as low pass filtering the input field might increase the accuracy of the approximation.

The study of laser link acquisition presented in this thesis provided a detailed analysis of laser link acquisition exclusively using heterodyne signals. For this purpose a realistic instrument model was developed, including accurate models of the interferometer signals and the data processing stage. This instrument model served as a key building block for the high-fidelity simulation developed in this thesis, to enable the comprehensive analysis of the line-of-sight calibration scan and the algorithm for the autonomous laser link acquisition. Multiple instances of the simulation code were run in parallel on the ATLAS cluster, in the scope of detailed parameter studies, in order to gather sufficient statistics for the line-of-sight calibration and the autonomous laser link acquisition. Furthermore, spatial scan patterns were analysed in detail. Taking into account pointing noise and the analysed scan patterns, an optimal scan sequence for the initial line-of-sight calibration for the case of large spatial uncertainties was presented. The optimum scan was found to be a fast Lissajous scan, followed by a discretely stepped hexagonal scan and a slow frequency scan. This order results in the smallest scan time and prevents large distortions of the spatial scan pattern due to the orbit prediction error, whereas frequency sweep rates are limited to levels that do not affect the signal-to-noise ratio. For this case, total scan times for the line-of-sight calibration scan were computed for several representative cases. For example, the total scan time is $T = 6.2$ h for the case of an uncertainty cone of radius 3 mrad, 100 frequency scan points and a desired capture range of 150 μ rad.

Limits to the resolution of the spatial scans were found to be 180 μ rad to 190 μ rad for the coherent sum and 230 μ rad to 270 μ rad for the incoherent sum of the photodiode channels. Hence, using the incoherent sum instead of the coherent sum during the line-of-sight calibration scan enables the use of coarser spatial scans which would potentially result in shorter scan times. Furthermore, the remaining alignment biases after the line-of-sight calibration scan were determined with the developed high-fidelity simulation. The remaining bias is bound by the maximum separation between the line-of-sight and the scan track for the case of a discretely stepped hexagonal scan and the slow scanning

axis of the Lissajous raster scan. In contrast, the width of the remaining distribution for the case of the fast scanning axis of the Lissajous scan is determined by the slew rate of the steering mirror at the centre of the Lissajous scan and the computation time for a single Fourier transform. For large uncertainty cone radii the remaining bias in the fast scanning axis may exceed the used line-of-sight to scan-track separation in the spatial scan.

Finally, an algorithm for the autonomous laser link acquisition was proposed that was tested with simulations for a broad range of parameters. The coherent and incoherent sum combinations were reviewed for the case of the autonomous laser link acquisition. The coherent sum combination was found to be a suitable indicator for the signal power in a single photodiode channel. For this case, two methods to determine the detection threshold and the necessary spatial capture ranges were discussed. Also, a slipping Lissajous scan was introduced as a possible scan type and expressions for the total scan time were given depending on the desired spatial capture range. For three different far-field intensity distributions the capture ranges, to ensure sufficient power in a single photodiode channel upon detection, were determined to be in the range between $106 \mu\text{rad}$ to $137 \mu\text{rad}$. For an angular margin of $20 \mu\text{rad}$, applied to the found spatial capture ranges to account for attitude jitter of the star-cameras, the found spatial scan times are in the range of 7.95 s to 4.08 s. For a frequency uncertainty of 100 MHz the total scan times were found in the range of 100 s to 54.4 s. It could be shown that the developed algorithm yields high success rates of more than 99% for all considered cases. Causes for the few remaining time outs and failures were identified and ways to prevent these were proposed.

Future work could focus on the investigation of different approaches to combine larger amounts of samples to generate more accurate line-of-sight estimates, as the estimates generated in this thesis take only a single peak value into account. This would potentially reduce the spatial uncertainty cone for a succeeding autonomous laser link acquisition. One way of improving the estimate for the fast scanning axis in the Lissajous raster scan would be to correlate the information about the scan position, slew rate and length of the Fourier transform to calculate a correction to the estimate.

For the autonomous laser link acquisition it might be beneficial to use the larger field-of-view provided by the incoherent sum combination of the photodiode channels, which provides sensitivity over nearly the complete spatial uncertainty cone that remains after the initial line-of-sight calibration. Investigation of an algorithm that makes use of this might lead to a faster more robust algorithm.

A. Normalisation of LP fibre modes

The on-axial electric field amplitude of the linear polarised fibre modes LP_{lm} is given in equation 2.5.4 and here repeated as follows:

$$E_0 = \sqrt{\frac{2P}{c_l}} \frac{\sigma}{V} \frac{1}{a J_l(\sigma)} \frac{K_l(\tau)}{\sqrt{K_{l-1}(\tau) K_{l+1}(\tau)}}. \quad (\text{A.0.1})$$

The electric field is normalised such that $|E_0|^2$ directly yields the intensity in units of W/m^2 . Here, P is the total power in the fibre mode, V is the normalised frequency or V -parameter. The parameter σ is found by solving the eigenvalue equation (2.5.6) which is connected to the normalised frequency and τ by $V = \sqrt{\sigma^2 + \tau^2}$. The constant c_l is either $c_l = 2\pi$ if $l = 0$ or $c_l = \pi$ if $l \neq 0$. This section provides a derivation of equation (A.0.1).

The total power in the fibre mode is the sum of the power in the core P_{core} and the cladding P_{clad} ,

$$P = P_{\text{core}} + P_{\text{clad}}. \quad (\text{A.0.2})$$

With help of the definition of the electric field of the fibre mode from equation (2.5.3) the power in the core and the cladding can be defined as:

$$P_{\text{core}} = \int_0^{2\pi} d\phi \int_0^a dr r \left| E_0 J_l\left(\frac{\sigma r}{a}\right) \cos(l\phi) \right|^2 \quad (\text{A.0.3})$$

$$P_{\text{clad}} = \int_0^{2\pi} d\phi \int_a^\infty dr r \left| E_0 \frac{J_l(\sigma)}{K_l(\tau)} K_l\left(\frac{\tau r}{a}\right) \cos(l\phi) \right|^2, \quad (\text{A.0.4})$$

where a denotes the fibre core radius, J_l is the Bessel function of the first kind of order l and K_l is the modified Bessel function of the second kind of order l . The cladding is assumed to be of infinite extent, which is within the assumptions made in the derivation of the LP fibre modes by Gloge et al. [Glo71] and does not represent an additional constraint. Both integrals for the power in the core and the cladding can be separated

in the two variables ϕ and r and written as:

$$P_{\text{core}} = |E_0|^2 \int_0^{2\pi} d\phi \cos^2(l\phi) \int_0^a dr r J_l^2\left(\frac{\sigma r}{a}\right) \quad (\text{A.0.5})$$

$$P_{\text{clad}} = |E_0|^2 \frac{J_l^2(\sigma)}{K_l^2(\tau)} \int_0^{2\pi} d\phi \cos^2(l\phi) \int_a^\infty dr r K_l^2\left(\frac{\tau r}{a}\right) \quad (\text{A.0.6})$$

The integral over the angular range is easily solved. The value of the integral is

$$c_l := \int_0^{2\pi} d\phi \cos^2(l\phi) = \begin{cases} 2\pi & \text{if } l = 0, \\ \pi & \text{if } l \neq 0. \end{cases} \quad (\text{A.0.7})$$

Also, the integral over the radial part can be analytically solved by using the following relationships:

$$\int dr r J_l^2(kr) = \frac{r^2}{2} [J_l^2(kr) - J_{l-1}(kr) J_{l+1}(kr)], \quad (\text{A.0.8})$$

$$\int dr r K_l^2(kr) = \frac{r^2}{2} [K_l^2(kr) - K_{l-1}(kr) K_{l+1}(kr)]. \quad (\text{A.0.9})$$

Inserting equation (A.0.8) into (A.0.5) and equation (A.0.9) into (A.0.6) one can compute the powers to:

$$P_{\text{core}} = |E_0|^2 \frac{c_l a^2}{2} J_l^2(\sigma) \left[1 - \frac{J_{l-1}(\sigma) J_{l+1}(\sigma)}{J_l^2(\sigma)} \right] \quad (\text{A.0.10})$$

$$P_{\text{clad}} = |E_0|^2 \frac{c_l a^2}{2} J_l^2(\sigma) \left[\frac{K_{l-1}(\tau) K_{l+1}(\tau)}{K_l^2(\tau)} - 1 \right] \quad (\text{A.0.11})$$

A last step in deriving the final result is to use the eigenvalue equation of the fibre modes (2.5.6) to express the Bessel functions J_l by the modified Bessel functions K_l . The eigenvalue equation is repeated here as follows:

$$\frac{J_{l-1}(\sigma)}{J_l(\sigma)} = -\frac{\tau}{\sigma} \frac{K_{l-1}(\tau)}{K_l(\tau)}. \quad (\text{A.0.12})$$

An alternative formulation of the eigenvalue equation can also be given in terms of Bessel functions of higher order, e.g.:

$$\frac{J_{l+1}(\sigma)}{J_l(\sigma)} = +\frac{\tau}{\sigma} \frac{K_{l+1}(\tau)}{K_l(\tau)}. \quad (\text{A.0.13})$$

The second form can be derived by inserting the following difference equations for the

Bessel functions, which can be found for example in [AS64], into the eigenvalue equation (A.0.12):

$$\frac{2l}{\sigma} J_l(\sigma) = J_{l+1}(\sigma) + J_{l-1}(\sigma) \quad (\text{A.0.14})$$

$$\frac{2l}{\tau} K_l(\tau) = K_{l+1}(\tau) - K_{l-1}(\tau) \quad (\text{A.0.15})$$

Using the two eigenvalue equations (A.0.12) and (A.0.13) the power in the core can also be given in terms of the modified Bessel functions of the second kind K_l by

$$P_{\text{core}} = |E_0|^2 \frac{c_l a^2}{2} J_l^2(\sigma) \left[1 + \frac{\tau^2}{\sigma^2} \frac{K_{l-1}(\tau) K_{l+1}(\tau)}{K_l^2(\tau)} \right] \quad (\text{A.0.16})$$

From here it is simple to calculate the total power of the LP fibre mode which by using the relationship $V = \sqrt{\tau^2 + \sigma^2}$ can be written as

$$P = P_{\text{core}} + P_{\text{clad}} = |E_0|^2 \frac{c_l a^2}{2} J_l^2(\sigma) \frac{V^2}{\sigma^2} \frac{K_{l-1}(\tau) K_{l+1}(\tau)}{K_l^2(\tau)}. \quad (\text{A.0.17})$$

This then directly leads to the anticipated result of the normalisation constant in terms of the power in the fibre mode that is given in equation (A.0.1).

B. Some Statistics

B.1. CDF of the noncentral χ^2 -distribution

The PDF of a random variable \hat{Z} that is distributed with a noncentral χ^2 -distribution with d degrees of freedom and noncentrality parameter λ is given by [Kay09]:

$$f_{\hat{Z}}(z; d, \lambda) = \begin{cases} \frac{1}{2} e^{-(z+\lambda^2)/2} \left(\frac{z}{\lambda^2}\right)^{(d-2)/4} I_{d/2-1}(\lambda\sqrt{z}) & \text{if } z \geq 0, \\ 0 & \text{if } z < 0, \end{cases} \quad (\text{B.1.1})$$

where $I_n(x)$ is the *modified Bessel function of the first kind of order n* that can be given in integral or infinite series form as:

$$I_n(x) = \frac{\left(\frac{1}{2}x\right)^n}{\sqrt{\pi} \Gamma\left(n + \frac{1}{2}\right)} \int_0^\pi \exp(x \cos \theta) \sin^{2n} \theta \, d\theta \quad (\text{B.1.2})$$

$$= \sum_{k=0}^{\infty} \frac{\left(\frac{1}{2}x\right)^{2k+n}}{k! \Gamma(n+k+1)}. \quad (\text{B.1.3})$$

The *cumulative distribution function* (CDF) of the noncentral χ^2 -distribution $F_{\hat{Z}}(x; d, \lambda)$ is then given by the integral:

$$F_{\hat{Z}}(z; d, \lambda) = \int_0^z f_{\hat{Z}}(y; d, \lambda) \, dy. \quad (\text{B.1.4})$$

Unfortunately, no simple form of the integral exists. However, it can be expressed in terms of the *Marcum Q-function* $Q_M(a, b)$ [Nut75] as:

$$F_{\hat{Z}}(z; d, \lambda) = 1 - Q_{d/2}(\lambda, \sqrt{z}). \quad (\text{B.1.5})$$

The Marcum Q-function is defined as:

$$Q_M(a, b) = \int_b^\infty x \left(\frac{x}{a}\right)^{M-1} e^{-(a+x)/2} I_{M-1}(ax) \, dx \quad (\text{B.1.6})$$

B.2. Transforming a PDF

A question arising in the context of the derivation of detection and false alarm probabilities is the transformation of the *probability density function* (PDF) of a random variable under an invertible function. For example let $X \sim U(0, 1)$ be uniformly distributed in the interval $[0, 1]$. Its PDF is then given by $f_X(x) = 1$. Let $g(x)$ be a bijective function from the interval $I = [0, 1]$ to the image of the interval under $g : I \rightarrow g(I)$. Be $Y = g(X)$ the transformed random variable. Then the probability density function $f_Y(y)$ of Y is given by:

$$f_Y(y) = \frac{dg^{-1}(y)}{dy} f_X(g^{-1}(y)) \quad (\text{B.2.1})$$

Bibliography

- [Ada02] David Adam. Gravity measurement: Amazing grace. *Nature*, 416(6876):10–11, Mar 2002.
- [AGJB13] F Ales, P. Gath, U. Johann, and C Braxmaier. Modeling and simulation of a laser ranging interferometer acquisition and guidance algorithm. In *AIAA Guidance, Navigation, and Control (GNC) Conference*. American Institute of Aeronautics and Astronautics, 2013.
- [AS64] Milton Abramowitz and Irene A. Stegun. *Handbook of Mathematical Functions with Formulas, Graphs, and Mathematical Tables*. Dover, New York, ninth dover printing, tenth gpo printing edition, 1964.
- [BAvdVW93] M.W. Beijersbergen, L. Allen, H.E.L.O. van der Veen, and J.P. Woerdman. Astigmatic laser mode converters and transfer of orbital angular momentum. *Optics Communications*, 96(1–3):123 – 132, 1993.
- [BDSE13] Zeb W. Barber, Jason R. Dahl, Tia L. Sharpe, and Baris I. Erkmen. Shot noise statistics and information theory of sensitivity limits in frequency-modulated continuous-wave ladar. *J. Opt. Soc. Am. A*, 30(7):1335–1341, Jul 2013.
- [BGS96] R. Borghi, F. Gori, and M. Santarsiero. Optimization of Laguerre-Gauss truncated series. *Optics Communications*, 125(4-6):197 – 203, 1996.
- [BH84] F. Bayer-Helms. Coupling coefficients of an incident wave and the modes of a spherical optical resonator in the case of mismatching and misalignment. *Appl. Opt.*, 23(9):1369–1380, May 1984.
- [Bor93] DM Boroson. LITE Engineering model 1. Operation and performance of the communications and beam-control subsystems. In Mecherle, GS, editor, *Free-space laser communication technologies V*, volume 1866 of *Proceedings of the society of photo-optical instrumentation engineers (SPIE)*, pages 73–82, 1993.

- [BSMM01] I.N. Bronstein, K.A. Semendjaev, G. Muisol, and H. Mühlig. *Taschenbuch der Mathematik, 5., überarbeitete und erweiterte Auflage*. Harri Deutsch Verlag, 2001.
- [Buc04] John A. Buck. *Fundamentals of Optical Fibers, Second Edition*. Wiley Series in Pure and Applied Optics. John Wiley & Sons, Inc., 2004.
- [CFAA10] Emmanuel Cagniot, Michael Fromager, and Kamel Ait-Ameur. Modeling the propagation of apertured high-order Laguerre-Gaussian beams by a user-friendly version of the mode expansion method. *J. Opt. Soc. Am. A*, 27(3):484–491, Mar 2010.
- [CG09] F. Cirillo and P.F. Gath. Control system design for the constellation acquisition phase of the LISA mission. In *Journal of Physics: Conference Series*, volume 154, page 012014 (7 pp.), 2009 2009. 7th International LISA Symposium, 16-20 June 2008, Barcelona, Spain.
- [Cox85] J. Allen Cox. Point target location using hexagonal detector arrays. In *Proc. SPIE*, volume 0570, pages 148–156, 1985.
- [Cra74] Harald Cramér. *Mathematical Methods of Statistics*. Princeton University Press, Uppsala, 1974.
- [CT65] James W. Cooley and John W. Tukey. An algorithm for the machine calculation of complex Fourier series. *Mathematics of Computation*, 19(90):pp. 297–301, 1965.
- [DBF⁺03] C. Dunn, W. Bertiger, G. Franklin, I. Harris, G. Kruizinga, T. Meehan, S. Nandi, D. Nguyen, T. Rogstad, J.B. Thomas, and J. Tien. The instrument on NASA’s GRACE mission: Augmentation of GPS to achieve unprecedented gravity field measurements. In *GPS World*, volume 14, page 16–28, 2003.
- [DF99] Alfredo Dubra and José A. Ferrari. Diffracted field by an arbitrary aperture. *American Journal of Physics*, 67(1):87–92, 1999.
- [DH98] N. Delen and B. Hooker. Free-space beam propagation between arbitrarily oriented planes based on full diffraction theory: a fast Fourier transform approach. *J. Opt. Soc. Am. A*, 15(4):857–867, Apr 1998.

- [DH01] Nuri Delen and Brian Hooker. Verification and comparison of a fast Fourier transform-based full diffraction method for tilted and offset planes. *Appl. Opt.*, 40(21):3525–3531, Jul 2001.
- [DK08] C.R. Doerr and H. Kogelnik. Dielectric waveguide theory. *Lightwave Technology, Journal of*, 26(9):1176–1187, 2008.
- [Ein16] Albert Einstein. Die Grundlagen der Allgemeinen Relativitätstheorie. *Die Annalen der Physik*, 49(7), 1916.
- [Fin75] David Fink. Coherent detection signal-to-noise. *Appl. Opt.*, 14(3):689–690, Mar 1975.
- [FS10] Andreas Freise and Kenneth A. Strain. Interferometer techniques for gravitational-wave detection. *Living Reviews in Relativity*, 13(1), 2010.
- [GBD94] WC Goltsos, DM Boroson, and CE Devoe. Functional testing of the LITE engineering model. In Mecherle, GS, editor, *Free-space laser communication technologies VI*, volume 2123 of *Proceedings of the society of photo-optical instrumentation engineers (SPIE)*, pages 75–84, 1994.
- [GDT⁺03] M Galassi, J Davies, J Theiler, B Gough, G Jungman, M Booth, and F Rossi. GNU scientific library reference manual , ISBN 0954161734. *URL:* <http://www.gnu.org/software/gsl>, 2003.
- [GKK⁺04] M. Guelman, A. Kogan, A. Kazarian, A. Livne, M. Orenstein, and H. Michalik. Acquisition and pointing control for inter-satellite laser communications. *Aerospace and Electronic Systems, IEEE Transactions on*, 40(4):1239–1248, 2004.
- [Glo71] D. Gloge. Weakly guiding fibers. *Appl. Opt.*, 10(10):2252–2258, Oct 1971.
- [GPMD76] W. A. Gambling, D.N. Payne, H. Matsumura, and R. B. Dyott. Determination of core diameter and refractive-index difference of single-mode fibres by observation of the far-field pattern. *Microwaves, Optics and Acoustics, IEE Journal on*, 1(1):13–17, 1976.
- [GSB⁺13] Oliver Gerberding, Benjamin Sheard, Iouri Bykov, Joachim Kullmann, Juan Jose Esteban Delgado, Karsten Danzmann, and Gerhard Heinzel. Phasemeter core for intersatellite laser heterodyne interferometry: modelling, simulations and experiments. *Classical and Quantum Gravity*, 30(23):235029, 2013.

- [Gut09] Allan Gut. *Multivariate Random Variables*. Springer Texts in Statistics. Springer New York, 2009.
- [Har78] F.J. Harris. On the use of windows for harmonic analysis with the discrete Fourier transform. *Proceedings of the IEEE*, 66(1):51–83, 1978.
- [Hec10] Gerald Hechenblaikner. Measurement of the absolute wavefront curvature radius in a heterodyne interferometer. *J. Opt. Soc. Am. A*, 27(9):2078–2083, Sep 2010.
- [Hei99] G. Heinzl. Electronic noise in interferometers. In *Gravitational Wave Detection II, Proceedings of the 2nd TAMA International Workshop on Gravitational Wave Detection, Tokyo October 19–22*. edited by S. Kawamura, N. Mio, Universal Academy Press, Tokyo, Japan, 1999.
- [Hei12] IFOCAD: A framework of C subroutines to plan and optimize the geometry of laser interferometers. Space Interferometry Group, AEI Hannover, <http://www.lisa.aei-hannover.de/ifocad/>, 2012.
- [HH79] Edwin Hewitt and Robert E. Hewitt. The Gibbs-Wilbraham phenomenon: An episode in Fourier analysis. *Archive for History of Exact Sciences*, 21(2):129–160, 1979.
- [HHL⁺07] K. H. Heng, Y. He, N. Liu, W. D. Zhong, and T. H. Cheng. Beam divergence shaping mechanism in laser intersatellite crosslink system. In *2007 6th international conference on information, communications & signal processing, vols 1-4*, pages 1614–1618, 2007.
- [HKC⁺10] F. Heine, H. Kämpfner, R. Czichy, R. Meyer, and M. Lutzer. Optical inter-satellite communication operational. In *Military Communications Conference, 2010 - MILCOM 2010*, pages 1583–1587, 2010.
- [Hol93] S. Holm. Optimum fft-based frequency acquisition with application to COSPAS-SARSAT. *Aerospace and Electronic Systems, IEEE Transactions on*, 29(2):464–475, 1993.
- [HQW⁺04] Michèle Heurs, Volker M. Quetschke, Benno Willke, Karsten Danzmann, and Ingo Freitag. Simultaneously suppressing frequency and intensity noise in a Nd:YAG nonplanar ring oscillator by means of the current-lock technique. *Opt. Lett.*, 29(18):2148–2150, Sep 2004.

- [HR04] C Hindman and L Robertson. Beaconless satellite laser acquisition - Modeling and feasibility. In *MILCOM 2004 - 2004 IEEE military communications conference, vols 1-3*, IEEE Military Communications Conference, pages 41–47, 2004.
- [HT75] R. A. Hulse and J. H. Taylor. Discovery of a pulsar in a binary system. *The Astrophysical Journal*, 195:L51–L53, January 1975.
- [IK93] Khan M. Iftexharuddin and Mohammad A. Karim. Acquisition by staring focal-plane arrays: pixel geometry effects. *Optical Engineering*, 32(11):2649–2656, 1993.
- [JTN⁺99] T Jono, M Toyoda, K Nakagawa, A Yamamoto, K Shiratama, T Kurii, and Y Koyama. Acquisition, tracking and pointing system of OICETS for free space laser communications. In Masten, MK and Stockum, LA, editor, *Acquisition, tracking, and pointing XIII*, volume 3692 of *Proceedings of the society of photo-optical instrumentation engineers (SPIE)*, pages 41–50, 1999.
- [Kay93] Steven M. Kay. *Fundamentals of Statistical Signal Processing, Volume 1: Estimation Theory*, volume Volume 1 of *Prentice Hall Signal Processing Series*. PTR Prentice-Hall Inc, 1993.
- [Kay09] Steven M. Kay. *Fundamentals of Statistical Signal Processing, Volume 2: Detection Theory*, volume Volum 2. Prentice-Hall Inc, New Jersey, 2009.
- [KB85] Thomas J. Kane and Robert L. Byer. Monolithic, unidirectional single-mode Nd:YAG ring laser. *Opt. Lett.*, 10(2):65–67, Feb 1985.
- [KPK81] W.C. Knight, Roger G. Pridham, and S.M. Kay. Digital signal processing for sonar. *Proceedings of the IEEE*, 69(11):1451–1506, 1981.
- [KS89] J.E. Kaufmann and E.A. Swanson. Laser intersatellite transmission experiment spatial acquisition, tracking, and pointing system. page 102, 1989.
- [Kul12] J. Kullmann. *Development of a digital phase measuring system with microradian precision for LISA*, Diss. 2012.
- [KWS⁺13] Evgenia Kochkina, Gudrun Wanner, Dennis Schmelzer, Michael Tröbs, and Gerhard Heinzl. Modeling of the general astigmatic Gaussian beam

- and its propagation through 3D optical systems. *Appl. Opt.*, 52(24):6030–6040, Aug 2013.
- [LS05] Robert Lange and Berry Smutny. Optical inter-satellite links based on homodyne BPSK modulation: heritage, status, and outlook. In *Proc. SPIE*, volume 5712, pages 1–12, 2005.
- [LYMT11] Xin Li, Siyuan Yu, Jing Ma, and Liying Tan. Analytical expression and optimization of spatial acquisition for intersatellite optical communications. *Opt. Express*, 19(3):2381–2390, Jan 2011.
- [Mar77] D. Marcuse. Loss analysis of single-mode fiber splices. *Bell System Technical Journal*, 56(5):703–718, 1977.
- [MHK05] PG Maghami, TT Hyde, and J Kim. An acquisition control for the laser interferometer space antenna. *Classical and Quantum Gravity*, 22(10, SI):S421–S428, MAY 21 2005. 5th International LISA Symposium/38th ESLAB Symposium, European Space & Technol Ctr, ESA, Noordwijk, NETHERLANDS, JUL 12-15, 2004.
- [MMRW94a] Euan Morrison, Brian J. Meers, David I. Robertson, and Henry Ward. Automatic alignment of optical interferometers. *Appl. Opt.*, 33(22):5041–5049, Aug 1994.
- [MMRW94b] Euan Morrison, Brian J. Meers, David I. Robertson, and Henry Ward. Experimental demonstration of an automatic alignment system for optical interferometers. *Appl. Opt.*, 33(22):5037–5040, Aug 1994.
- [MN98] Makoto Matsumoto and Takuji Nishimura. Mersenne twister: a 623-dimensionally equidistributed uniform pseudo-random number generator. *ACM Trans. Model. Comput. Simul.*, 8(1):3–30, jan 1998.
- [MP92] A. M. Mathai and Serge B. Provost. *Quadratic Forms in Random Variables - Theory and Applications*, volume Vol. 126 of *Statistics: textbook and monographs*. Marcel Dekker, Inc., 1992.
- [MS69] G. A. Massey and A. E. Siegman. Reflection and refraction of Gaussian light beams at tilted ellipsoidal surfaces. *Appl. Opt.*, 8(5):975–978, May 1969.

- [MS09] Kyoji Matsushima and Tomoyoshi Shimobaba. Band-limited angular spectrum method for numerical simulation of free-space propagation in far and near fields. *Opt. Express*, 17(22):19662–19673, Oct 2009.
- [MSW03] Kyoji Matsushima, Hagen Schimmel, and Frank Wyrowski. Fast calculation method for optical diffraction on tilted planes by use of the angular spectrum of plane waves. *J. Opt. Soc. Am. A*, 20(9):1755–1762, Sep 2003.
- [NC12] K Numata and J Camp. Precision laser development for interferometric space missions NGO, SGO, and GRACE Follow-On. *Journal of Physics: Conference Series*, 363(1):012054, 2012.
- [NCKS10] Kenji Numata, Jordan Camp, Michael A. Krainak, and Lew Stolpner. Performance of planar-waveguide external cavity laser for precision measurements. *Opt. Express*, 18(22):22781–22788, Oct 2010.
- [NL09] Victor Nascov and Petre Cătălin Logofătu. Fast computation algorithm for the Rayleigh-Sommerfeld diffraction formula using a type of scaled convolution. *Appl. Opt.*, 48(22):4310–4319, Aug 2009.
- [NP28a] J. Neyman and E. S. Pearson. On the Use and Interpretation of Certain Test Criteria for Purposes of Statistical Inference: Part I. *Biometrika*, 20A(1/2):pp. 175–240, 1928.
- [NP28b] J. Neyman and E. S. Pearson. On the Use and Interpretation of Certain Test Criteria for Purposes of Statistical Inference: Part II. *Biometrika*, 20A(3/4):pp. 263–294, 1928.
- [NP33] J. Neyman and E. S. Pearson. On the Problem of the Most Efficient Tests of Statistical Hypotheses. *Philosophical Transactions of the Royal Society of London. Series A, Containing Papers of a Mathematical or Physical Character*, 231(694-706):289–337, 1933.
- [Nut75] Albert H. Nuttall. Some integrals involving the Q_M function (Corresp.). *Information Theory, IEEE Transactions on*, 21(1):95–96, 1975.
- [OC00] Anna T. O’Neil and Johannes Courtial. Mode transformations in terms of the constituent Hermite–Gaussian or Laguerre–Gaussian modes and the variable-phase mode converter. *Optics Communications*, 181(1–3):35 – 45, 2000.

- [OKT⁺11] Satoru Odate, Chiaki Koike, Hidemitsu Toba, Tetsuya Koike, Ayako Sugaya, Katsumi Sugisaki, Katsura Otaki, and Kiyoshi Uchikawa. Angular spectrum calculations for arbitrary focal length with a scaled convolution. *Opt. Express*, 19(15):14268–14276, Jul 2011.
- [OS61] Harold Osterberg and Luther W. Smith. Closed solutions of Rayleigh’s diffraction integral for axial points. *J. Opt. Soc. Am.*, 51(10):1050–1054, Oct 1961.
- [PPS86] G Picchi, G Prati, and D Santerini. Algorithms for Spatial Laser Beacon Acquisition. *IEEE Transactions on Aerospace and Electronic Systems*, 22(2):106–114, MAR 1986.
- [PR03] Novak S. Petrović and Aleksandar D. Rakić. Modeling diffraction in free-space optical interconnects by the mode expansion method. *Appl. Opt.*, 42(26):5308–5318, Sep 2003.
- [PR05] Novak S. Petrović and Aleksandar D. Rakić. Modeling diffraction and imaging of laser beams by the mode-expansion method. *J. Opt. Soc. Am. B*, 22(3):556–566, Mar 2005.
- [RVF09] Matthew Rodell, Isabella Velicogna, and James S. Famiglietti. Satellite-based estimates of groundwater depletion in India. *Nature*, 460(7258):999–1002, Aug 2009.
- [SAC70] Jr. Stuart A. Collins. Lens-system diffraction integral written in terms of matrix optics. *J. Opt. Soc. Am.*, 60(9):1168–1177, Sep 1970.
- [SCMC99] H.C. So, Y.T. Chan, Q. Ma, and P.C. Ching. Comparison of various periodograms for sinusoid detection and frequency estimation. *Aerospace and Electronic Systems, IEEE Transactions on*, 35(3):945–952, 1999.
- [SH11] B. Sheard and G. Heinzel. *The GRACE-C interferometer*. Albert Einstein Institut, 2011.
- [SHD⁺12] B. S. Sheard, G. Heinzel, K. Danzmann, D. A. Shaddock, W. M. Klipstein, and W. M. Folkner. Intersatellite laser ranging instrument for the GRACE Follow-On mission. *Journal of Geodesy*, 86(12):1083–1095, DEC 2012.
- [Sie86] A.E. Siegman. *Lasers*. University Science Books, Sausalito, CA, 1986.

- [Sie93] Anthony E. Siegman. Defining, measuring, and optimizing laser beam quality. In *Proc. SPIE*, volume 1868, pages 2–12, 1993.
- [SKA01] M Scheinfeild, NS Kopeika, and S Arnon. Acquisition time calculation and influence of vibrations for micro satellite laser communication in space. In Masten, MK and Stockum, LA, editor, *Acquisition, tracking, and pointing XV*, volume 4365 of *Proceedings of the society of photo-optical instrumentation engineers (SPIE)*, pages 195–205, 2001.
- [Sny69] Allan W. Snyder. Asymptotic expressions for eigenfunctions and eigenvalues of a dielectric or optical waveguide. *Microwave Theory and Techniques, IEEE Transactions on*, 17(12):1130–1138, 1969.
- [Sny81] Allan W. Snyder. Understanding monomode optical fibers. *Proceedings of the IEEE*, 69(1):6–13, 1981.
- [Sny07] James J. Snyder. Modeling laser beam diffraction and propagation by the mode-expansion method. *Appl. Opt.*, 46(22):5056–5061, Aug 2007.
- [SSOH83] N. Shibata, Y. Sasaki, K. Okamoto, and T. Hosaka. Fabrication of polarization-maintaining and absorption-reducing fibers. *Lightwave Technology, Journal of*, 1(1):38–43, 1983.
- [ST91] B.E.A. Saleh and M.C. Teich. *Fundamentals of Photonics*. Wiley Series in Pure and Applied Optics. Wiley, 1991.
- [STF81] Nobuhiro Saga, Kazumasa Tanaka, and Otozo Fukumitsu. Diffraction of a Gaussian beam through a finite aperture lens and the resulting heterodyne efficiency. *Appl. Opt.*, 20(16):2827–2831, Aug 1981.
- [SW06] Fabian Shen and Anbo Wang. Fast-Fourier-transform based numerical integration method for the Rayleigh-Sommerfeld diffraction formula. *Appl. Opt.*, 45(6):1102–1110, Feb 2006.
- [TBM⁺09] M Tröbs, S Barke, J Möbius, M Engelbrecht, D Kracht, L d’Arcio, G Heinzl, and K Danzmann. Lasers for LISA: Overview and phase characteristics. *Journal of Physics: Conference Series*, 154(1):012016, 2009.
- [TBR⁺04] Byron D. Tapley, Srinivas Bettadpur, John C. Ries, Paul F. Thompson, and Michael M. Watkins. GRACE measurements of mass variability in the earth system. *Science*, 305(5683):503–505, 2004.

- [TBWR04] B. D. Tapley, S. Bettadpur, M. Watkins, and C. Reigber. The gravity recovery and climate experiment: Mission overview and early results. *Geophysical Research Letters*, 31(9):n/a–n/a, 2004.
- [TeF05] Michael Tröbs, Peter Weßels, and Carsten Fallnich. Power- and frequency-noise characteristics of an Yb-doped fiber amplifier and actuators for stabilization. *Opt. Express*, 13(6):2224–2235, Mar 2005.
- [TeF⁺06] M Tröbs, P Weßels, C Fallnich, M Bode, I Freitag, S Skorupka, G Heinzel, and K Danzmann. Laser development for LISA. *Classical and Quantum Gravity*, 23(8):S151, 2006.
- [TFdV⁺11] R. Thompson, W.M. Folkner, G. de Vine, W.M. Klipstein, K. McKenzie, R. Spero, N. Yu, M. Stephens, J. Leitch, R. Pierce, T. T Y Lam, and D.A. Shaddock. A flight-like optical reference cavity for GRACE Follow-On laser frequency stabilization. In *Frequency Control and the European Frequency and Time Forum (FCS), 2011 Joint Conference of the IEEE International*, pages 1–3, 2011.
- [Tho95] K. S. Thorne. Gravitational Waves. In E. W. Kolb and R. D. Peccei, editors, *Particle and Nuclear Astrophysics and Cosmology in the Next Millenium*, page 160, 1995.
- [TLL05] Shuyun Teng, Liren Liu, and De’an Liu. Analytic expression of the diffraction of a circular aperture. *Optik - International Journal for Light and Electron Optics*, 116(12):568 – 572, 2005.
- [TM80] J. H. Taylor and P. M. McCulloch. Evidence for the existence of gravitational radiation from measurements of the binary pulsar PSR 1913+16. In J. Ehlers, J. J. Perry, and M. Walker, editors, *Ninth Texas Symposium on Relativistic Astrophysics*, volume 336 of *Annals of the New York Academy of Sciences*, pages 442–446, February 1980.
- [TNO02] Toni Tolker-Nielsen and Gotthard Oppenhauser. In-orbit test result of an operational optical intersatellite link between ARTEMIS and SPOT4, SILEX. In *Proc. SPIE*, volume 4635, pages 1–15, 2002.
- [TO87] Kazumasa Tanaka and Naoyuki Ohta. Effects of tilt and offset of signal field on heterodyne efficiency. *Appl. Opt.*, 26(4):627–632, Feb 1987.

- [TTF78] Takashi Takenaka, Kazumasa Tanaka, and Otozo Fukumitsu. Signal-to-noise ratio in optical heterodyne detection for Gaussian fields. *Appl. Opt.*, 17(21):3466–3471, Nov 1978.
- [TY⁺04] Morio Toyoshima, Shiro Yamakawa, Toshihiko Yamawaki, Katsuyoshi Arai, Marcos Reyes, Angel Alonso, Zoran Sodnik, and Benoit Demelenne. Ground-to-satellite optical link tests between japanese laser communications terminal and european geostationary satellite ARTEMIS. In 5338, pages 1–15, 2004.
- [VW13] I. Velicogna and J. Wahr. Time-variable gravity observations of ice sheet mass balance: Precision and limitations of the GRACE satellite data. *Geophysical Research Letters*, 40(12):3055–3063, 2013.
- [WBD⁺00] B. Willke, S. Brozek, K. Danzmann, V. Quetschke, and S. Gossler. Frequency stabilization of a monolithic Nd:YAG ring laser by controlling the power of the laser-diode pump source. *Opt. Lett.*, 25(14):1019–1021, Jul 2000.
- [WBvdB⁺13] B. Wouters, J. L. Bamber, M. R. van den Broeke, J. T. M. Lenaerts, and I. Sasgen. Limits in detecting acceleration of ice sheet mass loss due to climate variability. *Nature Geosci*, 6(8):613–616, Aug 2013. Letter.
- [Wei72] R. Weiss. Electromagnetically coupled broadband gravitational antenna. In *RLE Quarterly Progress Report*, volume 105, page 54, 1972.
- [WFS⁺06] B. Ware, W.M. Folkner, D. Shaddock, R. Spero, P. Halverson, I. Harris, and T. Rogstad. Phase measurement system for inter-spacecraft laser metrology. In *Proceedings of the 2006 Earth Science Technology Conference*, 2006.
- [WHK⁺12] Gudrun Wanner, Gerhard Heinzl, Evgenia Kochkina, Christoph Mahrtdt, Benjamin S. Sheard, Sönke Schuster, and Karsten Danzmann. Methods for simulating the readout of lengths and angles in laser interferometers with Gaussian beams. *Optics Communications*, 285(24):4831 – 4839, 2012.
- [WMS⁺on] D. M. R. Wuchenich, C. Mahrtdt, B. S. Sheard, S. P. Francis, R. E. Spero, J. Miller, C. M. Mow-Lowry, W. M. Klipstein, G. Heinzl, K. Danzmann, D. E. McClelland, and D. A. Shaddock. Laser link acquisition demonstration for the GRACE Follow-On mission. manuscript in preparation.

- [WOMT05] Atsushi Wada, Takumi Ohtani, Yoko Miyamoto, and Mitsuo Takeda. Propagation analysis of the Laguerre-Gaussian beam with astigmatism. *J. Opt. Soc. Am. A*, 22(12):2746–2755, Dec 2005.
- [WZ71] L.A. Wainstein and V.D. Zubakov. *Extraction of Signals from Noise*. Dover Publications, Inc., 1971.

List of publications

- [Wuchenich] D.M.R. Wuchenich, **C. Mahrtdt**, B.S. Sheard, S. Francis, R.E. Spero, J. Miller, C.M. Mow-Lowry, W.M. Klipstein, G. Heinzl, K. Danzmann, D.E. McClelland, D.A. Shaddock, *Laser link acquisition demonstration for the GRACE Follow-On mission*, manuscript in preparation.
- [Kochkina] E. Kochkina, G. Heinzl, G. Wanner, V. Müller, **C. Mahrtdt**, B. Sheard, S. Schuster and K. Danzmann, *Simulating and Optimizing Laser Interferometers*, ASP Conference Series **467** (2012)
- [Wanner] G. Wanner, G. Heinzl, E. Kochkina, **C. Mahrtdt**, B.S. Sheard, S. Schuster, K. Danzmann, *Laser Ranging Interferometer for GRACE follow-on*, ICSSO conference proceedings (9-12 October 2011).
- [Sheard] B. Sheard, M. Dehne, O. Gerberding, H. Heinzl, **C. Mahrtdt**, V. Müller, and K. Danzmann, *Laser interferometry for future satellite gravimetry missions*, GEOTECHNOLOGIEN Science Report **17**, 160 (2010).
- [Harms] J. Harms, **C. Mahrtdt**, M. Otto, M. Prieß and K. Danzmann, *Subtraction-noise projection in gravitational-wave detector networks*, Phys.Rev. D **77**, 123010 (2008).

Acknowledgements

The final words in this thesis are devoted to thanking the many people that accompanied me a short or long time during the past years and made this work so enjoyable. The last years have been a fascinating and instructive time.

At first I want to thank Karsten Danzmann for giving me the opportunity to work at the Albert Einstein Institute, for his generous support and motivating words throughout the years.

Working on the GRACE Follow-On project for the last years was an exciting experience, especially because it was only well after the first year of my PhD that the project was initiated. Seeing it evolve from scratch was inspiring and highly motivating.

I am much obliged to Gerhard Heinzel for supervising this thesis and sharing his profound expertise in programming, optical simulations and physics in general with me. Without his continuous support and advice this work wouldn't have been possible.

Many thanks also go to Benjamin Sheard for answering every single question that I could have thought of in detail and for his outstanding job in leading the GRACE Follow-On division in the Space Interferometry Group. This work profited in many ways from his advice.

I also thank all other members of the Space Interferometry Group for the excellent atmosphere. It was a pleasure being part of it.

I am indebted to Daniel Shaddock for his noble support and inviting me to work with his group on the acquisition experiment. I learned a lot from the numerous helpful discussions and by working on the experiment which greatly helped me carry out the research that is written down in this thesis. Special thanks go to Danielle Wuchenich, Sam Francis and Conor Mow-Lowry for enjoyable times in the lab but also to the rest of the group for being excellent hosts during my stay.

I thank Bob Spero and Bill Klipstein for helpful discussion and input.

Also, many thanks go to the people who proof-read this thesis which are (in alphabetical order): Christoph Affeldt, Marina Dehne, Christian Gräf, Gerhard Heinzel, Birthe Klebow, Natalia Korsakova, Dirk Schütte, Thomas Schwarze, Benjamin Sheard and Gudrun Wanner. It goes without saying that all remaining errors are my own responsibility.

Last but not least, I owe my family a debt of gratitude for continued support throughout the last years and especially the last months.

Curriculum Vitae

✉ cmahrdt@web.de

Personal Details

Full Name Christoph Mahrdt
Date of Birth 29 January 1983
Place of Birth Lemgo

Education and Employment

- since 11/2013 **Scientific Assistant position**, *Max Planck Institute for Gravitational Physics*, Hannover.
- 02/2009 – present **Doctoral studies in the Space Interferometry Group**, *Max Planck Institute for Gravitational Physics*, Hannover.
- 02/2009 – 10/2013 **Scientific Assistant position**, *Institute for Gravitational Physics, Leibniz Universität Hannover*.
- 09/2012 – 10/2012 **Visiting Student**, *Centre for Gravitational Physics, Australian National University*, Canberra.
- 09/2011 – 10/2011 **Visiting Student**, *Centre for Gravitational Physics, Australian National University*, Canberra.
- 06/2008 **Degree “Diplom Physiker”**, awarded by *Leibniz Universität Hannover*.
- 10/2005 – 07/2006 **Physics studies**, *Lancaster University*, Lancaster, United Kingdom.
- 10/2002 – 07/2008 **Physics studies**, *Leibniz Universität Hannover*.
- 06/2002 **Abitur at Engelbert Kämpfer Gymnasium**, *Lemgo*.